NEW CHEMICAL TOOLS TO STUDY RNA DISTRIBUTION IN NEURONAL CELLS

DISSERTATION

zur Erlangung des Doktorgrades der Naturwissenschaften

Vorgelegt beim Fachbereich

Biochemie, Chemie und Pharmazie

der Johann Wolfgang Goethe-Universität

in Frankfurt am Main

von

Robin Klimek

aus Bad Homburg

Frankfurt am Main 2022

Vom Fachbereich Biochemie, Chemie und Pharmazie der

Johann Wolfgang Goethe-Universität Frankfurt als Dissertation angenommen.

Dekan:	Prof. Dr. Clemens Glaubitz
1. Gutachter:	Prof. Dr. Alexander Heckel
2. Gutachter:	Prof. Dr. Josef Wachtveitl
Datum der Disputation:	24.11.2022

Publikationen

(*‘ – die Beiträge dieser Autoren sind als gleich anzusehen)

[I] Differential regulation of local mRNA dynamics and translation following long-term potentiation and depression

P. G. Donlin-Asp, C. Polisseni, R. Klimek, A. Heckel, E. Schuman,

Proc. Natl. Acad. Sci. U. S. A. **202**1, *118* (13), DOI: 10.1073/pnas.2017578118

[II] Visible light-activatable Q-dye molecular beacons for long-term mRNA monitoring in neurons

R. Klimek, P. G. Donlin-Asp, C. Polisseni, V. Hanff, E. Schuman, A. Heckel,

Chem. Commun. **2021**, *57* (5), 12683-12686, DOI: 10.1039/D1CC05664F

[III] Photo-tethered molecular beacons for superior light-induction

R. Klimek*, M. Wang*, V. R. McKenney, E. Schuman, A. Heckel,

Chem. Commun. **2021**, *57*, 615-618, DOI: 10.1039/D0CC06704K

[IV] Inactivation of competitive decay channels leads to enhanced coumarin photochemistry

R. Klimek*, M. Asido*, V. Hermanns, S. Junek, J. Wachtveitl, A. Heckel,

Chem. Eur. J.. **2022**, 28, e202200647, DOI: 10.1002/chem.202200647

Table of content

1. Zusammenfassung

In den vergangenen Jahrzehnten war RNA das Forschungsobjekt unzähliger Universitäten und Pharmaunternehmen weltweit. Doch auch die breite Bevölkerung ist mit der Zulassung der mRNA basierten COVID-19 Impfstoffe[1] mit dem Aufbau und der Wirkweise von Nukleinsäuren in Berührung gekommen. Viele Wissenschaftler gehen davon aus, dass RNA in Zukunft eine immer größere Rolle in der Medizin und der Behandlung von Krankheiten spielen wird.[2–4] Doch nicht nur die Entwicklung von therapeutischen Oligonukleotiden ist von großem Interesse. Um die unzähligen Wirkungsmechanismen von Nukleinsäuren zu verstehen, ist noch immer viel Grundlagenforschung nötig. Dabei ist es zum Beispiel wichtig zu verstehen, wo Nukleinsäuren in der Zelle hergestellt werden, wohin sie transportiert werden und wie sie am Ankunftsort regulatorisch wirken. Da DNA und RNA mit bloßem Auge nicht sichtbar ist, wurden in den vergangenen Jahren viele Werkzeuge und Methoden entwickelt, um sie sichtbar zu machen.[5,6] Neben Protein-basierten Methoden (MS2, Pepper, dCas3), Fluorophor-Aptamer Paaren (Mango, Spinach, Broccoli) und Fluorophor-Quencher Paaren (SRB-2, Riboglow) haben sich vor allem molecular beacons als Werkzeug für die RNA-Visualisierung etabliert.[6] Gegenüber den zuvor genannten Methoden haben Sie den großen Vorteil, dass sie nicht nur zur Visualisierung exogener synthetischer, sondern auch von endogener RNA geeignet sind.

Die vorliegende Arbeit befasst sich mit der Synthese und Entwicklung von neuen Werkzeugen zur Visualisierung endogener RNA. Dabei wurden sowohl herkömmliche, als auch lichtaktivierbare Werkzeuge synthetisiert und in Zellexperimenten angewandt. Im ersten Schritt wurden molecular beacons zur Visualisierung von CamK2, Beta-actin und PSD95 mRNA hergestellt, die anschließend am Max-Planck-Institut für Hirnforschung in Frankfurt verwendet wurden, um deren Transportdynamiken in Neuronen zu untersuchen.[7] Molecular beacons sind Oligonukleotide mit einer Länge von ca. 25-35 Basen, die eine Stamm-Schleife Struktur ausbilden. Die Schleifenregion ist komplementär zur Ziel-RNA und der Stamm ist selbstkomplementär. An einem Ende des Oligonukleotids ist ein Fluorophor angebracht, am anderen Ende ein Quencher. Durch die räumliche Nähe der beiden Chromophore in der Stamm-Schleife Struktur wird das Emissionslicht des Fluorophors durch den Quencher abgefangen. Nur wenn der molecular beacon mit der Ziel-RNA hybridisiert, werden Fluorophor und

Quencher räumlich getrennt und es kann ein Fluoreszenzsignal detektiert werden. Im ersten Teilprojekt dieser Arbeit wurden insgesamt acht molecular beacons hergestellt. Die Zielsequenzen der Sonden waren in der 3‘-UTR von CamK2, Beta-actin und PSD95 mRNA lokalisiert. Es wurden pro mRNA zwei komplementäre Sonden verwendet. Eine davon war mit ATTO 565/BHQ2 und die andere mit ATTO 647N/BBQ-650 als Fluorophor/Quencher Paar ausgestattet. Weiterhin wurden zwei Sonden mit den genannten Chromophoren gegen GFP-mRNA synthetisiert, welche später als negativ-Kontrolle eingesetzt wurden. Zur Verbesserung der Stabilität gegenüber Nukleasen und der Hybridisierungsaffinität gegenüber RNA wurde ein 2’-OMe-Rückgrat verwendet. Die Sonden wurden nach erfolgreicher Synthese von Paul G. Donlin-Asp am Max-Planck-Institut für Hirnforschung in Neuronen transfiziert und die mRNA/beacon Hybride mit einer automatisierten Analyse-Pipeline, geschrieben von Claudio Polisseni, analysiert. Es ist bekannt, dass mRNA im Zellkern aus DNA transkribiert wird und im Anschluss zu den einzelnen Synapsen transportiert wird um dort lokal in Proteine übersetzt zu werden.[8] In der vorliegenden Arbeit wurde dieses Transportverhalten nun genauer untersucht. Es zeigte sich, dass mRNAs nicht nur einzeln, sondern auch in multimeren Komplexen, sogenannten „RNA-granules“ entlang der Dendriten transportiert werden. Die Transportgeschwindigkeiten der drei untersuchten mRNAs waren dabei sehr ähnlich (ca. 1 μm/s), sowohl für den Transport vom Zellkern weg (anterograde), als auch zum Zellkern zurück (retrograde). Auch die insgesamt zurückgelegten Distanzen unterschieden sich kaum. Alle drei mRNAs wurden im Durchschnitt etwa 20 μm über den gesamten Untersuchungszeitraum transportiert. Im nächsten Schritt wurde untersucht, ob die Assoziation von Ribosomen an der mRNA einen Einfluss auf die Transporteigenschaften hat. Dabei wurden die Zellen von Paul G. Donlin-Asp einmal mit Puromycin behandelt, welches eine Dissoziation von Ribosom und mRNA zur Folge hat und einmal mit Anisomycin, das die assoziierten Ribosomen an der mRNA einfriert. In diesen Experimenten wurde festgestellt, dass der Translationsstatus einen direkten Einfluss auf die Transporteigenschaften hat. Während die generelle Transportgeschwindigkeit gleich blieb, hat sich der Anteil der beweglichen mRNAs bei der Behandlung mit Puromycin deutlich erhöht. Dies kann damit erklärt werden, dass die mRNAs nicht mehr von den Ribosomen für eine lokale Translation festgehalten werden. Gleichzeitig hat sich der Anteil der temporär stationären mRNAs bei der Behandlung mit Anisomycin erhöht. Durch das Einfrieren der Ribosomen an der mRNA konnte diese nicht weiter

transportiert werden. Die zurückgelegten Distanzen der einzelnen mRNAs haben sich nicht signifikant geändert. Es wurden zusätzliche Experimente zum Transport unter Langzeitpotentierung (long-term potentiation, LTP) und Langzeitdepression (long-term depression, LTD) der Neuronen durchgeführt. Diese werden in der vorliegenden Zusammenfassung nicht genauer beschrieben. Insgesamt konnte gezeigt werden, dass sich chemisch modifizierte molecular beacons hervorragend zur Untersuchung von endogener RNA eignen. Durch die hohe Selektivität und Affinität zur Zielsequenz können gezielt Transporteigenschaften von mRNA in lebenden Zellen untersucht werden. Dennoch haben molecular beacons einen Nachteil. Die Untersuchungsdauer unter dem Mikroskop ist limitiert, da die organischen Fluorophore und Quencher nach einer gewissen Anzahl an Anregungen beginnen zu bleichen. Zwar wurden bei den oben beschriebenen Sonden bereits sehr photostabile Chromophore verwendet, jedoch war der Untersuchungszeitraum trotzdem auf nur 20 Minuten begrenzt. Daher wurden im nächsten Schritt chemisch modifizierte molecular beacons entwickelt, welche diese Limitierung umgehen können. Durch chemische Modifikationen wurde den Sonden eine lichtaktivierbare Komponente hinzugefügt mit dem Ziel die Anregungsfrequenz des Lasers über den Beobachtungszeitraum zu verringern. Genau gesagt wurde ein zweiter Quencher kovalent am Fluorophor über eine photolabile Schutzgruppe verknüpft. Durch dieses Design wurde das Emissionslicht des Fluorophors auch im hybridisierten Zustand mit der Ziel-RNA durch den zweiten Quencher abgefangen. Durch Licht mit einer Wellenlänge von 405 nm konnte die photolabile Schutzgruppe und damit der zweite Quencher abgespalten werden. Somit wurde nur ein Fluoreszenzsignal erhalten, wenn sowohl eine Hybridisierung, als auch eine Lichtaktivierung stattgefunden hat. Zur Realisierung dieses Konzepts wurde zunächst die photolabile Schutzgruppe – in diesem Fall ein Cumarin-Derivat – als Phosphoramidit über eine achtstufige Synthese hergestellt. Es wurde ein Cumarin-Derivat gewählt, da sich diese Chromophore, im Gegensatz zum kommerziell erhältlichen *o*-Nitrobenzyl, mit sichtbarem Licht photolysieren lassen. Für Anwendungen in Zellen ist es vorteilhaft, Licht längerer Wellenlängen zu verwenden, da dieses eine geringere Zelltoxizität aufweist.[9,10] Gleichzeit ist das Absorptionsspektrum von Cumarin aber noch nicht so weit rotverschoben, als dass es mit der Absorption des verwendeten Fluorophors ATTO 565 interferiert. Somit war eine orthogonale Anregung möglich. Nach erfolgreicher Synthese des Phosphoramidits wurden drei lichtaktivierbare molecular beacons per Festphasensynthese hergestellt.

Als Zielsequenzen wurden die bereits zuvor positiv getesteten 3'UTR Abschnitte aus dem ersten Teilprojekt gegen CamK2, Beta-actin und eine Negativkontrolle gegen GFP-mRNA verwendet. Die *in vitro* Fluoreszenzexperimente der lichtkativierbaren molecular beacons zeigten das gewünschte Verhalten. Bei Hybridisierung mit der komplementären RNA war kein signifikanter Fluoreszenzanstieg zu beobachten, da das Emissionslicht vom zweiten Quencher abgefangen wurde. Auch bei Photolyse der Schutzgruppe, ohne Zugabe einer komplementären Sequenz, blieb eine signifikante Erhöhung der Fluoreszenzintensität aus, da der Quencher am gegenüberliegenden Ende des Oligonukleotids noch immer in räumlicher Nähe war. Nur wenn Lichtaktivierung und die Anwesenheit einer Ziel-RNA gegeben waren, konnte ein deutliches Emissionslicht detektiert werden. Die lichtaktivierbaren molecular beacons wurden im Anschluss von Paul Donlin-Asp am Max-Planck-Institut für Hirnforschung in kultivierte hippocampale Neuronen transfiziert. Vor der Aktivierung mit einem 405 nm Laser konnte lediglich Hintergrundfluoreszenz detektiert werden. Ein definiertes Areal im Zellkörper wurde dann mit dem Laser lokal bestrahlt, woraufhin dort eine starke Erhöhung der Fluoreszenzintensität beobachtet wurde. Dieses Experiment bewies, dass eine lokale Aktivierung in Zellen ohne toxische Nebeneffekte möglich war. Nun konnten die mRNA/molecular beacon Hybride in der Zelle untersucht werden. Da durch die lokale Aktivierung im Zellkörper der genaue Ursprung jedes fluoreszenten Signals bekannt war, konnte die Anregungsfrequenz für den Fluorophor deutlich gesenkt werden. Anstatt ein Mal pro Sekunde anzuregen, wie es im ersten Teilprojekt der Fall war, wurde die Frequenz mit den lichtaktivierbaren molecular beacons auf ein Mal alle zehn Minuten reduziert. Dies hatte zur Folge, dass die mRNAs über einen Zeitraum von 14 Stunden beobachtet werden konnten, anstatt lediglich 20 Minuten. Mit dieser Technik war es zum Beispiel möglich, die Halbwertszeit zu berechnen, die eine mRNA braucht um die gesamten Dendriten zu populieren. Mit dieser Art der lichtaktivierbaren molecular beacons konnte also mit Hilfe eines Laser-Pulses eine Subpopulation an mRNAs sichtbar gemacht werden. Jedoch waren alle molecular beacons dazu in der Lage mit ihren Ziel-Sequenzen zu hybridisieren, sobald sie transfiziert wurden. Im nächsten Schritt sollte nicht nur die Visualisierung von RNA, sondern auch die Hybridisierung durch Licht steuerbar gemacht werden. Dafür wurde eine neue Klasse von molecular beacons entwickelt, die über photolabile Schutzgruppen zyklisiert wurden. Durch die Zyklisierung sollte es ihnen nicht mehr möglich sein, mit der Ziel-RNA zu hybridisieren. Um dieses Konzept zu realisieren,

wurde zunächst ein Cytidin-analoges Phosphoramidit hergestellt, das an seinem Phosphor(III)-Atom eine photolabile Schutzgruppe trug. Diese Schutzgruppe war mit einem Alkin-Rest verknüpft, welcher sich photolytisch abspalten lässt. Das Phosphoramidit wurde an zwei Positionen in der Schleifenregion eines molecular beacons angebracht. Anschließend wurden die beiden Alkine mithilfe eines Bisazids über eine kupferkatalysierte Cycloaddition miteinander verknüpft. Das resultierende zyklische Oligonukleotid war nicht mehr in der Lage, mit einem komplementären Gegenstrang zu hybridisieren, was sich durch *in vitro* Fluoreszenzmessungen beweisen ließ. Die Zugabe der Zielsequenz führte zu keinem Fluoreszenzanstieg. Erst nach Aktivierung mit Licht konnte die volle Aktivität des molecular beacons hergestellt werden. Die Sonde wurde im Anschluss von Mantian Wang am Max-Planck-Institut für Hirnforschung in kultivierte hippocampale Neuronen transfiziert. Vor Lichtaktivierung konnte lediglich Hintergrundfluoreszenz in der Zelle beobachtet werden. Nach Bestrahlung des Zellkörpers mit 365 nm Licht konnten definierte Hybridisierungssignale detektiert werden. Mit diesem Experiment wurde gezeigt, dass die Hybridisierung eines molecular beacons lokal in einer lebenden Zelle mit Licht gesteuert werden kann. Dies grenzt die gerade beschriebenen Sonden deutlich von den vorher vorgestellten ab, welche ihre Anwendung nicht in der Hybridisierungskontrolle, sondern in der Verlängerung der Visualisierungsdauer fanden.

In den bisher beschriebenen Teilprojekten ging es es darum, Oligonukleotide mit lichtaktivierbaren Elementen auszustatten und lokal in Zellen zu aktivieren. Dabei ist es bei Zellexperimenten besonders wichtig, Schutzgruppen zu verwenden, die besonders effizient photolysiert werden, um lichtinduzierte Zellschänden zu vermeiden. Daher wurde im letzten Teil der vorliegenden Arbeit die Photolyseeffizienz einer Cumarin-Schutzgruppe, wie sie im zweiten Teilprojekt verwendet wurde, systematisch optimiert. Da zur Optimierung von Cumarin-Schutzgruppen wenig bekannt ist, wurde sich an der breit untersuchten Optimierung von Cumarin-Fluorophoren orientiert.[11] Diese besagt, dass es vorteilhaft ist, alternative Abregungspfade wie *twisted intramolecular charge transfer* (TICT) zu inhibieren, welche hauptsächlich durch freie Rotation um den Elektronendonor am Cumarin zustande kommen.[12] Daher wurden vier neue Cumarin-Schutzgruppen hergestellt, welche in ihrer Rotation um die C-N Bindung durch einen Ringschluss eingeschränkt waren. Sowohl Pholyseexperimente, als auch Fluoreszenzmessungen, welche zum

Teil von Volker Hermanns und Marvin Asido am Institut für Physikalische und Theoretische Chemie durchgeführt wurden, zeigten einen deutlichen positiven Effekt der neuen rigiden Cumarin Strukturen, verglichen mit häufig verwendetem 7-Diethylaminocumarin (DEACM). Transiente Absorptionsmessungen von Marvin Asido gaben Einblicke in die zugrunde liegenden photophysikalischen Effekte. Dabei konnte zum Beispiel beobachtet werden, dass das Anbringen einer Abgangsgruppe die Lebensdauer des angeregten Zustands deutlich reduziert. Insgesamt konnte durch die Planarisierung des Cumarin Grundgerüstes eine Verbesserung der Photolyseffizienz bei 405 nm um den Faktor 12 erreicht werden. Es wird erwartet, dass die neue Cumarin-basierte Schutzgruppe in Zukunft eine breite Anwendung in Zellexperimenten findet, wie sie in den vorherigen Teilprojekten beschrieben wurden.

2. Introduction

Today's knowledge of the human genome, as well as DNA and RNA, goes back more than a hundred years.[13] Many scientists have been involved in studying the structure and function of nucleic acids.[14] All discoveries are culminating today in modern RNA therapeutics and vaccines that are also used to combat the global pandemic.[15] A brief history: The discovery of nucleic acids began in 1869 when Johann Friedrich Miescher discovered the so-called “nuclein”. He described it as a very different substance from the proteins he was looking for in white blood cells.[16] Later his discovery was renamed “nucleic acid”. In 1919, Phoebus Levene – a Russian biochemist – discovered that nucleic acids are macromolecules consisting of phosphorus, sugar and four nitrogen-containing bases.[17] These are adenine (A), guanine (G), cytosine (C) and thymine (T). In 1944, it was proven by Oswald Avery, Colin MacLeod and Maclyn McCarty in New York that DNA is a substance that carries the genetic information in bacteria.[18,19] The rules of base pairing were first published in 1950 by Erwin Chargaff. Adenine pairs with thymine and cytosine with guanine through hydrogen-bonding.[20] However, one of the most prominent findings about DNA was the discovery of its double-helix structure in 1953. This was mostly credited to James Watson and Francis Crick (“Watson-Crick base pairing”).[21] Later it turned out that they solely used the data of other scientists, such as Rosalind Franklin. Her X-ray diffraction data of crystallized DNA was a milestone to understanding the DNA double-helix.[22] In 1962, the Nobel price has been awarded to Watson and Crick, together with Maurice Wilkins for their research on the nucleic acid structure. Unfortunately, Rosalind Franklin did not receive the recognition she deserved during her lifetime.

A year earlier, however, it was discovered that DNA is not the only information carrier in organisms.[23,24] mRNA serves as a messenger between DNA as genetic material and the proteins produced.[25] The central dogma of molecular biology was established. It states that DNA is converted into RNA (transcription) and that this is subsequently translated into proteins by the ribosomes (translation).[26] However, it turned out that transferring genetic information was not the only function that RNA has. In the many decades that followed up to the present day, new mechanisms and functions of RNA that are not only based on being transported and translated have been discovered all the time.[27] The so-called “regulatory RNA” seems to play important roles at many levels of epigenetic processes that control the differentiation and development of diverse

organisms. Also, RNA seems to play an important role in human evolution. Some of the most widely studied regulatory mechanisms are alternative splicing, alternative polyadenylation and RNA editing.[28] Today, knowledge of these regulatory processes can also be used for therapeutic purposes.[29] These include antisense oligonucleotides, aptamers, small interfering RNAs (siRNAs), microRNAs and mRNA.[4] RNA therapeutics can be used today to treat for example spinal muscular atrophy, Duchenne muscular dystrophy, dry eye disease and many others.[30]

In addition to the therapeutic use, in recent years, particular emphasis has been placed on the precise localization of regulatory RNA processes in individual cells.[31] Due to the heterogeneous structure of cells, it is necessary to be able to investigate the underlying mechanisms in a spatially and temporally resolved manner. Hundreds of RNAs are known to accumulate at various cellular structures where they contribute to natural cellular function.[32,33] To study the exact mechanism of action of different RNAs in the cell, it is necessary to develop chemical tools to visualize them. Therefore, the presented work addresses the development of chemical probes to study the distribution of mRNA and non-coding RNA in living cells. Both conventional fluorescent tools are being developed to monitor RNA and RNP distribution in cells, as well as probes that can be activated with light. In this context, the use of light enables even higher spatial and temporal precision as a non-invasive external stimulus. In the course of this work, light-activatable tools are incorporated into probes for RNA localization. Also, completely novel photocleavable elements with improved properties are designed and developed. This will be yet another small contribution towards understanding the immense complexity of the functions of nucleic acids in living organisms.

2.1. Photolabile protecting groups

In order to investigate or control spatially and temporally resolved processes, it is necessary to develop and use chemical tools that allow precise activation. It is often difficult to monitor biochemical processes with sufficient accuracy, especially in cell tissue and other organisms. One of the most prominent approaches to achieving accurate control is the use of photolabile protecting groups (PPGs) that are also known as photocages.[34–38] PPGs are small (usually organic) compounds that inactivate the chemical or biological function of a target molecule. When the inactivated compounds are exposed to light of a specific wavelength, a directed bond break is induced, and the target molecules are released. This spatio-temporal activation can be used, for example, for on demand drug release,[39] controlling coagulation in blood,[40] or promoting skin repair in diabetic mice.[41] The choice of the protection group and the type of regulation depends specifically on the biological question. The following chapter will provide an overview of the known to date PPGs and how their photochemical properties can be modulated.

2.1.1. Design and structure of photocages

When it comes to designing PPGs, several factors are essential.[34] The compound needs a high extinction coefficient at the wavelength used. It should be soluble and stable in the biological medium. Furthermore, the PPGs should not be toxic or generate toxic reaction products. In addition to these general properties, two parameters of PPGs in particular have been optimized in recent years – the uncaging cross section (1) and the absorption wavelength (2). The uncaging cross section (1) is defined as the product of the extinction coefficient ε at the irradiated wavelength and the uncaging quantum yield Φ_u, which in turn is the quotient of the photons used for photolysis divided by the total amount of photons added. To improve the uncaging cross section, a number of attempts were made to inhibit competitive relaxation pathways of PPGs in the excited state.[42–45] Important parameters for this optimization will be discussed later. Nevertheless, it is also important to have PPGs with absorption properties in the red-light spectrum (parameter 2). In the so-called phototherapeutic window,[46] the applied light can be optimally used by the chromophore since no parts of the biological tissue absorb light in this area. The phototherapeutic window is located around 600 nm to 850 nm. A large number of PPGs are available today to cover the entire spectrum

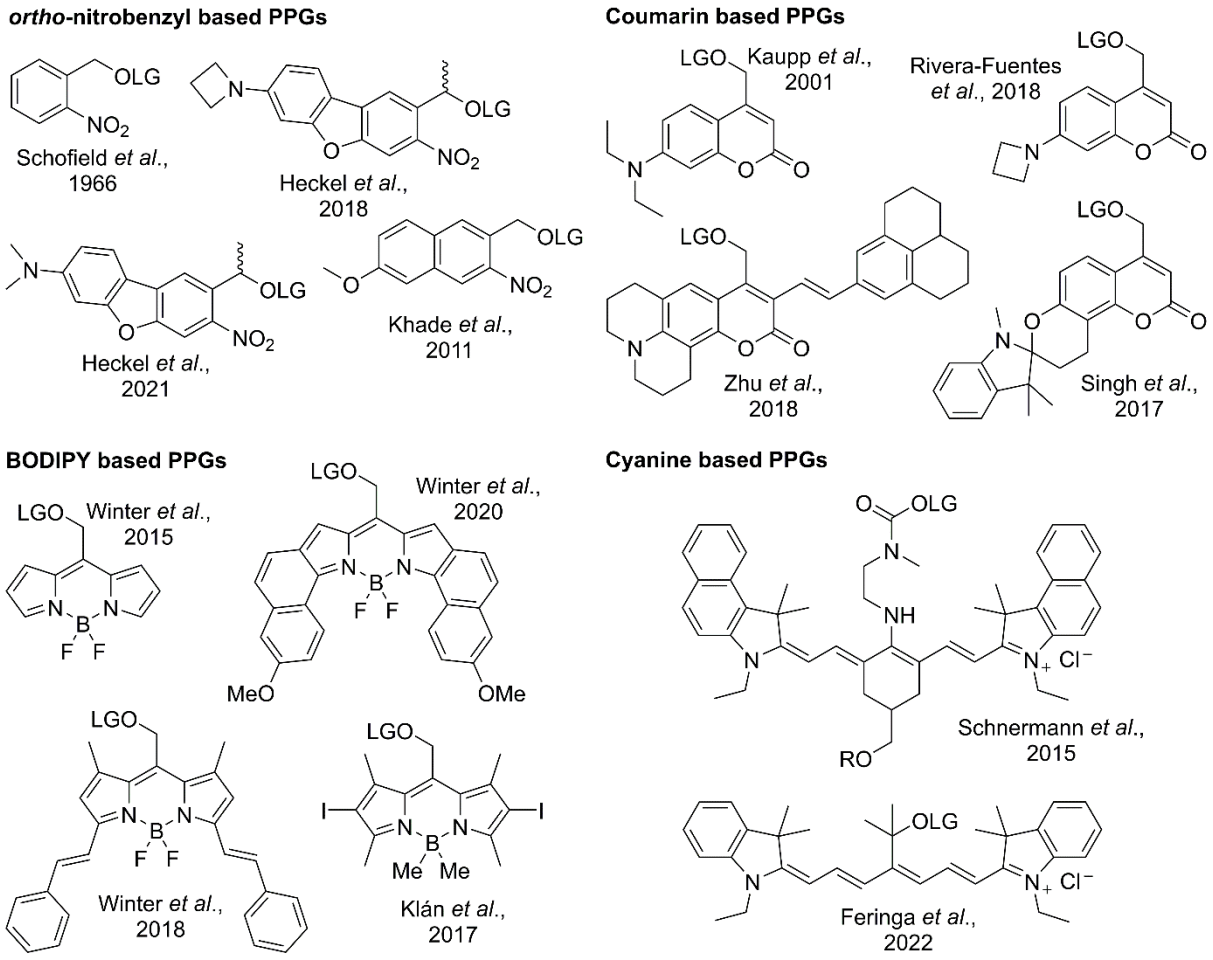

Figure 1: Overview of the most commonly used photolabile protecting groups in the literature. They can be divided into four groups. (i) ortho-nitrobenzyl-based PPGs, (ii) coumarin-based PPGs, (iii) BODIPY-based PPGs and (iv) cyanine-based PPGs.

from UV to NIR light.[34,47,48] An overview of some well-characterized protection groups known from the literature is given in Figure 1.[40,42,56–59,43,49–55] Although now there are a great number of molecular scaffolds for PPGs, four chromophore classes are mostly used as protecting groups.

The first class is the *ortho*-nitrobenzyl (*o*NB) based compounds. Their photochemical activity was discovered by Barltrop *et al*. in 1966.[60] Advantages of these compounds are the simple synthesis and the possibility to release a large number of functional groups.[61–63] However, the drawback is the absorption maximum, which is only around 260 nm for unmodified *o*NB. An improvement of the *o*NB protecting group is nitrodibenzofuran (NDBF), in which the π-system is synthetically expanded.[64] Ellis-Davies *et al.* shifted the absorption wavelength above 300 nm and demonstrated promising two-photon absorption properties. Both the excitation wavelength and photolysis efficiency were later adjusted and improved in various studies.[50,51,65] Becker

et al., for example, showed that DMA-NDBF has unique photochemical properties.[50] This photocage was only activatable with two-photon light, whereas one-photon illumination did not lead to any photolysis. In a second study, Becker *et al.* demonstrated how a small change in the DMA-NDBF structure – resulting in Az-NDBF – led to faster photolysis. This photocage can also release its leaving group using one-photon excitation.[51] They were able to photolytically release the biologically relevant neurotransmitter glutamate using both 420 nm and 530 nm light.

The second class is boron dipyromethene (BODIPY) derivatives. Weinstain's[55] and Winter's[66] research groups concurrently studied the uncaging of *meso*-methyl BODIPY in 2015. The absorption maxima of their derivatives were located around 500 nm, but it has since been possible to tune the excitation wavelengths up to 700 nm.[56] Although they exhibit good extinction coefficients at low-energy light, the quantum yields for uncaging are often comparatively low.[34,47] However, this problem was addressed by Winter *et al*. in 2020.[42] They synthesized new BODIPY photocages that blocked access to unproductive singlet internal conversion conical intersections. This design led to conformationally restrained boron-methylated BODIPY derivatives with high uncaging quantum yields of 0.04, absorption in the phototherapeutic window and extinction coefficients over 120000 M^{-1} cm^{-1}. In recent years, BODIPY has become the most prominent example of modern photocages absorbing red light. The recent structural modifications on BODIPY photocages and their influence on the

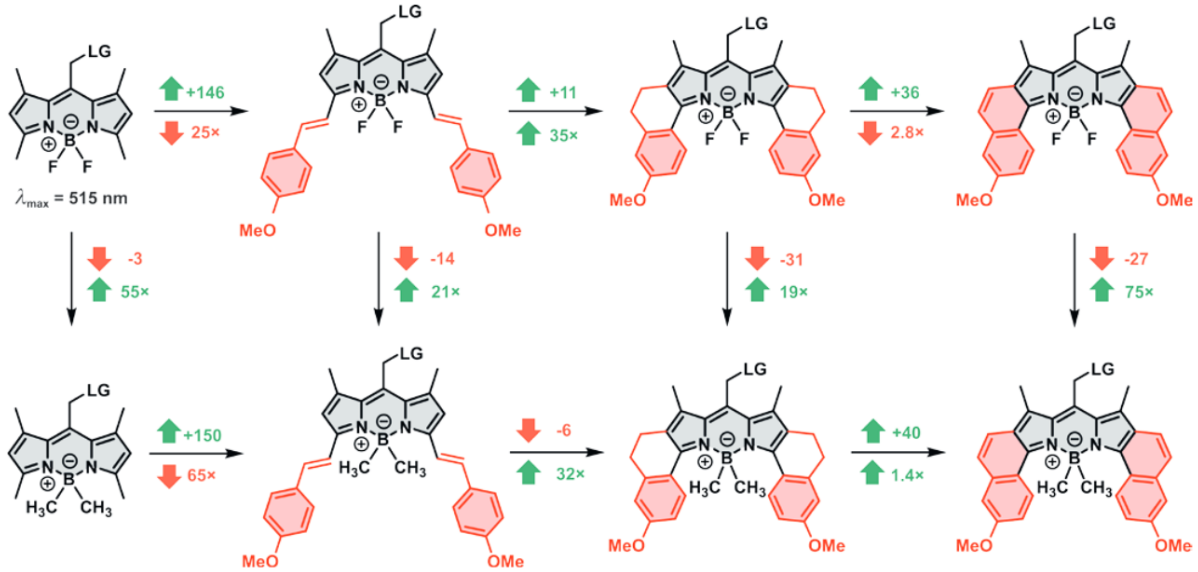

Figure 2: Structural modifications on BODIPY photocages and their influence on absorption maxima (top number, in nm) and uncaging quantum yield (bottom number). Taken from Stacko et al., 2021.

photophysical and photochemical properties are summarized in Figure 2 taken from Stacko *et al*..[67]

As a third interesting class, cyanine cages have to be mentioned, especially due to their excitation wavelength. As photocages they were first introduced by the Schnermann group[58,68,69] that formerly engineered cyanine scaffolds to NIR emitting fluorophores for fluorescence microscopy and other applications.[70–72] In 2015 they presented the first cyanine antibody-drug conjugate (ADC) using cyanine as a linker between a small molecule and a biomacromolecule to release the drug with 690 nm light.[69] Although their photocage was the most red shifted at that time, a clear drawback was the generation of singlet oxygen during the uncaging process which is known to cause severe cell damage.[73,74] This problem was solved in 2022 by Feringa *et al*., who for the first time presented a cyanine photocage that could release its leaving group even in a degassed medium (Figure 3).[59] As a result, singlet oxygen was also not generated. Instead of the photooxidation mechanism described by Schnermann *et al*., Feringa proposed a carbo-cation mediated photoheterolysis next to the carbon atom that gains the most electron density after excitation. They designed this novel PPG using DFT-based computational methods calculating frontier molecular orbital (FMO)

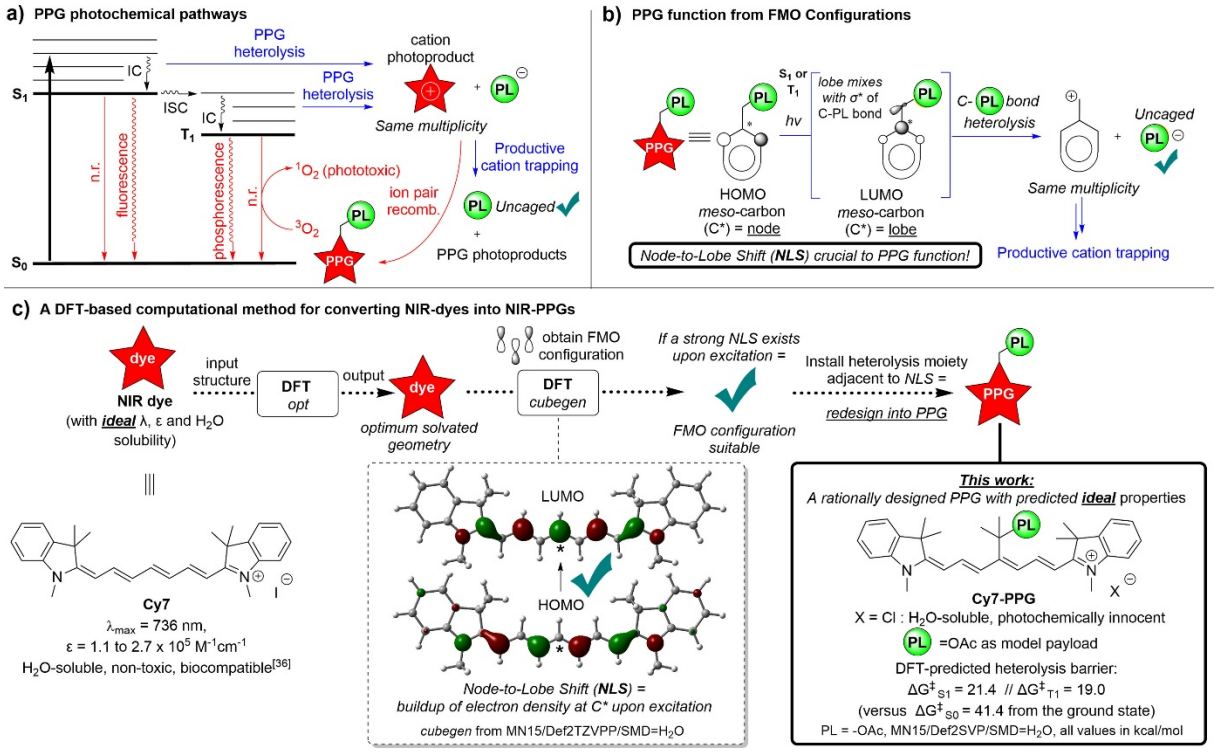

Figure 3: a) General overview of photophysical effects leading to photouncaging of cyanine PPGs. b) FMO theory that is crucial to PPG function. c) DFT-based workflow for design of cyanine based PPGs by Feringa et al. 2022.

densities. However, Stacko *et al.* have disagreed with Feringa *et al.* by showing that uncaging with a similar cyanine photocage was not possible in a degassed medium a short time after.[75] The question regarding which proposed mechanism is the correct one will need to be discussed in future studies.

The last widely applied group of PPGs are coumarin-based photocages. This scaffold has probably undergone the most modifications to date. It is a very robust system and the photophysical and photochemical properties can be tuned by many different methods. In Chapter 2.1.2 their development and photochemical properties are discussed in more detail.

2.1.2. Coumarin photocages

The first use of coumarin as a photolabile protecting group was reported by Givens *et al*. in 1984.[76] They were able to release a diethyl phosphate by irradiating (7-methoxycoumarin-4-yl) methyl diethyl phosphate. In general, coumarin chromophores have properties that make them very suitable candidates as PPGs. These include high absorbances in the UV/Vis range, high photosensitivity, fast photocleavage in the nanosecond range and strong fluorescence of the photocleavage products.[77] In recent years, a variety of new coumarin PPGs have been introduced (see Figure 4), in which two parameters, in particular, have been photochemically engineered – (1) the uncaging efficiency (1) and the absorption wavelength (2). The modulation of the uncaging efficiency (1) has been mainly influenced by two prominent works. One study goes back to Gonçalvez *et al.* in 2013.[78]. Instead of a diethylamino-moiety at

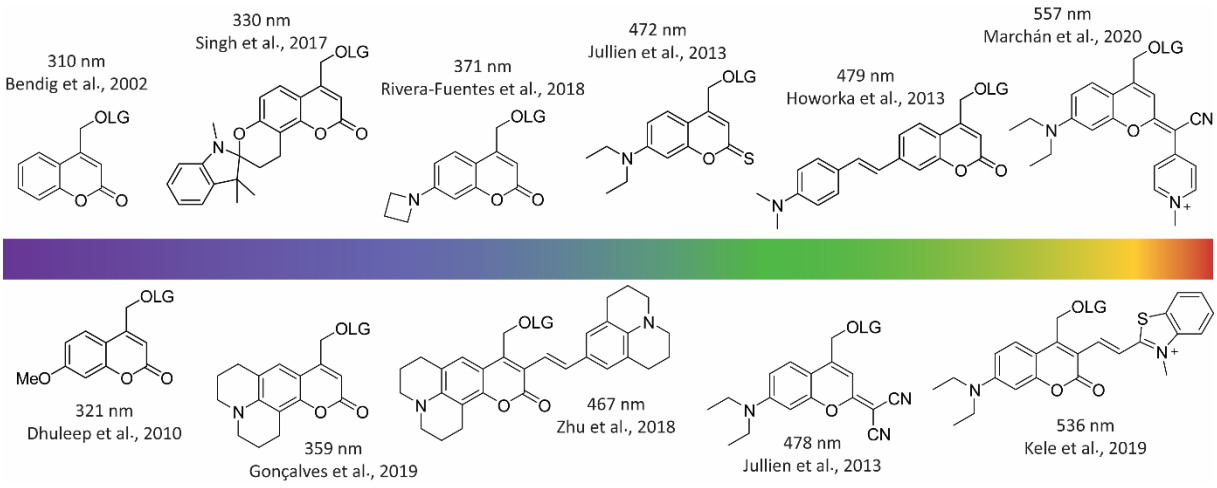

Figure 4: Evolution of the coumarin photocage in recent years. Modifications on several positions led to a significant red-shift of the PPG.

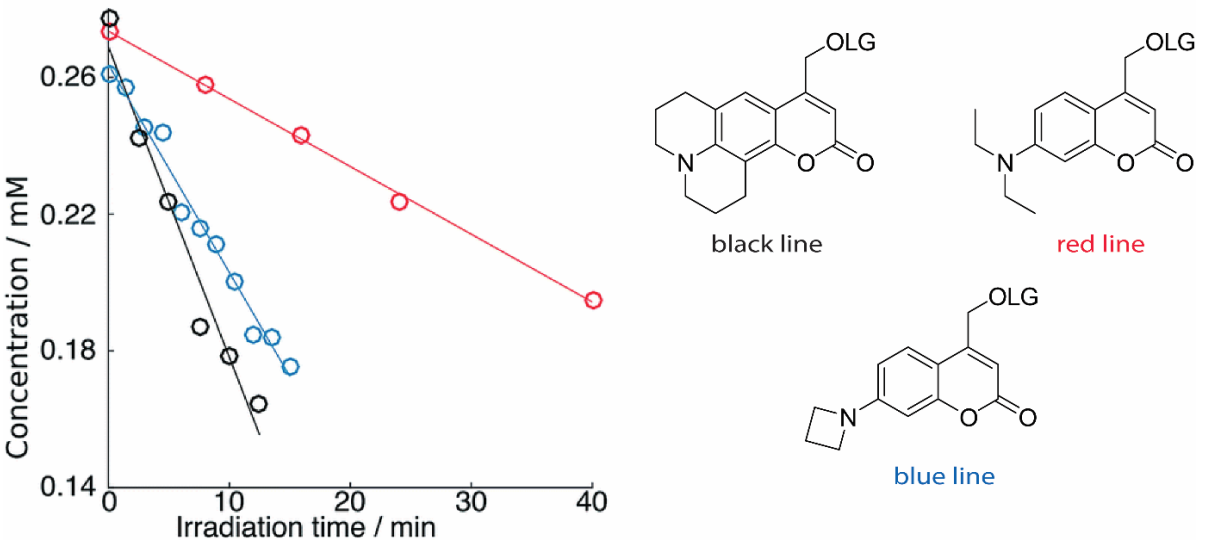

Figure 5: Photolysis experiments of three differently substituted coumarin PPGs. Azetidinyl- and julolidinyl-substitutions on the coumarin scaffold lead to an enhanced photolysis rate compared to DEACM. Figure taken and adapted from Rivera-Fuentes et al. 2018.

position 7,[35] Gonçalvez *et al.* installed a julolidine moiety. Julolidine residues in donor-acceptor fluorophores are well known to deactivate a twisted intramolecular charge transfer (TICT) state (see chapter 2.1.3).[79] Although the 2013 study did not directly compare photolysis efficiency with other coumarins, Rivera-Fuentes *et al.*[43] showed in 2018 that julolidine-substituted coumarins can be photolyzed more efficiently than DEACM (see Figure 5). They attributed this to the absence of a TICT state due to the fused ring systems around the nitrogen electron donor at position 7. In the same study, they introduced an azetidinyl-substituted coumarin, which also showed significantly increased uncaging quantum yield compared to DEACM. Here, they did not explain the increased photolysis efficiency by the absence of a TICT state, but by a change in the H-bonding in the coumarin excited state. However, to date, only a few studies have appeared that investigated a systematic improvement in the uncaging quantum yield of coumarins. In those that have been done so far, a modification of the 7-position turned out to be the most promising. One field that has been studied much more broadly up to this point is the shifting of the absorption maximum of coumarin PPGs (parameter 2). To create a bathochromic shift, several positions of the coumarin backbone can be modified.[53,80] An interesting approach was made by Jullien *et al*. who replaced the carbonyl at position 2 with a malonitrile moiety.[81] Using this modification, they were able to shift the absorption maximum to 478 nm, which equals a 99 nm bathochromic shift compared to DEACM. In the same manuscript they presented the substitution of the carbonyl oxygen with a sulfur atom, resulting in a 472 nm absorption.

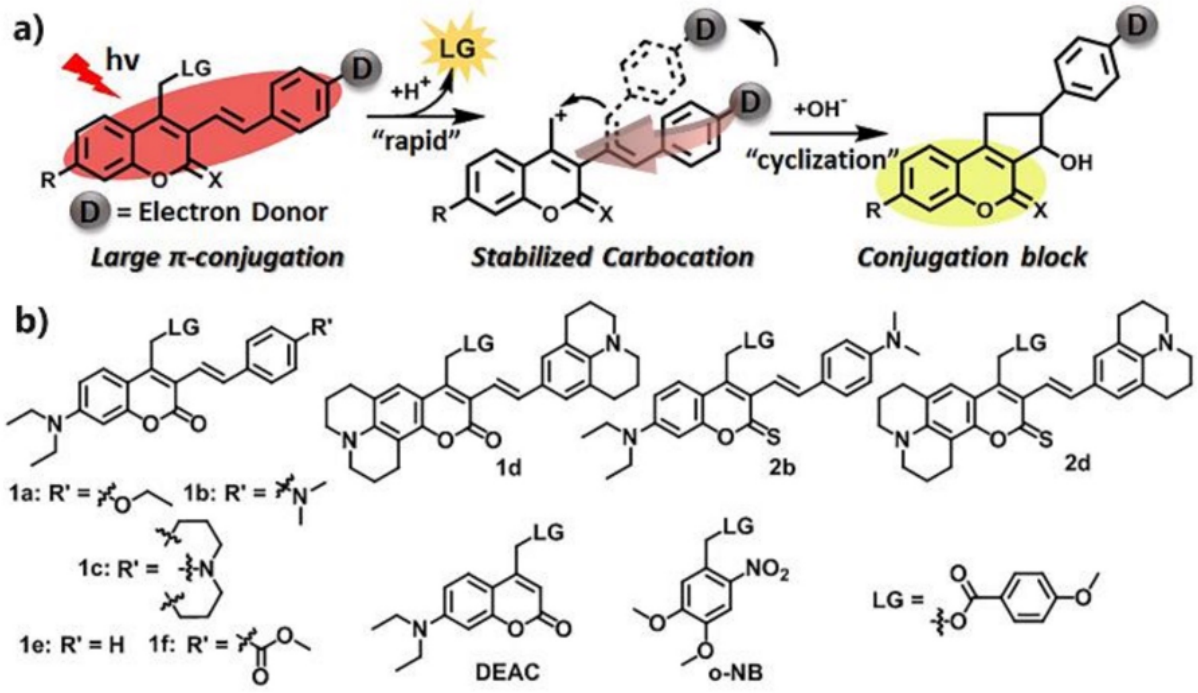

Figure 6: a) Mechanism of the photo-uncaging of styryl-conjugated coumarins according to Zhu et al.. b) Chemical structures of coumarin photocages that are discussed in the study. Figure taken with permission from Zhu et al. 2018.

A different strategy was used in 2018 by Zhu *et al.*.[54] They expanded the coumarin π-system at the 3-position (Figure 6). Using electron-rich styryl moieties the coumarin absorption was shifted to 467 nm. In addition, their coumarin had the advantage that the π-conjugation at the 3-position was disrupted during the photocleavage process because of an intramolecular cyclization rearrangement. Therefore, the absorbance of the photoproduct did not interfere with the photocage, which made their coumarin superior to previously described PPGs. Also the *Kele* group used a π-extension at the 3-position to red-shift the coumarin absorption spectrum.[82] A key feature of their compounds was a heterocycle moiety, including a quaternary nitrogen with a negatively charged counterion. This did not only modulate the absorption properties, but also increased the water solubility and led to high 2P-uncaging cross sections. A major drawback of their new coumarin photocages was the challenging synthesis and the possibility for *cis*/*trans* isomerization at the exocyclic double bond in 3-position, which might lead to poorer uncaging quantum yields. In 2020 Marchán *et al*.[83] published new red-shifted coumarins that combined some of the ideas of Jullien *et al*. and Kele *et al.*. They replaced the carbonyl function at 2-position with cyano(*N*-alkyl-4-pyridinium)-methylene moieties similar to the malonitrile Jullien *et al.* used. Additionally, this alkylated and positively charged heterocycle moiety increased water

solubility and the electron-withdrawing character. Therefore, their best compound showed an absorbance maximum of 557 nm. Another method to shift the absorption maximum to longer wavelengths is replacing the bridging oxygen atom at position 1 with other functional groups, such as $Si(Me)_2$[84] or CF_2.[85] In 2019, Wang *et al*. introduced a dimethylsilyl group at the C1 position. Using density functional theory (DFT), they showed that the σ*-orbital of the two exocyclic bonds at the silicon-atom strongly interact with the π*-system of the coumarin scaffold. This leads to a strong delocalization of the π-electrons and a lowered energy of the LUMO in $Si(Me)_2$ coumarins. As a result, a moderate shift of the absorption maximum to a 447 nm in MeOH was possible. In 2020, Schnermann *et al.*[85] achieved an even larger red shift by introducing a CF_2 group that replaced the cyclic oxygen atom. The absorption maximum of diethylaminocoumarin could thus be shifted by 109 nm to 491 nm (Figure 7). When a nitrile group was now additionally introduced at the C2 position, a shift of 217 nm for emission and 140 nm for absorption could be obtained. As a result, the absorption maximum was above 600 nm and the emission was in the NIR range. However, these substitutions have so far only been applied to coumarins acting solely as fluorophores, not as PPGs.

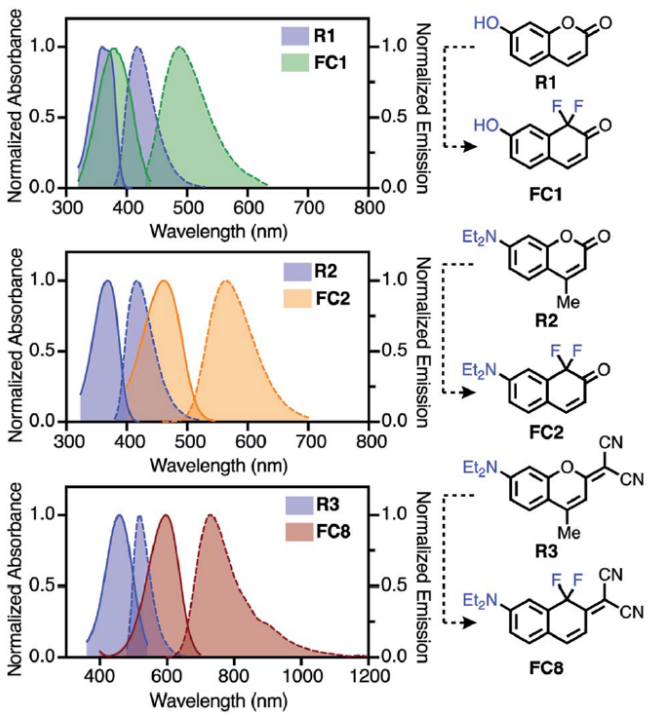

Figure 7: Comparison of absorption and emission spectra of unsubstituted and CF_2 substituted coumarins. Taken from Schnermann et al., 2020.

2.1.3. Relaxation pathways of excited states

By absorbing light, a given molecule can possibly enter an electronically excited state S_n. From this excited state, the absorbed energy can be released *via* several relaxation pathways (see Jablonski diagram, Figure 8).[86,87] In any case, the system first wants to return to the vibrational ground state of the first excited state S_1. If it is in a higher

electronically excited state S_n after excitation, it decays from this state to S_1 *via* internal conversion. In S_1, the molecule can either be in the ground vibrational state, or in an excited vibrational state. In the latter case, an oscillation relaxation into the vibrational ground state of S_1 occurs. With the emission of a photon, a transition to any vibrational state of the electronic ground state S_0 is subsequently possible. This process is called fluorescence. It can always occur when the emission of photons is fast compared to non-radiative relaxation processes.[77,86] Due to this fast rate, the lifetime of fluorescence, which is the average time between excitation and restoring the ground state, is between 10^{-7} and 10^{-9} s.[86] Due to the non-radiative transformation processes following excitation that are described above, the energy of the emitted photon is usually smaller than the energy of the absorbed photon. As a result, the emission spectrum of the molecule is shifted to a longer wavelength. This is called the Stokes shift.[88] The second pathway by which photons can be emitted from the excited state is called phosphorescence.[87,89] During phosphorescence, a transition of the molecule from the S_1 vibrational ground state to the first excited triplet state T_1 occurs upon spin

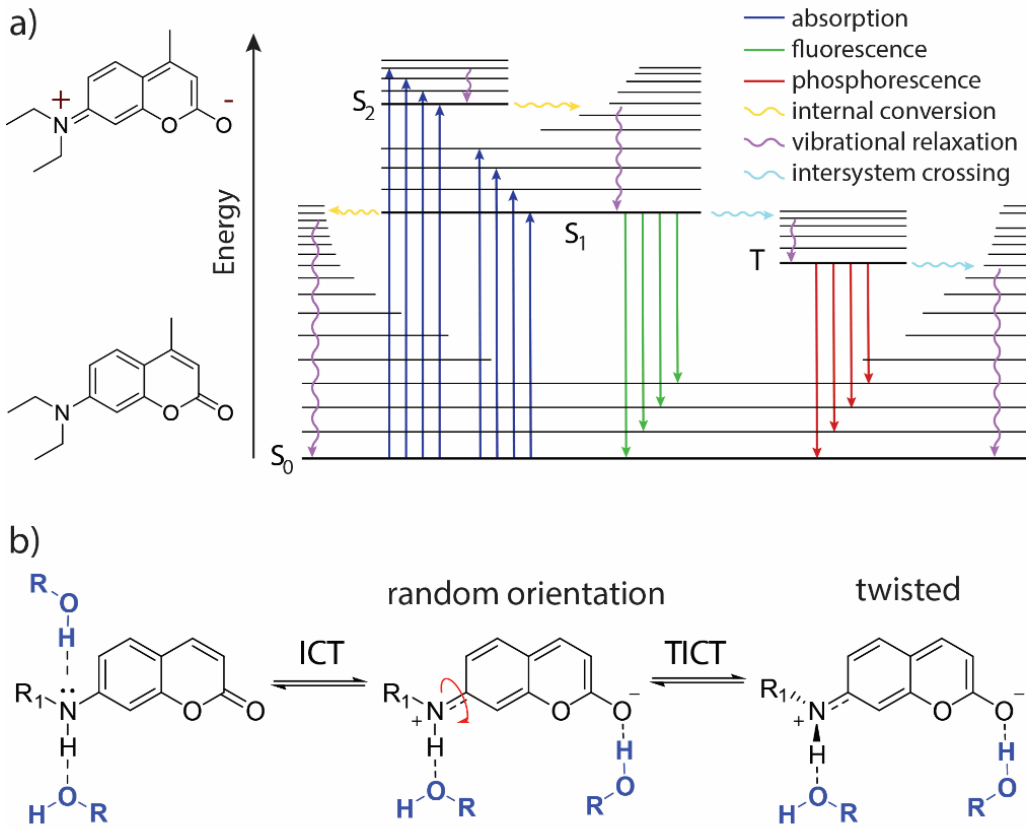

Figure 8: a) Jablonski diagram showing possible photophysical pathways after excitation of an exemplary coumarin chromophore. b) General model for TICT and hydrogen bonding on coumarin molecules. Figure taken from Klimek et. al. 2022.

inversion, which is called intersystem crossing (ISC). This process is quite unlikely to occur because it changes the multiplicity of the spin. Transitions from a singlet to a triplet state, however, are quantum mechanically forbidden transitions. Therefore, they occur much more slowly, giving phosphorescence a much longer lifetime of up to 10 s.[87,90]

Another very prominent process that can occur upon light excitation is charge transfer (CT).[91,92] It represents a fundamental step in many biochemical processes such as photosynthesis, respiration or nitrogenases.[93] In general, charge transfers can be divided into two categories. If the charge transfer takes place from an electron-rich donor (D) to an electron-poor acceptor (A) of two different molecules, it is known as an intermolecular CT. However, if the donor and acceptor are in the same molecule, we refer to the phenomenon as intramolecular charge transfer (ICT). Excitation with the light of an appropriate wavelength enables the transfer of an electron from the donor part of the molecule to the acceptor part in the excited state. This results in a different charge distribution in the excited state than in the ground state. In most cases, charge transfer occurs in molecules in which the donor and acceptor groups are connected by conjugated π-electrons. In rare cases, however, transfer through space is also possible when transfer is being hindered by the absence of conjugation.[94,95]

Intramolecular charge transfer was first described by Lippert *et al*. in 1961.[96] They observed an additional, red-shifted emission (A band) in polar solvents within the emission spectrum of (dimethyl)aminobenzonitrile (DMABN) in addition to the expected emission band (B band). This second band was inconsistent with the Kasha's rule, which states that fluorescence results from emission from the first excited singlet state.[97] Lippert *et al*. concluded that the B band resulted from the locally excited (LE) state. The A band, however, arose from an ICT state stabilized by polar solvents.[96,97] The discovery of the unexpected photochemical properties of DMABN resulted in a large number of experimental and theoretical investigations.[98] Nevertheless, there are still a variety of different opinions and theories on the exact mechanism of ICT.[99,100] One of the dominant theories is the so-called twisted ICT (TICT) model. This model was first postulated by Grabowski *et al*. in the 1970s and has been refined several times in recent years.[101–103] It states that, as described previously, the LE state is more polar due to its ICT character and is therefore stabilized in polar solvents.[104] However, further stabilization can be achieved if rotation occurs around the single bond between

the phenyl ring and the dimethylamino group. This rotation leads to a TICT state with a dihedral angle θ of approximately 90° (Figure 8, b). This rotation is driven by the minimization of the Coulomb interaction. In the ICT state, two unpaired electrons are present in the frontier orbitals: one is localized in the acceptor part and the other in the donor. The rotation around the single bond between these parts of the molecule minimizes the repulsive interaction between the unpaired electrons and leads to complete charge separation and an enhancement of the dipole moment.[104,105] The emission from the TICT state is bathochromically shifted because the fluorophore undergoes a considerable change in its geometry to a more energetically favorable state compared to the locally excited state. Transition from the TICT state to the ground state occurs mainly radiationless, which is expected to result in a low TICT fluorescence quantum yield.[104,105] Rotation is very sensitive to the sample microenvironment and thus can be used to obtain information about it. This makes compounds that exhibit TICT fluorescence a widely requested and studied class of compounds.

2.2. Tools for RNA visualization

One of the biggest challenges in studying RNA in living cells is its visualization. Of course, nucleic acids are not visible to the naked eye, so (bio)chemical tools must be prepared to make the RNA observable.[6] For this purpose, mainly fluorescent tools are used today. The following is an overview of the various methods that can be used to visualize RNA in modern biology based on a review article by Braselmann *et al.*.[6]

In general, fluorescent tools for RNA visualization can be divided into four categories (see Figure 9). The first category is protein-based methods, like MS2,[106–108] Pepper[109] or dCas13[110] (see Figure 10). All these methods rely on RNA binding proteins that are typically fused to a fluorescent protein (FP). The fused protein systems can bind tightly to a certain RNA sequence which often forms a specific secondary structure. In the MS2 system, the K_d value of the protein-RNA interaction is in the range of 1 nM.[111] The FPs can be easily exchanged by cloning, resulting in different fluorescent colors, brightness or photostability. It is also possible to use several different RNA-binding proteins for different RNAs in one cell since most of them are orthogonal, e.g., MS2 and PP7.[6]

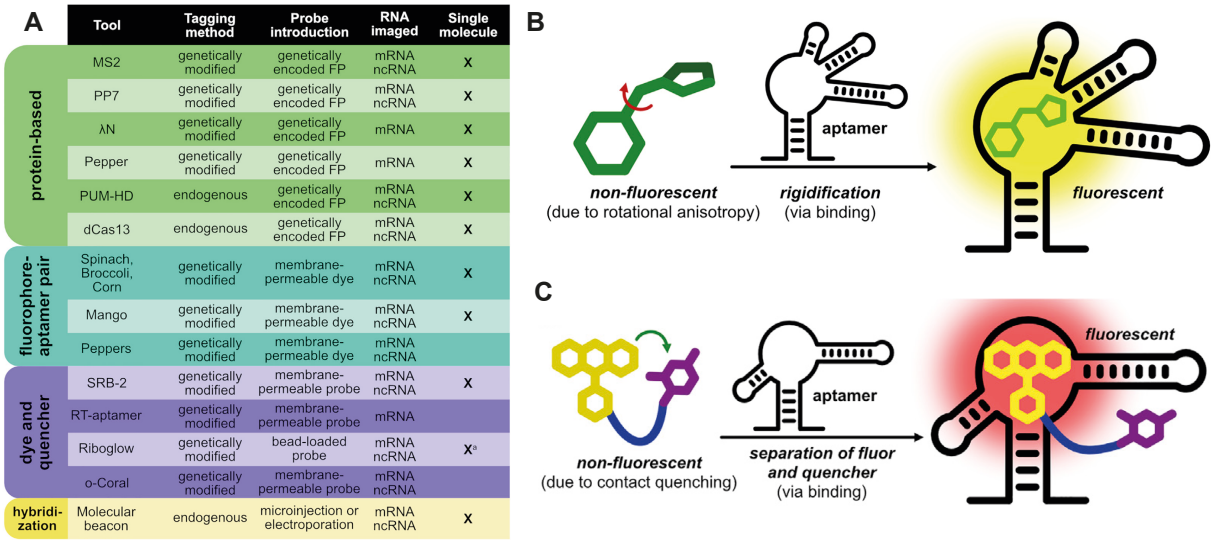

Figure 9: Overview of the different tools for RNA visualization described in this chapter. B: Schematic example of a fluorophore aptamer pair. The fluorophore becomes rigid upon binding to the aptamer, leading to a significant increase in its fluorescence. C: Schematic example of a dye-quencher pair. In free solution fluorophore and quencher perform contact-quenching. When bound to the respective aptamer, fluorophore and quencher get separated leading to a fluorescence intensity increase. Figures taken with permission from Palmer et al., 2020.[6]

The second category is fluorophore-aptamer pairs, like Broccoli,[112] Spinach[113] or Mango II.[114,115] They are small molecules designed to emit a fluorescent signal only when bound to the corresponding aptamer (see Figure 9). In bulk solution, the fluorophores have great conformational flexibility, in most cases the ability to *cis-trans* isomerize. Because of this flexibility, fluorescence is off in solution. Only when bound to the correct aptamer the fluorescence is turned on due to the limited flexibility. This method is most often used to stain and monitor mRNA or non-coding RNA in cells.

As a third tool, dye-quencher pairs should be mentioned.[116–119] Here, the fluorophore is usually covalently linked to a quencher *via* a long, freely flexible carbon chain (see Figure 9). In free solution, the two chromophores perform contact-quenching due to their attractive chemical interactions. When bound to the RNA aptamer, fluorophore and quencher get separated and the fluorescence increases significantly. As an example, the fluorescence of sulforhodamine B (SRB-2, K_d = 1.3 μM) increases 100-fold *in vitro* when it binds to the aptamer.[116] An advantage of this method compared to the previously described fluorophore aptamer pairs is the significantly increased photostability and higher brightness of the chromophores used.[6] Here, the experimenter is not limited to fluorophores that can lose their energy in fast decay channels like isomerization or rotation. Instead, optimized and stable dyes without

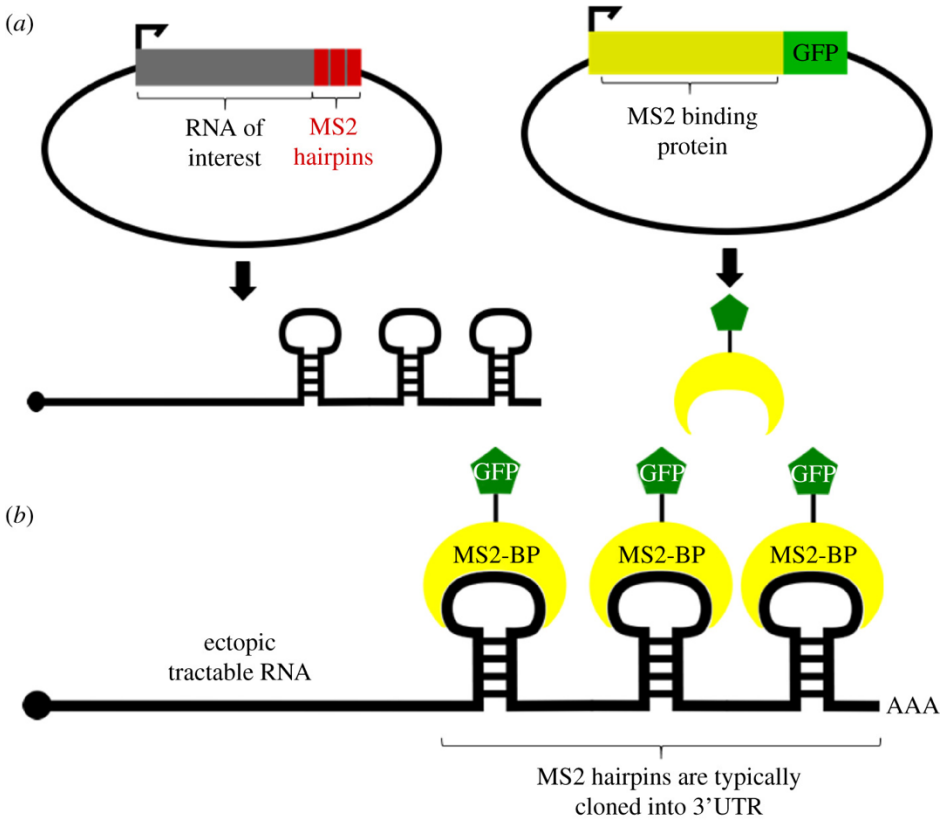

Figure 10: General mechanism of MS2 RNA tagging. (a) This technique requires two constructs. The first construct encodes the RNA of interest fused with MS2 RNA downstream. The second construct encodes the MS2 binding protein fused to GFP as fluorescent reporter. (b) Both constructs are translated after transfection. The MS2 hairpins are recognized by the MS2 binding proteins leading to the possibility to track the RNA of interest via a fluorescence readout. Figure taken from Gorospe et al., 2018.

significant photobleaching and enhanced brightness can be used. In a recent publication by Jäschke *et al.*,[120] an SRB-2 derivative was used for the first time for high-resolution microscopy. While the fluorophore exchanged rapidly from the aptamer, its background fluorescence in solution was at the same time enormously reduced by the quencher.

The last category of tools for fluorescent labeling of RNA are molecular beacons (MBs). Their functionality will be discussed in detail in the next chapter.

2.2.1. Molecular beacons – design and application

Molecular beacons (MBs) are widely used tools for the visualization of RNA.[121] They consist of a single-stranded DNA or RNA labeled at opposite ends with a fluorophore and a quencher.[122] The RNA sequence is chosen in a way that the strand folds into a three-dimensional stem-loop structure. 5'- and 3'- ends are thus self-complementary, while the formed loop is complementary to the target sequence. Due to the spatial proximity of the fluorophore and quencher, there is no fluorescence signal in the unbound state. When the MB binds to the desired RNA sequence, the fluorophore and quencher are separated, and the fluorescence increases significantly (Figure 11, A). MBs were first developed by Tyagi and Kramer in 1995.[123] They used a DABCYL quencher to inhibit an EDANS fluorescence. In general, a fluorescence increase from the unbound to the bound state of 20-100 can be achieved for certain MBs with careful selection of the attached chromophores.[124] Due to the antisense technology, also multiplexing with MBs is possible.[125] MBs have already been used in many biological applications for tracking a variety of RNAs, for example, mRNA,[126] rRNA[127] or

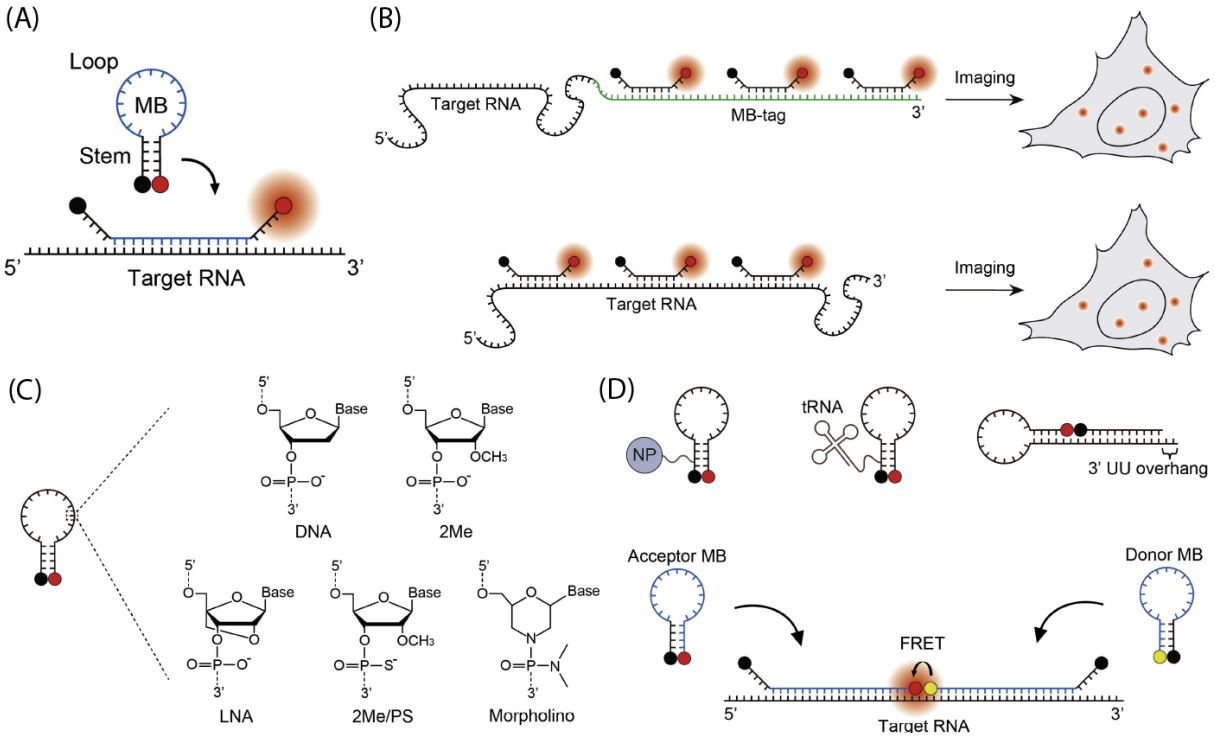

Figure 11: (A) General function of a molecular beacon. (B) Different approaches for RNA tagging. In the MB-tag approach a sequence is fused to the RNA of interest that contains several repetitive binding sites for one MB (top). Using direct labeling the MB has a loop sequence that is complementary to the RNA of interest itself (bottom). (C) Examples of chemical modifications that can increase cell stability and binding affinity of MBs. (D) Approaches to minimize nuclear entry using nanoparticles (NP), a tRNA molecule or an siRNA-like element (top). (D) Dual FRET MB system. Taken from Chen et al., 2020.

miRNA.[128] It is feasible to introduce MBs into cells *via* several methods. These include electroporation, microinjection, toxin-mediated membrane permeabilization or heavy metal bioballistic gas guns.[129–131]

When it comes to monitoring single RNA molecules in cells using MBs, in most cases one of two different methods is applied (Figure 11, B).[121] The first method is the so-called MB-tag approach. Here, the RNA to be visualized is genetically modified to add a repetitive tandem sequence that the beacons can bind to. This allows for a much brighter signal through intensity amplification. Vargas *et al.* first conducted such an experiment by attaching 96 tandem repeats to a GFP mRNA to monitor it.[132] The second option is the direct-labeling approach. Compared to MB-tag, the advantage of this approach is that no additional sequence has to be attached to the RNA of interest. The MBs bind to an endogenous part of the single strand. Accordingly, it is also possible to study endogenous RNA with this method, as shown by Turner-Bridger *et al*. 2018.[126] A clear disadvantage, however, is that single-stranded RNA is almost exclusively folded,[133] making it difficult to find suitable sections that are accessible for MB binding.

Of course, since MBs are intended to be used *in vivo* in most cases, it is important that they are stable in cells and bind efficiently to the target RNA (Figure 11, C). The chemical modifications that can be used in this process generally apply to antisense oligonucleotides and are discussed hereafter. Modifications that affect nuclease stability can be introduced at several positions. One of the most prominent modifications is replacing an oxygen atom on the phosphate backbone with a sulfur atom,[134] resulting in an increased oligonucleotide stability. This substitution is often combined with modified nucleobases or sugar-backbones. For the latter, mainly 2'-OMe-RNA, 2'-F-RNA, LNA and 2'-MOE-RNA, which have an enormous impact on the hybridization properties, are used.[135,136]

<u>2'-OMe-RNA:</u>

The introduction of a methyl group at the 2' position is one of the oldest and few naturally occurring modifications. By using 2'-OMe-RNA, the thermal stability of 2'-OMe RNA/RNA duplexes could be significantly increased compared to DNA/RNA duplexes.[137] In addition, the stability of enzymatic degradation is increased.[138]

However, the duplexes formed are RNAse H inactive and therefore cannot be used for these kinds of applications.[138]

2-'F-RNA:

For 2'-F-RNA, the 2'-OH is exchanged with a fluorine atom. The large electron density of the fluorine atom directs the ribose into the more stable form of the C3'-endo conformation, thus increasing the thermal duplex stability upon hybridization to a target RNA.[139] In 1993, Kawasaki *et al*.[140] established the following order of X/RNA duplex stabilities: X= 2'-F-RNA > 2'-OMe-RNA > RNA > DNA. Furthermore, this modification has increased thermal stability compared to a complementary RNA sequence. This is due to an increase in binding enthalpy due to stronger Watson-Crick base pairing[141] and increased polarization of the 2'-hydrogen atom.[142] 2'-F-RNA has been widely used as siRNA due to its ability to be readily incorporated due to the small size of the fluorine atom.[143] As a result, 2'-F-modified siRNAs have been shown to have both increased nuclease stability in human plasma as well as increased inhibitory function compared to conventional siRNAs.[144]

LNA:

Locked nucleic acid (LNA) describes the modification of sugar by a covalent bridging of the 2'-OH with the 4' carbon atom. LNA was presented independently by Obika *et al*., 1997[145] and Koshkin *et al*., 1998[146]. High stability to enzymatic degradation by endo/exo-nucleases as well as high thermal stability and increased selectivity towards a target sequence are among other advantages that LNA has in comparison to DNA or RNA. These are due to the fixation of ribose in C3'-endo conformation and the consequent structural inflexibility. Additionally, this explains the 4.0-6.0 °C increase in the melting temperature of oligomers per single incorporation of an LNA-modified T.[146] Furthermore, incorporation of LNA nucleotides into an RNA sequence results in higher target specificity.[147]

2'-MOE-RNA:

2'-methoxyehtyl RNA is one of the most commonly used modifications in ASO technology.[148] This is due to the many advantages that this modification brings. These advantages include its use as a flanking agent in gapmers to increase RNase H activity and splicing.[149] However, this activity is less pronounced than other modifications, such as 2'-OMe RNA, due to the size of the 2' residue. Nevertheless, MOE modification

increased the stability of single and double stranded siRNA against degradation by nucleases. In addition, the introduction of a second oxygen atom close to another leads to the restriction of the ability to rotate around the ethyl compound. This leads to a stable configuration of oxygen atoms relative to each other. Moreover, this further favors the C3' endo conformation of the sugar and increases the binding affinity.[150] Another unique feature of the 2'-methoxyethyl residue is the intercalation of a water molecule between the phosphate residue and the 2' modification. This, in turn, increases steric hindrance and thus nuclease stability.[150]

Morpholinos:

Morpholino building blocks are nonionic RNA/DNA analogs.[151] The negatively charged oxygen-atom at the phosphate backbone is substituted with an uncharged $N(Me)_2$ residue. Due to the altered backbone, morpholino oligonucleotides are more stable against nuclease digestion. While they can bind to complementary target RNA sequences by Watson-Crick base pairing, morpholinos are less likely to perform unspecific binding to proteins due to their neutral charge.[152] Despite their many advantageous properties, other sugar modifications are more often used because morpholino building blocks are very expensive and comparatively difficult to produce.

Besides the lack of specificity and stability of the MBs themselves, one major origin of false positive signals is the transport of MBs to the nucleus. This is the location in the cell where the most nonspecific opening occurs.[153–155] Therefore, several strategies were developed to prevent MB nuclear entry (Figure 11, D). One option is the attachment of nanoparticles/quantum dots that are too large to be transported through nuclear pore channels.[121,155] It is also possible to link an MB to tRNAs[154] or siRNAs.[156] Both attached domains can be used to facilitate nuclear export and therefore minimize a false-positive signal in the nucleus. The last two modifications have the additional advantage over nanoparticles in that they interfere with cell delivery at a lower extent.[121]

Another method to prevent false-positive signals is the use of a donor-acceptor MB system.[125,157,158] Here, two MB are designed to bind directly one after the other in spatial proximity to a target sequence (Figure 11, D). In the hybridized state, the fluorophores are thus located directly adjacent to each other, and FRET can occur between the two chromophores. The presence of this energy transfer precludes the

possibility that the fluorescent signal resulted from the degradation of the MB. A related option is to produce a ratiometric MB in which a second fluorophore is placed in the loop region.[159] By excitation of both fluorophores and subsequent colocalization it is possible to exclude false-positive signals due to degradation.

2.2.2. Light-activatable molecular beacons

MBs are great tools to observe intracellular RNA transport. However, they have a particular drawback. MBs give a fluorescent signal as soon as they arrive in the cell. With conventional MBs, there is no possibility to give the signal spatial and temporal resolution. To circumvent this problem, several methods have been developed in the past to make MBs light activatable. In 2012, Joshi *et al.* presented loop-caged beacons (Figure 12).[160] In this approach the loop region of the MB was equipped with five to seven NPE photocages at the nucleobases. Therefore, the hybridization with the target sequence was blocked because Watson-Crick base pairing was prevented. Their MB was designed complementary to housekeeping gene glyceraldehyde-3-phosphate dehydrogenase (GAPDH) according to Nitin *et al.*.[161] Joshi *et al.* showed that full activity of the two loop caged MBs could be restored using 366 nm light. Photolysis was demonstrated freely diffusing in a cuvette and with target DNA immobilized on a glass slide. A second approach was made by Tan *et al.* (see Figure 13).[162] They used a photolabile linker to “lock” the MB between the 5’ and 3’ terminus. Due to the strong connection of the opposite ends, the MB was unable to leave its stem-loop conformation. The connection was formed using two different strategies. The first was

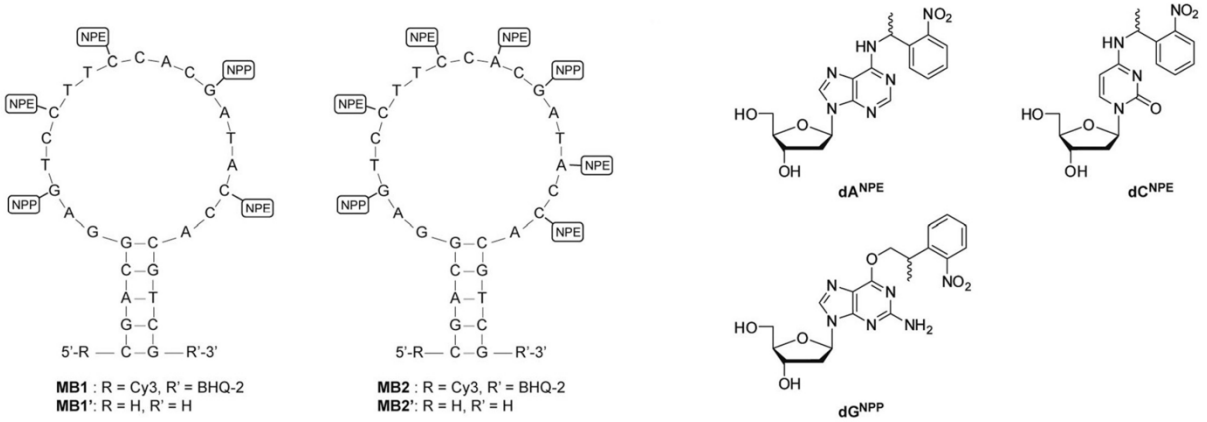

Figure 12: Loop-caged molecular beacons presented by Heckel et al. in 2012 (left). Photolabile NPE groups (right) attached to the nucleobases in the loop hindered hybridization of the MB with the target sequence. Five to seven photocages were needed to efficiently prevent hybridization. 365 nm light was used to cleave the NPE groups and restore the natural functionality of the MBs. Taken with permission from Joshi et al., 2012.

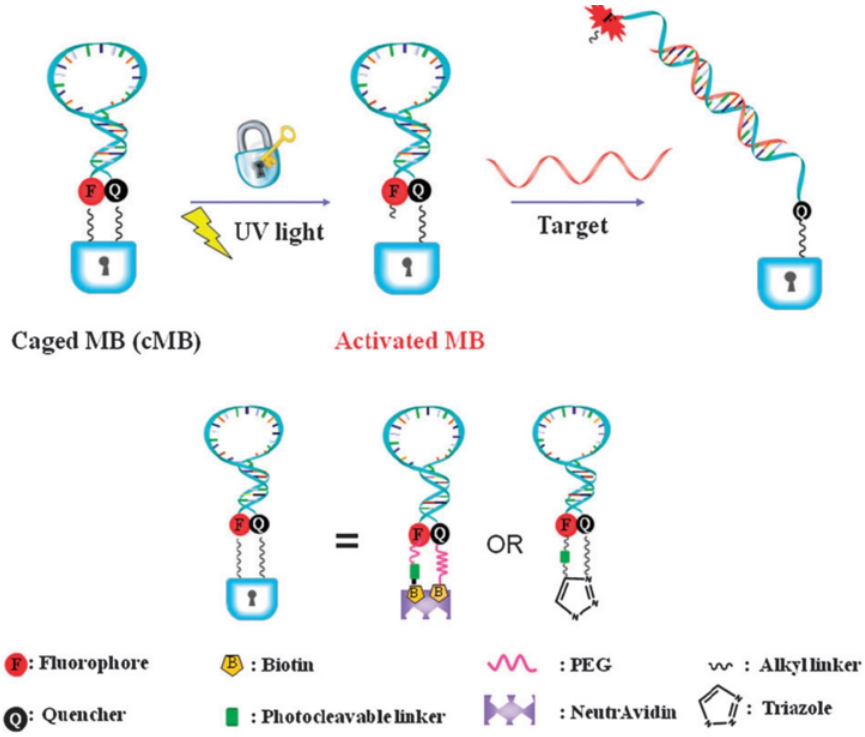

Figure 13: Schematic representation and working principle of „locked molecular beacons". Taken with permission from Tan et al., 2011.

a covalent bond *via* a copper-catalyzed cycloaddition with an alkyne and an azide moiety. Alternatively, they were also able to use a non-covalent biotin-neutrAvidin interaction (K_D = 10^{-15} M) to lock hybridization. Either way, an *o*-nitrobenzyl group served as spacer between fluorophore and the "lock", forcing the molecular beacon to stay in its inactive state. In addition, they inserted a PEG moiety between fluorophore/quencher and the biotin to reduce steric hindrance. Therefore, the two terminal biotin residues should be able to bind to the same neutrAvidin molecule. However, when target DNA was added, the MBs already showed a slight increase in fluorescence, that was fully restored when Tan *et al.* applied UV light. This small increase "was most likely a result of partial binding of cDNA to the cMB, which slightly destabilized or distorted the MB's stem-loop structure and as a consequence, elongated the distance between the fluorophore and the quencher" – Tan *et al*. 2011.[162] In other words, the locked MBs were partially able to bind the target sequence even before light-activation. This MB design was adopted in 2018 by Dmochowski *et al.* who additionally improved the synthesis of the cyclized oligonucleotides.[163]

The third strategy to make MBs light-inducible was presented by Rinne *et al. (*Figure 14).[164] In their approach, they did not want to make hybridization light-activatable. Illumination with an appropriate wavelength should only visualize a subpopulation of

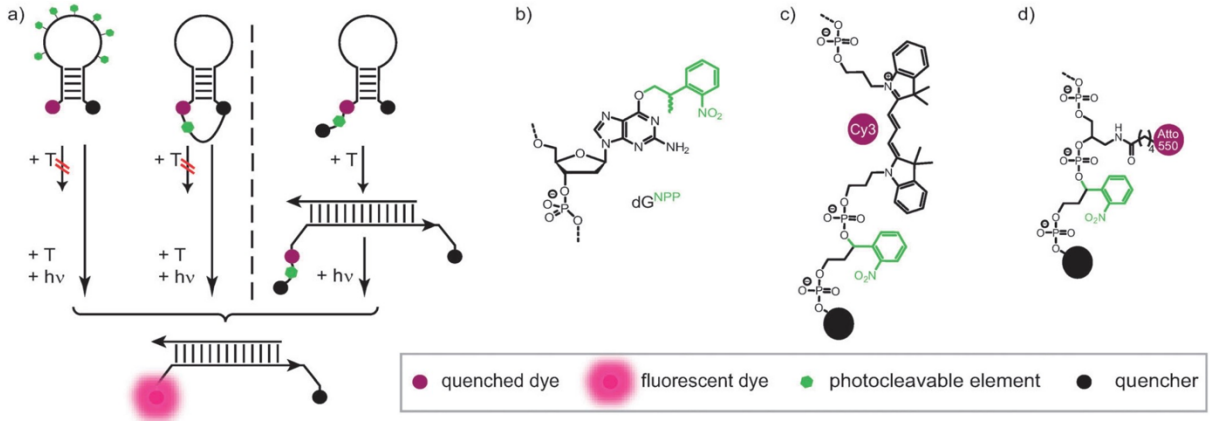

Figure 14: a) Comparison of the two previously described approached to make MBs light-activatable and Q-dye beacons developed by Heckel et al. 2013. b) Photolabile protecting group that was used to prevent Watson-Crick base paring in (a), left. c,d) Quencher and dye combinations used in the design of Q-dye beacons. Taken with permission from Rinne et al. 2013.

double helices. Therefore, they presented so called "Q-dye beacons", which were equipped with a second quencher next to the fluorophore that was linked *via* an NPE-photocage. Depending on the application, an advantage of this design is that the MB can bind to the target sequence before photoactivation. This avoids any delay in monitoring due to slow binding- or hybridization-kinetics. The Q-dye MBs consisted of 2'-OMe RNA and targeted the so-called Balbiani ring mRNA which is responsible for the production of salivary polypeptides.[165] Using this approach Rinne *et al*. were able to enormously reduce the background signal before light-activation. The best performance was achieved with the Cy3 Q-dye beacon which showed an overall fluorescence increase of 167 after illumination and target addition. In addition to the *in vitro* experiments, they also showed the application of Q-dye beacons in *C. tentans* salivary gland cell nuclei using confocal laser scanning microscopy.

Regardless of which type of MB is used, it is important to choose suitable fluorophores. Among other parameters, excitation wavelength, photostability and fluorescence quantum yield of the attached organic dye play an important role. An overview of the most prominent fluorophores is given in the next chapter.

2.2.3. Small-molecule fluorophores

The information in this chapter is based on two review articles from Jun *et al.*, 2020[166] and Grimm *et al.*, 2022.[167] To visualize biomolecules with distinct precision, it is necessary to develop suitable small-molecule fluorescent probes. In the last years, a large number of organic dyes have been synthesized and structurally tailored and optimized in terms of wavelength, stokes-shift and photostability.[11] However, most of the fluorophores are generated from just a few organic molecular scaffolds.[168–170] These are quinolines, coumarins, styrenes, naphthalimides, xanthones, fluorescein, BODIPYs, rhodamines, cyanines and substituted fluorescein and rhodamine derivatives (e.g. TokyoMagenta) (see Figure 15).[11] Nevertheless, only fluorescein and indocyanine green are FDA-approved contrast agents for optical imaging in human health studies. According to Jun *et al.*[11] fluorescein was the most widely studied fluorophore in 2020 with more than 15000 publications in the SciFinder database (see

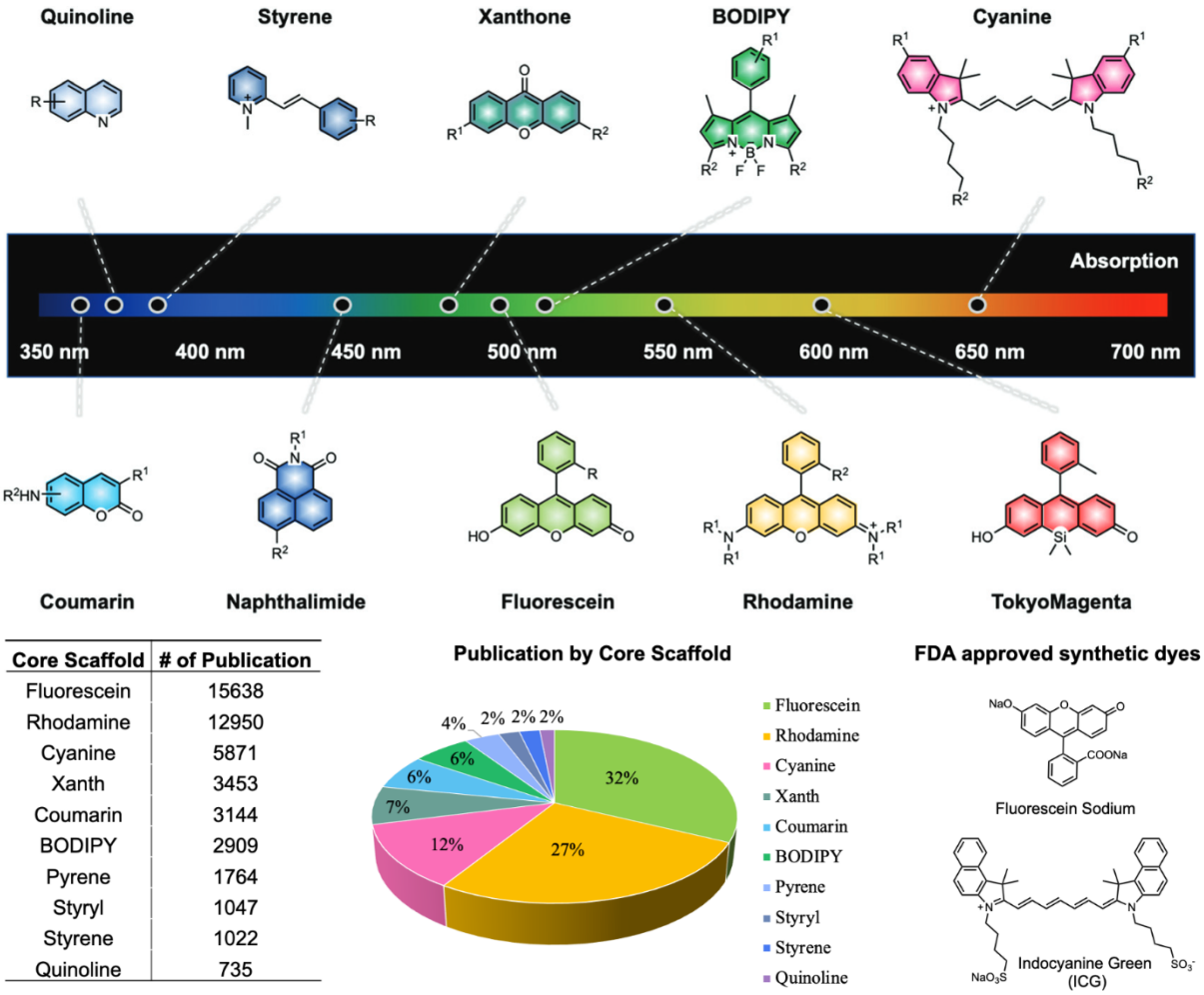

Core Scaffold	# of Publication
Fluorescein	15638
Rhodamine	12950
Cyanine	5871
Xanth	3453
Coumarin	3144
BODIPY	2909
Pyrene	1764
Styryl	1047
Styrene	1022
Quinoline	735

Figure 15: Molecular scaffolds of most commonly used organic fluorescent dyes sorted by absorption wavelength. Figure adapted from Jun et al. 2020.

Figure 15), followed by rhodamine with nearly 13000 publications. Unsurprisingly, quinoline had the lowest number of publications (only 735), which is probably due to the unfavorable blue-shifted absorption. In general, fluorophores for *in vivo* imaging should ideally be non-cytotoxic, excitable with wavelengths above 750 nm to allow deep cell penetration, substantially bright and highly selective to the target. Those strict requirements highlight that there is still a great need for the ideal fluorophore.

Fortunately, nowadays there are known principles to rationally modulate the photophysical properties of the above-described molecular scaffolds. There are three general guidelines for the design of organic fluorophores.[11] (1) Electron-donating and electron-withdrawing groups can be attached to the core to modulate absorption and emission spectra of the fluorophores. For example the replacement of the terminal oxygen atoms in fluorescein with nitrogen atoms results in the rhodamine core with a more red-shifted absorption. (2) Controlling photoinduced electron transfer (PeT) and restricted bond rotation can be used to change the brightness of the fluorophores. The replacement of dimethylamino substituents with azetidinyl substituents in coumarins and rhodamines can, for example, lead to enhanced brightness due to restricted rotation around the C-N bond.[171] (3) The fluorescence readout can be changed using combinations of several fluorophores that can undergo FRET or PeT. FRET can e.g. be used to measure distances between two different sites in biomacromolecules.[172] The knowledge of fine-tuning photophysical properties of organic dyes resulted in a large number of visible and NIR dyes that can be used for imaging. An overview is given in Figure 16.[167]

In the UV/violet range there are three different classes of fluorophores. The most prevalent are coumarins, e.g., ATTO 390 or Alexa Fluor 430. They can be attached to biomolecules *via* different types of conjugation chemistry (NHS, click, maleimide). The second class is fluorogenic DNA stains, e.g., 4,6-diaminido-2-phenylindole (DAPI) or Hoechst 33342. DAPI is a DNA-specific probe that binds to the minor groove of A-T rich sequences forming a fluorescent complex.[173] The third class is based on sulfonated pyrene molecules, e.g., Alexa Fluor 405 or Cascade Blue.[174] Overall, fluorophores that can be excited in the UV/violet range are often used as reference markers for cellular structures. Due to the short excitation wavelength, the use of these dyes can lead to phytotoxic effects and elicits high autofluorescence from endogenous fluorophores.[167]

In modern biological imaging fluorescent dyes in the blue range are very popular. Typically, they are excited with 488 nm using an Ar-ion laser.[167] As mentioned above, fluorescein and its derivatives are the most commonly used fluorophores in this spectral range, despite the low photostability and low cell permeability. Rhodamine 110 is the second important scaffold that is used in many commercially available blue fluorophores. The fluorescence quantum yield or brightness can be tuned by implementing rotationally restricted substituents at the distal nitrogen atoms.[171] In addition, many BODIPY dyes can be excited with 488 nm. They exhibit high extinction and brightness but suffer from low stokes-shifts that often can lead to self-quenching.[11] Another drawback of BODIPY dyes is their relatively high lipophilicity.[175] To stain RNA aptamers or small proteins in the blue spectral range the fluorinated GFP chromophore analogue DFHBI[176] or HMBR[177] are widely used.

The green window is localized in the spectral range around 560 nm.[167] To red-shift the absorption wavelengths of fluorescein and rhodamine dyes the xanthene oxygen can be replaced with a quaternary carbon atom.[178] Prominent examples are carbofluorescein[179] and some carborhodamine-based ATTO dyes.[180] Another class is *N*-alkylated rhodamines such as tetramethylrhodamine (TMR) or JF_{549}.[181] Rigidification of the rhodamine structure in some dialkylrhodamine compounds can also lead to a tuned absorption wavelength in the green excitation window. Examples are ATTO 550 and Alexa Fluor 546.[182] The last class is indocyanine dyes[183] like Cy3.[184] Improvements to the structure have been made. Those led to Alexa Fluor 555 and Cy3b which exhibit enhanced brightness and stability.[185]

Red light excitable fluorophores can absorb light between 620 and 700 nm. While it remains challenging to develop fluorescent proteins in this excitation windows, there are many small-molecules available. Again, indocyanine dyes[183] like Cy5 and some variants are often used for imaging.[186] Two prominent improved versions of Cy5 are for example Cy5B[187] and Alexa Fluor 647 which exhibit enhanced photon output. This

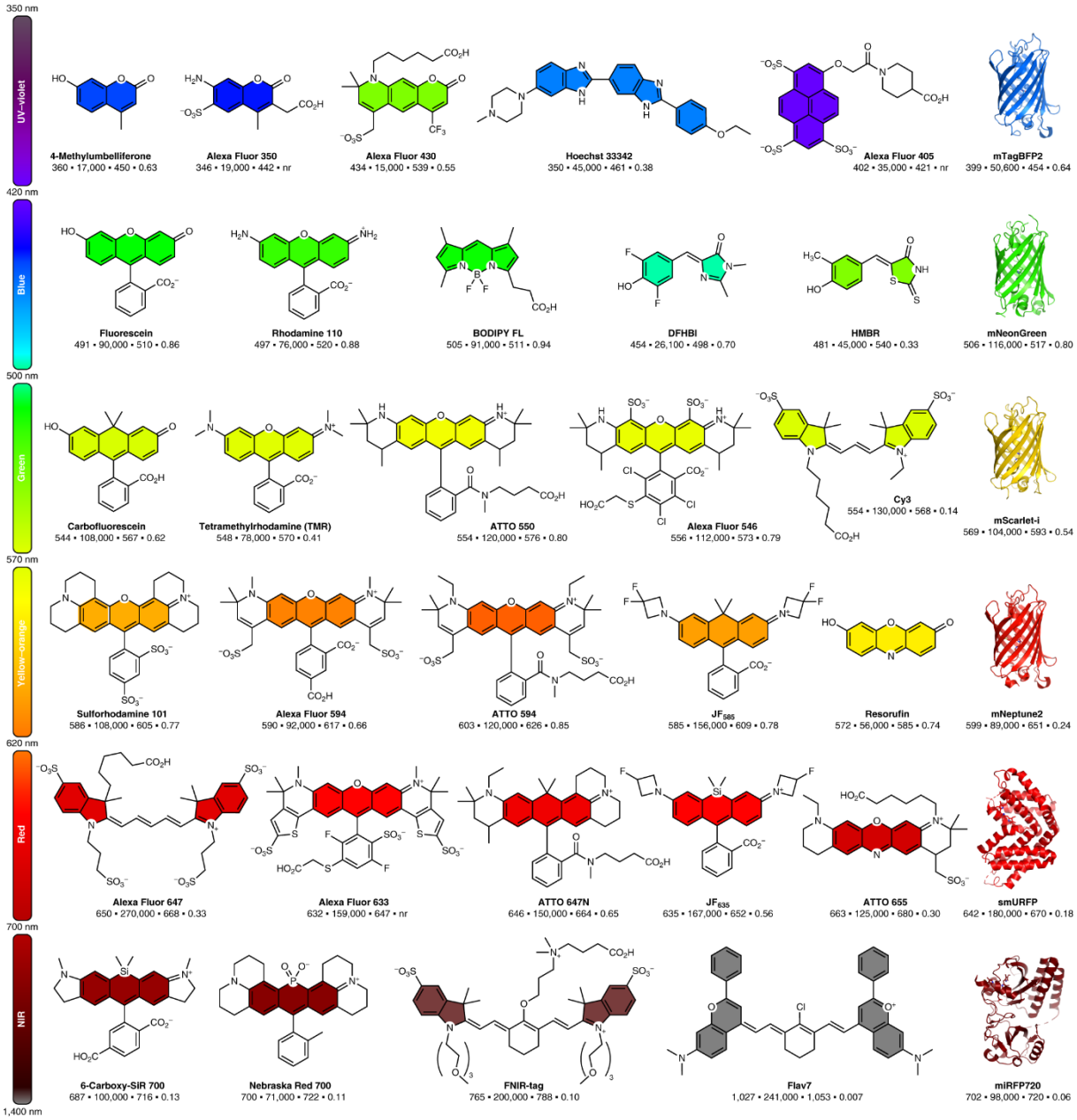

Figure 16: Overview of small molecule organic fluorophores that can be excited with UV- to NIR-light. Taken from Grimm et al. 2022.

increased fluorescence quantum yield and lifetime can be rationalized by conformationally restraint structure motifs at the indocyanine backbone.[45] Another class is the rhodamine scaffold that just reaches this spectral window with the oxygen-containing Alexa Fluor 633.[188,189] To further red-shift rhodamines the oxygen atom has to be replaced by a dimethylcarbon group resulting in carborhodamines. The most prominent and widely used fluorophore of this class probably is ATTO 647N.[190,191] Also a dimethylsilicon motif can be used to replace the oxygen in rhodamines.[192,193] This results in Si-rhodamines which exhibit a bathochromic shift of about 100 nm compared

to the parent xanthenes. Apart from modified rhodamines, highly derivatized phenoxazines can be used for imaging in the red window, e.g., ATTO 655.[194]

In the NIR window (> 700 nm), two classes of fluorophores can be used. The first is modified rhodamines. Si-rhodamines can be pushed into the NIR, e.g., SiR 700 which can be used for superresolution microscopy.[195] Phosphination of the rhodamine scaffold can also shift the absorption wavelength to the NIR. Nebraska Red exhibits high photostability and brightness.[196] The rhodamine oxygen in the NIR dye JF_{724} is replaced by a sulfone moiety, resulting in a large bathochromic absorption shift.[197] Unfortunately, sulfonated rhodamines often suffer from a low fluorescence quantum yield. The second class in the NIR window is cyanine dyes. Cy7 can be synthesized by further extension of the polymethine chain combined with substituents that avoid aggregation of the small molecules.[70]

When organic fluorophores are combined with molecular beacons or other oligonucleotides, the attachment is usually done post-synthetically, e.g., *via* NHS labeling. Another possibility to fluorescently label DNA and RNA is the direct incorporation of fluorescent nucleobases. Those are discussed in the following chapter.

2.2.4. Fluorescent nucleobases

The information described in this chapter is based on a review article by Kool *et al.* 2017.[198] Fluorescent nucleobases are DNA and RNA based-analogues that are chemically modified to have specific fluorescent properties for the analysis of nucleic acids. Thereby, the RNA in which the fluorescent nucleobase is incorporated, retains its chemical and biological functions, such as base pairing, stacking or biochemical interactions with proteins and enzymes. Fluorescent nucleobases can be used as chemical tools to study nucleic acid structures, RNA activity or nucleic acid interactions.[199] In general, they can be divided into two categories. The first category is canonical fluorescent nucleobases, where Watson-Crick like base-pairing is preserved and the structures are very similar to the native nucleobases. On the other hand, there are non-canonical fluorescent nucleobases where more dramatic changes can be made to the molecule's architecture (see Figure 17). Both categories can be used for different applications and have their advantages and disadvantages. The development and applications are discussed in this chapter.

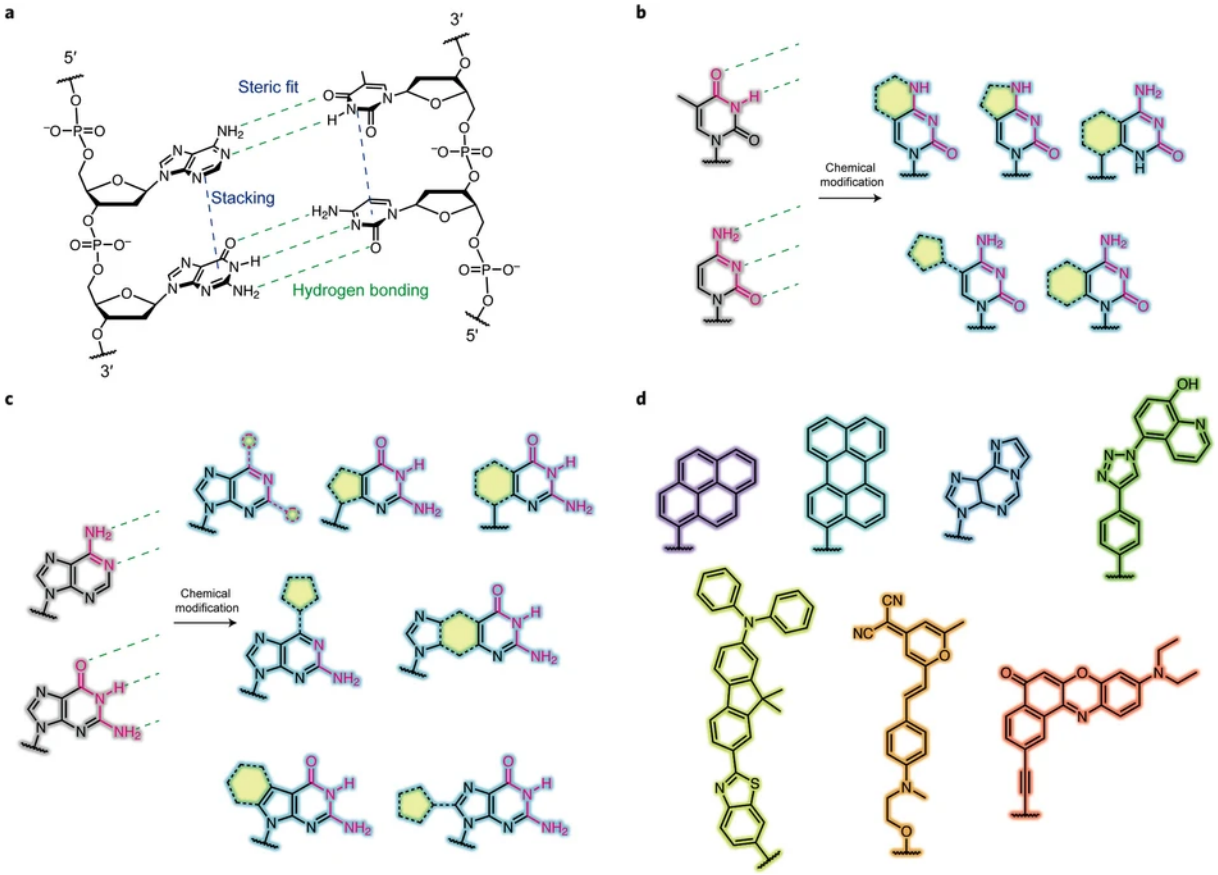

Figure 17: Structures of natural nucleobases and their fluorescent analogs. a) Hydrogen-bonding sites in a typical DNA/RNA double helix. b) Canonical pyrimidine natural nucleobases and possible modifications for fluorescence enhancement. c) Canonical purine nucleobases and possible modifications for fluorescence enhancement. d) Non-canonical fluorescent nucleobases. Figure taken from Kool et al. 2017.

Canonical fluorescent nucleobases:

Per definition, canonical fluorescent nucleobases are based on the purine or pyrimidine architecture and have at least two positions for Watson-Crick hydrogen bonding allowing them to form base pairs in a double helix (see Figure 18). Therefore, the positions to chemically modify the nucleobase for enhanced fluorescent properties are constrained because the base-pairing positions cannot be used. In addition, the electronic arrangement of the purine or pyrimidine π-system must be considered when substituents are added to modulate the fluorescent properties. As already discussed in the previous chapter on the design and development of photolabile protecting groups, it is desirable to shift the absorption and emission wavelengths to the red to avoid cell damage caused by high energy light. Due to the few positions available, this was difficult to achieve, according to recent literature.

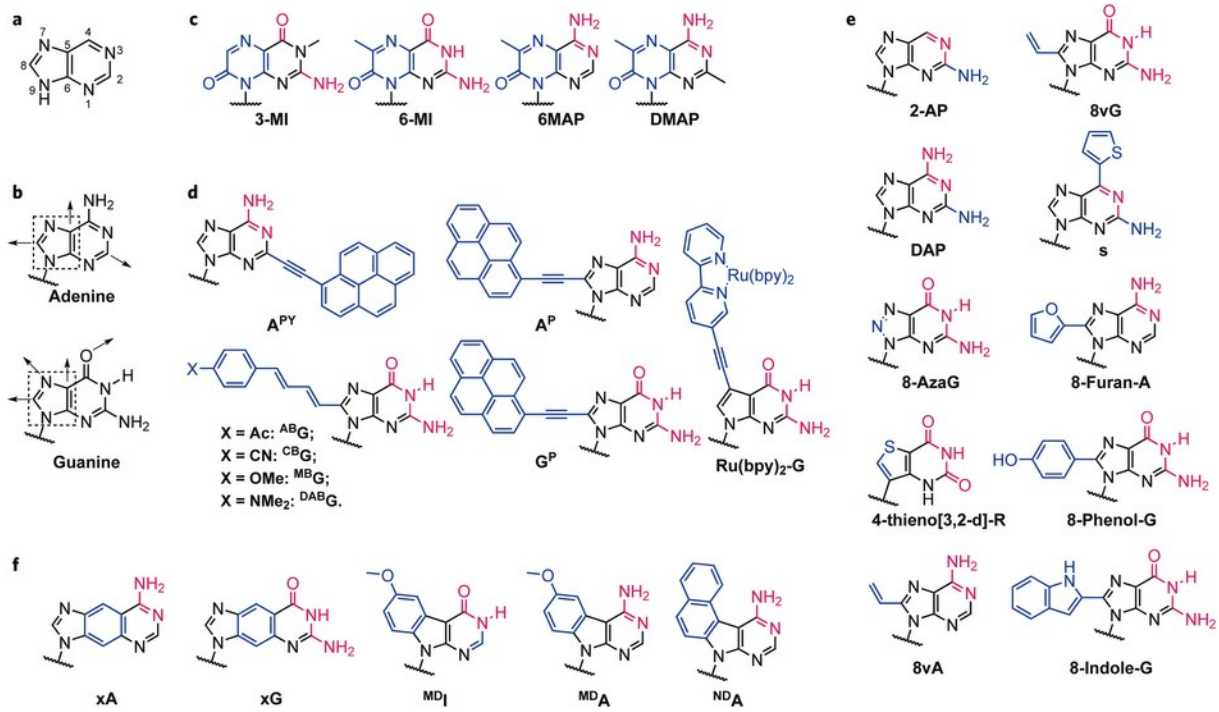

Figure 18: Overview of possible modifications of purine nucleobases to enhance fluorescence properties. a) General purine scaffold. b) Adenine and guanine scaffolds. c) Modified purine ring structures. d) Extensions of the π-system using conjugated linkers and fluorophores. e) Modified substituents on the purine scaffold. f) Purine ring fusions. Figure taken from Kool et al. 2017.

Purine fluorescence enhancing modifications mainly occur at the 2/8 positions of adenine or the 7/8 positions of guanine. In general, there are four types of modifications that can lead to altered fluorescence properties in purines: (i) modified ring structures (Figure 18, c), (ii) extending the π-system *via* conjugated linkers (Figure 18, d), (iii) modified substituent on the purine scaffold (Figure 18, e) and (iv) purine ring fusions (Figure 18, f). A prominent example for type (i) is pteridines (Figure 18, c), where the five-membered purine ring is replaced by a pyrazine six-membered ring system to enhance excitation wavelength and fluorescence properties. Using this replacement the fluorescence quantum yields can be increased by up to four orders of magnitude and an up to 100 nm bathochromic shift can be achieved.[200–202] This alteration is due to the increased conjugation of the six-membered ring which results in a smaller energy gap between HOMO and LUMO. Regarding type (ii) modifications, the positions 2 and 8 are the most used for extending the π-system with conjugated linkers. These positions are synthetically accessible and do not disturb the base paring of the fluorescent nucleobase (Figure 18, d). Careful structural modifications led to fluorescent nucleobases that can be activated with ultraviolet to blue light (380-420 nm) and emit light with 450-480 nm.[203–205] Popular substituents for the extension are

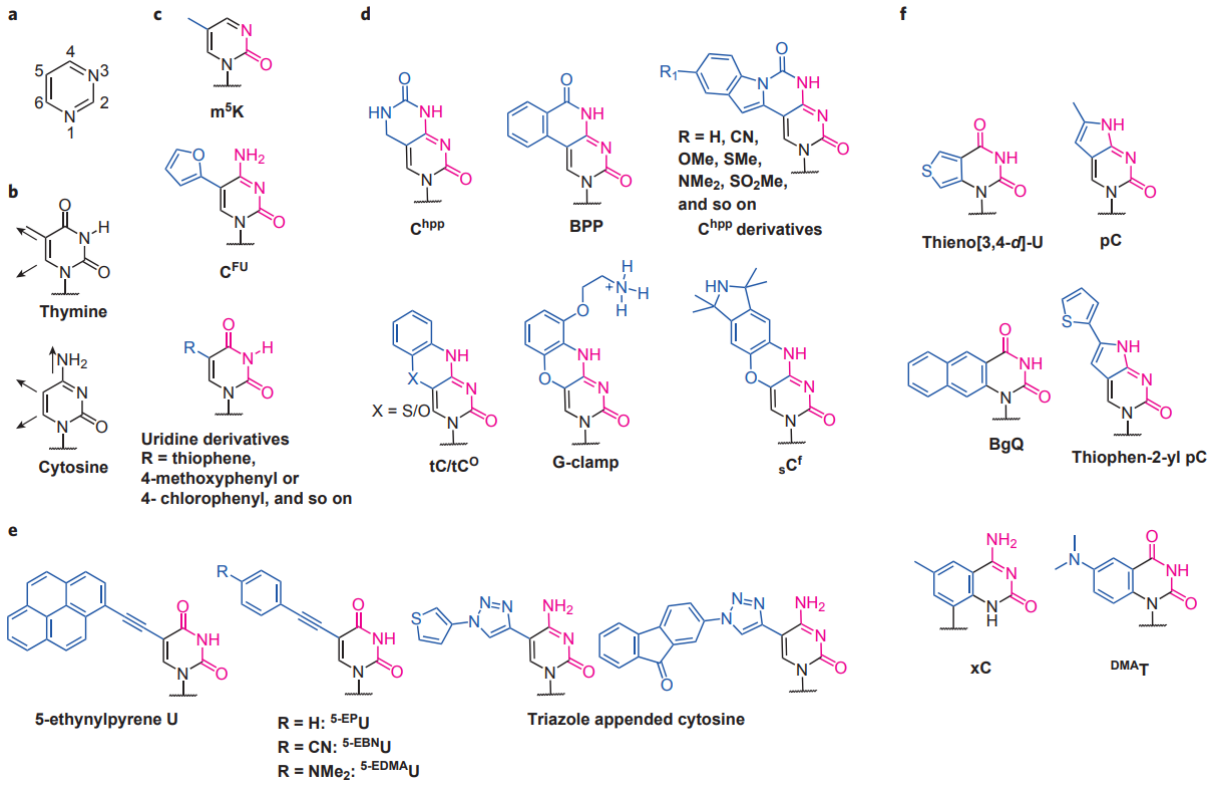

Figure 19: Overview of possible modifications of pyrimidine nucleobases to enhance fluorescence properties. a) General pyrimidine scaffold. b) Thymine and cytosine scaffolds. c, d) Modified purine ring structures. e) Extensions of the π-system using conjugated linkers and fluorophores. f) Pyrimidine ring fusions. Figure taken from Kool et al. 2017.

pyrene fluorophores or ruthenium bi-pyridyl fluorophores, which are coupled *via* alkyne linkers. Type (iii), the modification of purine substituents currently is the most widespread modification used to design fluorescent nucleobases (Figure 18, e). We take guanine as an example. The carbon atom at position 8 can be replaced by a nitrogen which results in an environmentally sensitive emission at 347 nm in solution which is shifted to 377 nm when the nucleoside is incorporated into an oligonucleotide.[206,207] Another possibility is the replacement of the nitrogen at position 7 with a sulfur atom, which leads to a red-shifted emission of 351 nm in water with a high fluorescence quantum yield.[208,209] Also adding certain functional groups, e.g., vinyl to position 8 can dramatically increase the fluorescence quantum yield to more than 0.72 with a 400 nm emission maximum at the guanine scaffold.[210] Many more examples can be found in recent literature.[198] The last type (iv) of modifications is purine ring fusions (Figure 18, f). As fusion substituents, mostly benzene or naphthalene functional groups are attached to the positions 7 and 8 to preserve base-pairing sites. The attached rings result in an expansion of the π-system and therefore

an absorption redshift and an increase in the fluorescence quantum yield. Examples of this type of modification are lin-benzoadenine and lin-benzoguanine that have a fluorescence emission at 393 nm and 413 nm in an aqueous solution.[211] It is also possible to insert a phenyl-group between the five- and the six-membered rings of the purine. The resulting nucleobases exhibit fluorescence quantum yields of more than 0.40 and show a significant redshift due to the enlargement of the π-system.[212]

On pyrimidine nucleobases, there are fewer modification sites available due to the smaller ring size. In contrast to the purine nucleobases, the modifications on pyrimidines can be divided into three categories and focus on the positions 4, 5 and 6. The categories are (i) modified pyrimidine substituents (Figure 19, c,d), (ii) extended fluorescent scaffolds using conjugated linkers (Figure 19, e) and (iii) ring-fused pyrimidine ring systems (Figure 19, f). The earliest examples in category (i) utilized position 5 of the cytosine and thymine scaffold for the attachment of different substituents. The addition of a furane group resulted in a weakly fluorescent cytosine with an emission maximum at 443 nm.[213] Several uracil derivatives, on the other hand, were substituted with thiophene, 4-methoxyphenyl or chlorinated phenyl groups (Figure 19, c) to enhance the push-pull character of the nucleobases and therefore improve the fluorescence properties.[214] The positive effects of altering pyrimidine substituents can be further enhanced when the substitution leads to enhanced rigidity combined with increased conjugation. Bi- and tricyclic deoxycytidine derivatives exhibited an enormously high fluorescence intensity with stokes shifts up to 120 nm (Figure 19, d).[215] In the second category (ii), fluorescent molecules like pyrene, fluorenone or BODIPY are used to extend the pyrimidine π-system *via* conjugated linkers (Figure 19, e). To maintain the ability for base-pairing and to take advantage of the conjugation with the 5,6 double bond, nearly all modifications in this category have taken place at position 5. For example, 5-ethynylpyrene U exhibits a strongly redshifted absorption at 392 nm, while its emission maximum is at 424 nm.[216] Other modifications like triazole, thiophene or fluorenone also show a bathochromic absorption shift, but their fluorescence properties are only moderate.[198,217] Therefore, some optimization is still required. The last category (iii) of pyrimidine modification is ring fusion (Figure 19, f). Additional rings can either be attached to positions 4, 5 or positions 5, 6 to have a strong influence on the fluorescence properties while at the same time they do not perturb Watson-Crick base-pairing. If, for example, naphthalene is fused to thymine, the resulting benzoquinazoline-derivative shows a remarkable fluorescence quantum

yield of 0.82 with an emission maximum at 434 nm.[218] A dimethylamino-phenyl group that is fused to the positions 5, 6 of thymine is even capable of forming electrostatic interactions with mercury.[219] This complex can be used in live cells to explore mercury metabolism *via* a fluorescent readout.

Non-canonical fluorescent nucleobases:

Unlike canonical nucleobases, non-canonical nucleobases do not necessarily require hydrogen-bonding capability. Also, the purine or pyrimidine basic core does not have to be preserved. Therefore, there are many more possibilities to fine-tune the photophysical properties. Compared to canonical nucleobases, they are relatively unexplored and at the same time the number of new chromophores is growing steadily. In general, non-canonical fluorescent nucleobases can be divided into two different categories: (i) nucleobases that consist of polycyclic hydrocarbons and (ii) planar and heterocyclic fluorophores (Figure 20). The first examples of the category (i) were pyrene, phenanthrene, perylene and benzopyrene, which were introduced to DNA and RNA as new C-glycosidic fluorophores in the 1990s and 2000s.[220–222] By incorporating multiple fluorophores into a DNA or RNA, many structural properties, or enzymatic activities could be studied *via* photophysical energy transfer.[223,224] Nowadays, a variety of different hydrocarbon-based fluorophores with different excitation wavelengths and fluorescence properties are available. They are shown in Figure 20, c as examples.[225,226] A particularly interesting polycyclic hydrocarbon at this point is phenethynylpyrene deoxyriboside (Figure 20, d).[227] This dimeric dye is able to switch emission from green to blue light upon irradiation with blue light. The UV light causes a bis-alkyne-dependent [2+2+2] cycloaddition which results in a spatial separation of the formerly stacked pyrene units. Thereby, they lose their excimer emission properties (Figure 20, d). As the second category (ii), planar and heterocyclic fluorophores have to be mentioned. One possibility to create a non-canonical analogue is to replace the nucleobase at the sugar with a fluorophore known from the literature. Prominent examples are coumarin C-ribosides,[228] Nile Red nucleosides[229] or porphyrin C-ribosides[230] (Figure 20, e). If multiple individual fluorophores (“fluorosides”) are assembled into a DNA strand they display unique fluorescent properties, depending

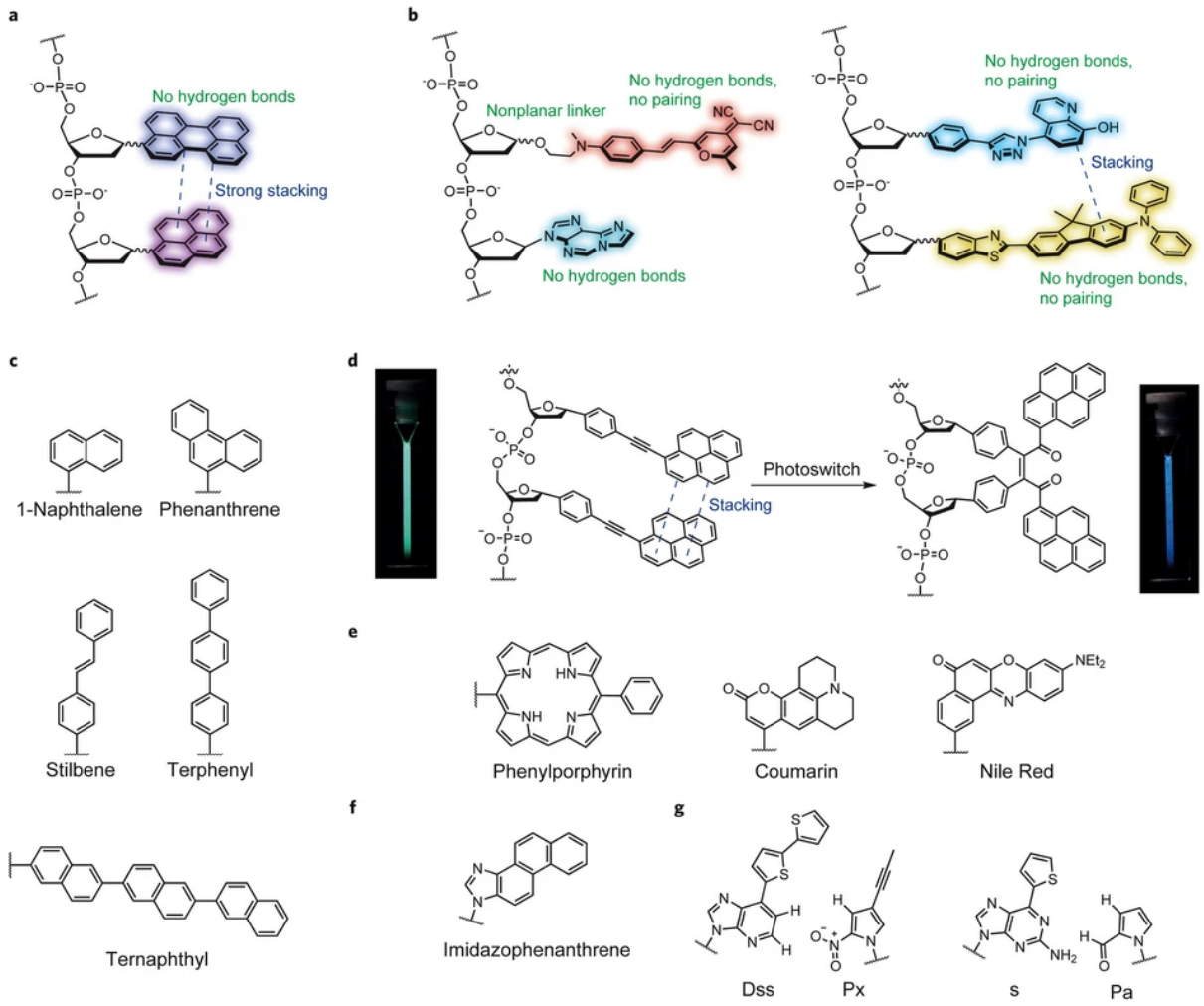

Figure 20: Examples for non-canonical nucleobases. a) Stacking mechanism of fluorophores based on aromatic hydrocarbons. b) Fluorescent nucleobases composed of planar heterocyclic fluorophores. c) Example structures of aromatic hydrocarbons. d) Photoinduced cycloaddition of two adjacent phenethynylpyrene nucleobases. e) Known fluorophores as C-glycosidic nucleobases. f) Simple heterocyclic nucleobase that is used in the detection of DNA repair. g) Non-canonical nucleobases forming unnatural base pairing.

on the exact sequence and stacking modes.[231] While non-canonical nucleobases are often brighter and more photo-stable, they also have certain limitations. One major drawback is, as mentioned above, the inability of non-canonical nucleobases to build hydrogen bonds. Therefore, Watson-Crick pairing is lost which results in e.g. less stable double helices. In addition, many enzymes rely on hydrogen bonding sites at nucleosides to incorporate them into a DNA or RNA strand. To circumvent this problem, a lot of research has been done, e.g., using polymerases that do not require templates. This allowed the incorporation of large non-canonical nucleobases as fluorophores.[232] Also, some large some non-canonical nucleobases undergo very

strong stacking interactions, allowing them to form base pairs even without hydrogen bonding.[233]

3. Aim of this work

The aim of this work was the development of new tools to study RNA in neurons. As an initial step, molecular beacons had to be prepared to investigate the transportation of mRNA in hippocampal neurons in the lab of Prof. Dr. Erin Schuman at the Max-Planck-Institute for Brain Research in Frankfurt. By visualizing RNA in cells, the goal was to observe how individual RNAs and their clusters move and are transported along dendrites. More specifically, transport velocities, traveled distances and overall distribution in the cell should be examined. In addition, it was aimed to monitor how long-term potentiation (LTP) and long-term depression (LTD) affect the parameters mentioned just above. As target mRNAs Camk2a, Beta-actin and Psd95 mRNA, which play important roles in neuronal cell function were chosen. For each mRNA, two MBs that are complementary to two different parts of the respective RNA had to be designed and synthesized. Those MBs have to be equipped with two different fluorophores, respectively.

In the next step these MBs should then be further improved. One problem with conventional beacons is that the fluorophores bleach with increasing monitoring time. This disadvantage should be circumvented by providing light-activatable molecular beacons. More specifically, in this project it should be possible to activate a subpopulation of RNA locally in a specific area of the cell. By knowing the exact origin of the visualized RNA, it should be possible to reduce the light sampling rate significantly. Less light will result in less bleaching which in turn results in longer monitoring time. As part of this project, light-activatable MBs for CamK2 and Beta-actin mRNA should be synthesized. To activate them with visible light, a 405 nm cleavable coumarin-linker had to be synthesized and incorporated into the MBs in the first place. The design was expected to lead to significantly reduced background and high spatial and temporal resolution. Imaging experiments should be performed in the lab of Prof. Dr. Erin Schuman at the Max-Planck-Institute for Brain Research in Frankfurt.

Consequently, not only the visualization itself but also the hybridization of MBs should become light-activatable. Controlled hybridization can be of great advantage, especially for RNA processing and regulation by ncRNA. In this part of the work, so-called "photo-tethers"[234] should be attached to the phosphate backbone of MBs. These can be chemically linked to each other after the solid-phase synthesis, preventing hybridization with a complementary strand. A light pulse was then supposed to remove

the photo-tethers and restore the natural conformation of the MB. Only after removing the photolabile protecting groups, hybridization should be possible. For this purpose, nuclease-resistant 2'-OMe phosphoramidites containing the respective photo-tethers have to be synthesized and then incorporated into MBs. Target sequence for the synthesized beacons should be miR-98, which plays an important role in hippocampal neurons. Biological experiments should be performed in the group of Prof. Dr. Erin Schuman at the Max-Planck-Institute for Brain Research.

Lastly, in order to use light-activatable probes for the investigation of RNA, it is important to develop photolabile protecting groups that release the leaving group efficiently. Therefore, in the last part of this work, the uncaging of coumarin protecting groups should be systematically analyzed and improved. To enhance the photolysis of coumarins it may be helpful to compare the fluorescence properties of these. Since photolysis and fluorescence occur on approximately the same time scale, fluorescence can provide a good first indication of how efficiently a chromophore can photochemically release its leaving group. Guided by this principle, the task of the project was to develop new coumarin protecting groups based on the well-characterized fluorophore ATTO 390[235,236] and to systematically investigate its photophysical and photochemical properties. Together with the research group of Prof. Dr. Josef Wachtveitl the underlying photophysical principles should be investigated in a time-resolved manner. In this study, special emphasis should be placed on the effects of a twisted intramolecular charge transfer (TICT) and therefore inhibited rotation around the donor-moiety in coumarins to the uncaging reaction. The aim was to develop a new coumarin protecting group with enhanced uncaging efficiency that can be used in future biological experiments.

4. Results and Discussion

In this chapter the main results and conclusions of the projects introduced in Chapter 3 are explained and discussed. Most of the results have been published throughout the doctoral thesis and are referenced at the appropriate position.

4.1. MBs for the investigation of mRNA dynamics in neurons

The results in this chapter were previously published in reference [I] “Differential regulation of local mRNA dynamics and translation following long-term potentiation and depression”.[7] Biological experiments described in this chapter were performed by Dr. Paul Donlin-Asp at the Max-Planck-Institute for Brain Research in Frankfurt under the supervision of Prof. Dr. Erin Schuman. The development of the analysis tool pipeline was done by Dr. Claudio Polisseni at the Max-Planck-Institute for Brain Research, imaging facility.

Synaptic plasticity is the most important mechanism for learning and memory and describes an activity-dependent strengthening or weakening of synaptic transmission.[237,238] In this context, mRNA transport and local translation play a crucial role. After synthesis in the nucleus, mRNAs are transported to the individual synapses where they are translated locally.[8] However, the exact transport processes of the individual mRNAs have not yet been precisely clarified. Therefore, MBs for three different neuronal mRNAs (CamK2, Beta-actin and PSD95) were synthesized in this project to track them under basal conditions and after plasticity.

MBs were prepared by oligonucleotide solid-phase synthesis.[239,240] The cycle is shown in Figure 21. The phosphoramidite method was used for oligonucleotide preparation. Protected phosphoramidites of the respective nucleotides or modifications are subsequently coupled from the 3'- to the 5'-end. Solid-phase synthesis has many advantages over synthesis in solution. Very small preparation scales are possible (in this case 1 µmol). The phosphoramidites are stable when exposed to ambient air, and the synthesis takes little time due to automation. The reagents can be used in high excess and each coupling of a phosphoramidite to the growing strand is followed by automated purification. In addition, the individual coupling steps have yields of about 99% each. In most cases, the first nucleotide or chromophore is already linked to the solid phase. In some cases, however, universal CPG supports are used to which no

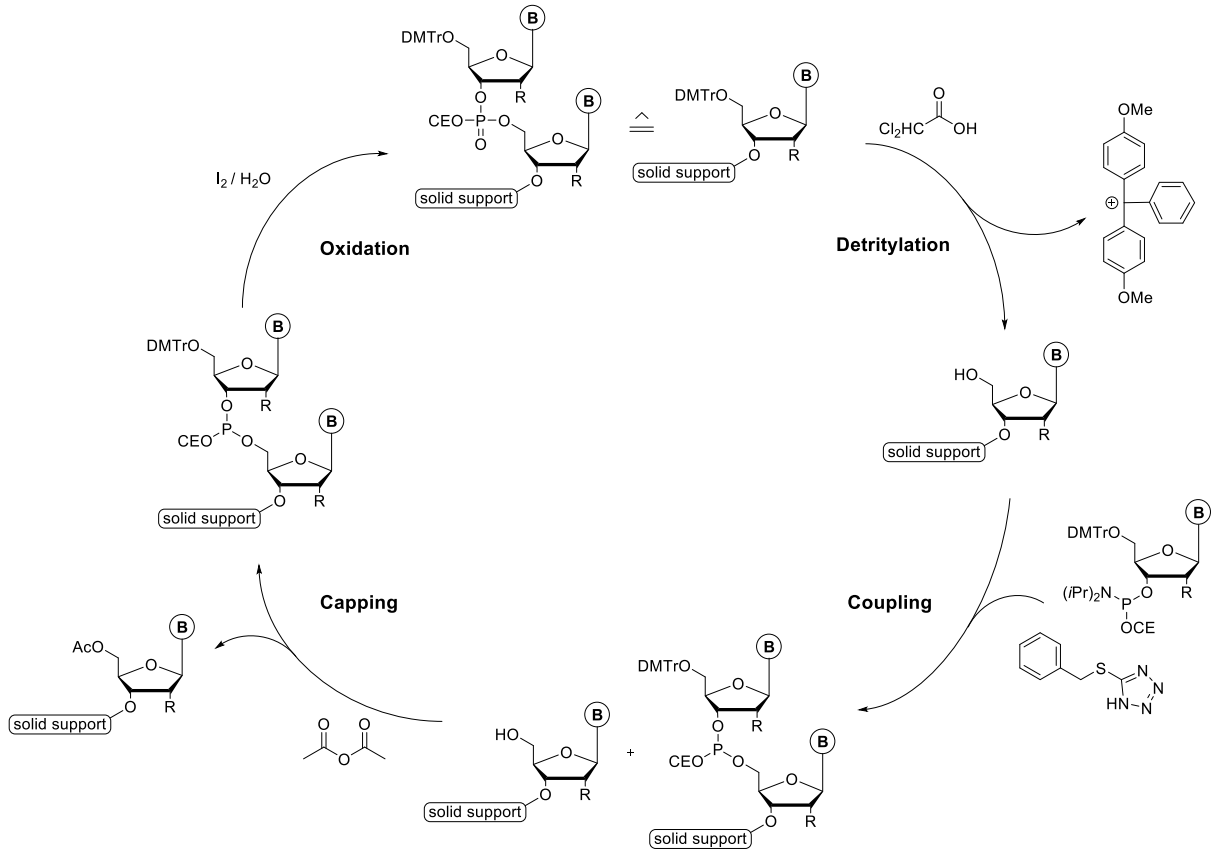

Figure 21: General cycle of the oligonucleotide solid-phase synthesis. Step 1: Detritylation using acid. Step 2: Coupling of monomer n+1. Step 3: Capping of unreacted monomer. Step 4: Oxidation of P(III) to P(V).

nucleotide has yet been attached. The phosphoramidites themselves are protected at the 5'-OH with DMTr-groups, which can be cleaved under acidic conditions. The phosphate at the 3'-OH position is protected by a β-cyanoethyl group that can be cleaved under basic conditions. The exocyclic amino groups of bases A, G and C are protected with permanent protecting groups. They can be removed by alkaline hydrolysis after the solid-phase synthesis. At the same time, in most cases, the final strand is cleaved from the solid-phase and the cyanoethyl groups are removed.

The phosphoramidite method can be divided into four steps. In the first step, the DMTr protecting group of the growing strand is cleaved with the help of e.g., dichloroacetic acid (detritylation). Then, the next nucleotide is activated by BTT (benzylthiotetrazole) and coupled to the free 5'-OH of the previous nucleotide. However, also other tetrazole-based activation reagents can be used for coupling. The unreacted 5'-OH groups are acetylated (capping) with Ac_2O or similar anhydrides in the third step. Therefore, they cannot react further and are excluded from the synthesis cycle. Finally, phosphorus(III)

is oxidized to phosphorus(V) in an iodine-pyridine-water mixture and the cycle starts again.

The three MBs consisted of a 2'-OMe backbone and were equipped with either ATTO565 and BHQ2 or ATTO647N and BBQ-650 as fluorophores and quenchers. The loop sequences were complementary to the UTRs of CamK2a, β-actin and Psd95 mRNA that are highly abundant in neurons[241] and translationally regulated by plasticity.[242–245] In addition, a negative control MB against GFP mRNA, which was expected not to show a fluorescent signal in cells, was synthesized. The MBs were transfected to primary rat hippocampal neuronal cultures by Dr. Paul Donlin-Asp. After transfection, endogenous mRNA dynamics were monitored for 20 minutes using a laser frame rate of 1/s. A Matlab analysis pipeline written by Dr. Claudio Polisseni was used to quantify the mRNA dynamics (Figure 22, A-C). The pipeline allowed to calculate e.g., the cumulative distances traveled (Figure 22, D) or the active transport velocities (Figure 22, E). Visualized mRNAs were divided into four categories: anterograde (the puncta were actively moving away from the soma), retrograde (the puncta were actively moving towards the soma) confined (the puncta did not move more than 0.5 µm within a certain time period but then switched to anterograde or retrograde movement) and stationary (the puncta did not move within the entire imaging period and were therefore excluded from further analysis). The analysis

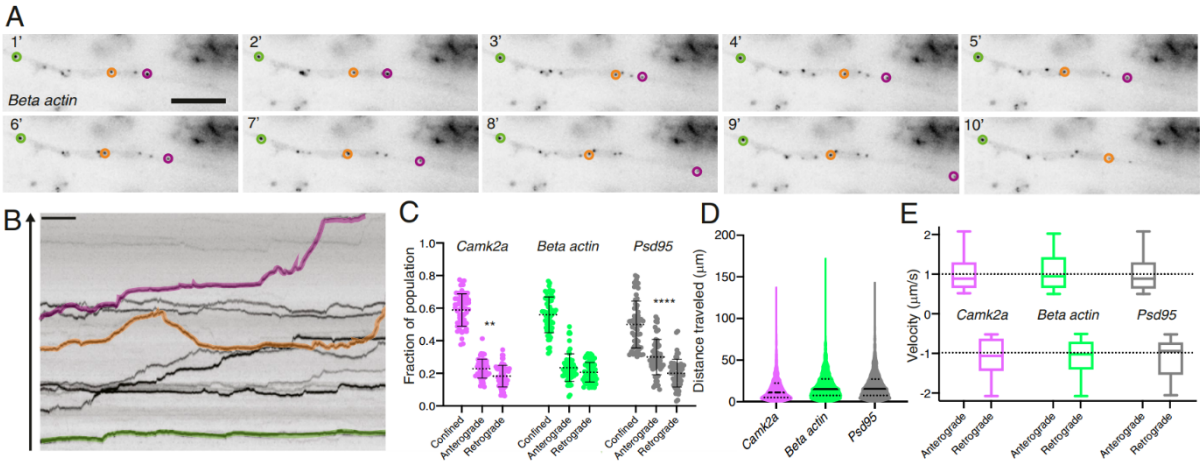

Figure 22: (A) Single images of β-actin mRNA taken every minute for a period of ten minutes. As examples, individual mRNAs are marked as stationary (green) or confined with periods of motility (magenta and orange). (B) Kymograph from the first ten minutes of imaging. The y-axis marks anterograde movement along the dendrite. (C) Quantification of the dynamic states of CamK2a, β-actin and Psd95 mRNA. (D) Cumulative distances traveled for the individual mRNAs over the whole imaging period. (E) mRNA velocity for anterograde and retrograde movement. Taken from Donlin-Asp et al., 2021.

revealed that all three mRNAs spent most of the time in a confined state (Figure 22, C). As expected, for active movement the mRNAs were more likely to be transported anterogradely than retrogradely. This is a logical explanation for the fact that mRNAs can also be translated locally in synapses far away from the cell body.

In the next step, it was investigated whether the translational status of an mRNA has an effect on its dynamics. Therefore, two different elongation inhibitors were used (Figure 23, A). Puromycin causes a release of the nascent peptide chain and dissociation of mRNA and ribosome,[246] and anisomycin freezes ribosomes on the mRNAs they are currently translating. The analysis showed that puromycin led to enhanced mRNA motility and less confined mRNA, most likely caused by the dissociation of ribosome and nucleic acids (Figure 23, B-E). On the other hand, the treatment with anisomycin resulted in the opposite effect, which means decreased mobility due to the freezing of ribosome and mRNA. Interestingly, both treatments did not change the active transport velocities of any mRNA and did not alter the fraction of the stationary population. These findings are quite consistent with the hypothesis that mRNAs in neurons are transported in a quiescent non-translating state.[247,248] It was

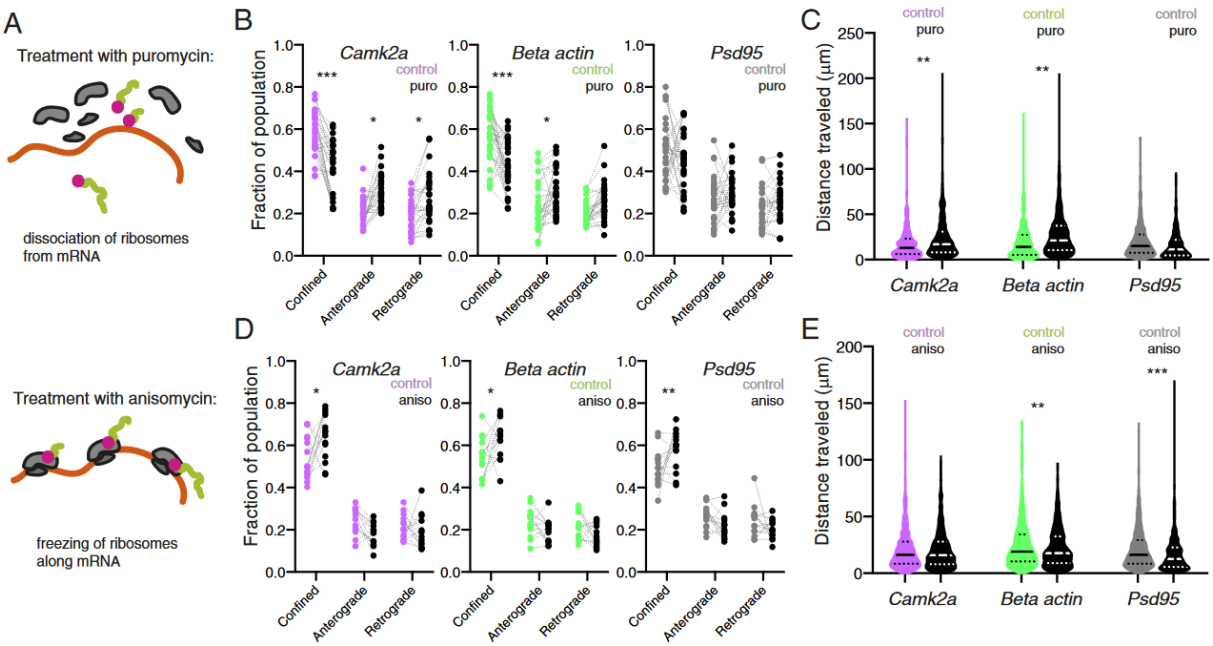

Figure 23: (A) Schematic mechanism of puromycin and anisomycin treatment of neuronal cells. Puromycin leads to dissociation of mRNA and ribosomes whereas anisomycin leads to the freezing of the ribosomes. (B,D) Comparison of the mobility states of all three mRNAs before and after chemical treatment. (C,E) Comparison of the traveled distances of all three mRNAs before and after chemical treatment. Taken from Donlin-Asp et al., 2021.

demonstrated that the translational status of a certain mRNA has an effect on its overall dynamics in the dendrite.

Furthermore, it was assessed whether mRNA dynamics can be modulated with synaptic plasticity.[249] Therefore, two forms of protein synthesis-dependent synaptic plasticity were performed: chemical long-term potentiation (cLTP)[250] and metabotropic glutamate receptor-mediated long-term depression (mGluR-LTD).[251] For all three

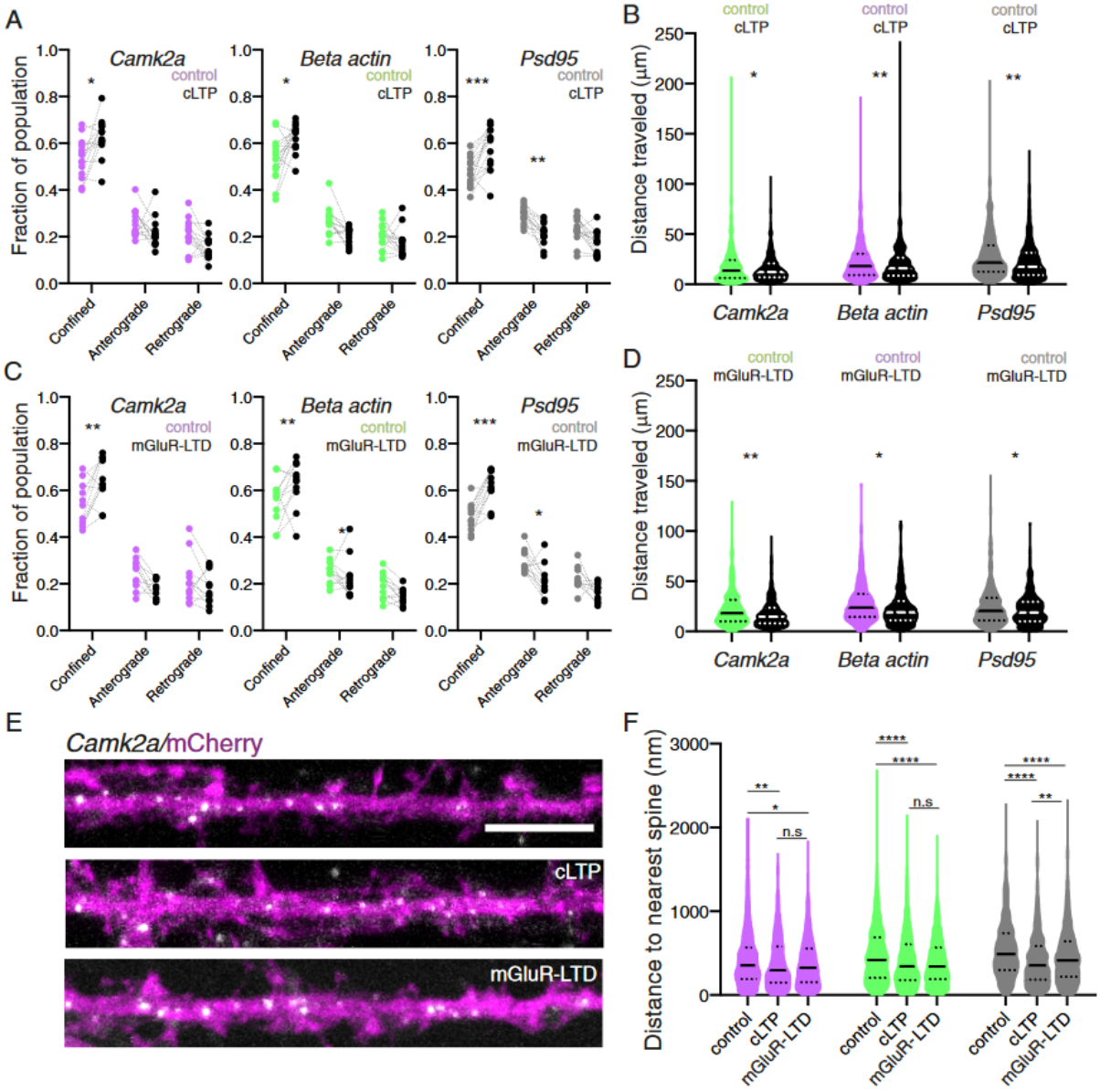

Figure 24: (A) Comparison of the mobility states of all three mRNAs before and after cLTP. (B) Comparison of the traveled distances of all three mRNAs before and after cLTP. (C) Comparison of the mobility states of all three mRNAs before and after mGluR-LTD. (D) Comparism of the traveled distances of all three mRNAs before and after mGluR-LTD. (E) Images of CamK2a RNA FISH experiment under cLTP and mGluR-LTD conditions. Neuron stained with mCherry. (F) Mean distance of mRNAs to the nearest dendritic spine during plasticity. Purple: CamK2a, green: β-actin, grey: Psd95. Taken from Donlin-Asp et al., 2021.

mRNAs the introduction of cLTP led to a decreased mRNA motility (Figure 24, A). Also, the mean cumulative distance traveled was significantly reduced (Figure 24, B). The same effects were observed when mGluR-LTD was applied (Figure 24, C and D). The experiments demonstrated that both forms of protein synthesis-dependent synaptic plasticity have comparable effects on the motility of mRNAs that are used to remodel the protein landscape at the synapses. This is further underlined by high-resolution smFISH experiments that were used to measure the mean distance of a single mRNA granule to the nearest dendritic spine (Figure 24, E and F). It was shown that after cLTP and mGluR-LTD, the mean distance between an RNA and a dendritic spine decreased significantly after cLTP and mGluR-LTD. This data suggests an increased spine association during plasticity combined with enhanced local translation at the single synapses.

In the last step, the dynamics of the protein synthesis in neuronal cells were explored in real time during the two different forms of synaptic plasticity. However, since these experiments are only marginally related to the MBs prepared in this work, they are not described in detail. For a detailed description, please refer to reference [I].[7]

Overall, this project demonstrated how chemically modified MBs can be used to monitor mRNA in real time. Appropriate selection of target sequence, secondary structure, stem length and the corresponding chromophores can be used to stain and visualize specific nucleic acids in living cells. To perform quantifications, it is particularly important to use fluorophores and quenchers that are photostable. However, even with the best fluorophores currently available, RNAs can only be monitored with MBs over a period of minutes. After this time, the organic chromophores begin to bleach and can no longer be used to visualize, or even quantify, RNA. For some biological questions, however, it would be interesting to monitor nucleic acid transport over longer timescales. Therefore, it is important to develop methods to extend the maximum monitoring duration. The development of such a method will be part of the following chapter.

4.2. Visible light-activatable Q-dye molecular beacons

The results in this chapter were previously published in reference [II] “Visible light-activatable Q-dye molecular beacons for long-term mRNA monitoring in neurons”.[252] Biological experiments described in this chapter were performed by Dr. Paul Donlin-Asp at the Max Planck Institute for Brain Research in Frankfurt under the supervision of Prof. Dr. Erin Schuman. The development of the analysis tool pipeline was done by Dr. Claudio Polisseni at the Max Planck Institute for Brain Research, imaging facility. Parts of the results were previously published in the bachelor thesis of Vanessa Hanff[253] who is a co-author of the above-mentioned publication.

One of the biggest challenges in monitoring mRNA is the bleaching of the used fluorophores. Bleaching is the phenomenon of undesired chemical reactions after irradiation that can lead to a reduction of luminescence.[254] Due to this phenomenon, the application time of fluorescent probes, such as MBs, is limited. In recent literature, MBs have only been used for the timescale of minutes to monitor RNA.[7,126] Therefore, it is of enormous interest to develop new tools to extend the limited monitoring time. One way to circumvent photobleaching is the use of light-activatable MBs. Once

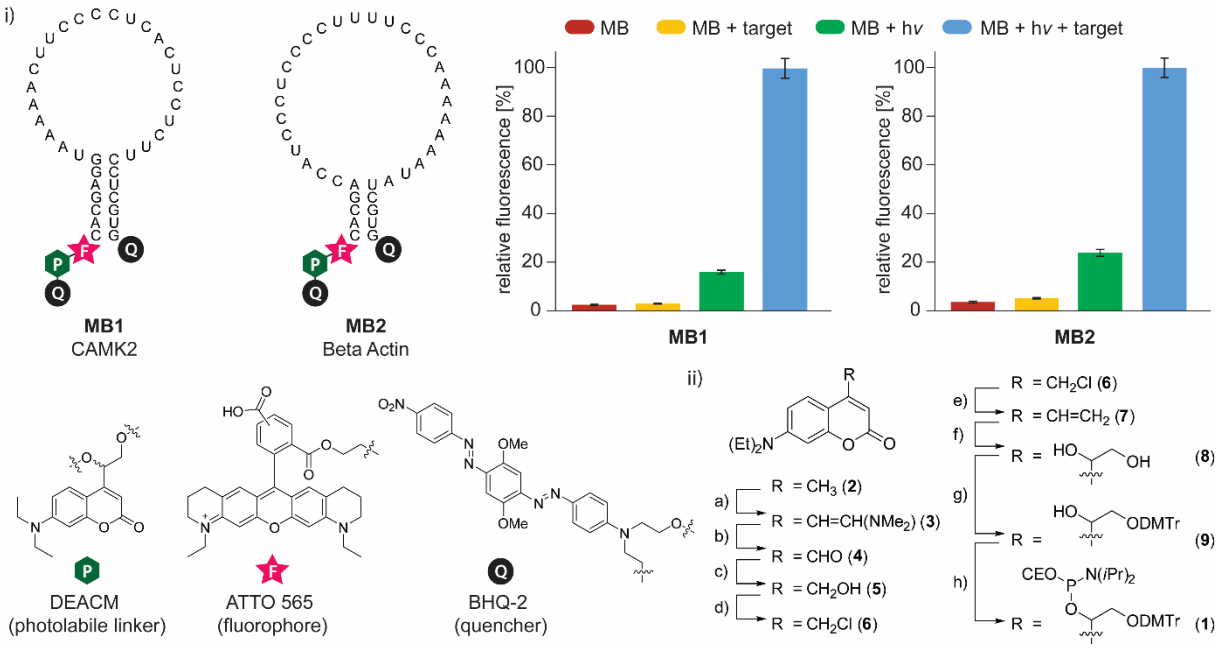

*Figure 25: i) Predicted chemical structure and chemical modifications of the MBs used in this chapter. Plate-based fluorescence assay of MB1 and MB2. Only after light activation and target hybridization, the MBs showed a high fluorescence intensity. ii) Chemical synthesis of phosphoramidite **1**. a: DMF-DMA, 94 %, b: $NaIO_4$, 97 %, c: $NaBH_4$, 64 %, d: 4-methylsulfonic acid chloride, 81 %, e: PPh_3, formaldehyde, 65 %, f: OsO_4, NMO, 59 %, g: DMTr-Cl, DIPEA, 72 %, h: 2-cyanoethoxy-N,N-diisopropylaminochloro-phosphine, DIPEA, 95 %.Taken from Klimek et al. 2021.*

transfected, the probes can be locally activated in a specific area of the cell. By knowing the exact origin of the species, it is theoretically possible to reduce the light-sampling rate significantly, which would result in delayed photobleaching. Therefore, the overall monitoring time could be increased.

For this application, Q-dye beacons[164] are the most promising candidates because they can hybridize with the target RNA even before activation. This means that there is no kinetic hindrance, and thus, no time delay after activation. However, a disadvantage of the Q-dye beacons known from literature is their excitation wavelength, which is so far limited to the UV range. UV light is known to cause severe cell damage which is unfavorable for a long-term application in cells.[9] Therefore, Q-dye beacons that are activatable with visible light to reduce cell damage and enable long-term mRNA monitoring were developed in this work (see Figure 25). While it is important that the photolabile protecting group absorbs visible light, it should not interfere with the absorption of the fluorophore and quencher to ensure orthogonality. Therefore, in this work, DEACM was chosen as protecting group, which has already been used for strand breaks in oligonucleotides and has its absorption maximum of about 400 nm.[255] As fluorophore and quencher ATTO565 and BHQ2 (see Figure 25) were chosen due to their well-characterized photophysical properties. The absorption spectra of all chromophores used are shown in Figure 26.

The photolabile coumarin strand break phosporamidite **1** was prepared according to protocols of Weinrich *et al.*[256] and Weyel *et al.*[255] (Figure 25, ii). Starting from commercially available 7-diethylaminocoumarin **2**, the reaction with DMF-DMA leads to enamine **3**. Oxidative cleavage of the exocyclic double bond with $NaIO_4$ results in aldehyde **4** which can be reduced to alcohol **5** using $NaBH_4$. The subsequent reaction with 4-methylsulfonic acid chloride does not lead to the corresponding tosylate, but to chloride **6**. A similar reaction was observed for benzyl alcohols with electron-withdrawing residues.[257] Ding *et al.* found that for their

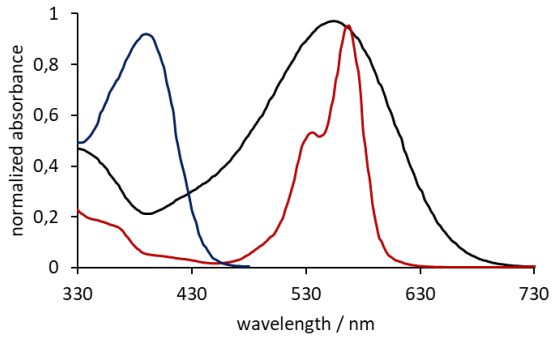

Figure 26: Absorption spectra of DEACM (blue) used for light-induced strand break, ATTO 565 (red) as hybridization sensing fluorophore and BHQ2 (black) as a quencher. Due to the shifted maxima, the strand break can be induced orthogonally.

system, the possible tosylates are formed *in situ* and subsequently substituted by the less favorable nucleophile chloride. A similar mechanism is conceivable for the above reaction. The following Wittig reaction of **6** with triphenylphosphine and formaldehyde led to alkene **7**, which was subsequently oxidized to diol **8** in an Upjohn dihydroxylation using OsO_4 and *N*-methylmorpholine-*N*-oxide. To use the coumarin in RNA solid-phase synthesis, the primary hydroxy group of **8** was selectively tritylated with DMTr-Cl. The resulting compound **9** was then reacted with 2-cyanoethoxy-*N*,*N*-diisopropylaminochloro-phosphine yielding in phosphoramidite **1**.

As target sequences for the new light-activatable molecular beacons CamK2 (**MB1**) and Beta actin (**MB2**) mRNA were chosen. They play an important role in neuronal activity.[7] In this project, the exact same MB structures as in Chapter 4.1 (Figure 25) were used because it was already known that these sequences can be used to monitor RNA in neurons. In addition, their specificity was already demonstrated in reference [I],[7] which made them promising candidates for this project. For solid-phase RNA synthesis, chemically modified 2'-OMe building blocks were used to effectively protect the MBs against endonucleases.[258,259] 2'-OMe RNA also has a higher binding affinity and selectivity towards RNA compared to DNA oligonucleotides.[260,261] In general, MB target binding highly depends on its secondary structure. Ideally, the loop region should not contain any intramolecular base pairs. For *in vivo* studies, this can

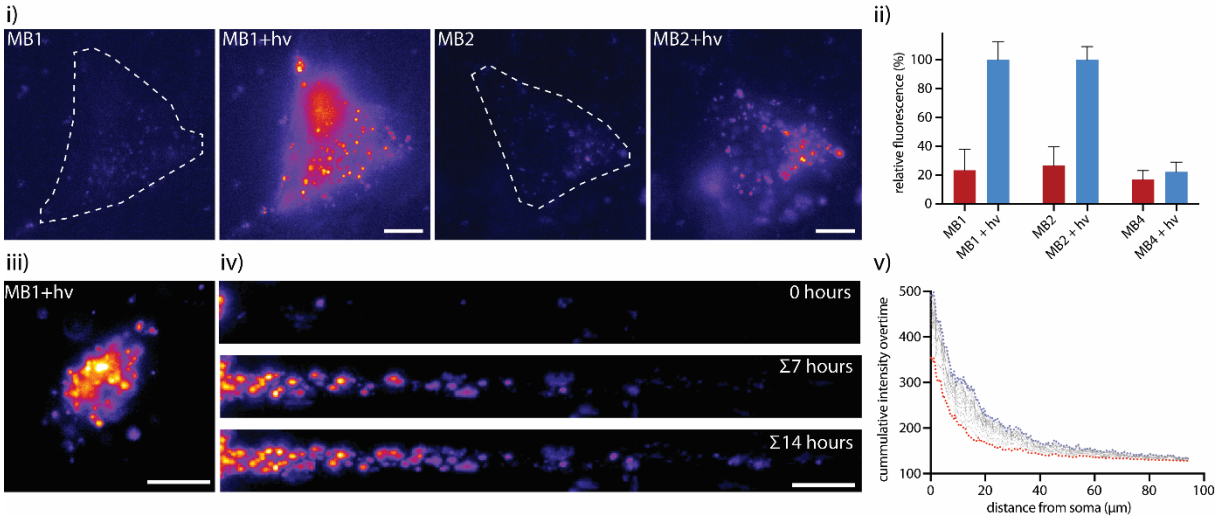

Figure 27: i) Light-activation of MB1 and MB2 in hippocampal neurons. The dashed lines indicate the activation area. ii) Fluorescence intensity quantification in the indicated area before and after light-activation. iii) Light-activation of MB1 in a neuronal cell body. iv) Max-intensity projections of MB1 populating the dendrite at 0 hours, 7 hours and 14 hours. v) Calculated time for CAMK2 populating the whole dendrite. Taken from Klimek et al. 2021.

sometimes be hard to accomplish for a given target RNA sequence. The loop domain typically contains between 18 and 30 nucleotides.[262] For the MBs used in this work, a loop length of 25-28 nucleotides was chosen in order to balance specificity and target binding affinity.[263] Beacons with longer stems have an improved ability to discriminate between different targets. However, this comes along with a lower hybridization rate. For this study, beacons with stem lengths between five and seven base pairs were used. Secondary structure prediction was performed with *Mfold*.[264]

After successful solid-phase synthesis fluorescence and uncaging experiments were performed with **MB1** and **MB2**. The results of the fluorescence experiments are shown in Figure 25. Both MBs showed a very low background signal without irradiation or target addition. As expected, if CamK2 or Beta-actin mRNA were added, the signal would not rise significantly. However, the application of 405 nm light without target addition led to a minimal increase in fluorescence for both beacons **MB1** and **MB2**. This can be rationalized by the fact that the covalently linked quencher has a significantly higher quencher efficiency than the quencher at the opposite end of the stem because it is closer to the fluorophore. However, only when both conditions – target addition and illumination with 405 nm light – were true, a significant increase in fluorescence intensity was observed for both molecular beacons (40-fold for **MB1** and 28-fold for **MB2**).

To test whether the new light-activated molecular beacons can also be applied in cells, they were transfected into cultured hippocampal neurons by Dr. Paul Donlin-Asp at the Max-Planck-Institute for Brain Research. After successful transfection, only a weak background signal could be observed in the cell bodies (see Figure 27). To activate the molecular beacons a 405 nm laser was used within the whole cell body, as indicated in Figure 27. This light pulse visualized a sub-population of molecular beacons that were already hybridized with the target sequence. To verify the specificity, a negative control **MB4** was transfected. **MB4** was also supplied with a fluorophore, two quenchers and a photolabile DEACM linker having the same secondary structure as **MB1** and **MB2**. However, the loop sequence was complementary to GFP mRNA. Therefore, **MB4** was expected not to give a fluorescent signal after photo-activation which turned out to be true after the application of 405 nm light. This indicates that the signals of **MB1** and **MB2** occur not due to unspecific binding.

The light-activated visualization of CamK2 and Beta-actin mRNA now allowed tracking by repeated excitation of the fluorophore. In contrast to previous studies where the dye had to be excited every second,[7,126] the newly synthesized Q-dye beacons allowed to reduce the light-sampling rate to one pulse every ten minutes. This allowed the experimenter to monitor the mRNA dynamics for more than 14 hours which is the longest time period known in literature to date. During the whole monitoring period, no photo-bleaching was observed. Using this technique, it was possible to calculate the half-life for Beta-actin mRNA populating the dendrite was three hours. This was in agreement with the reported half-life of four hours known from literature.[265] As another control experiment, a Q-dye beacon **MB3** with an *o*-nitrobenzyl protecting group was prepared. It had the same sequence and structure as **MB2** but could not be activated with visible light. It turned out that **MB3** could also be activated in the cell. However, the large amount of light required for photolysis caused death of the cell after a short time, and therefore long-term monitoring was not possible. This again underlines the high benefit of the new Q-dye beacons that are activatable with visible light.

In summary, this project demonstrated how MBs are chemically modified to make them light-activatable. Through light activation, it was possible to significantly reduce the laser sampling rate and thus extend the monitoring time to more than 14 hours. A careful selection of fluorophore, quencher and a photolabile protecting group made it possible to excite the chromophores orthogonally. By using light in the visible range, cell damage was avoided and the MBs could be used in living neuronal cells for long-term monitoring. However, the MBs were able to hybridize with the target RNA once they entered the cell. The next step in the development of light-activatable MBs would be a chemical modification to actually prevent hybridization with a complementary RNA strand. The formation of a double helix should only become possible after irradiation with light of a suitable wavelength. Such a chemical tool would make it possible, for example, to regulate RNAs in cells in a spatiotemporally resolved way. The design and realization of such a tool are described in the following chapter.

4.3. Photo-tethered molecular beacons

The results in this chapter were previously published in reference [III] “Photo-tethered molecular beacons for superior light-induction”.[266] Biological experiments described in this chapter were performed by Dr. Mantian Wang at the Max Planck Institute for Brain Research in Frankfurt under the supervision of Prof. Dr. Erin Schuman. Parts of the results were already published in the master thesis of Vivien R. McKenney,[267] who is a co-author of the above-mentioned publication.

One of the major drawbacks of conventional MBs is that they immediately hybridize with the target RNA once transfected. This can be problematic, for example, if one wants to regulate only a certain part of the cell with antisense RNA, or if the desired biological experiment has a time delay after transfection. To increase the spatial and temporal resolution of RNA monitoring in cells, it would therefore be advantageous to chemically modify the MBs so that they cannot form a double helix with a counter strand. When hybridization is first enabled by an external stimulus - such as light - specific parts of cells can be locally excited and analyzed, which can lead to significantly increased precision. In the literature, two methods are already known to regulate the hybridization of MBs with light, as described in Chapter 2.2.2. However, both methods have significant disadvantages. Joshi *et al.* showed that hybridization of MBs can be prevented by photolabile protecting groups located on nucleobases in the loop region.[160] Although this method showed strong efficacy and good on/off behavior of the oligonucleotides, approximately 7 photolabile protecting groups had to be placed in the loop region to completely prevent hybridization. Due to this high number, only part of the photocages may be cleaved by light, leaving partially active RNAs in the cell. Another problem is that high light intensities must be used to cleave the many photocages, which in turn can lead to cell damage.[10,268] The second method developed by Tan *et al.* made advantage of the cyclization of the MB using a photolabile linker between the 3’ and 5’ end.[162] Since a double strand has a much longer persistence length than a single strand, their MB showed a smaller hybridization signal. However, their fluorescence measurements also demonstrated that the cyclized MB could interact to some extent with the complementary RNA. This was probably because their RNA ring after cyclization was very large, and therefore, partial interactions between MB and target RNA were possible. In summary, the disadvantages of the two methods

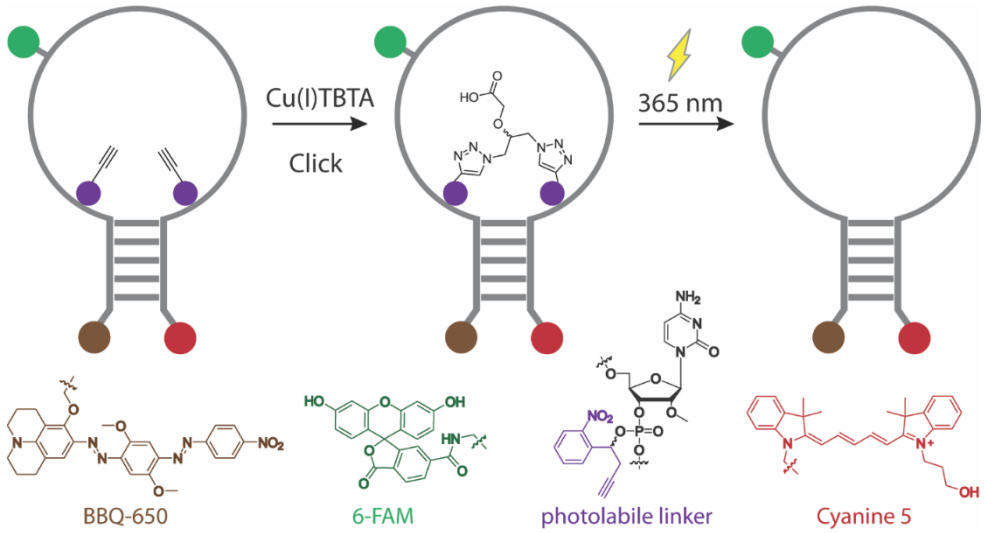

Figure 28: General mechanism of photo-tethered molecular beacons. Two photo-tethers are installed in the loop region of the MB. Using a Cu(I)-catalyzed cycloaddition with a bisazide the two photocages are covalently linked to each other. In this state, the MB is not able to hybridize with the target sequence. Illumination with 365 nm light leads to cleavage of the photocages. Therefore, the native form is restored and the MB can form a double helix. Taken from Klimek et al. 2021.

are that in method 1 (Joshi *et al.*),[160] a large number of photocages had to be used and that in method 2 (Tan *et al.*),[162] the ring after cyclization was too large to efficiently prevent hybridization. Therefore, the aim of this project was to develop a new type of MBs that circumvent the previously mentioned drawbacks. To prevent a large number of photocages, cyclization is a good first approach. However, the protecting groups must be positioned in a way that the resulting ring is preferably small to efficiently prevent double helix formation. Therefore, we decided to use photo-tethers presented by Seyfried *et al.*[234] and Müller *et al.*[269] and install them in the phosphodiester-backbone in the loop region (see Figure 28). This type of photolabile protecting group contains an alkyne group that can be placed at two different positions in an RNA strand. After solid-phase synthesis, the two alkynes can be connected in a copper-catalyzed click reaction, resulting in the cyclization of the oligonucleotide. By irradiation with light, the phosphate groups of the RNA backbone are released, and the oligonucleotide is recovered in its native form. Seyfried *et al.* showed circularized oligonucleotides can be used to prevent the hybridization of DNA with ring sizes of 10 to 30 nucleotides.[234] This type of photolabile protecting group provided the name "photo-tethered MBs" to the oligonucleotides presented in this project. We selected miR-98 as the target sequence for the MBs, which is one of the most abundant miRNAs in hippocampal neurons. In order to prepare a suitable light-activatable probe, the optimal stem-loop structure of the MB had to be tested beforehand. This structure should later be used

as a positive control for the induction ratio. Therefore, four different MBs which were all complementary to miR-98 but differed in their stem-length and composition were synthesized (see Figure 29). The backbone of MBs consisted of 2'-OMe-RNA to ensure decreased degradation by nucleases. In addition to the fluorophore at the end of the stem, a second fluorophore was placed in the loop region. This should ensure easy identification of transfected cells and allow the discrimination of a false-positive signal by co-localization of both fluorophores. **MB1** – **MB4** had stem lengths between 4 and 6 base pairs. Secondary structure prediction was done using *Mfold*.[264] 6-FAM was used as tracking fluorophore and Cy5 as hybridization sensing fluorophore. Both fluorophores can be excited orthogonally due to their different absorption maxima. After solid-phase synthesis, a fluorescence assay was performed with **MB1** – **MB4**. The fluorescence of Cy5 at 670 nm was measured before and after addition of miR-98. While **MB2** and **MB4** did not show promising on/off ratios (2- to 5-fold fluorescence increase after addition of miR-98), **MB1** and **MB3** had a more promising induction behavior (20- and 10-fold fluorescence increase after addition of miR-98). The

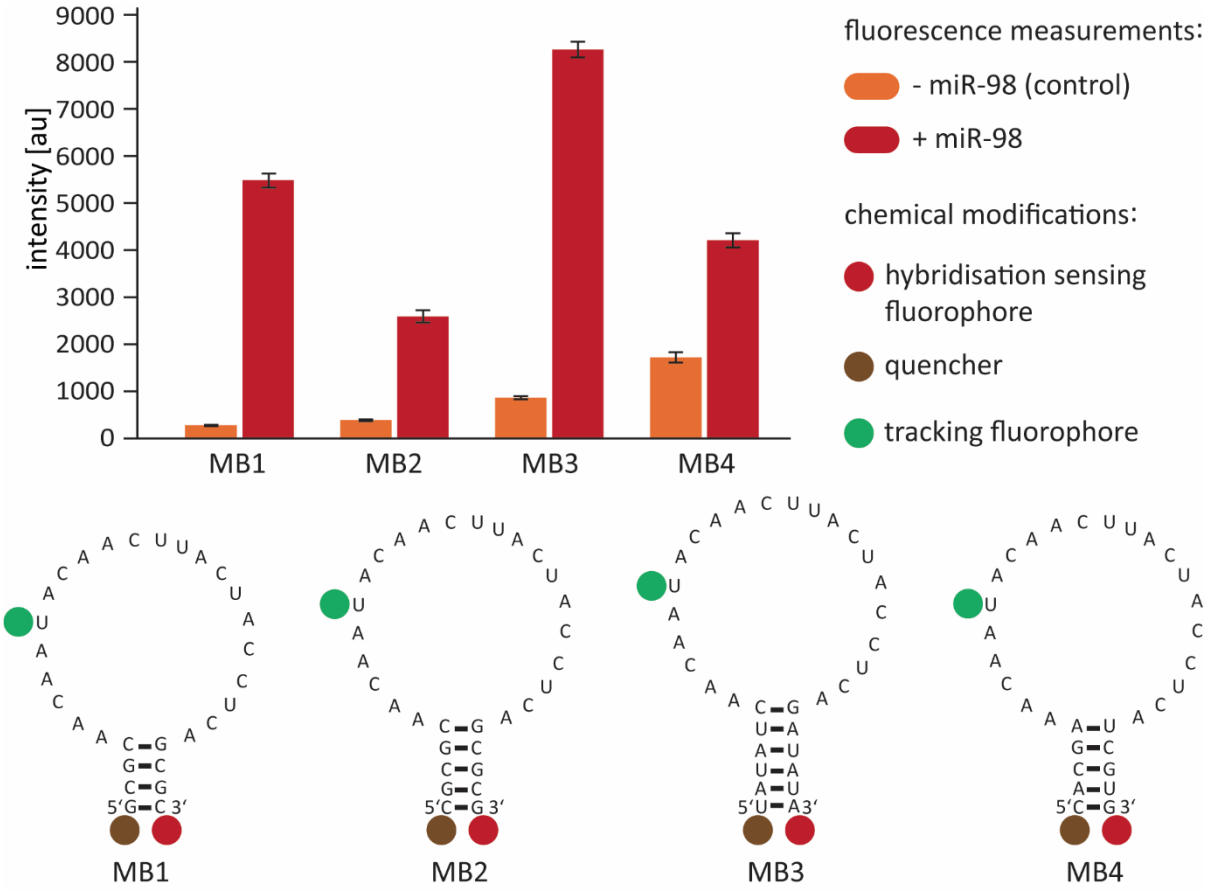

Figure 29: Structures and fluorescence intensity assay results of MB1-MB4 before and after the addition of target miR-98. Taken from Klimek et al. 2021.

hybridization ability of all synthesized MBs was also demonstrated with a native PAGE experiment (see Figure 30). It demonstrated that all MBs have a mobility shift after addition of miR-98. However, due to the fluorescence results shown in Figure 29, further experiments and circularization were performed with analogues of **MB1** and **MB3** that were considered as the best candidates.

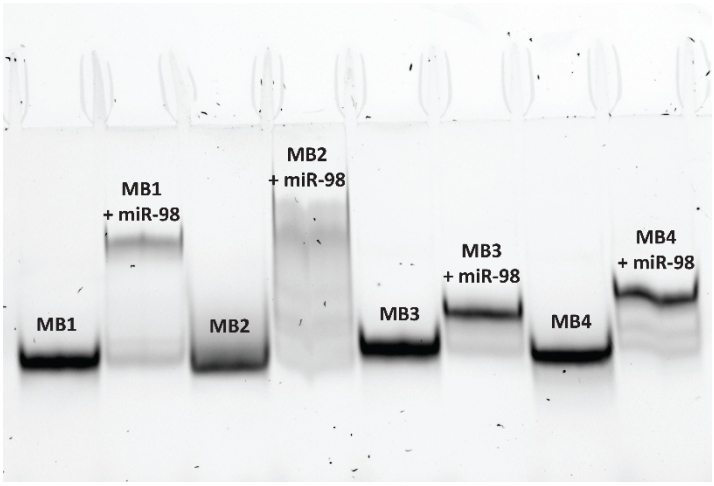

Figure 30: Native PAGE experiment for MB1-MB4. Addition of target miR-98 resulted in a mobility shift that indicates formation of a double helix.

To make the MBs light-activatable, photolabile phosphoramidites had to be prepared. In this study we decided to use a photolabile 2'-OMe-C analogue that can be installed at different positions in the loop. The chemical synthesis is described in more detail in reference [III].[266] After chemical synthesis, the phosphoramidite was installed at several different positions in the loop of **MB1** and **MB3**. The different structures and fluorescence properties are described in the manuscript and supporting information of reference [III].[266] However, the best results in terms of on/off ratio before and after light activation were achieved with **ptMB3** (photo-tethered molecular beacon 3) (see Figure 31). In this MB the two photo-tethers were attached close to the stem to prevent hybridization with the target miR-98. Before light-activation and addition of miR-98, **ptMB3** shows almost no fluorescence. The addition of target RNA did not lead to a significant signal increase. Only when light was applied to the sample, the fluorescence intensity of the hybridization sensing fluorophore increased to 98% of the fluorescence of the positive control **MB3** when miR-98 is added (Figure 31). In contrast to the Q-dye MBs presented in Chapter 4.2, the signal increase of **ptMB3** was due to the light-induced ability to hybridize with a complementary strand. Q-dye MBs can already form a double helix before light-activation. Photo-tethered MBs, on the other hand, cannot hybridize before light activation because of their cyclized structure. It was also demonstrated that hybridization of **ptMB3** and miR-98 before light-activation was hindered permanently by measuring the fluorescence intensity over minutes (Figure 31, b). After addition of miR-98, the signal intensity did not increase. In contrast, the fluorescence intensity of

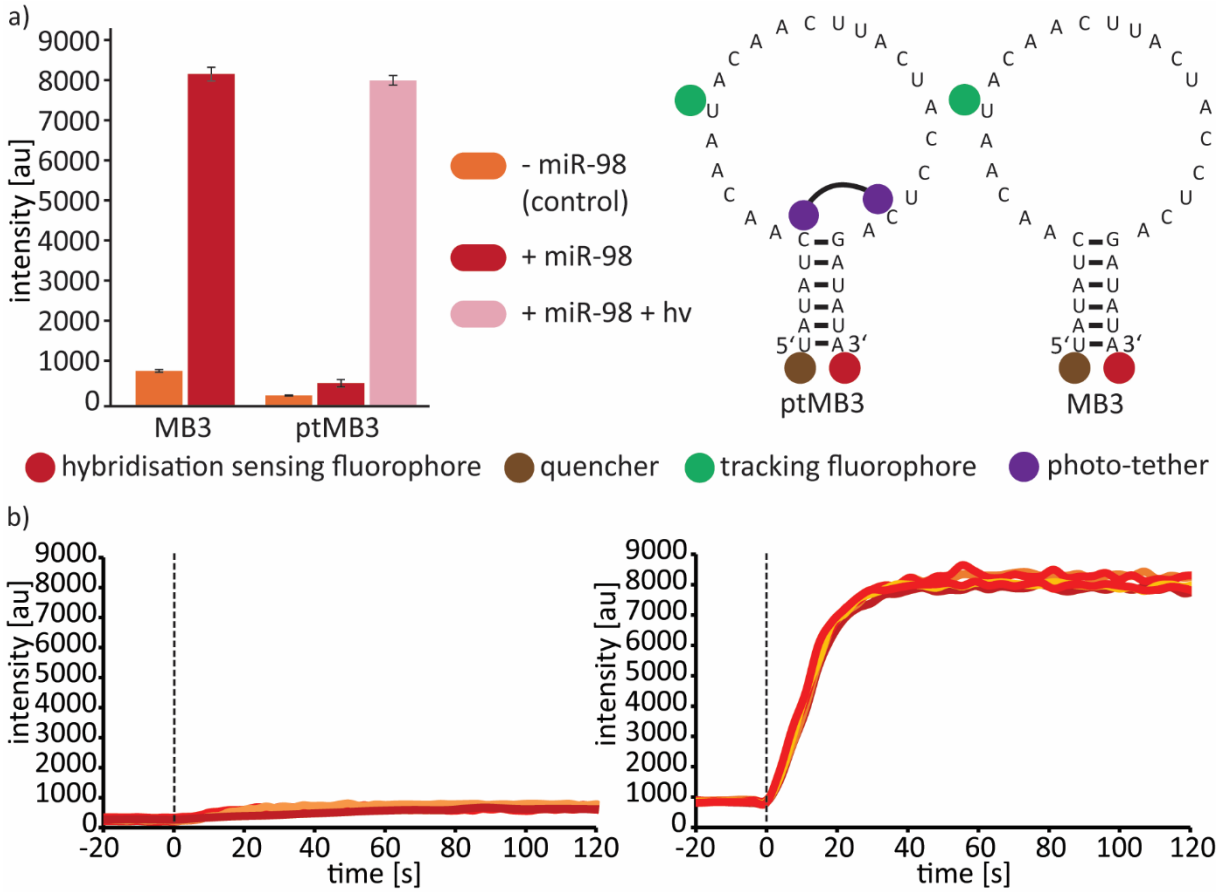

Figure 31: a) Secondary structures and fluorescence assay results of ptMB3 compared to MB3 before and after light-activation. b) Fluoresence kinetics of ptMB3 (left) and MB3 (right) after addition of target miR-98. Addition of miR-98 is indicated by the dashed line. Taken from Klimek et al. 2021

positive control **MB3** raised immediately after addition of miR-98. This experiment proved that the formation of a **ptMB3** double helix was hindered not only kinetically.

The next step was to evaluate the performance of the light-activatable MBs *in vivo*. The experiments in this paragraph were performed by Dr. Mantian Wang at the Max-Planck-Institute for Brain Research. **ptMB3** was transfected into cultured hippocampal neurons. Imaging was performed two to four hours after transfection. The tracking fluorophore 6-FAM was used to identify transfected cells and showed a distribution of **ptMB3** over the soma (Figure 32, left). Similar to the *in vitro* experiments (Figure 32), the hybridization sensing fluorophore Cy5 did not show a significant signal before activation with a 355 nm laser (Figure 33, middle). Again, this observation indicates that hybridization of **ptMB3** and target RNA is hindered. After light-activation over the whole soma, the appearance of new hybridization sensing signals was observed (Figure 33, right). Therefore, it was concluded that these new signals are associated with a hybridization event of **ptMB3** and miR-98.

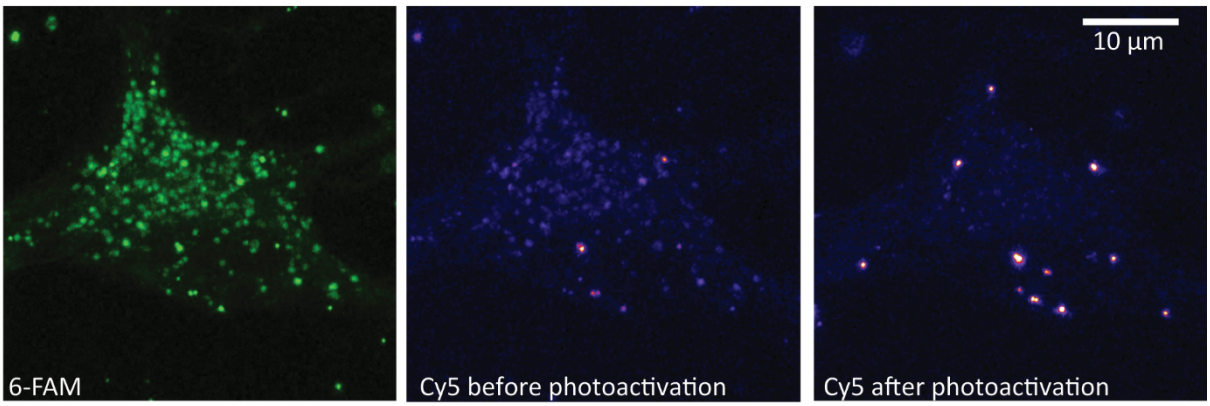

Figure 32: Images of ptMB3 in a hippocampal neuron. The green tracking fluorophore 6-FAM shows the even distribution of the MB over the whole soma (left). Before light-activation the hybridization-sensing fluorophore Cy5 does not show a significant signal (middle). After light-activation with a 355 nm laser, a Cy5 hybridization signal is present that indicates double helix formation of ptMB3 and miR-98 (right). Taken from Klimek et al. 2021

In conclusion, it was demonstrated that MB hybridization can be controlled spatiotemporally using photo-tethers. The attachment and covalent linkage of the two photolabile protecting groups in the loop region resulted in a circularized oligonucleotide that was not able to hybridize with target miR-98 *in vitro* and *in vivo*. Only when light was applied, the native form of the MB was restored, and it was able to form a double helix. This property clearly separates ptMBs from the light-activatable O-dye MBs from reference [II]. Q-dye MBs can also be activated with light, but they can form a double helix with a complementary opposite strand even before irradiation. These two types of activatable MBs can be used complementarily for different biological questions. While Q-dye MBs are more suitable for RNA monitoring, ptMBs can be used for spatially and temporally resolved regulation.

In order to gain spatiotemporal control of biochemical reactions and pathways, e.g., RNA transport that was described in previous chapters, it is important to develop efficient photocages. To be precise, the photocage has to use the applied light in the most efficient way to induce a bond break. This allows the light intensity to be reduced, minimizing cell damage. For the Q-dye MBs presented in reference [II], DEACM was used as a photolabile protecting group. This photocage is widely used because it is well understood and easy to prepare, but it has a poor uncaging efficiency. The last goal of the presented thesis was to optimize the uncaging efficiency of coumarin-based photocages to get a superior uncaging behavior in future biological experiments.

4.4. Systematic improvement of coumarin PPGs

The results in this chapter were previously published in reference [IV] “Inactivation of competitive decay channels leads to enhanced coumarin photochemistry”.[270] The spectroscopic data described in this chapter was measured and analyzed by Marvin Asido at the Institute of Physical and Theoretical Chemistry in Frankfurt under the supervision of Prof. Dr. Josef Wachtveitl. Parts of the steady-state fluorescence and absorption measurements were performed by Volker Hermanns under supervision of Prof. Dr. Alexander Heckel. Parts of the photocage synthesis were already published in the bachelor thesis of Marco Salustros.[271]

In Chapter 4.2, a coumarin PPG was used to induce a strand break in an oligonucleotide. Coumarin was selected instead of *o*-nitrobenzyl in order to use visible light und reduce cell damage.[252] It was demonstrated that the red-shift led to an enhanced cell viability when light was applied. Nevertheless, the photolysis process can be further optimized. As described in detail in Chapter 2.1, two parameters are of particular importance in the optimization of photolabile protecting groups: the absorption wavelength and the uncaging efficiency. In this project, the aim was to systematically improve the second parameter on a coumarin protecting group. To date, there are very few studies that systematically examine uncaging efficiency. On the other hand, however, there are a large number of studies that have optimized fluorophores (see Chapter 2.2.3). These are particularly interesting because uncaging and fluorescence occur on a similar time scale (nanoseconds after irradiation). Therefore, the idea was to use the broad knowledge of fluorophore optimization to improve the uncaging efficiency of coumarin protecting groups. To be precise, the

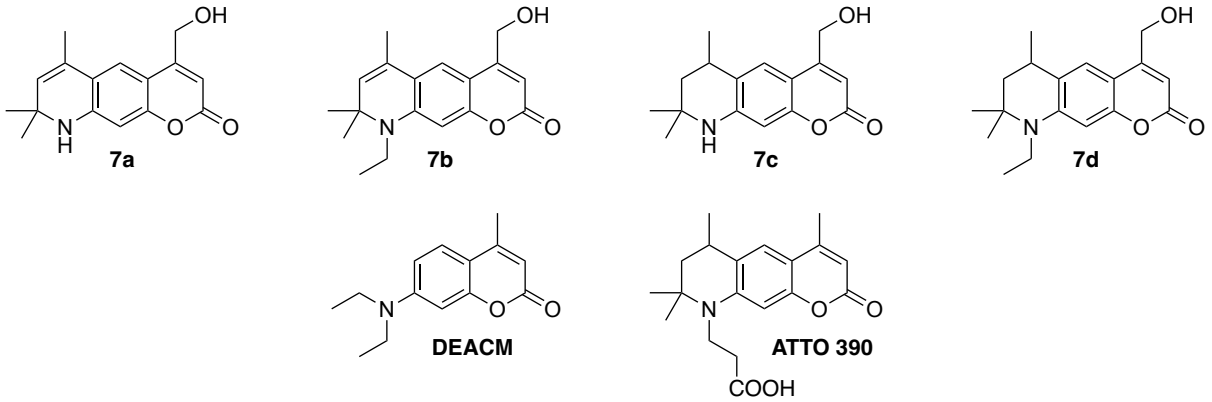

*Figure 33: Structures of ATTO 390, DEACM and ATTO 390 based photocages **7a**-**d** developed in this work. DEACM was used as reference compound to compare photolysis efficiency.*

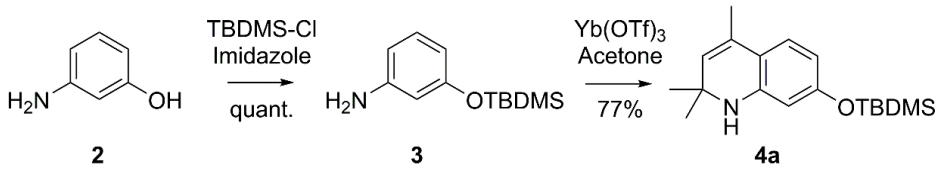

*Figure 34: Synthesis of quinolin **4a** starting from aminophenol **2**.*

coumarin-based fluorophore ATTO 390 that has a fluorescence quantum yield of 90%[235,236] was used as a scaffold for the optimization process. Based on ATTO 390, four new coumarin photocages were designed (see Figure 33). For all of them, the leaving group was attached to the 4-methyl group which is known to induce a heterolytic bond cleavage after irradiation for many examples.[34] As described in Chapter 2.1.3, fluorescence quantum yield for donor-acceptor fluorophores (as coumarin) is increased when rotation around the electron-donor is restricted.[12] Therefore, the four new photocages were equipped with a six-membered ring at the 7-position to inhibit rotation. In two of the molecules (**7a** and **7b**), an additional double bond was introduced in the ring system to further planarize the molecule. This should further restrict rotation and possible energy loss by TICT states. Molecules **7b** and **7d** were equipped with an additional ethyl group at the nitrogen atom. This modification is supposed to eliminate a possible hydrogen bonding site that is known to eventually lead to non-radiative decay of the excited state in polar solvents.[272–276] The synthesis started from commercially available 3-aminophenol **2** (see Figure 34). The hydroxyl group was protected with TBDMS in a quantitative yield resulting in compound **3**. In the next step, the first six-membered ring around the nitrogen was built up using acetone and $Yb(OTf)_3$ as catalyst in a Doebner-Miller type reaction. A possible

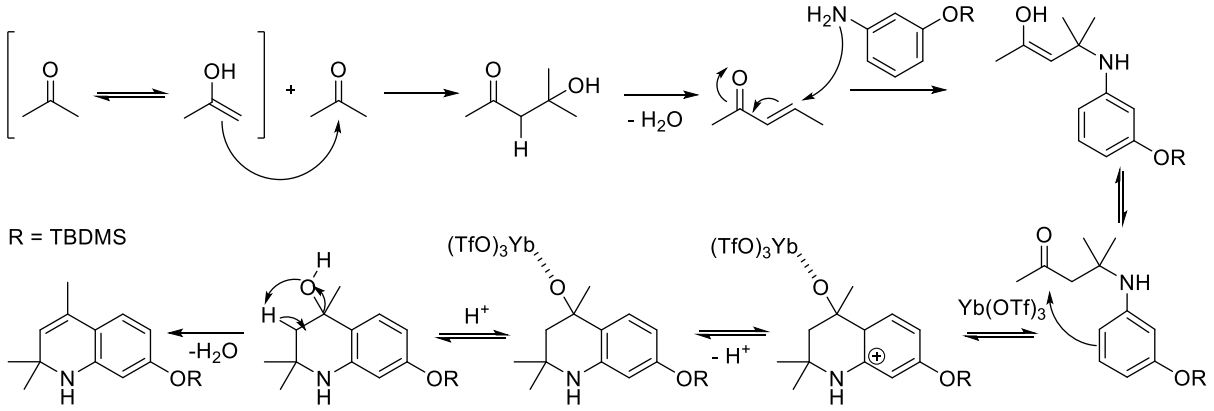

*Figure 35: Possible mechanism for the formation of compound **4a**. Two acetone molecules are reacted in an aldol-condensation and -addition. In the next step, a Doebner-Miller type reaction between the resulting 2-oxo-3-penten and the TBDMS-protected aminophenol leads to the formation of **4a**.*

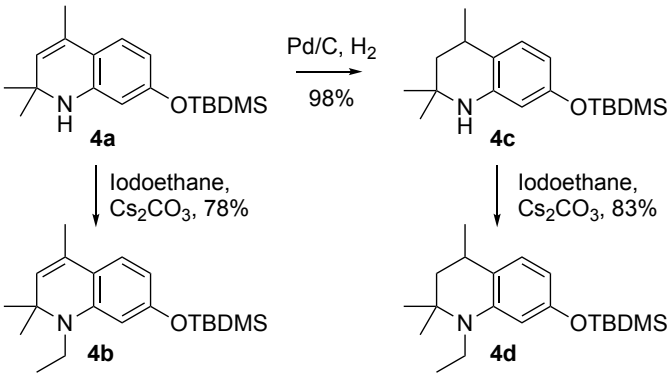

*Figure 36: Alkylation and hydrogenation of compound **4a** resulting in **4b**-**4d**.*

mechanism of this reaction is shown in Figure 36. After the ring closure, the double bond and the nitrogen motif had to be functionalized. Therefore, the double bond of **4a** was reduced using H_2 gas and a Pd/C catalyst resulting in dihydroquinoline **4c**. Compounds **4a** and **4c** can then be reacted with iodoethane and Cs_2CO_3 under microwave irradiation to perform a nucleophilic substitution at the nitrogen atom. These reactions resulted in the four functionalized precursor molecules **4a**-**d** (see Figure 35) that are used to synthesize the final compounds in the next steps.

To functionalize the oxygen atom, the TBDMS protecting groups of **4a**-**d** had to be removed (Figure 37). This was done using TBAF and AcOH giving molecules **5a**-**d** in ca. 90% yields. Pechmann condensation with sodium diethyl oxalacetate led to coumarin esters **6a**-**d** in moderate yields. During this reaction, a lot of side products occurred that were hard to separate from the main compound. Nevertheless, reduction of coumarin esters with $NaBH_4$ resulted in the final protecting groups **7a**-**d**.

Steady-state absorption spectra, fluorescence spectra and fluorescence quantum yield of **7a**-**d** in different solvents (see Figure 38, a) were recorded by Volker Hermanns und Marvin Asido, who are co-authors of the publication that this chapter is based on. A detailed discussion can be found in reference [IV].[270] In summary, the results showed that the above-mentioned photophysical properties are very similar to the parent compound ATTO 390. At the same time, fluorescence intensity and quantum yield of

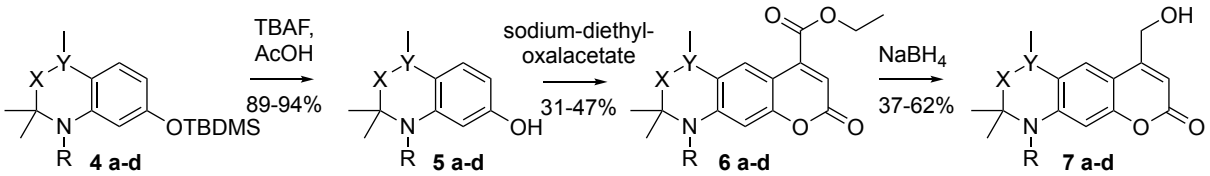

*Figure 37: Synthesis of coumarin-alcohols **7a**-**d** starting from **4a**-**d**. a: R = H, X = CH, Y = C, b: R = ethyl, X = CH, Y = C, c: R = H, X = CH_2, Y = CH, d: R = H, X = CH_2, Y = CH.*

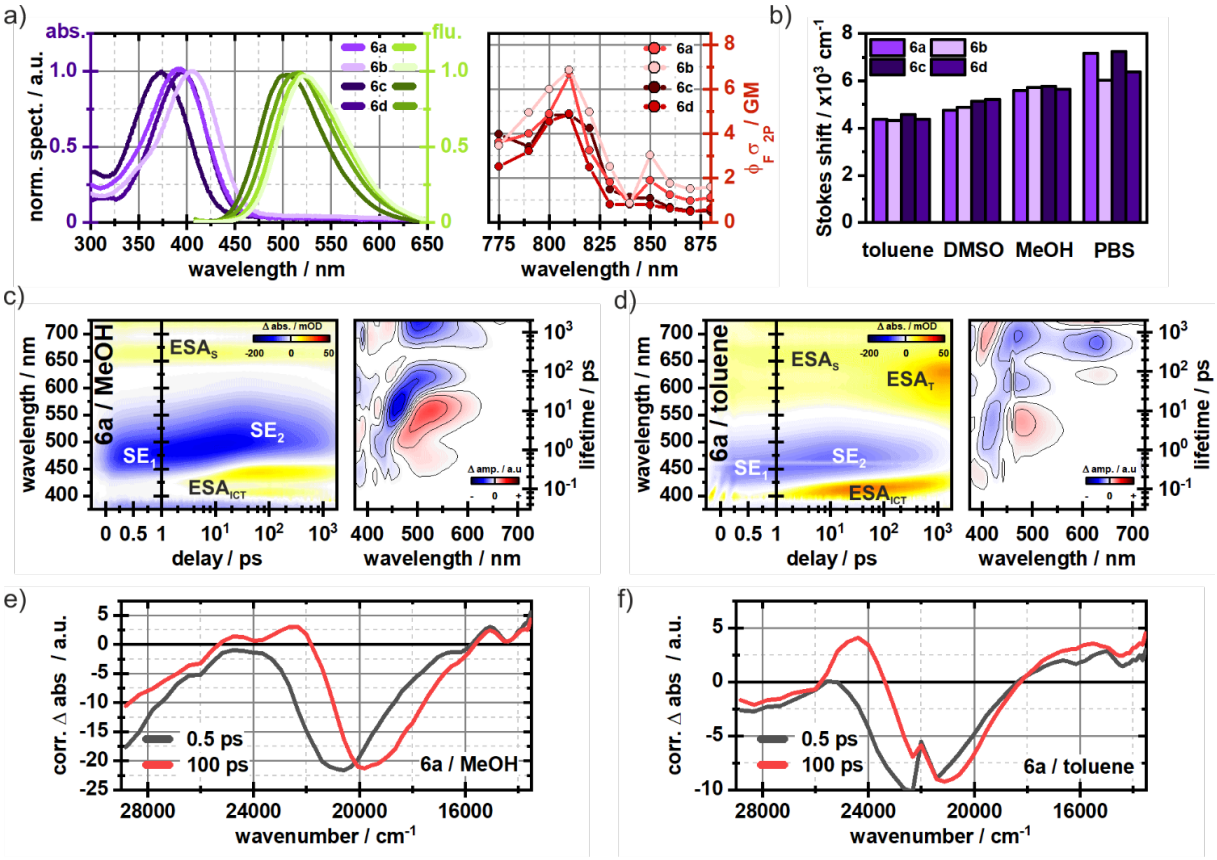

*Figure 38: a) Steady-state absorption and fluorescence spectra of compounds **6a-d** and the respective two-photon absorption spectra. b) stokes-shifts of compounds **6a-d**. c) Ultrafast transient absorption measurement of compound **6a** in MeOH. d) Ultrafast transient absorption measurement of compound **6a** in toluene. e, f) Dynamic stokes-shifts of compound **6a** in MeOH and toluene at comparing 0.5 ps and 100 ps after excitation.*

7a-d are a lot higher compared to the widely used photolabile protecting group DEACM (structure shown in Figure 33). This indicated that competitive relaxation pathways are efficiently blocked and the newly synthesized compounds lose their excitation energy mainly *via* fluorescence. Two-photon excited fluorescence (TPEF) experiments showed that **7a-d** cannot only be excited with UV and blue light but also in the NIR region (see Figure 38, a). The underlying photophysical dynamics were examined using ultrafast transient absorption spectroscopy in the Wachtveitl lab performed by Marvin Asido (see Figure 38, c). Overall, a strong solvent dependency was observed for the formation of an ICT from the nitrogen of the amine group (charge donor) to the carbonyl group (charge acceptor) (see Chapter 2.1.3). Also, hydrogen bonding at the nitrogen atom influenced the excited state dynamics. The solvent reorientation and resulting stabilization of the excited state can be observed looking at time-resolved stokes shifts 0.5 ps and 100 ps after excitation (see Figure X). Overall, polar solvents

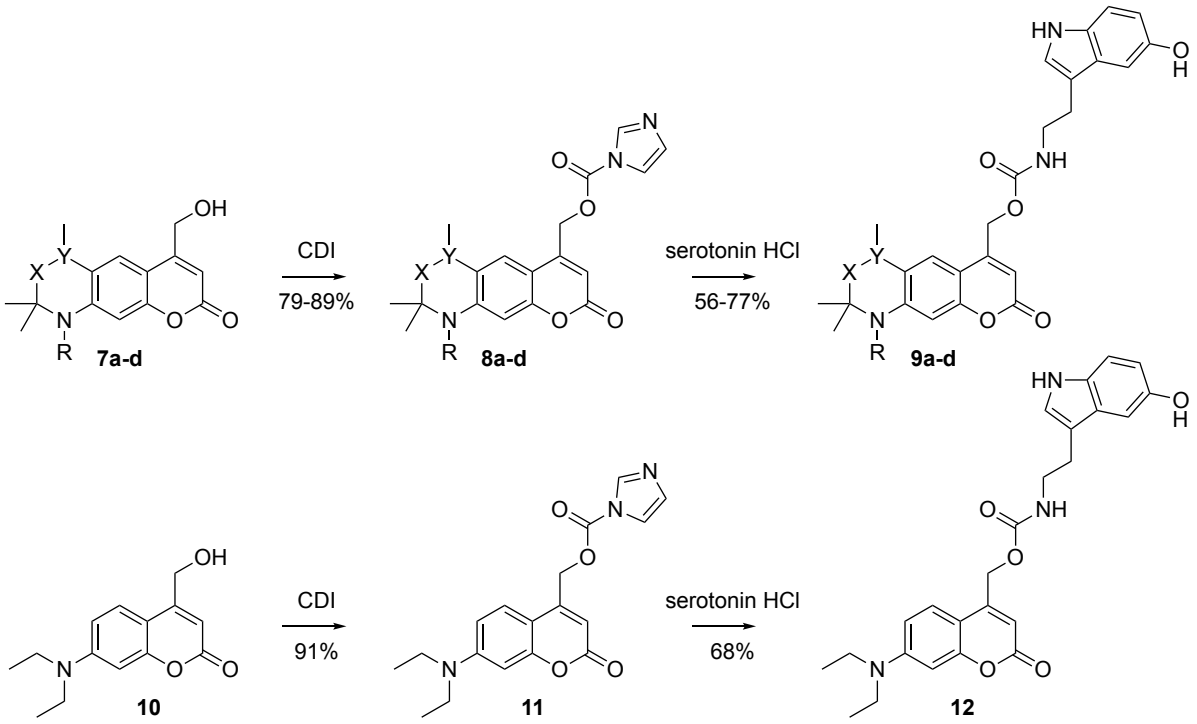

*Figure 39: Synthesis of coumarin-protected serotonin compounds **9a-d** and **12**. a: R = H, X = CH, Y = C, b: R = ethyl, X = CH, Y = C, c: R = H, X = CH_2, Y = CH, d: R = H, X = CH_2, Y = CH.*

like MeOH have a stronger stabilizing effect and the ICT state than unpolar solvents like toluene. For a more detailed discussion see reference [IV].[270]

However, the goal of this project was not to increase fluorescence but to design and synthesize new photolabile protecting groups with enhanced uncaging efficiency. To test the performance of the newly synthesized photocages **7a-d** and the influence of the planar and rigid structures, a leaving group had to be attached to the exocyclic hydroxyl group at position 4. This position is known to undergo heterolytic bond cleavage after excitation for the general coumarin structure.[80] As leaving group, the biologically relevant neurotransmitter serotonin was attached. This biomolecule plays an important role in signal transduction in the central nervous system.[277] The synthesis started with the reaction of **7a-d** and carbonyldiimidazole to prepare precursor molecules **8a-d**. After column chromatography, serotonin added to **8a-d** under microwave irradiation resulting in photolabile protected serotonin derivatives **9a-d** (see Figure 39). The same synthetic procedure was used to prepare DEACM-protected serotonin **12** as reference for photolysis experiments. The synthesis of DEACM-OH **10** was done according to Weinrich *et al.*.[256]

After preparation the photolysis efficiency of **9a-d** was compared to reference compound **12**. The photolysis experiments were performed by Volker Hermanns. **9a-**

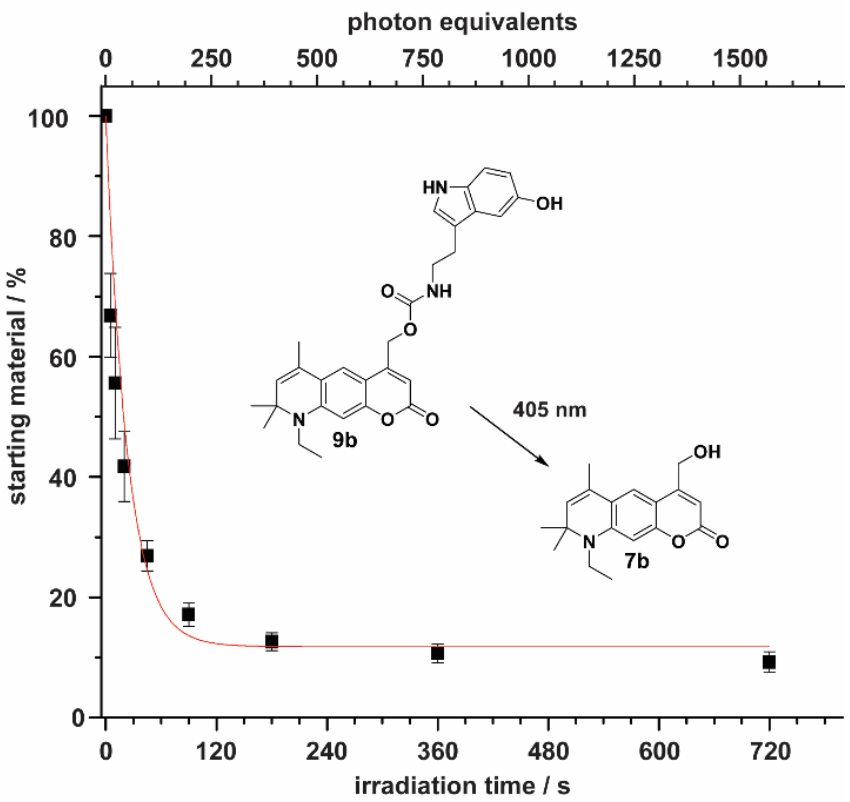

Figure 40: Exemplary photolysis curve of compound 9b in PBS/MeOH (1:1). Photolysis product 7b was identified via mass spectrometry. Figure taken from Klimek et al. 2022.

d and **12** were dissolved in PBS/MeOH (1:1). For coumarin photolysis protic solvents are needed to capture the carbo-cation that is formed during uncaging.[80] To make the photolysis experiments comparable, quantum yields of all compounds were measured at 405 nm. A fulgide derivative was used as actinometer.[278] An exemplary photolysis curve of **9b** is shown in Figure 40. Remaining curves can be found in the supporting information of reference [IV].[270] It was demonstrated that after ca. 200 photon equivalents, about 90% of the starting material **9b** released the neurotransmitter serotonin. Overall, all newly synthesized compounds **9a**-**d** showed a higher uncaging efficiency than reference compound DEACM **12**. The double bound in **9a**-**b** that further rigidifies the coumarin scaffold compared to **9c**-**d** has a higher impact on the uncaging efficiency than the additional ethyl group in **9b** and **8d**. This indicates that the TICT state plays a more important role than H-bonding at the coumarin electron donor. For the best compound **9b** the uncaging efficiency was increased 12-fold compared to **12**. Summarizing the uncaging experiments, the aim to develop a photolabile coumarin protecting group with enhanced uncaging efficiency was achieved. The best compound was **9b** which was equipped with a double bond and an ethyl group at the nitrogen. A detailed discussion of the photochemical properties of all compounds can be found in

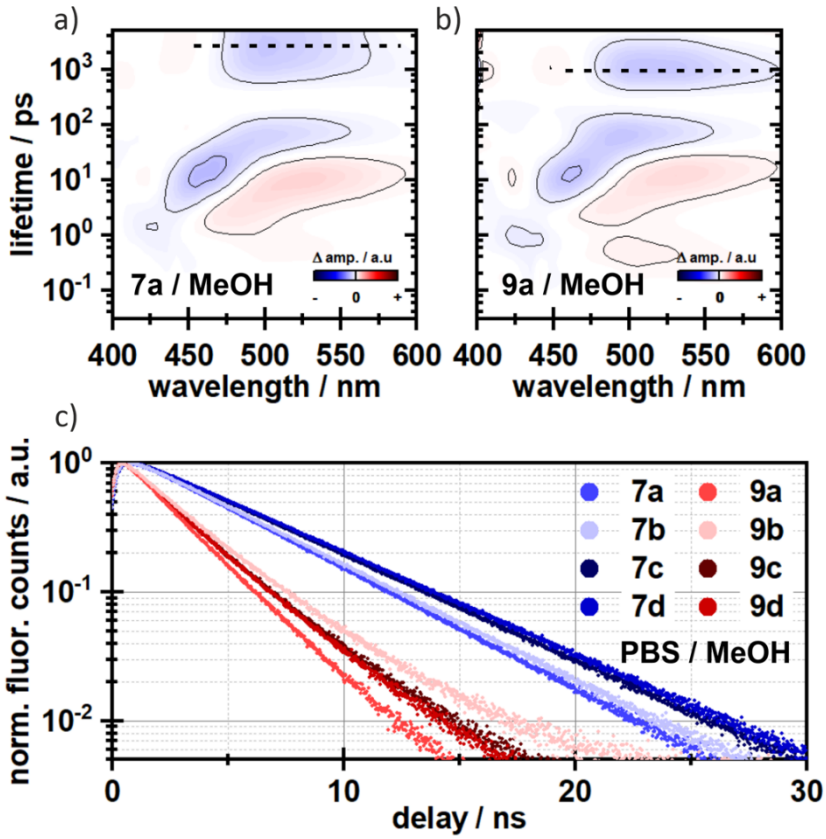

*Figure 41: a, b) Ultrafast transient absorption spectroscopy experiments of **7a** and **9a**. The depopulation of the excited state in **9a** is shifted towards shorter timescales. c) Time-correlated single photon counting (TCSPC) measurements of compounds **7a-d** and **9a-d**. The fluorescence lifetimes of **9a-d** are approximately 2 times faster than **7a-d**. Figure taken from Klimek et al. 2022.*

reference [IV].[270] In the last step, it was investigated by Marvin Asido whether uncaging as additional decay channel can be observed by ultrafast transient absorption spectroscopy. An exemplary experiment for **9a** is shown in Figure 41. To be precise, compound **9a** with a leaving group was compared to the previously measured **7a** that does not have a leaving group. Besides very similar photophysical signatures, it was observed that the excited state decay of **9a** shifted towards earlier times when it was compared to **7a**. This trend can also be seen in TCSPC measurements in PBS/MeOH (1:1). While the excited state of **7a-d** were depopulated between 4.6 and 5.4 ns, the fluorescence lifetimes of **9a-d** were found to be between 2.0 and 2.6 ns. This reduction is most likely due to the possibility of **9a-d** to undergo heterolytic bond cleavage after excitation. The TCSPC experiments are shown in Figure 41.

In summary, it was possible to design and develop four new coumarin-based photocages derived from the well-characterized fluorophore ATTO 390 with an enhanced uncaging efficiency. Inhibition of competitive decay channels like H-bonding

or TICT resulted in a 12-fold increase in the uncaging cross section of the best compound. Ultrafast transient absorption spectroscopy gave insights into the underlying photophysical mechanisms. The coumarin photocages developed here have a strong solvent dependency in their uncaging and fluorescence behavior. Overall, this project demonstrated that it can be a good strategy to learn from the optimization of organic fluorophores when it comes to the development of new photocages.

5. Conclusion

This work addressed the development of non-light-activatable as well as light-activatable tools to monitor RNA in living cells. It was demonstrated that carefully designed molecular beacons can be used to stain three different mRNAs against CamK2, Beta-actin and PSD-95 in neurons.[7] The RNAs were monitored for 20 minutes and the extracted data was used to determine transport velocities, distances traveled and the overall mRNA distribution together with scientists from the Max-Planck-Institute for Brain Research. It was investigated how different forms of altered translation or chemical long-term potentiation and depression can affect the RNA transport processes, and it was quantified in what copy number the nucleic acids are transported. In the next step, to get an insight into how RNA transport works on a long time scale, the molecular beacons were chemically modified to make them light-activatable, resulting in Q-dye molecular beacons.[252] A photocleavable second quencher allowed to locally activate a subpopulation of RNAs in the cell body. Therefore, the light-sampling rate for monitoring could be decreased from 1 frame/second to 1 frame/10 minutes. This technique allowed, for the first time, to monitor mRNA in neurons for more than 14 hours. The light-activatable molecular beacons were used, e.g., to quantify the time a certain mRNA species needs to populate the whole dendrite at the Max-Planck-Institute for Brain Research. To further improve the light-activatable probes, photo-tethered molecular beacons were designed.[266] Compared to the Q-dye beacons, light-activation of photo-tethered molecular beacons can be used to trigger RNA hybridization with a complementary strand. This concept was realized by the installation of two photolabile protecting groups on the phosphate backbone[234] which were linked after solid phase synthesis. It was demonstrated that hybridization with target miR-98 was only possible after irradiation. This new type of molecular beacon was used in hippocampal neurons to spatiotemporally induce miRNA double helix formation at the Max-Planck-Institute for Brain Research. Lastly, a new superior coumarin-based photocage that allows efficient uncaging of biomolecules was developed.[270] Together with scientists from the Institute of Physical and Theoretical Chemistry photolabile protecting groups with inhibited alternative relaxation pathways were designed, synthesized and characterized. The uncaging efficiency compared to the photocage used for the above-described Q-dye beacons was improved 12-fold. It is anticipated that this new photocage will find broad application in future biological experiments.

6. Literature

(1) Polack, F. P.; Thomas, S. J.; Kitchin, N.; Absalon, J.; Gurtman, A.; Lockhart, S.; Perez, J. L.; Pérez Marc, G.; Moreira, E. D.; Zerbini, C.; Bailey, R.; Swanson, K. A.; Roychoudhury, S.; Koury, K.; Li, P.; Kalina, W. V.; Cooper, D.; Frenck, R. W.; Hammitt, L. L.; Türeci, Ö.; Nell, H.; Schaefer, A.; Ünal, S.; Tresnan, D. B.; Mather, S.; Dormitzer, P. R.; Şahin, U.; Jansen, K. U.; Gruber, W. C. Safety and Efficacy of the BNT162b2 MRNA Covid-19 Vaccine. *N. Engl. J. Med.* **2020**, *383* (27), 2603–2615. https://doi.org/10.1056/nejmoa2034577.

(2) Bhatti, G. K.; Khullar, N.; Sidhu, I. S.; Navik, U. S.; Reddy, A. P.; Reddy, P. H.; Bhatti, J. S. Emerging Role of Non-coding RNA in Health and Disease. *Metab. Brain Dis.* **2021**, *36* (6), 1119–1134. https://doi.org/10.1007/s11011-021-00739-y.

(3) Hogan, M. J.; Pardi, N. MRNA Vaccines in the COVID-19 Pandemic and Beyond. *Annu. Rev. Med.* **2022**, *73*, 17–39. https://doi.org/10.1146/annurev-med-042420-112725.

(4) Damase, T. R.; Sukhovershin, R.; Boada, C.; Taraballi, F.; Pettigrew, R. I.; Cooke, J. P. The Limitless Future of RNA Therapeutics. *Front. Bioeng. Biotechnol.* **2021**, *9*, 161. https://doi.org/10.3389/fbioe.2021.628137.

(5) Sang, L.; Yang, L.; Ge, Q.; Xie, S.; Zhou, T.; Lin, A. Subcellular Distribution, Localization, and Function of Noncoding RNAs. *Wiley Interdiscip. Rev. RNA* **2022**, e1729. https://doi.org/10.1002/wrna.1729.

(6) Braselmann, E.; Rathbun, C.; Richards, E. M.; Palmer, A. E. Illuminating RNA Biology: Tools for Imaging RNA in Live Mammalian Cells. *Cell Chemical Biology*. Elsevier Ltd August 20, 2020, pp 891–903. https://doi.org/10.1016/j.chembiol.2020.06.010.

(7) Donlin-Asp, P. G.; Polisseni, C.; Klimek, R.; Heckel, A.; Schuman, E. M. Differential Regulation of Local MRNA Dynamics and Translation Following Long-Term Potentiation and Depression. *Proc. Natl. Acad. Sci. U. S. A.* **2021**, *118* (13), 2017578118. https://doi.org/10.1073/PNAS.2017578118.

(8) Glock, C.; Heumüller, M.; Schuman, E. M. MRNA Transport & Local Translation in Neurons. *Current Opinion in Neurobiology*. Elsevier Ltd August 1, 2017, pp 169–177. https://doi.org/10.1016/j.conb.2017.05.005.

(9) Pattison, D. I.; Davies, M. J. Actions of Ultraviolet Light on Cellular Structures. *Exs*. Birkhäuser Basel 2006, pp 131–157. https://doi.org/10.1007/3-7643-7378-4_6.

(10) Nakajima, S.; Lan, L.; Kanno, S. I.; Takao, M.; Yamamoto, K.; Eker, A. P. M.; Yasui, A. UV Light-Induced DNA Damage and Tolerance for the Survival of Nucleotide Excision Repair-Deficient Human Cells. *J. Biol. Chem.* **2004**, *279* (45), 46674–46677. https://doi.org/10.1074/jbc.M406070200.

(11) Jun, J. V.; Chenoweth, D. M.; Petersson, E. J. Rational Design of Small Molecule Fluorescent Probes for Biological Applications. *Org. Biomol. Chem.* **2020**, *18* (30), 5747–5763. https://doi.org/10.1039/d0ob01131b.

(12) Debnath, T.; Ghosh, H. N. An Insight of Molecular Twisting of Coumarin Dyes. *ChemistrySelect* **2020**, *5* (30), 9461–9476. https://doi.org/10.1002/slct.202001751.

(13) DNA Discovery | When was DNA Discovered? | AncestryDNA® Learning Hub https://www.ancestry.com/c/dna-learning-hub/dna-discovery (accessed Jul 15, 2022).

(14) Pray, L. Discovery of DNA Double Helix: Watson and Crick | Learn Science at Scitable https://www.nature.com/scitable/topicpage/discovery-of-dna-structure-and-function-

watson-397/ (accessed Mar 31, 2022).

(15) Chaudhary, N.; Weissman, D.; Whitehead, K. A. MRNA Vaccines for Infectious Diseases: Principles, Delivery and Clinical Translation. *Nat. Rev. Drug Discov.* **2021**, *20* (11), 817–838. https://doi.org/10.1038/s41573-021-00283-5.

(16) Dahm, R. Friedrich Miescher and the Discovery of DNA. *Dev. Biol.* **2005**, *278* (2), 274–288. https://doi.org/10.1016/j.ydbio.2004.11.028.

(17) Hunter, G. K. Phoebus Levene and the Tetranucleotide Structure of Nucleic Acids. *Ambix* **1999**, *46* (2), 73–103. https://doi.org/10.1179/amb.1999.46.2.73.

(18) Ghose, T. Oswald Avery: The Professor, DNA, and the Nobel Prize That Eluded Him. *Can. Bull. Med. Hist.* **2004**, *21* (1), 135–144. https://doi.org/10.3138/cbmh.21.1.135.

(19) Cobb, M. Oswald Avery, DNA, and the Transformation of Biology. *Curr. Biol.* **2014**, *24* (2), R55–R60. https://doi.org/10.1016/j.cub.2013.11.060.

(20) Manchester, K. L. Historical Opinion: Erwin Chargaff and His “rules” for the Base Composition of DNA: Why Did He Fail to See the Possibility of Complementarity? *Trends Biochem. Sci.* **2008**, *33* (2), 65–70. https://doi.org/10.1016/j.tibs.2007.10.009.

(21) Watson, J. D.; Crick, F. H. C. Molecular Structure of Nucleic Acids: A Structure for Deoxyribose Nucleic Acid. *Nature* **1953**, *171* (4356), 737–738. https://doi.org/10.1038/171737a0.

(22) Percec, V.; Xiao, Q. The Legacy of Rosalind E. Franklin: Landmark Contributions to Two Nobel Prizes. *Chem* **2021**, *7* (3), 529–536. https://doi.org/10.1016/j.chempr.2021.02.020.

(23) Brenner, S.; Jacob, F.; Meselson, M. An Unstable Intermediate Carrying Information from Genes to Ribosomes for Protein Synthesis. *Nature* **1961**, *190* (4776), 576–581. https://doi.org/10.1038/190576a0.

(24) Gros, F.; Hiatt, H.; Gilbert, W.; Kurland, C. G.; Risebrough, R. W.; Watson, J. D. Unstable Ribonucleic Acid Revealed by Pulse Labelling of Escherichia Coli. *Nature* **1961**, *190* (4776), 581–585. https://doi.org/10.1038/190581a0.

(25) Cobb, M. Who Discovered Messenger RNA? *Curr. Biol.* **2015**, *25* (13), R526–R532. https://doi.org/10.1016/J.CUB.2015.05.032.

(26) Crick, F. Central Dogma of Molecular Biology. *Nature* **1970**, *227* (5258), 561–563. https://doi.org/10.1038/227561a0.

(27) Morris, K. V.; Mattick, J. S. The Rise of Regulatory RNA. *Nat. Rev. Genet. 2014 156* **2014**, *15* (6), 423–437. https://doi.org/10.1038/nrg3722.

(28) Licatalosi, D. D.; Darnell, R. B. RNA Processing and Its Regulation: Global Insights into Biological Networks. *Nat. Rev. Genet.* **2010**, *11* (1), 75–87. https://doi.org/10.1038/nrg2673.

(29) Dammes, N.; Peer, D. Paving the Road for RNA Therapeutics. *Trends Pharmacol. Sci.* **2020**, *41* (10), 755–775. https://doi.org/10.1016/J.TIPS.2020.08.004.

(30) Winkle, M.; El-Daly, S. M.; Fabbri, M.; Calin, G. A. Noncoding RNA Therapeutics — Challenges and Potential Solutions. *Nat. Rev. Drug Discov.* **2021**, *20* (8), 629–651. https://doi.org/10.1038/s41573-021-00219-z.

(31) Statello, L.; Guo, C. J.; Chen, L. L.; Huarte, M. Gene Regulation by Long Non-Coding RNAs and Its Biological Functions. *Nat. Rev. Mol. Cell Biol.* **2021**, *22* (2), 96–118. https://doi.org/10.1038/s41580-020-00315-9.

(32) Ryder, P. V.; Lerit, D. A. RNA Localization Regulates Diverse and Dynamic Cellular Processes. *Traffic* **2018**, *19* (7), 496–502. https://doi.org/10.1111/TRA.12571.

(33) Das, S.; Vera, M.; Gandin, V.; Singer, R. H.; Tutucci, E. Intracellular MRNA Transport and Localized Translation. *Nat. Rev. Mol. Cell Biol.* **2021**, *22* (7), 483–504. https://doi.org/10.1038/s41580-021-00356-8.

(34) Weinstain, R.; Slanina, T.; Kand, D.; Klán, P. Visible-to-NIR-Light Activated Release: From Small Molecules to Nanomaterials. *Chemical Reviews*. American Chemical Society December 23, 2020, pp 13135–13272. https://doi.org/10.1021/acs.chemrev.0c00663.

(35) Klán, P.; Šolomek, T.; Bochet, C. G.; Blanc, A.; Givens, R.; Rubina, M.; Popik, V.; Kostikov, A.; Wirz, J. Photoremovable Protecting Groups in Chemistry and Biology: Reaction Mechanisms and Efficacy. *Chem. Rev.* **2013**, *113* (1), 119–191. https://doi.org/10.1021/cr300177k.

(36) Brieke, C.; Rohrbach, F.; Gottschalk, A.; Mayer, G.; Heckel, A. Light-Controlled Tools. *Angew. Chem. Int. Ed.* **2012**, *51* (34), 8446–8476. https://doi.org/10.1002/anie.201202134.

(37) Ankenbruck, N.; Courtney, T.; Naro, Y.; Deiters, A. Optochemical Control of Biological Processes in Cells and Animals. *Angew. Chem. Int. Ed.* **2018**, *57* (11), 2768–2798. https://doi.org/10.1002/anie.201700171.

(38) Lechner, V. M.; Nappi, M.; Deneny, P. J.; Folliet, S.; Chu, J. C. K.; Gaunt, M. J. Visible-Light-Mediated Modification and Manipulation of Biomacromolecules. *Chem. Rev.* **2022**, *122* (2), 1752–1829. https://doi.org/10.1021/acs.chemrev.1c00357.

(39) Palvai, S.; Moody, C. T.; Pandit, S.; Brudno, Y. On-Demand Drug Release from Click-Refillable Drug Depots. *Mol. Pharm.* **2021**, *18* (10), 3920–3925. https://doi.org/10.1021/acs.molpharmaceut.1c00535.

(40) Müller, P.; Sahlbach, M.; Gasper, S.; Mayer, G.; Müller, J.; Pötzsch, B.; Heckel, A. Controlling Coagulation in Blood with Red Light. *Angew. Chem. Int. Ed.* **2021**, *60* (41), 22441–22446. https://doi.org/10.1002/anie.202108468.

(41) Lucas, T.; Schäfer, F.; Müller, P.; Eming, S. A.; Heckel, A.; Dimmeler, S. Light-Inducible AntimiR-92a as a Therapeutic Strategy to Promote Skin Repair in Healing-Impaired Diabetic Mice. *Nat. Commun.* **2017**, *8* (1), 1–9. https://doi.org/10.1038/ncomms15162.

(42) Shrestha, P.; Dissanayake, K. C.; Gehrmann, E. J.; Wijesooriya, C. S.; Mukhopadhyay, A.; Smith, E. A.; Winter, A. H. Efficient Far-Red/Near-IR Absorbing BODIPY Photocages by Blocking Unproductive Conical Intersections. *J. Am. Chem. Soc.* **2020**, *142* (36), 15505–15512. https://doi.org/10.1021/jacs.0c07139.

(43) Bassolino, G.; Nançoz, C.; Thiel, Z.; Bois, E.; Vauthey, E.; Rivera-Fuentes, P. Photolabile Coumarins with Improved Efficiency through Azetidinyl Substitution. *Chem. Sci.* **2018**, *9* (2), 387–391. https://doi.org/10.1039/c7sc03627b.

(44) Matikonda, S. S.; Hammersley, G.; Kumari, N.; Grabenhorst, L.; Glembockyte, V.; Tinnefeld, P.; Ivanic, J.; Levitus, M.; Schnermann, M. J. Impact of Cyanine Conformational Restraint in the Near-Infrared Range. *J. Org. Chem.* **2020**, *85* (9), 5907–5915. https://doi.org/10.1021/acs.joc.0c00236.

(45) Michie, M. S.; Götz, R.; Franke, C.; Bowler, M.; Kumari, N.; Magidson, V.; Levitus, M.; Loncarek, J.; Sauer, M.; Schnermann, M. J. Cyanine Conformational Restraint in the Far-Red Range. *J. Am. Chem. Soc.* **2017**, *139* (36), 12406–12409. https://doi.org/10.1021/jacs.7b07272.

(46) Weissleder, R. A Clearer Vision for in Vivo Imaging: Progress Continues in the

Development of Smaller, More Penetrable Probes for Biological Imaging. *Nat. Biotechnol.* **2001**, *19* (4), 316–317. https://doi.org/10.1038/86684.

(47) Josa-Culleré, L.; Llebaria, A. In the Search for Photocages Cleavable with Visible Light: An Overview of Recent Advances and Chemical Strategies. *ChemPhotoChem* **2021**, *5* (4), 298–316. https://doi.org/10.1002/cptc.202000253.

(48) Jia, S.; Sletten, E. M. Spatiotemporal Control of Biology: Synthetic Photochemistry Toolbox with Far-Red and Near-Infrared Light. *ACS Chem. Biol.* **2021**. https://doi.org/10.1021/acschembio.1c00518.

(49) Barltrop, J. A.; Plant, P. J.; Schofield, P. Photosensitive Protective Groups. *Chem. Commun.* **1966**, *0* (22), 822–823. https://doi.org/10.1039/C19660000822.

(50) Becker, Y.; Unger, E.; Fichte, M. A. H.; Gacek, D. A.; Dreuw, A.; Wachtveitl, J.; Walla, P. J.; Heckel, A. A Red-Shifted Two-Photon-Only Caging Group for Three-Dimensional Photorelease. *Chem. Sci.* **2018**, *9* (10), 2797–2802. https://doi.org/10.1039/c7sc05182d.

(51) Becker, Y.; Roth, S.; Scheurer, M.; Jakob, A.; Gacek, D. A.; Walla, P. J.; Dreuw, A.; Wachtveitl, J.; Heckel, A. Selective Modification for Red-Shifted Excitability: A Small Change in Structure, a Huge Change in Photochemistry. *Chem. - Eur. J.* **2021**, *27* (6), 2212–2218. https://doi.org/10.1002/chem.202003672.

(52) Singh, A. K.; Khade, P. K. 7-Methoxy-3-Nitro-2-Naphthalenemethanol - A New Phototrigger for Caging Applications. *Tetrahedron Lett.* **2011**, *52* (38), 4899–4902. https://doi.org/10.1016/j.tetlet.2011.07.043.

(53) Barman, S.; Das, J.; Biswas, S.; Maiti, T. K.; Pradeep Singh, N. D. A Spiropyran-Coumarin Platform: An Environment Sensitive Photoresponsive Drug Delivery System for Efficient Cancer Therapy. *J. Mater. Chem. B* **2017**, *5* (21), 3940–3944. https://doi.org/10.1039/c7tb00379j.

(54) Lin, Q.; Yang, L.; Wang, Z.; Hua, Y.; Zhang, D.; Bao, B.; Bao, C.; Gong, X.; Zhu, L. Coumarin Photocaging Groups Modified with an Electron-Rich Styryl Moiety at the 3-Position: Long-Wavelength Excitation, Rapid Photolysis, and Photobleaching. *Angew. Chem. Int. Ed.* **2018**, *57* (14), 3722–3726. https://doi.org/10.1002/anie.201800713.

(55) Rubinstein, N.; Liu, P.; Miller, E. W.; Weinstain, R. Meso-Methylhydroxy BODIPY: A Scaffold for Photo-Labile Protecting Groups. *Chem. Commun.* **2015**, *51* (29), 6369–6372. https://doi.org/10.1039/c5cc00550g.

(56) Peterson, J. A.; Wijesooriya, C.; Gehrmann, E. J.; Mahoney, K. M.; Goswami, P. P.; Albright, T. R.; Syed, A.; Dutton, A. S.; Smith, E. A.; Winter, A. H. Family of BODIPY Photocages Cleaved by Single Photons of Visible/Near-Infrared Light. *J. Am. Chem. Soc.* **2018**, *140* (23), 7343–7346. https://doi.org/10.1021/jacs.8b04040.

(57) Slanina, T.; Shrestha, P.; Palao, E.; Kand, D.; Peterson, J. A.; Dutton, A. S.; Rubinstein, N.; Weinstain, R.; Winter, A. H.; Klán, P. In Search of the Perfect Photocage: Structure-Reactivity Relationships in Meso-Methyl BODIPY Photoremovable Protecting Groups. *J. Am. Chem. Soc.* **2017**, *139* (42), 15168–15175. https://doi.org/10.1021/jacs.7b08532.

(58) Zhang, Y.; Yan, C.; Zheng, Q.; Jia, Q.; Wang, Z.; Shi, P.; Guo, Z. Harnessing Hypoxia-Dependent Cyanine Photocages for In Vivo Precision Drug Release. *Angew. Chem. Int. Ed.* **2021**, *60* (17), 9553–9561. https://doi.org/10.1002/anie.202017349.

(59) Alachouzos, G.; Schulte, A. M.; Mondal, A.; Szymanski, W.; Feringa, B. L. Computational Design, Synthesis, and Photochemistry of Cy7-PPG, an Efficient NIR-Activated Photolabile Protecting Group for Therapeutic Applications**. *Angew. Chem. Int. Ed.* **2022**, e202201308. https://doi.org/10.1002/anie.202201308.

(60) Barltrop, J. A.; Plant, P. J.; Schofield, P. Photosensitive Protective Groups. *Chem. Commun.* **1966**, *0* (22), 822–823. https://doi.org/10.1039/C19660000822.

(61) Patchornik, A.; Amit, B.; Woodward, R. B. Photosensitive Protecting Groups. *J. Am. Chem. Soc.* **1970**, *92* (21), 6333–6335. https://doi.org/10.1021/ja00724a041.

(62) Kaplan, J. H.; Ellis-Davies, G. C. Photolabile Chelators for the Rapid Photorelease of Divalent Cations. *Proc. Natl. Acad. Sci. U. S. A.* **1988**, *85* (17), 6571–6575. https://doi.org/10.1073/pnas.85.17.6571.

(63) Aujard, I.; Benbrahim, C.; Gouget, M.; Ruel, O.; Baudin, J. B.; Neveu, P.; Jullien, L. O-Nitrobenzyl Photolabile Protecting Groups with Red-Shifted Absorption: Syntheses and Uncaging Cross-Sections for One- And Two-Photon Excitation. *Chem. - Eur. J.* **2006**, *12* (26), 6865–6879. https://doi.org/10.1002/chem.200501393.

(64) Momotake, A.; Lindegger, N.; Niggli, E.; Barsotti, R. J.; Ellis-Davies, G. C. R. The Nitrodibenzofuran Chromophore: A New Caging Group for Ultra-Efficient Photolysis in Living Cells. *Nat. Methods* **2006**, *3* (1), 35–40. https://doi.org/10.1038/nmeth821.

(65) Bader, T. K.; Xu, F.; Hodny, M. H.; Blank, D. A.; Distefano, M. D. Methoxy-Substituted Nitrodibenzofuran-Based Protecting Group with an Improved Two-Photon Action Cross-Section for Thiol Protection in Solid Phase Peptide Synthesis. *J. Org. Chem.* **2020**, *85* (3), 1614–1625. https://doi.org/10.1021/acs.joc.9b02751.

(66) Goswami, P. P.; Syed, A.; Beck, C. L.; Albright, T. R.; Mahoney, K. M.; Unash, R.; Smith, E. A.; Winter, A. H. BODIPY-Derived Photoremovable Protecting Groups Unmasked with Green Light. *J. Am. Chem. Soc.* **2015**, *137* (11), 3783–3786. https://doi.org/10.1021/jacs.5b01297.

(67) Štacko, P.; Šolomek, T. Photoremovable Protecting Groups: Across the Light Spectrum to near- Infrared Absorbing Photocages. *Chimia* **2021**, *75* (10), 873–881. https://doi.org/10.2533/chimia.2021.873.

(68) Gorka, A. P.; Nani, R. R.; Zhu, J.; Mackem, S.; Schnermann, M. J. A Near-IR Uncaging Strategy Based on Cyanine Photochemistry. *J. Am. Chem. Soc.* **2014**, *136* (40), 14153–14159. https://doi.org/10.1021/ja5065203.

(69) Nani, R. R.; Gorka, A. P.; Nagaya, T.; Kobayashi, H.; Schnermann, M. J. Near-IR Light-Mediated Cleavage of Antibody-Drug Conjugates Using Cyanine Photocages. *Angew. Chem. Int. Ed.* **2015**, *127* (46), 13839–13842. https://doi.org/10.1002/ange.201507391.

(70) Luciano, M. P.; Crooke, S. N.; Nourian, S.; Dingle, I.; Nani, R. R.; Kline, G.; Patel, N. L.; Robinson, C. M.; Difilippantonio, S.; Kalen, J. D.; Finn, M. G.; Schnermann, M. J. A Nonaggregating Heptamethine Cyanine for Building Brighter Labeled Biomolecules. *ACS Chem. Biol.* **2019**, *14* (5), 934–940. https://doi.org/10.1021/ACSCHEMBIO.9B00122/SUPPL_FILE/CB9B00122_SI_001.PDF.

(71) Gidi, Y.; Payne, L.; Glembockyte, V.; Michie, M. S.; Schnermann, M. J.; Cosa, G. Unifying Mechanism for Thiol-Induced Photoswitching and Photostability of Cyanine Dyes. *J. Am. Chem. Soc.* **2020**, *142* (29), 12681–12689. https://doi.org/10.1021/JACS.0C03786/SUPPL_FILE/JA0C03786_SI_001.PDF.

(72) Matikonda, S. S.; Helmerich, D. A.; Meub, M.; Beliu, G.; Kollmannsberger, P.; Greer, A.; Sauer, M.; Schnermann, M. J. Defining the Basis of Cyanine Phototruncation Enables a New Approach to Single-Molecule Localization Microscopy. *ACS Cent. Sci.* **2021**, *7* (7), 1144–1155. https://doi.org/10.1021/ACSCENTSCI.1C00483/SUPPL_FILE/OC1C00483_SI_001.PDF.

(73) Bhatt, M.; Pandey, S. S.; Tiwari, A. K.; Tiwari, B. S. Plastid-Mediated Singlet Oxygen in Regulated Cell Death. *Plant Biol.* **2021**, *23* (5), 686–694. https://doi.org/10.1111/plb.13260.

(74) Agnez-Lima, L. F.; Melo, J. T. A.; Silva, A. E.; Oliveira, A. H. S.; Timoteo, A. R. S.; Lima-Bessa, K. M.; Martinez, G. R.; Medeiros, M. H. G.; Di Mascio, P.; Galhardo, R. S.; Menck, C. F. M. DNA Damage by Singlet Oxygen and Cellular Protective Mechanisms. *Mutat. Res. - Rev. Mutat. Res.* **2012**, *751* (1), 15–28. https://doi.org/10.1016/j.mrrev.2011.12.005.

(75) Janeková, H.; Russo, M.; Ziegler, U.; Štacko, P. Photouncaging of Carboxylic Acids from Cyanine Dyes with Near-Infrared Light**. *Angew. Chem. Int. Ed.* **2022**, e202204391. https://doi.org/10.1002/anie.202204391.

(76) Givens, R. S.; Matuszewski, B. Photochemistry of Phosphate Esters: An Efficient Method for the Generation of Electrophiles1. *J. Am. Chem. Soc.* **1984**, *106* (22), 6860–6861. https://doi.org/10.1021/ja00334a075.

(77) Schade, B.; Hagen, V.; Schmidt, R.; Herbrich, R.; Krause, E.; Eckardt, T.; Bendig, J. Deactivation Behavior and Excited-State Properties of (Coumarin-4- Yl)Methyl Derivatives. 1. Photocleavage of (7-Methoxycoumarin-4-Yl)Methyl- Caged Acids with Fluorescence Enhancement. *J. Org. Chem.* **1999**, *64* (25), 9109–9117. https://doi.org/10.1021/jo9910233.

(78) Piloto, A. M.; Hungerford, G.; Costa, S. P. G.; Gonçalves, M. S. T. Photoinduced Release of Neurotransmitter Amino Acids from Coumarin-Fused Julolidine Ester Cages. *Eur. J. Org. Chem.* **2013**, *2013* (34), 7715–7723. https://doi.org/10.1002/ejoc.201300730.

(79) Wang, C.; Chi, W.; Qiao, Q.; Tan, D.; Xu, Z.; Liu, X. Twisted Intramolecular Charge Transfer (TICT) and Twists beyond TICT: From Mechanisms to Rational Designs of Bright and Sensitive Fluorophores. *Chem. Soc. Rev.* **2021**, *50* (22), 12656–12678. https://doi.org/10.1039/d1cs00239b.

(80) Eckardt, T.; Hagen, V.; Schade, B.; Schmidt, R.; Schweitzer, C.; Bendig, J. Deactivation Behavior and Excited-State Properties of (Coumarin-4-Yl)Methyl Derivatives. 2. Photocleavage of Selected (Coumarin-4-Yl)Methyl-Caged Adenosine Cyclic 3′,5′-Monophosphates with Fluorescence Enhancement. *J. Org. Chem.* **2002**, *67* (3), 703–710. https://doi.org/10.1021/jo010692p.

(81) Fournier, L.; Aujard, I.; Le Saux, T.; Maurin, S.; Beaupierre, S.; Baudin, J. B.; Jullien, L. Coumarinylmethyl Caging Groups with Redshifted Absorption. *Chem. - Eur. J.* **2013**, *19* (51), 17494–17507. https://doi.org/10.1002/chem.201302630.

(82) Bojtár, M.; Kormos, A.; Kis-Petik, K.; Kellermayer, M.; Kele, P. Green-Light Activatable, Water-Soluble Red-Shifted Coumarin Photocages. *Org. Lett.* **2019**, *21* (23), 9410–9414. https://doi.org/10.1021/acs.orglett.9b03624.

(83) López-Corrales, M.; Rovira, A.; Gandioso, A.; Bosch, M.; Nonell, S.; Marchán, V. Transformation of COUPY Fluorophores into a Novel Class of Visible-Light-Cleavable Photolabile Protecting Groups. *Chem. - Eur. J.* **2020**, *26* (69), 16222–16227. https://doi.org/10.1002/chem.202002314.

(84) Li, C.; Wang, T.; Li, N.; Li, M.; Li, Y.; Sun, Y.; Tian, Y.; Zhu, J.; Wu, Y.; Zhang, D.; Cui, X. Hydrogen-Bonding-Induced Bathochromic Effect of Si-Coumarin and Its Use in Monitoring Adipogenic Differentiation. *Chem. Commun.* **2019**, *55* (78), 11802–11805. https://doi.org/10.1039/c9cc05895h.

(85) Matikonda, S. S.; Ivanic, J.; Gomez, M.; Hammersley, G.; Schnermann, M. J. Core Remodeling Leads to Long Wavelength Fluoro-Coumarins. *Chem. Sci.* **2020**, *11* (28),

7302–7307. https://doi.org/10.1039/d0sc02566f.

(86) Lakowicz, J. R. *Principles of Fluorescence Spectroscopy*; Springer, 2006. https://doi.org/10.1007/978-0-387-46312-4.

(87) McGown, L. B.; Nithipahkom, K. Molecular Fluorescence and Phosphorescence. *Appl. Spectrosc. Rev.* **2000**, *35* (4), 353–393. https://doi.org/10.1081/ASR-100101229.

(88) Stokes, G. XXX. On the Change of Refrangibility of Light. *Philos. Trans. R. Soc. London* **1852**, *142*, 463–562. https://doi.org/10.1098/rstl.1852.0022.

(89) Schulman, S. G. (Stephen G. Fluorescence and Phosphorescence Spectroscopy. *Fluoresc. Phosphorescence Spectrosc.* **1977**, 288. https://doi.org/10.1016/c2013-0-02750-8.

(90) Atkins, P. W. (Peter W.; Friedman, R. *Molecular Quantum Mechanics*; 1956; Vol. 9. https://doi.org/10.1063/1.3059924.

(91) Misra, R.; Bhattacharyya, S. P. Medium Effect on ICT Process: Theory and Experiments. In *Intramolecular Charge Transfer*; Wiley-VCH Verlag GmbH & Co. KGaA: Weinheim, Germany, 2018; pp 115–148. https://doi.org/10.1002/9783527801916.ch4.

(92) Mallick, A.; Purkayastha, P.; Chattopadhyay, N. Photoprocesses of Excited Molecules in Confined Liquid Environments: An Overview. *J. Photochem. Photobiol. C Photochem. Rev.* **2007**, *8* (3), 109–127. https://doi.org/10.1016/j.jphotochemrev.2007.06.001.

(93) Holtzhauer, M.; Mohr, P. Electron and Proton Transfer in Chemistry and Biology. *Zeitschrift für Phys. Chemie* **1994**, *186* (1), 119–119. https://doi.org/10.1524/zpch.1994.186.part_1.119.

(94) Hammer, C. A.; Falahati, K.; Jakob, A.; Klimek, R.; Burghardt, I.; Heckel, A.; Wachtveitl, J. Sensitized Two-Photon Activation of Coumarin Photocages. *J. Phys. Chem. Lett.* **2018**, *9* (6), 1448–1453. https://doi.org/10.1021/acs.jpclett.7b03364.

(95) Misra, R.; Bhattacharyya, S. P. Intramolecular Charge Transfer: Theory and Applications. *Intramol. Charg. Transf.* **2018**.

(96) Lippert, E.; Lüder, W.; Moll, F.; Nägele, W.; Boos, H.; Prigge, H.; Seibold-Blankenstein, I. Umwandlung von Elektronenanregungsenergie. *Angew. Chem. Int. Ed.* **1961**, *73* (21), 695–706. https://doi.org/10.1002/ange.19610732103.

(97) Rappoport, D.; Furche, F. Photoinduced Intramolecular Charge Transfer in 4-(Dimethyl)Aminobenzonitrile - A Theoretical Perspective. *J. Am. Chem. Soc.* **2004**, *126* (4), 1277–1284. https://doi.org/10.1021/ja037806u.

(98) Rappoport, D.; Furche, F. Photoinduced Intramolecular Charge Transfer in 4- (Dimethyl) Aminobenzonitrile - A Theoretical Perspective. *J. Am. Chem. Soc.* **2004**, No. 126, 1277–1284.

(99) Rettig, W.; Bliss, B.; Dirnberger, K. Pseudo-Jahn-Teller and TICT-Models: A Photophysical Comparison of Meta- and Para-DMABN Derivatives. *Chem. Phys. Lett.* **1999**, *305* (1–2), 8–14. https://doi.org/10.1016/S0009-2614(99)00316-4.

(100) Zachariasse, K. A. Comment on “Pseudo-Jahn-Teller and TICT-Models: A Photophysical Comparison of Meta-and Para-DMABN Derivatives” [Chem. Phys. Lett. 305 (1999) 8]: The PICT Model for Dual Fluorescence of Aminobenzonitriles. *Chem. Phys. Lett.* **2000**, *320* (1–2), 8–13. https://doi.org/10.1016/S0009-2614(00)00230-X.

(101) Rotkiewicz, K.; Grellmann, K. H.; Grabowski, Z. R. Reinterpretation of the Anomalous Fluorescense of P-n,n-Dimethylamino-Benzonitrile. *Chem. Phys. Lett.* **1973**, *19* (3), 315–318. https://doi.org/10.1016/0009-2614(73)80367-7.

(102) Grabowski, Z. R. Electron Transfer in Flexible Molecules and Molecular Ions. *Pure Appl. Chem.* **1993**, *65* (8), 1751–1756.

(103) Grabowski, Z. R.; Rotkiewicz, K.; Rettig, W. Structural Changes Accompanying Intramolecular Electron Transfer: Focus on Twisted Intramolecular Charge-Transfer States and Structures. *Chemical Reviews*. American Chemical Society October 2003, pp 3899–4031. https://doi.org/10.1021/cr940745l.

(104) Liese, D.; Haberhauer, G. Rotations in Excited ICT States – Fluorescence and Its Microenvironmental Sensitivity. *Isr. J. Chem.* **2018**, *58* (8), 813–826. https://doi.org/10.1002/ijch.201800032.

(105) Rettig, W. Ladungstrennung in Angeregten Zuständen Entkoppelter Systeme – TICT-Verbindungen Und Implikationen Für Die Entwicklung Neuer Laserfarbstoffe Sowie Für Den Primärprozeß von Sehvorgang Und Photosynthese. *Angew. Chem. Int. Ed.* **1986**, *98* (11), 969–986. https://doi.org/10.1002/ange.19860981104.

(106) Valegård, K.; Murray, J. B.; Stonehouse, N. J.; Van Den Worm, S.; Stockley, P. G.; Liljas, L. The Three-Dimensional Structures of Two Complexes between Recombinant MS2 Capsids and RNA Operator Fragments Reveal Sequence-Specific Protein-RNA Interactions. *J. Mol. Biol.* **1997**, *270* (5), 724–738. https://doi.org/10.1006/jmbi.1997.1144.

(107) Peabody, D. S. The RNA Binding Size of Bacteriophage MS2 Coat Protein. *EMBO J.* **1993**, *12* (2), 595–600. https://doi.org/10.1002/j.1460-2075.1993.tb05691.x.

(108) Johansson, H. E.; Liljas, L.; Uhlenbeck, O. C. RNA Recognition by the MS2 Phage Coat Protein. *Semin. Virol.* **1997**, *8* (3), 176–185. https://doi.org/10.1006/smvy.1997.0120.

(109) Wu, J.; Zaccara, S.; Khuperkar, D.; Kim, H.; Tanenbaum, M. E.; Jaffrey, S. R. Live Imaging of MRNA Using RNA-Stabilized Fluorogenic Proteins. *Nat. Methods* **2019**, *16* (9), 862–865. https://doi.org/10.1038/s41592-019-0531-7.

(110) Yang, L. Z.; Wang, Y.; Li, S. Q.; Yao, R. W.; Luan, P. F.; Wu, H.; Carmichael, G. G.; Chen, L. L. Dynamic Imaging of RNA in Living Cells by CRISPR-Cas13 Systems. *Mol. Cell* **2019**, *76* (6), 981-997.e7. https://doi.org/10.1016/j.molcel.2019.10.024.

(111) Carey, J.; Uhlenbeck, O. C.; Cameron, V.; de Haseth, P. L. Sequence-Specific Interaction of R17 Coat Protein with Its Ribonucleic Acid Binding Site. *Biochemistry* **1983**, *22* (11), 2601–2610. https://doi.org/10.1021/bi00280a002.

(112) Li, X.; Kim, H.; Litke, J. L.; Wu, J.; Jaffrey, S. R. Fluorophore-Promoted RNA Folding and Photostability Enables Imaging of Single Broccoli-Tagged MRNAs in Live Mammalian Cells. *Angew. Chem. Int. Ed.* **2020**, *132* (11), 4541–4548. https://doi.org/10.1002/ange.201914576.

(113) Paige, J. S.; Wu, K. Y.; Jaffrey, S. R. RNA Mimics of Green Fluorescent Protein. *Science.* **2011**, *333* (6042), 642–646. https://doi.org/10.1126/science.1207339.

(114) Autour, A.; Jeng, S. C. Y.; Cawte, A. D.; Abdolahzadeh, A.; Galli, A.; Panchapakesan, S. S. S.; Rueda, D.; Ryckelynck, M.; Unrau, P. J. Fluorogenic RNA Mango Aptamers for Imaging Small Non-Coding RNAs in Mammalian Cells. *Nat. Commun.* **2018**, *9* (1), 1–12. https://doi.org/10.1038/s41467-018-02993-8.

(115) Cawte, A. D.; Unrau, P. J.; Rueda, D. S. Live Cell Imaging of Single RNA Molecules with Fluorogenic Mango II Arrays. *Nat. Commun.* **2020**, *11* (1), 1–11. https://doi.org/10.1038/s41467-020-14932-7.

(116) Sunbul, M.; Jäschke, A. SRB-2: A Promiscuous Rainbow Aptamer for Live-Cell RNA Imaging. *Nucleic Acids Res.* **2018**, *46* (18), e110–e110. https://doi.org/10.1093/nar/gky543.

(117) Sato, S.; Watanabe, M.; Katsuda, Y.; Murata, A.; Wang, D. O.; Uesugi, M. Live-Cell Imaging of Endogenous MRNAs with a Small Molecule. *Angew. Chem. Int. Ed.* **2015**, *127* (6), 1875–1878. https://doi.org/10.1002/ange.201410339.

(118) Yatsuzuka, K.; Sato, S. I.; Pe, K. B.; Katsuda, Y.; Takashima, I.; Watanabe, M.; Uesugi, M. Live-Cell Imaging of Multiple Endogenous MRNAs Permits the Direct Observation of RNA Granule Dynamics. *Chem. Commun.* **2018**, *54* (52), 7151–7154. https://doi.org/10.1039/c8cc03805h.

(119) Braselmann, E.; Wierzba, A. J.; Polaski, J. T.; Chromiński, M.; Holmes, Z. E.; Hung, S. T.; Batan, D.; Wheeler, J. R.; Parker, R.; Jimenez, R.; Gryko, D.; Batey, R. T.; Palmer, A. E. A Multicolor Riboswitch-Based Platform for Imaging of RNA in Live Mammalian Cells. *Nat. Chem. Biol.* **2018**, *14* (10), 964–971. https://doi.org/10.1038/s41589-018-0103-7.

(120) Sunbul, M.; Lackner, J.; Martin, A.; Englert, D.; Hacene, B.; Grün, F.; Nienhaus, K.; Nienhaus, G. U.; Jäschke, A. Super-Resolution RNA Imaging Using a Rhodamine-Binding Aptamer with Fast Exchange Kinetics. *Nat. Biotechnol.* **2021**, *39* (6), 686–690. https://doi.org/10.1038/s41587-020-00794-3.

(121) Mao, S.; Ying, Y.; Wu, R.; Chen, A. K. Recent Advances in the Molecular Beacon Technology for Live-Cell Single-Molecule Imaging. *iScience* **2020**, *23* (12), 101801. https://doi.org/10.1016/j.isci.2020.101801.

(122) Ma, Z.; Wu, X.; Krueger, C. J.; Chen, A. K. Engineering Novel Molecular Beacon Constructs to Study Intracellular RNA Dynamics and Localization Ma Z et Al/Molecular Beacons for Single-Molecule RNA Imaging. *Genomics, Proteomics and Bioinformatics*. Beijing Genomics Institute October 1, 2017, pp 279–286. https://doi.org/10.1016/j.gpb.2017.04.004.

(123) Tyagi, S.; Kramer, F. R. Molecular Beacons: Probes That Fluoresce Upon Hybridization. *Nat. Biotechnol.* **1996**, *14* (3), 303–308. https://doi.org/10.1038/nbt0396-303.

(124) Marras, S. A. E.; Kramer, F. R.; Tyagi, S. Efficiencies of Fluorescence Resonance Energy Transfer and Contact-Mediated Quenching in Oligonucleotide Probes. *Nucleic Acids Res.* **2002**, *30* (21), e122–e122. https://doi.org/10.1093/nar/gnf121.

(125) Bratu, D. P.; Cha, B. J.; Mhlanga, M. M.; Kramer, F. R.; Tyagi, S. Visualizing the Distribution and Transport of MRNAs in Living Cells. *Proc. Natl. Acad. Sci. U. S. A.* **2003**, *100* (23), 13308–13313. https://doi.org/10.1073/pnas.2233244100.

(126) Turner-Bridger, B.; Jakobs, M.; Muresan, L.; Wong, H. H. W.; Franze, K.; Harris, W. A.; Holt, C. E. Single-Molecule Analysis of Endogenous β-Actin MRNA Trafficking Reveals a Mechanism for Compartmentalized MRNA Localization in Axons. *Proc. Natl. Acad. Sci. U. S. A.* **2018**, *115* (41), E9697–E9706. https://doi.org/10.1073/pnas.1806189115.

(127) Gerasimova, Y. V.; Kolpashchikov, D. M. Detection of Bacterial 16S RRNA Using a Molecular Beacon-Based X Sensor. *Biosens. Bioelectron.* **2013**, *41* (1), 386–390. https://doi.org/10.1016/j.bios.2012.08.058.

(128) Bidar, N.; Oroojalian, F.; Baradaran, B.; Eyvazi, S.; Amini, M.; Jebelli, A.; Hosseini, S. S.; Pashazadeh-Panahi, P.; Mokhtarzadeh, A.; de la Guardia, M. Monitoring of MicroRNA Using Molecular Beacons Approaches: Recent Advances. *TrAC - Trends in Analytical Chemistry*. Elsevier B.V. October 1, 2020, p 116021. https://doi.org/10.1016/j.trac.2020.116021.

(129) Chen, A. K.; Rhee, W. J.; Bao, G.; Tsourkas, A. Delivery of Molecular Beacons for Live-Cell Imaging and Analysis of RNA. *Methods Mol. Biol.* **2011**, *714*, 159–174. https://doi.org/10.1007/978-1-61779-005-8_10.

(130) Monroy-Contreras, R.; Vaca, L. Molecular Beacons: Powerful Tools for Imaging RNA in Living Cells. *J. Nucleic Acids* **2011**, *2011*. https://doi.org/10.4061/2011/741723.

(131) George, L.; Indig, F. E.; Abdelmohsen, K.; Gorospe, M. Intracellular RNA-Tracking Methods. *Open Biol.* **2018**, *8* (10), 180104. https://doi.org/10.1098/rsob.180104.

(132) Vargas, D. Y.; Raj, A.; Marras, S. A. E.; Kramer, F. R.; Tyagi, S. Mechanism of MRNA Transport in the Nucleus. *Proc. Natl. Acad. Sci. U. S. A.* **2005**, *102* (47), 17008–17013. https://doi.org/10.1073/pnas.0505580102.

(133) Fallmann, J.; Will, S.; Engelhardt, J.; Grüning, B.; Backofen, R.; Stadler, P. F. Recent Advances in RNA Folding. *J. Biotechnol.* **2017**, *261*, 97–104. https://doi.org/10.1016/j.jbiotec.2017.07.007.

(134) Iannitti, T.; Morales-Medina, J.; Palmieri, B. Phosphorothioate Oligonucleotides: Effectiveness and Toxicity. *Curr. Drug Targets* **2014**, *15* (7), 663–673. https://doi.org/10.2174/1389450115666140321100304.

(135) Prakash, T. P. An Overview of Sugar-Modified Oligonucleotides for Antisense Therapeutics. *Chem. Biodivers.* **2011**, *8* (9), 1616–1641. https://doi.org/10.1002/cbdv.201100081.

(136) Sharma, V. K.; Sharma, R. K.; Singh, S. K. Antisense Oligonucleotides: Modifications and Clinical Trials. *Medchemcomm* **2014**, *5* (10), 1454–1471. https://doi.org/10.1039/c4md00184b.

(137) Inoue, H.; Hayase, Y.; Imura, A.; Iwai, S.; Miura, K.; Ohtsuka, E. Synthesis and Hybridization Studies on Two Complementary Nona(2'-o-Methyl)Ribonucleotides. *Nucleic Acids Res.* **1987**, *15* (15), 6131–6148. https://doi.org/10.1093/nar/15.15.6131.

(138) Inoue, H.; Hayase, Y.; Iwai, S.; Ohtsuka, E. Sequence-Dependent Hydrolysis of RNA Using Modified Oligonucleotide Splints and RNase H. *FEBS Lett.* **1987**, *215* (2), 327–330. https://doi.org/10.1016/0014-5793(87)80171-0.

(139) Deleavey, G. F.; Damha, M. J. Designing Chemically Modified Oligonucleotides for Targeted Gene Silencing. *Chem. Biol.* **2012**, *19* (8), 937–954. https://doi.org/10.1016/j.chembiol.2012.07.011.

(140) Kawasaki, A. M.; Casper, M. D.; Freier, S. M.; Lesnik, E. A.; Zounes, M. C.; Cummins, L. L.; Gonzalez, C.; Dan Cook, P. Uniformly Modified 2′-Deoxy-2′-Fluoro Phosphorothioate Oligonucleotides as Nuclease-Resistant Antisense Compounds with High Affinity and Specificity for RNA Targets. *J. Med. Chem.* **1993**, *36* (7), 831–841. https://doi.org/10.1021/jm00059a007.

(141) Pallan, P. S.; Greene, E. M.; Jicman, P. A.; Pandey, R. K.; Manoharan, M.; Rozners, E.; Egli, M. Unexpected Origins of the Enhanced Pairing Affinity of 2'-Fluoro-Modified RNA. *Nucleic Acids Res.* **2011**, *39* (8), 3482–3495. https://doi.org/10.1093/nar/gkq1270.

(142) Martin-Pintado, N.; Deleavey, G. F.; Portella, G.; Campos-Olivas, R.; Orozco, M.; Damha, M. J.; González, C. Backbone FC-H···O Hydrogen Bonds in 2′F-Substituted Nucleic Acids. *Angew. Chem. Int. Ed.* **2013**, *52* (46), 12065–12068. https://doi.org/10.1002/anie.201305710.

(143) Manoharan, M.; Akinc, A.; Pandey, R. K.; Qin, J.; Hadwiger, P.; John, M.; Mills, K.; Charisse, K.; Maier, M. A.; Nechev, L.; Greene, E. M.; Pallan, P. S.; Rozners, E.; Rajeev, K. G.; Egli, M. Unique Gene-Silencing and Structural Properties of 2′-Fluoro-Modified SiRNAs. *Angew. Chem. Int. Ed.* **2011**, *123* (10), 2332–2336. https://doi.org/10.1002/ange.201006519.

(144) Layzer, J. M.; McCaffrey, A. P.; Tanner, A. K.; Huang, Z.; Kay, M. A.; Sullenger, B. A. In Vivo Activity of Nuclease-Resistant SiRNAs. *Rna* **2004**, *10* (5), 766–771.

https://doi.org/10.1261/rna.5239604.

(145) Obika, S.; Nanbu, D.; Hari, Y.; Morio, K. I.; In, Y.; Ishida, T.; Imanishi, T. Synthesis of 2'-O,4'-C-Methyleneuridine and -Cytidine. Novel Bicyclic Nucleosides Having a Fixed C3-Endo Sugar Puckering. *Tetrahedron Lett.* **1997**, *38* (50), 8735–8738. https://doi.org/10.1016/S0040-4039(97)10322-7.

(146) Koshkin, A. A.; Singh, S. K.; Nielsen, P.; Rajwanshi, V. K.; Kumar, R.; Meldgaard, M.; Olsen, C. E.; Wengel, J. LNA (Locked Nucleic Acids): Synthesis of the Adenine, Cytosine, Guanine, 5-Methylcytosine, Thymine and Uracil Bicyclonucleoside Monomers, Oligomerisation, and Unprecedented Nucleic Acid Recognition. *Tetrahedron* **1998**, *54* (14), 3607–3630. https://doi.org/10.1016/S0040-4020(98)00094-5.

(147) Kierzek, E.; Ciesielska, A.; Pasternak, K.; Mathews, D. H.; Turner, D. H.; Kierzek, R. The Influence of Locked Nucleic Acid Residues on the Thermodynamic Properties of 2′-O-Methyl RNA/RNA Heteroduplexes. *Nucleic Acids Res.* **2005**, *33* (16), 5082–5093. https://doi.org/10.1093/nar/gki789.

(148) Crooke, S. T.; Liang, X. H.; Baker, B. F.; Crooke, R. M. Antisense Technology: A Review. *J. Biol. Chem.* **2021**, *296*, 100416. https://doi.org/10.1016/j.jbc.2021.100416.

(149) Vickers, T. A.; Zhang, H.; Graham, M. J.; Lemonidis, K. M.; Zhao, C.; Dean, N. M. Modification of MyD88 MRNA Splicing and Inhibition of IL-1β Signaling in Cell Culture and in Mice with a 2′- O -Methoxyethyl-Modified Oligonucleotide . *J. Immunol.* **2006**, *176* (6), 3652–3661. https://doi.org/10.4049/jimmunol.176.6.3652.

(150) Teplova, M.; Minasov, G.; Tereshko, V.; Inamati, G. B.; Cook, P. D.; Manoharan, M.; Egli, M. Crystal Structure and Improved Antisense Properties of 2'-O-(2- Methoxyethyl)-RNA. *Nat. Struct. Biol.* **1999**, *6* (6), 535–539. https://doi.org/10.1038/9304.

(151) Corey, D. R.; Abrams, J. M. Morpholino Antisense Oligonucleotides: Tools for Investigating Vertebrate Development. *Genome Biol.* **2001**, *2* (5), 1–3. https://doi.org/10.1186/gb-2001-2-5-reviews1015.

(152) Moulton, J. D.; Shan, J. Gene Knockdowns in Adult Animals: PPMOs and Vivo-Morpholinos. *Molecules* **2009**, *14* (3), 1304–1323. https://doi.org/10.3390/molecules14031304.

(153) Tyagi, S.; Alsmadi, O. Imaging Native β-Actin MRNA in Motile Fibroblasts. *Biophys. J.* **2004**, *87* (6), 4153–4162. https://doi.org/10.1529/biophysj.104.045153.

(154) Mhlanga, M. M.; Vargas, D. Y.; Fung, C. W.; Kramer, F. R.; Tyagi, S. TRNA-Linked Molecular Beacons for Imaging MRNAs in the Cytoplasm of Living Cells. *Nucleic Acids Res.* **2005**, *33* (6), 1902–1912. https://doi.org/10.1093/nar/gki302.

(155) Chen, A. K.; Behlke, M. A.; Tsourkas, A. Avoiding False-Positive Signals with Nuclease-Vulnerable Molecular Beacons in Single Living Cells. *Nucleic Acids Res.* **2007**, *35* (16), e105–e105. https://doi.org/10.1093/nar/gkm593.

(156) Chen, A. K.; Davydenko, O.; Behlke, M. A.; Tsourkas, A. Ratiometric Bimolecular Beacons for the Sensitive Detection of RNA in Single Living Cells. *Nucleic Acids Res.* **2010**, *38* (14), e148–e148. https://doi.org/10.1093/nar/gkq436.

(157) Tsourkas, A.; Behlke, M. A.; Xu, Y.; Bao, G. Spectroscopic Features of Dual Fluorescence/Luminescence Resonance Energy-Transfer Molecular Beacons. *Anal. Chem.* **2003**, *75* (15), 3697–3703. https://doi.org/10.1021/ac034295l.

(158) Santangelo, P. J.; Nix, B.; Tsourkas, A.; Bao, G. Dual FRET Molecular Beacons for MRNA Detection in Living Cells. *Nucleic Acids Res.* **2004**, *32* (6), e57–e57. https://doi.org/10.1093/nar/gnh062.

(159) Feng, X.; Kang, W.; Wu, X.; Wang, S.; Liu, F. Quantitative Detection and Real-Time Monitoring of Endogenous MRNA at the Single Live Cell Level Using a Ratiometric Molecular Beacon. *ACS Appl. Mater. Interfaces* **2019**, *11* (32), 28752–28761. https://doi.org/10.1021/acsami.9b12394.

(160) Ballabh Joshi, K.; Vlachos, A.; Mikat, V.; Deller, T.; Heckel, A. Light-Activatable Molecular Beacons with a Caged Loop Sequence. *Chem. Commun.* **2012**, *48* (22), 2746–2748. https://doi.org/10.1039/c2cc16654b.

(161) Nitin, N.; Santangelo, P. J.; Kim, G.; Nie, S.; Bao, G. Peptide-Linked Molecular Beacons for Efficient Delivery and Rapid MRNA Detection in Living Cells. *Nucleic Acids Res.* **2004**, *32* (6), e58–e58. https://doi.org/10.1093/nar/gnh063.

(162) Wang, C.; Zhu, Z.; Song, Y.; Lin, H.; Yang, C. J.; Tan, W. Caged Molecular Beacons: Controlling Nucleic Acid Hybridization with Light. *Chem. Commun.* **2011**, *47* (20), 5708–5710. https://doi.org/10.1039/c1cc10481k.

(163) Yang, L.; Kim, H. B.; Sul, J. Y.; Yeldell, S. B.; Eberwine, J. H.; Dmochowski, I. J. Efficient Synthesis of Light-Triggered Circular Antisense Oligonucleotides Targeting Cellular Protein Expression. *ChemBioChem* **2018**, *19* (12), 1250–1254. https://doi.org/10.1002/cbic.201800012.

(164) Rinne, J. S.; Kaminski, T. P.; Kubitscheck, U.; Heckel, A. Light-Inducible Molecular Beacons for Spatio-Temporally Highly Defined Activation. *Chem. Commun.* **2013**, *49* (47), 5375–5377. https://doi.org/10.1039/c3cc42420k.

(165) Daneholt, B. Assembly and Transport of a Premessenger RNP Particle. *Proc. Natl. Acad. Sci. U. S. A.* **2001**, *98* (13), 7012–7017. https://doi.org/10.1073/pnas.111145498.

(166) Jun, J. V.; Chenoweth, D. M.; Petersson, E. J. Rational Design of Small Molecule Fluorescent Probes for Biological Applications. *Org. Biomol. Chem.* **2020**, *18* (30), 5747–5763. https://doi.org/10.1039/D0OB01131B.

(167) Grimm, J. B.; Lavis, L. D. Caveat Fluorophore: An Insiders' Guide to Small-Molecule Fluorescent Labels. *Nat. Methods* **2022**, *19* (2), 149–158. https://doi.org/10.1038/s41592-021-01338-6.

(168) Terai, T.; Nagano, T. Small-Molecule Fluorophores and Fluorescent Probes for Bioimaging. *Pflügers Arch. - Eur. J. Physiol. 2013 4653* **2013**, *465* (3), 347–359. https://doi.org/10.1007/S00424-013-1234-Z.

(169) Lavis, L. D.; Raines, R. T. Bright Ideas for Chemical Biology. *ACS Chem. Biol.* **2008**, *3* (3), 142–155. https://doi.org/10.1021/CB700248M/SUPPL_FILE/CB700248M-FILE007.PDF.

(170) Lavis, L. D.; Raines, R. T. Bright Building Blocks for Chemical Biology. *ACS Chem. Biol.* **2014**, *9* (4), 855–866. https://doi.org/10.1021/CB500078U/ASSET/IMAGES/LARGE/CB-2014-00078U_0003.JPEG.

(171) Grimm, J. B.; Muthusamy, A. K.; Liang, Y.; Brown, T. A.; Lemon, W. C.; Patel, R.; Lu, R.; Macklin, J. J.; Keller, P. J.; Ji, N.; Lavis, L. D. A General Method to Fine-Tune Fluorophores for Live-Cell and in Vivo Imaging. *Nat. Methods* **2017**, *14* (10), 987–994. https://doi.org/10.1038/nmeth.4403.

(172) Meiser, N.; Fuks, C.; Hengesbach, M. Cooperative Analysis of Structural Dynamics in RNA-Protein Complexes by Single-Molecule Förster Resonance Energy Transfer Spectroscopy. *Mol. 2020, Vol. 25, Page 2057* **2020**, *25* (9), 2057. https://doi.org/10.3390/MOLECULES25092057.

(173) Kapuscinski, J. DAPI: A DMA-Specific Fluorescent Probe. *Biotech. Histochem.* **1995**,

70 (5), 220–233. https://doi.org/10.3109/10520299509108199.

(174) Whitaker, J. E.; Haugland, R. P.; Moore, P. L.; Hewitt, P. C.; Reese, M.; Haugland, R. P. Cascade Blue Derivatives: Water Soluble, Reactive, Blue Emission Dyes Evaluated as Fluorescent Labels and Tracers. *Anal. Biochem.* **1991**, *198* (1), 119–130. https://doi.org/10.1016/0003-2697(91)90515-U.

(175) Loudet, A.; Burgess, K. BODIPY Dyes and Their Derivatives: Syntheses and Spectroscopic Properties. *Chem. Rev.* **2007**, *107* (11), 4891–4932. https://doi.org/10.1021/cr078381n.

(176) You, M.; Jaffrey, S. R. Structure and Mechanism of RNA Mimics of Green Fluorescent Protein. *Annu. Rev. Biophys.* **2015**, *44*, 187–206. https://doi.org/10.1146/annurev-biophys-060414-033954.

(177) Tebo, A. G.; Moeyaert, B.; Thauvin, M.; Carlon-Andres, I.; Böken, D.; Volovitch, M.; Padilla-Parra, S.; Dedecker, P.; Vriz, S.; Gautier, A. Orthogonal Fluorescent Chemogenetic Reporters for Multicolor Imaging. *Nat. Chem. Biol.* **2021**, *17* (1), 30–38. https://doi.org/10.1038/s41589-020-0611-0.

(178) Aaron, C.; Barker, C. C. Steric Effects in Di- and Tri-Arylmethane Dyes. Part X. Electronic Absorption Spectra of Bridged Derivatives of Malachite Green and Crystal Violet. *J. Chem. Soc. B Phys. Org.* **1971**, No. 0, 319–324. https://doi.org/10.1039/J29710000319.

(179) Grimm, J. B.; Sung, A. J.; Legant, W. R.; Hulamm, P.; Matlosz, S. M.; Betzig, E.; Lavis, L. D. Carbofluoresceins and Carborhodamines as Scaffolds for High-Contrast Fluorogenic Probes. *ACS Chem. Biol.* **2013**, *8* (6), 1303–1310. https://doi.org/10.1021/cb4000822.

(180) Arden-Jacob, J.; Frantzeskos, J.; Kemnitzer, N. U.; Zilles, A.; Drexhage, K. H. New Fluorescent Markers for the Red Region. *Spectrochim. Acta - Part A Mol. Biomol. Spectrosc.* **2001**, *57* (11), 2271–2283. https://doi.org/10.1016/S1386-1425(01)00476-0.

(181) Grimm, J. B.; English, B. P.; Chen, J.; Slaughter, J. P.; Zhang, Z.; Revyakin, A.; Patel, R.; Macklin, J. J.; Normanno, D.; Singer, R. H.; Lionnet, T.; Lavis, L. D. A General Method to Improve Fluorophores for Live-Cell and Single-Molecule Microscopy. *Nat. Methods* **2015**, *12* (3), 244–250. https://doi.org/10.1038/nmeth.3256.

(182) Panchuk-Voloshina, N.; Haugland, R. P.; Bishop-Stewart, J.; Bhalgat, M. K.; Millard, P. J.; Mao, F.; Leung, W. Y.; Haugland, R. P. Alexa Dyes, a Series of New Fluorescent Dyes That Yield Exceptionally Bright, Photostable Conjugates. *J. Histochem. Cytochem.* **1999**, *47* (9), 1179–1188. https://doi.org/10.1177/002215549904700910.

(183) Mustroph, H. Cyanine Dyes. *Phys. Sci. Rev.* **2020**, *5* (5). https://doi.org/10.1515/psr-2019-0145.

(184) Mujumdar, R. B.; Ernst, L. A.; Mujumdar, S. R.; Lewis, C. J. Cyanine Dye Labeling Reagents: Sulfoindocyanine Succinimidyl Esters. *Bioconjug. Chem.* **1993**, *4* (2), 105–111. https://doi.org/10.1021/bc00020a001.

(185) Cooper, M.; Ebner, A.; Briggs, M.; Burrows, M.; Gardner, N.; Richardson, R.; West, R. Cy3B™: Improving the Performance of Cyanine Dyes. *J. Fluoresc.* **2004**, *14* (2), 145–150. https://doi.org/10.1023/B:JOFL.0000016286.62641.59.

(186) Shi, C.; Wu, J. B.; Pan, D. Review on Near-Infrared Heptamethine Cyanine Dyes as Theranostic Agents for Tumor Imaging, Targeting, and Photodynamic Therapy. *J. Biomed. Opt.* **2016**, *21* (5), 050901. https://doi.org/10.1117/1.jbo.21.5.050901.

(187) Eiring, P.; McLaughlin, R.; Matikonda, S. S.; Han, Z.; Grabenhorst, L.; Helmerich, D. A.; Meub, M.; Beliu, G.; Luciano, M.; Bandi, V.; Zijlstra, N.; Shi, Z.; Tarasov, S. G.; Swenson,

R.; Tinnefeld, P.; Glembockyte, V.; Cordes, T.; Sauer, M.; Schnermann, M. J. Targetable Conformationally Restricted Cyanines Enable Photon-Count-Limited Applications**. *Angew. Chem. Int. Ed.* **2021**, *133* (51), 26889–26897. https://doi.org/10.1002/ange.202109749.

(188) Liu, J.; Diwu, Z.; Leung, W. Y.; Lu, Y.; Patch, B.; Haugland, R. P. Rational Design and Synthesis of a Novel Class of Highly Fluorescent Rhodamine Dyes That Have Strong Absorption at Long Wavelengths. *Tetrahedron Lett.* **2003**, *44* (23), 4355–4359. https://doi.org/10.1016/S0040-4039(03)00938-9.

(189) Shen, Z.; Lu, Z.; Chhatbar, P. Y.; O'Herron, P.; Kara, P. An Artery-Specific Fluorescent Dye for Studying Neurovascular Coupling. *Nat. Methods* **2012**, *9* (3), 273–276. https://doi.org/10.1038/nmeth.1857.

(190) Velasco, M. G. M.; Allgeyer, E. S.; Yuan, P.; Grutzendler, J.; Bewersdorf, J. Absolute Two-Photon Excitation Spectra of Red and Far-Red Fluorescent Probes. *Opt. Lett.* **2015**, *40* (21), 4915. https://doi.org/10.1364/ol.40.004915.

(191) Bachman, J. L.; Pavlich, C. I.; Boley, A. J.; Marcotte, E. M.; Anslyn, E. V. Synthesis of Carboxy ATTO 647N Using Redox Cycling for Xanthone Access. *Org. Lett.* **2020**, *22* (2), 381–385. https://doi.org/10.1021/acs.orglett.9b03981.

(192) Fu, M.; Xiao, Y.; Qian, X.; Zhao, D.; Xu, Y. A Design Concept of Long-Wavelength Fluorescent Analogs of Rhodamine Dyes: Replacement of Oxygen with Silicon Atom. *Chem. Commun.* **2008**, No. 15, 1780–1782. https://doi.org/10.1039/b718544h.

(193) Koide, Y.; Urano, Y.; Hanaoka, K.; Terai, T.; Nagano, T. Evolution of Group 14 Rhodamines as Platforms for Near-Infrared Fluorescence Probes Utilizing Photoinduced Electron Transfer. *ACS Chem. Biol.* **2011**, *6* (6), 600–608. https://doi.org/10.1021/cb1002416.

(194) Buschmann, V.; Weston, K. D.; Sauer, M. Spectroscopic Study and Evaluation of Red-Absorbing Fluorescent Dyes. *Bioconjug. Chem.* **2003**, *14* (1), 195–204. https://doi.org/10.1021/bc025600x.

(195) Lukinavičius, G.; Reymond, L.; Umezawa, K.; Sallin, O.; D'Este, E.; Göttfert, F.; Ta, H.; Hell, S. W.; Urano, Y.; Johnsson, K. Fluorogenic Probes for Multicolor Imaging in Living Cells. *J. Am. Chem. Soc.* **2016**, *138* (30), 9365–9368. https://doi.org/10.1021/jacs.6b04782.

(196) Zhou, X.; Lai, R.; Beck, J. R.; Li, H.; Stains, C. I. Nebraska Red: A Phosphinate-Based near-Infrared Fluorophore Scaffold for Chemical Biology Applications. *Chem. Commun.* **2016**, *52* (83), 12290–12293. https://doi.org/10.1039/c6cc05717a.

(197) Grimm, J. B.; Tkachuk, A. N.; Xie, L.; Choi, H.; Mohar, B.; Falco, N.; Schaefer, K.; Patel, R.; Zheng, Q.; Liu, Z.; Lippincott-Schwartz, J.; Brown, T. A.; Lavis, L. D. A General Method to Optimize and Functionalize Red-Shifted Rhodamine Dyes. *Nat. Methods* **2020**, *17* (8), 815–821. https://doi.org/10.1038/s41592-020-0909-6.

(198) Xu, W.; Chan, K. M.; Kool, E. T. Fluorescent Nucleobases as Tools for Studying DNA and RNA. *Nat. Chem.* **2017**, *9* (11), 1043–1055. https://doi.org/10.1038/NCHEM.2859.

(199) Wilhelmsson, L. M.; Tor, Y. Fluorescent Analogs of Biomolecular Building Blocks: Design and Applications. *Fluoresc. Analog. Biomol. Build. Blocks Des. Appl.* **2016**, 1–418. https://doi.org/10.1002/9781119179320.

(200) Hawkins, M. E.; Pfleiderer, W.; Balis, F. M.; Porter, D.; Knutson, J. R. Fluorescence Properties of Pteridine Nucleoside Analogs as Monomers and Incorporated into Oligonucleotides. *Anal. Biochem.* **1997**, *244* (1), 86–95. https://doi.org/10.1006/abio.1996.9879.

(201) Hawkins, M. E.; Pfleiderer, W.; Jungmann, O.; Balis, F. M. Synthesis and Fluorescence Characterization of Pteridine Adenosine Nucleoside Analogs for DNA Incorporation. *Anal. Biochem.* **2001**, *298* (2), 231–240. https://doi.org/10.1006/abio.2001.5399.

(202) Hawkins, M. E. Fluorescent Pteridine Nucleoside Analogs: A Window on DNA Interactions. *Cell Biochem. Biophys.* **2001**, *34* (2), 257–281. https://doi.org/10.1385/CBB:34:2:257.

(203) Young, J. S.; Jin, H. R.; Byeang, H. K. Quencher-Free, End-Stacking Oligonucleotides for Probing Single-Base Mismatches in DNA. *Org. Lett.* **2005**, *7* (22), 4931–4933. https://doi.org/10.1021/OL0518582/SUPPL_FILE/OL0518582SI20050910_071640.PDF.

(204) Wagner, C.; Rist, M.; Mayer-Enthart, E.; Wagenknecht, H. A. 1-Ethynylpyrene-Modified Guanine and Cytosine as Optical Labels for DNA Hybridization. *Org. Biomol. Chem.* **2005**, *3* (11), 2062–2063. https://doi.org/10.1039/B504079E.

(205) Förster, U.; Lommel, K.; Sauter, D.; Grünewald, C.; Engels, J. W.; Wachtveitl, J. 2-(1-Ethynylpyrene)-Adenosine as a Folding Probe for RNA—Pyrene in or Out. *ChemBioChem* **2010**, *11* (5), 664–672. https://doi.org/10.1002/CBIC.200900778.

(206) Wierzchowski, J.; Wielgus-Kutrowska, B.; Shugar, D. Fluorescence Emission Properties of 8-Azapurines and Their Nucleosides, and Application to the Kinetics of the Reverse Synthetic Reaction of Purine Nucleoside Phosphorylase. *Biochim. Biophys. Acta - Gen. Subj.* **1996**, *1290* (1), 9–17. https://doi.org/10.1016/0304-4165(95)00181-6.

(207) Da Costa, C. P.; Fedor, M. J.; Scott, L. G. 8-Azaguanine Reporter of Purine Ionization States in Structured RNAs. *J. Am. Chem. Soc.* **2007**, *129* (11), 3426–3432. https://doi.org/10.1021/ja067699e.

(208) Tor, Y.; Del Valle, S.; Jaramillo, D.; Srivatsan, S. G.; Rios, A.; Weizman, H. Designing New Isomorphic Fluorescent Nucleobase Analogues: The Thieno[3,2-d]Pyrimidine Core. *Tetrahedron* **2007**, *63* (17), 3608–3614. https://doi.org/10.1016/j.tet.2007.01.075.

(209) Zhu, Z.; Shao, H.; Dong, X.; Li, N.; Ning, B. Y.; Ning, X. J.; Zhao, L.; Zhuang, J. Electronic Band Structure and Sub-Band-Gap Absorption of Nitrogen Hyperdoped Silicon. *Sci. Rep.* **2015**, *5* (1), 1–9. https://doi.org/10.1038/srep10513.

(210) Nadler, A.; Strohmeier, J.; Diederichsen, U. 8-Vinyl-2′-Deoxyguanosine as a Fluorescent 2′-Deoxyguanosine Mimic for Investigating DNA Hybridization and Topology. *Angew. Chem. Int. Ed.* **2011**, *50* (23), 5392–5396. https://doi.org/10.1002/anie.201100078.

(211) Leonard, N. J.; Sprecker, M. A.; Morrice, A. G. Defined Dimensional Changes in Enzyme Substrates and Cofactors. Synthesis of Lin-Benzoadenosine and Enzymic Evaluation of Derivatives of the Benzopurines. *J. Am. Chem. Soc.* **1976**, *98* (13), 3987–3994. https://doi.org/10.1021/ja00429a040.

(212) Hernández, A. R.; Kool, E. T. The Components of XRNA: Synthesis and Fluorescence of a Full Genetic Set of Size-Expanded Ribonucleosides. *Org. Lett.* **2011**, *13* (4), 676–679. https://doi.org/10.1021/ol102915f.

(213) Greco, N. J.; Tor, Y. Simple Fluorescent Pyrimidine Analogues Detect the Presence of DNA Abasic Sites. *J. Am. Chem. Soc.* **2005**, *127* (31), 10784–10785. https://doi.org/10.1021/ja052000a.

(214) Pesnot, T.; Wagner, G. K. Novel Derivatives of UDP-Glucose: Concise Synthesis and Fluorescent Properties. *Org. Biomol. Chem.* **2008**, *6* (16), 2884–2891. https://doi.org/10.1039/b805216f.

(215) Miyata, K.; Mineo, R.; Tamamushi, R.; Mizuta, M.; Ohkubo, A.; Taguchi, H.; Seio, K.;

Santa, T.; Sekine, M. Synthesis and Fluorescent Properties of Bi- and Tricyclic 4-N-Carbamoyldeoxycytidine Derivatives. *J. Org. Chem.* **2007**, *72* (1), 102–108. https://doi.org/10.1021/jo0617767.

(216) Korshun, V. A.; Prokhorenko, I. A.; Gontarev, S. V.; Skorobogatyi, M. V.; Balakin, K. V.; Manasova, E. V.; Malakhov, A. D.; Berlin, Y. A. New Pyrene Derivatives for Fluorescent Labeling of Oligonucleotides. *Nucleosides and Nucleotides* **1997**, *16* (7–9), 1461–1464. https://doi.org/10.1080/07328319708006206.

(217) Dodd, D. W.; Swanick, K. N.; Price, J. T.; Brazeau, A. L.; Ferguson, M. J.; Jones, N. D.; Hudson, R. H. E. Blue Fluorescent Deoxycytidine Analogues: Convergent Synthesis, Solid-State and Electronic Structure, and Solvatochromism. *Org. Biomol. Chem.* **2010**, *8* (3), 663–666. https://doi.org/10.1039/B919921G.

(218) Godde, F.; Toulmé, J. J.; Moreau, S. Benzoquinazoline Derivatives as Substitutes for Thymine in Nucleic Acid Complexes. Use of Fluorescence Emission of Benzo[g]Quinazoline-2,4-(1H, 3H)- Dione in Probing Duplex and Triplex Formation. *Biochemistry* **1998**, *37* (39), 13765–13775. https://doi.org/10.1021/bi9811967.

(219) Schmidt, O. P.; Mata, G.; Luedtke, N. W. Fluorescent Base Analogue Reveals T-HgII-T Base Pairs Have High Kinetic Stabilities That Perturb DNA Metabolism. *J. Am. Chem. Soc.* **2016**, *138* (44), 14733–14739. https://doi.org/10.1021/jacs.6b09044.

(220) Ren, R. X. F.; Chaudhuri, N. C.; Paris, P. L.; Rumney IV, S.; Kool, E. T. Naphthalene, Phenanthrene, and Pyrene as DNA Base Analogues: Synthesis, Structure, and Fluorescence in DNA. *J. Am. Chem. Soc.* **1996**, *118* (33), 7671–7678. https://doi.org/10.1021/ja9612763.

(221) Kool, E. T. Replacing the Nucleobases in DNA with Designer Molecules. *Acc. Chem. Res.* **2002**, *35* (11), 936–943. https://doi.org/10.1021/ar000183u.

(222) Spadafora, M.; Mehiri, M.; Burger, A.; Benhida, R. Friedel-Crafts and Modified Vorbrüggen Ribosylation. A Short Synthesis of Aryl and Heteroaryl-C-Nucleosides. *Tetrahedron Lett.* **2008**, *49* (25), 3967–3971. https://doi.org/10.1016/j.tetlet.2008.04.105.

(223) Sun, L.; Wang, M.; Kool, E. T.; Taylor, J. S. Pyrene Nucleotide as a Mechanistic Probe: Evidence for a Transient Abasic Site-like Intermediate in the Bypass of Dipyrimidine Photoproducts by T7 DNA Polymerase. *Biochemistry* **2000**, *39* (47), 14603–14610. https://doi.org/10.1021/bi001446v.

(224) Dai, N.; Kool, E. T. Fluorescent DNA-Based Enzyme Sensors. *Chem. Soc. Rev.* **2011**, *40* (12), 5756–5770. https://doi.org/10.1039/c0cs00162g.

(225) Wojciechowski, F.; Lietard, J.; Leumann, C. J. 2-Pyrenyl-DNA: Synthesis, Pairing, and Fluorescence Properties. *Org. Lett.* **2012**, *14* (20), 5176–5179. https://doi.org/10.1021/ol302150a.

(226) Grigorenko, N. A.; Leumann, C. J. 2-Phenanthrenyl-DNA: Synthesis, Pairing, and Fluorescence Properties. *Chem. - Eur. J.* **2009**, *15* (3), 639–645. https://doi.org/10.1002/chem.200801135.

(227) Chan, K. M.; Kölmel, D. K.; Wang, S.; Kool, E. T. Color-Change Photoswitching of an Alkynylpyrene Excimer Dye. *Angew. Chem. Int. Ed.* **2017**, *56* (23), 6497–6501. https://doi.org/10.1002/anie.201701235.

(228) Coleman, R. S.; Madaras, M. L. Synthesis of a Novel Coumarin C-Riboside as a Photophysical Probe of Oligonucleotide Dynamics. *J. Org. Chem.* **1998**, *63* (16), 5700–5703. https://doi.org/10.1021/jo980478+.

(229) Okamoto, A.; Tainaka, K.; Fujiwara, Y. Nile Red Nucleoside: Design of a

Solvatofluorochromic Nucleoside as an Indicator of Micropolarity around DNA. *J. Org. Chem.* **2006**, *71* (9), 3592–3598. https://doi.org/10.1021/jo060168o.

(230) Morales-Rojas, H.; Kool, E. T. A Porphyrin C-Nucleoside Incorporated into DNA. *Org. Lett.* **2002**, *4* (25), 4377–4380. https://doi.org/10.1021/ol0267376.

(231) Gao, J.; Strässler, C.; Tahmassebi, D.; Kool, E. T. Libraries of Composite Polyfluors Built from Fluorescent Deoxyribosides. *J. Am. Chem. Soc.* **2002**, *124* (39), 11590–11591. https://doi.org/10.1021/JA027197A/SUPPL_FILE/JA027197A_S1.PDF.

(232) Cho, Y.; Kool, E. T. Enzymatic Synthesis of Fluorescent Oligomers Assembled on a DNA Backbone. *ChemBioChem* **2006**, *7* (4), 669–672. https://doi.org/10.1002/cbic.200500515.

(233) Matray, T. J.; Kool, E. T. Selective and Stable DNA Base Pairing without Hydrogen Bonds. *J. Am. Chem. Soc.* **1998**, *120* (24), 6191–6192. https://doi.org/10.1021/ja9803310.

(234) Seyfried, P.; Eiden, L.; Grebenovsky, N.; Mayer, G.; Heckel, A. Photo-Tethers for the (Multi-)Cyclic, Conformational Caging of Long Oligonucleotides. *Angew. Chem. Int. Ed.* **2017**, *56* (1), 359–363. https://doi.org/10.1002/anie.201610025.

(235) Luo, D.; Kuang, C.; Liu, X.; Wang, G. Experimental Investigations on Fluorescence Excitation and Depletion of ATTO 390 Dye. *Opt. Laser Technol.* **2013**, *45* (1), 723–725. https://doi.org/10.1016/j.optlastec.2012.05.003.

(236) ATTO-TEC GmbH - ATTO 390 https://www.atto-tec.com/product_info.php?info=p1_atto-390.html (accessed Feb 10, 2022).

(237) Herring, B. E.; Nicoll, R. A. Long-Term Potentiation: From CaMKII to AMPA Receptor Trafficking. *Annu. Rev. Physiol.* **2016**, *78*, 351–365. https://doi.org/10.1146/annurev-physiol-021014-071753.

(238) Dieterich, D. C.; Kreutz, M. R. Proteomics of the Synapse - A Quantitative Approach to Neuronal Plasticity. *Mol. Cell. Proteomics* **2016**, *15* (2), 368–381. https://doi.org/10.1074/mcp.R115.051482.

(239) Eritja, R. Solid-Phase Synthesis of Modified Oligonucleotides. *Int. J. Pept. Res. Ther.* **2007**, *13* (1–2), 53–68. https://doi.org/10.1007/s10989-006-9053-0.

(240) Itakura, K.; Rossi, J. J.; Wallace, R. B. Synthesis and Use of Synthetic Oligonucleotides. *Annu. Rev. Biochem.* **1984**, *53*, 323–356. https://doi.org/10.1146/annurev.bi.53.070184.001543.

(241) Cajigas, I. J.; Tushev, G.; Will, T. J.; Tom Dieck, S.; Fuerst, N.; Schuman, E. M. The Local Transcriptome in the Synaptic Neuropil Revealed by Deep Sequencing and High-Resolution Imaging. *Neuron* **2012**, *74* (3), 453–466. https://doi.org/10.1016/j.neuron.2012.02.036.

(242) Muddashetty, R. S.; Nalavadi, V. C.; Gross, C.; Yao, X.; Xing, L.; Laur, O.; Warren, S. T.; Bassell, G. J. Reversible Inhibition of PSD-95 MRNA Translation by MiR-125a, FMRP Phosphorylation, and MGluR Signaling. *Mol. Cell* **2011**, *42* (5), 673–688. https://doi.org/10.1016/J.MOLCEL.2011.05.006/ATTACHMENT/D93158D5-7A1F-421A-ACD5-F034CC7FDD0F/MMC1.PDF.

(243) Buxbaum, A. R.; Wu, B.; Singer, R. H. Single β-Actin MRNA Detection in Neurons Reveals a Mechanism for Regulating Its Translatability. *Science.* **2014**, *343* (6169), 419–422. https://doi.org/10.1126/SCIENCE.1242939/SUPPL_FILE/BUXBAUM.SM.PDF.

(244) Yoon, Y. J.; Wu, B.; Buxbaum, A. R.; Das, S.; Tsai, A.; English, B. P.; Grimm, J. B.;

Lavis, L. D.; Singer, R. H. Glutamate-Induced RNA Localization and Translation in Neurons. *Proc. Natl. Acad. Sci. U. S. A.* **2016**, *113* (44), E6877–E6886. https://doi.org/10.1073/PNAS.1614267113/SUPPL_FILE/PNAS.1614267113.SM09.AVI.

(245) Aakalu, G.; Smith, W. B.; Nguyen, N.; Jiang, C.; Schuman, E. M. Dynamic Visualization of Local Protein Synthesis in Hippocampal Neurons. *Neuron* **2001**, *30* (2), 489–502. https://doi.org/10.1016/S0896-6273(01)00295-1.

(246) Azzam, M. E.; Algranati, I. D. Mechanism of Puromycin Action: Fate of Ribosomes after Release of Nascent Protein Chains from Polysomes. *Proc. Natl. Acad. Sci. U. S. A.* **1973**, *70* (12 (II)), 3866–3869. https://doi.org/10.1073/pnas.70.12.3866.

(247) Graber, T. E.; Hébert-Seropian, S.; Khoutorsky, A.; David, A.; Yewdell, J. W.; Lacaille, J. C.; Sossin, W. S. Reactivation of Stalled Polyribosomes in Synaptic Plasticity. *Proc. Natl. Acad. Sci. U. S. A.* **2013**, *110* (40), 16205–16210. https://doi.org/10.1073/pnas.1307747110.

(248) Doyle, M.; Kiebler, M. A. Mechanisms of Dendritic MRNA Transport and Its Role in Synaptic Tagging. *EMBO J.* **2011**, *30* (17), 3540–3552. https://doi.org/10.1038/emboj.2011.278.

(249) Sutton, M. A.; Schuman, E. M. Dendritic Protein Synthesis, Synaptic Plasticity, and Memory. *Cell* **2006**, *127* (1), 49–58. https://doi.org/10.1016/j.cell.2006.09.014.

(250) Hafner, A. S.; Penn, A. C.; Grillo-Bosch, D.; Retailleau, N.; Poujol, C.; Philippat, A.; Coussen, F.; Sainlos, M.; Opazo, P.; Choquet, D. Lengthening of the Stargazin Cytoplasmic Tail Increases Synaptic Transmission by Promoting Interaction to Deeper Domains of PSD-95. *Neuron* **2015**, *86* (2), 475–489. https://doi.org/10.1016/j.neuron.2015.03.013.

(251) Ramiro-Cortés, Y.; Israely, I. Long Lasting Protein Synthesis- and Activity-Dependent Spine Shrinkage and Elimination after Synaptic Depression. *PLoS One* **2013**, *8* (8), e71155. https://doi.org/10.1371/journal.pone.0071155.

(252) Klimek, R.; Donlin-Asp, P. G.; Polisseni, C.; Hanff, V.; Schuman, E. M.; Heckel, A. Visible Light-Activatable Q-Dye Molecular Beacons for Long-Term MRNA Monitoring in Neurons. *Chem. Commun.* **2021**, *57* (94), 12683–12686. https://doi.org/10.1039/d1cc05664f.

(253) Hanff, V. Synthese Eines Lichtaktivierbaren Molecular Beacons Zur Zeitaufgelösten MRNA-Lokalisation in Neuronen, Goethe University Frankfurt am Main, 2019.

(254) Demchenko, A. P. Photobleaching of Organic Fluorophores: Quantitative Characterization, Mechanisms, Protection*. *Methods Appl. Fluoresc.* **2020**, *8* (2), 022001. https://doi.org/10.1088/2050-6120/AB7365.

(255) Weyel, X. M. M.; Fichte, M. A. H.; Heckel, A. A Two-Photon-Photocleavable Linker for Triggering Light-Induced Strand Breaks in Oligonucleotides. *ACS Chem. Biol.* **2017**, *12* (8), 2183–2190. https://doi.org/10.1021/acschembio.7b00367.

(256) Weinrich, T.; Gränz, M.; Grünewald, C.; Prisner, T. F.; Göbel, M. W. Synthesis of a Cytidine Phosphoramidite with Protected Nitroxide Spin Label for EPR Experiments with RNA. *Eur. J. Org. Chem.* **2017**, *2017* (3), 491–496. https://doi.org/10.1002/ejoc.201601174.

(257) Ding, R.; He, Y.; Wang, X.; Xu, J.; Chen, Y.; Feng, M.; Qi, C. Treatment of Alcohols with Tosyl Chloride Does Not Always Lead to the Formation of Tosylates. *Molecules* **2011**, *16* (7), 5665–5673. https://doi.org/10.3390/molecules16075665.

(258) Lennox, K. A.; Behlke, M. A. A Direct Comparison of Anti-MicroRNA Oligonucleotide

Potency. *Pharm. Res.* **2010**, *27* (9), 1788–1799. https://doi.org/10.1007/s11095-010-0156-0.

(259) Zamaratski, E.; Pradeepkumar, P. I.; Chattopadhyaya, J. A Critical Survey of the Structure-Function of the Antisense Oligo/RNA Heteroduplex as Substrate for RNase H. *J. Biochem. Biophys. Methods* **2001**, *48* (3), 189–208. https://doi.org/10.1016/S0165-022X(01)00149-X.

(260) Khvorova, A.; Watts, J. K. The Chemical Evolution of Oligonucleotide Therapies of Clinical Utility. *Nature Biotechnology*. Nature Publishing Group March 1, 2017, pp 238–248. https://doi.org/10.1038/nbt.3765.

(261) Majlessi, M.; Nelson, N. C.; Becker, M. M. Advantages of 2'-O-Methyl Oligoribonucleotide Probes for Detecting RNA Targets. *Nucleic Acids Res.* **1998**, *26* (9), 2224–2229. https://doi.org/10.1093/nar/26.9.2224.

(262) Zheng, J.; Yang, R.; Shi, M.; Wu, C.; Fang, X.; Li, Y.; Li, J.; Tan, W. Rationally Designed Molecular Beacons for Bioanalytical and Biomedical Applications. *Chem. Soc. Rev.* **2015**, *44* (10), 3036–3055. https://doi.org/10.1039/c5cs00020c.

(263) Tsourkas, A.; Behlke, M. A.; Rose, S. D.; Bao, G. Hybridization Kinetics and Thermodynamics of Molecular Beacons. *Nucleic Acids Research*. February 15, 2003, pp 1319–1330. https://doi.org/10.1093/nar/gkg212.

(264) Zuker, M.; Markham, N. The Mfold Web Server | mfold.rit.albany.edu http://unafold.rna.albany.edu/?q=mfold (accessed Feb 10, 2020).

(265) Tushev, G.; Glock, C.; Heumüller, M.; Biever, A.; Jovanovic, M.; Schuman, E. M. Alternative 3′ UTRs Modify the Localization, Regulatory Potential, Stability, and Plasticity of MRNAs in Neuronal Compartments. *Neuron* **2018**, *98* (3), 495-511.e6. https://doi.org/10.1016/j.neuron.2018.03.030.

(266) Klimek, R.; Wang, M.; McKenney, V. R.; Schuman, E. M.; Heckel, A. Photo-Tethered Molecular Beacons for Superior Light-Induction. *Chem. Commun.* **2021**, *57* (5), 615–618. https://doi.org/10.1039/d0cc06704k.

(267) McKenney, V. R. Polyzyklische Lichtaktivierbare Molecular Beacons, Goethe University Frankfurt am Main, 2020.

(268) Sinha, R. P.; Häder, D. P. UV-Induced DNA Damage and Repair: A Review. *Photochem. Photobiol. Sci.* **2002**, *1* (4), 225–236. https://doi.org/10.1039/b201230h.

(269) Müller, P.; Seyfried, P.; Frühauf, A.; Heckel, A. Phosphodiester Photo-Tethers for the (Multi-)Cyclic Conformational Caging of Oligonucleotides. In *Methods in Enzymology*; Academic Press Inc., 2019; Vol. 624, pp 89–111. https://doi.org/10.1016/bs.mie.2019.04.019.

(270) Klimek, R.; Asido, M.; Hermanns, V.; Junek, S.; Wachtveitl, J.; Heckel, A. Inactivation of Competitive Decay Channels Leads to Enhanced Coumarin Photochemistry. *Chem. – A Eur. J.* **2022**, e202200647. https://doi.org/10.1002/chem.202200647.

(271) Salustros, M. Verwendung Verschiedener ATTO 390-Derivate Als Photolabile Schutzgruppen, Goethe University Frankfurt am Main, 2020.

(272) Jones, G.; Jackson, W. R.; Choi, C. Y.; Bergmark, W. R. Solvent Effects on Emission Yield and Lifetime for Coumarin Laser Dyes. Requirements for a Rotatory Decay Mechanism. *J. Phys. Chem.* **1985**, *89* (2), 294–300. https://doi.org/10.1021/j100248a024.

(273) Liu, Y.; Ding, J.; Liu, R.; Shi, D.; Sun, J. Revisiting the Electronic Excited-State Hydrogen Bonding Dynamics of Coumarin Chromophore in Alcohols: Undoubtedly Strengthened

Not Cleaved. *J. Photochem. Photobiol. A Chem.* **2009**, *201* (2–3), 203–207. https://doi.org/10.1016/j.jphotochem.2008.10.016.

(274) Wells, N. P.; McGrath, M. J.; Siepmann, J. I.; Underwood, D. F.; Blank, D. A. Excited State Hydrogen Bond Dynamics: Coumarin 102 in Acetonitrile-Water Binary Mixtures. *J. Phys. Chem. A* **2008**, *112* (12), 2511–2514. https://doi.org/10.1021/jp710889t.

(275) Zhou, P.; Song, P.; Liu, J.; Han, K.; He, G. Experimental and Theoretical Study of the Rotational Reorientation Dynamics of 7-Animocoumarin Derivatives in Polar Solvents: Hydrogen-Bonding Effects. *Phys. Chem. Chem. Phys.* **2009**, *11* (41), 9440–9449. https://doi.org/10.1039/b910043a.

(276) López Arbeloa, T.; López Arbeloa, F.; Tapia Estévez, M. J.; López Arbeloa, I. Binary Solvent Effects on the Absorption and Emission of 7-Aminocoumarins. *J. Lumin.* **1994**, *59* (6), 369–375. https://doi.org/10.1016/0022-2313(94)90064-7.

(277) Carhart-Harris, R. L.; Nutt, D. J. Serotonin and Brain Function: A Tale of Two Receptors. *Journal of Psychopharmacology*. SAGE Publications Ltd September 1, 2017, pp 1091–1120. https://doi.org/10.1177/0269881117725915.

(278) Reinfelds, M.; Hermanns, V.; Halbritter, T.; Wachtveitl, J.; Braun, M.; Slanina, T.; Heckel, A. A Robust, Broadly Absorbing Fulgide Derivative as a Universal Chemical Actinometer for the UV to NIR Region. *ChemPhotoChem* **2019**, *3* (6), 441–449. https://doi.org/10.1002/cptc.201900010.

7. Table of Figures

8. References

Reference [I]: „Differential regulation of local mRNA dynamics and translation following long-term potentiation and depression”

Donlin-Asp, P. G.; Polisseni, C.; Klimek, R.; Heckel, A.; Schuman, E. M., Proc. Natl. Acad. Sci. U. S. A. **2021**, *118* (13), 2017578118.

Author contributions:

Paul G. Donlin-Asp:

- transfected nuclease-resistant molecular beacons in neurons
- imaged mRNA-MB hybrids
- analyzed puncta for mRNA monitoring
- performed synaptic plasticity experiments
- wrote and edited the manuscript

Claudio Polisseni:

- developed analysis tool pipeline
- designed cell experiments
- edited the manuscript

Robin Klimek:

- designed and synthesized nuclease-resistant molecular beacons
- prepared oligonucleotides for cell use
- performed fluorescence characterization of molecular beacons *in vitro*
- edited the manuscript

Erin M. Schuman:

- supervised project and experiments
- edited the manuscript

Alexander Heckel:

- supervised project and experiments
- edited the manuscript

Differential regulation of local mRNA dynamics and translation following long-term potentiation and depression

Paul G. Donlin-Asp[a], Claudio Polisseni[a], Robin Klimek[b], Alexander Heckel[b], and Erin M. Schuman[a,1]

[a]Department of Synaptic Plasticity, Max Planck Institute for Brain Research, 60438 Frankfurt, Germany; and [b]Institute for Organic Chemistry and Chemical Biology, Goethe-University Frankfurt, 60438 Frankfurt, Germany

This contribution is part of the special series of Inaugural Articles by members of the National Academy of Sciences elected in 2020.

Contributed by Erin M. Schuman, January 29, 2021 (sent for review August 19, 2020; reviewed by Simon L. Bullock and Robert H. Singer)

Decades of work have demonstrated that messenger RNAs (mRNAs) are localized and translated within neuronal dendrites and axons to provide proteins for remodeling and maintaining growth cones or synapses. It remains unknown, however, whether specific forms of plasticity differentially regulate the dynamics and translation of individual mRNA species. To address this, we targeted three individual synaptically localized mRNAs, *CamkIIa*, *β-actin*, *Psd95*, and used molecular beacons to track endogenous mRNA movements. We used reporters and CRISPR/Cas9 gene editing to track mRNA translation in cultured neurons. We found alterations in mRNA dynamic properties occurred during two forms of synaptic plasticity, long-term potentiation (cLTP) and depression (mGluR-LTD). Changes in mRNA dynamics following either form of plasticity resulted in an enrichment of mRNA in the vicinity of dendritic spines. Both the reporters and tagging of endogenous proteins revealed the transcript-specific stimulation of protein synthesis following cLTP or mGluR-LTD. As such, the plasticity-induced enrichment of mRNA near synapses could be uncoupled from its translational status. The enrichment of mRNA in the proximity of spines allows for localized signaling pathways to decode plasticity milieus and stimulate a specific translational profile, resulting in a customized remodeling of the synaptic proteome.

mRNA | local protein synthesis | mRNA beacons | mRNA localization | neuron protein synthesis

Synaptic plasticity requires the rapid and robust remodeling of the proteome (1). Both the strengthening (long-term potentiation, LTP) and the weakening of synaptic connections (long-term depression, LTD) requires proteome remodeling (2). Neurons use diverse mechanisms to achieve this regulation, including the posttranslational modifications of proteins (2), transcriptional changes (3), and translational changes (4). Indeed, neurons can rapidly regulate and control synaptic proteomes by localizing and translating messenger RNAs (mRNAs) in axons and dendrites (5–12). A number of key synaptic proteins are encoded by translationally regulated mRNAs, including ARC (13–15), fragile X mental retardation protein (FMRP) (16), postsynaptic density 95 (PSD-95) (16, 17), and CAMK2a (18). Given the capacity for protein synthesis in distal compartments, a fundamental question is how dendritically and axonally localized mRNAs become recruited near synapses and then translationally regulated locally during plasticity.

Current evidence suggests that single mRNAs, bound by RNA-binding proteins (RBPs), interact with the cytoskeleton for long-distance transport from the cell body to the dendrites and axons (19, 20). Both localization (19) and translational regulatory elements (21) are present in the 5′ and 3′ untranslated regions (UTRs) of mRNAs. Trans-acting factors, including RBPs and microRNAs (miRNAs), interact with UTR elements to regulate mRNA localization and translation; these interactions are also regulated by plasticity. mRNAs are believed to be transported in a translationally quiescent state, likely only engaged in translation near synapses (22, 23). The dynamic and bidirectional (22, 24–26) scanning behavior of mRNAs in dendrites allows, in principle, for the capture and translation of mRNAs as needed for proteome maintenance and remodeling (22, 23). Our understanding of these processes, however, is largely derived from live imaging experiments for a limited number of individual candidate mRNAs including *β-actin* (22, 25) and *Arc* (27); the relationship between the sequestration/capture of RNAs and their translation during plasticity is not well understood.

To address this, we used molecular beacons to track and quantify the dynamics of three endogenous mRNAs under basal conditions and after plasticity. We found that induction of either chemically induced LTP (cLTP) or metabotropic glutamate receptor LTD (mGluR-LTD) resulted in a widespread attenuation of mRNA motility and led to an enrichment of mRNA near dendritic spines. These altered mRNA dynamics and availability near synapses was accompanied for some, but not all, mRNAs by enhanced translation of either a reporter or a CRISPR/Cas9-tagged endogenous protein. This dissociation allows for the

Significance

Local protein synthesis is important for neuronal function and synaptic plasticity. Thousands of mRNAs are found in axons and dendrites, and it is believed that regulating their dynamic transport and distribution is a key determinant of where and when proteins are made. In this work we quantitatively assessed the dynamic transport of three synaptically localized mRNAs in live cultured neurons without exogenous stimulation and following induction of two distinct forms of synaptic plasticity. Coupling observations of mRNA dynamics with live imaging of endogenous protein synthesis dynamics, we found that alterations in mRNA movements occur independently of their translational state, indicating a multistep mechanism of capture and decoding of an mRNA to determine when translation occurs.

Author contributions: P.G.D.-A., C.P., R.K., A.H., and E.M.S. designed research; P.G.D.-A., C.P., and R.K. performed research; P.G.D.-A. and C.P. analyzed data; P.G.D.-A. and E.M.S. wrote the paper; and A.H. and E.M.S. supervised the project.

Reviewers: S.L.B., Medical Research Council Laboratory of Molecular Biology; and R.H.S., Albert Einstein College of Medicine.

The authors declare no competing interest.

See QnAs, e2103717118, in vol. 118, issue 13.

[1]To whom correspondence may be addressed. Email: erin.schuman@brain.mpg.de.

This article contains supporting information online at https://www.pnas.org/lookup/suppl/doi:10.1073/pnas.2017578118/-/DCSupplemental.

Published March 26, 2021.

enrichment of mRNAs near spines where localized signaling pathways can control which specific sets of transcripts are translated.

Results

Tracking Endogenous mRNA Dynamics in Live Neurons. To assess endogenous mRNA dynamics, we focused on *Camk2a*, *β-actin*, and *Psd95* as they are abundant in neuronal dendrites (28) and are translationally regulated by plasticity (18, 22, 29, 30). To track these mRNAs, we employed molecular beacons (Fig. 1*A*) (31). These mRNA-specific complementary oligonucleotides bear both a fluorophore and a quencher; the binding of a beacon to its targeted mRNA separates the fluorophore and quencher, resulting in a fluorescent signal that can be tracked in live cells. Similar probes have recently been used to track endogenous *β-actin* in *Xenopus* axons (32), yielding dynamic properties similar to those observed in vivo using the MS2–*β-actin* mouse (25).

In living primary rat hippocampal neuronal cultures (day in vitro [DIV] 21+) molecular beacons targeting endogenous *Camk2a*, *β-actin*, or *Psd95* mRNA (*Materials and Methods*) were imaged to report on endogenous mRNA dynamics for up to 20 min (Movies S1–S3). A nontargeting GFP probe showed no specific signal in the soma or dendrites (Movie S4). Interestingly, we observed a heterogenous size distribution for the mRNA puncta, with larger pronounced particles seen near the soma (Movies S1–S3), similar to what has been reported previously for *β-actin* (25). In addition, we detected a number of apparent dendritic mRNA–mRNA fusion events (*SI Appendix*, Fig. S1*A* and Movie S5), suggesting that these mRNAs can exist in a heterogenous copy number state, in addition to proposed modes

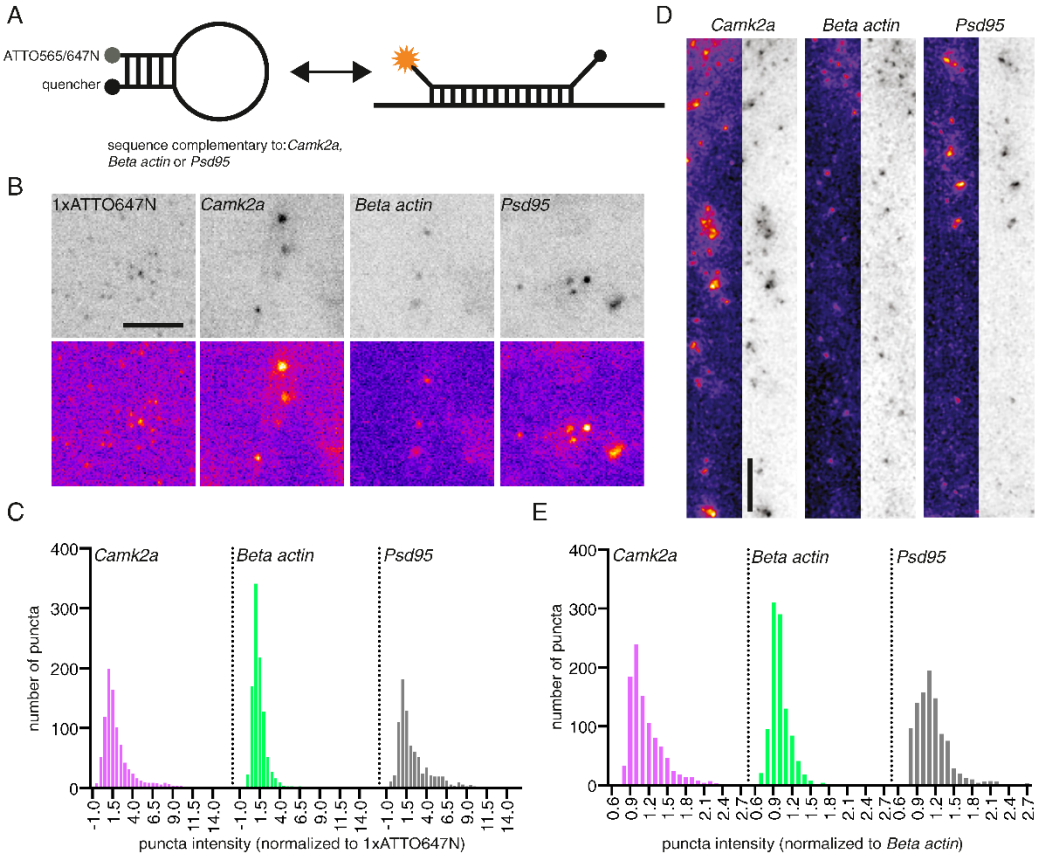

Fig. 1. Dendritic mRNAs exist within varied copy number states. (*A*) Scheme of the molecular beacon design used in this study. A 5-nt stem, with a reporter fluorophore on one side and a quencher dye on the other side, were linked with a 26-nt complementary sequence to *Camk2a*, *β-actin*, or *Psd95* mRNAs. When not hybridized to a target mRNA, the stem holds the reporter and quencher in proximity, preventing fluorescence. Upon binding to a target mRNA, the stem loop opens, and fluorescence can be detected in a reversible manner. (*B*) Example images of Gatta quant standard and beacon-labeled neurons shows a heterogenous distribution of particle intensities in live neurons. (Scale bar, 5 μm.) Data shown acquired at 5% laser power. (*C*) Quantification of the distribution of beacon intensity relative to single fluor labeled ATTO647 standard. Atto647N *Camk2a* (19 cells, 921 mRNA granules), Atto647N *β-actin* (21 cells, 1,003 mRNA granules), Atto647N *Psd95* (18 cells, 829 mRNA granules). (*D*) Example smFISH images of dendritically localized *β-actin*, *Camk2a*, and *Psd95*. (Scale bar, 5 μm.) (*E*) Quantification of the distribution of smFISH intensity. *Camk2a* (15 cells, 1,005 mRNA granules), *β-actin* (15 cells, 1,005 mRNA granules), *Psd95* (15 cells, 1,005 mRNA granules).

of single mRNA transport in axons and dendrites (29, 32, 33). To assess this quantitatively, we analyzed the intensity of the individual beacon puncta (i.e., mRNA granules) and compared it with a commercially synthesized standard containing a single ATTO647N fluorophore anchored on a glass coverslip (*Materials and Methods*). Using this standard, we determined that a sizeable fraction of each mRNA exhibited an intensity consistent with a single mRNA molecule (Fig. 1 *B* and *C* and *SI Appendix*, Fig. S1 *A–C*). *β-Actin* mRNAs, in particular, were often detected in a range consistent with a single copy number state (Fig. 1*C* and *SI Appendix*, Fig. S1 *A–C*), in line with previous reports (29, 32). Interestingly, while both *Camk2a* and *Psd95* mRNAs also were detected as single copy granules, a noticeable fraction of each population existed in a multimeric state (Fig. 1*C* and *SI Appendix*, Fig. S1 *A–C*), indicating that higher-order (containing more than a single mRNA) mRNA granules exist within the dendrite. To validate this, we performed single molecule FISH (smFISH) (*Materials and Methods*). Assessing the intensity of RNA puncta in the dendrite, we found a wider range of intensities for *Camk2a* and *Psd95* compared with *β-actin*, consistent with a multimeric copy number state (Fig. 1 *D* and *E* and *SI Appendix*, Fig. S1*D*). Taken together, these data suggest that while the majority of these dendritically localized mRNAs exists in a single copy number state, higher-order multimeric states exist and may be a transcript-specific feature, likely determined through specific sets of RBPs bound to particular mRNAs.

To capture the dynamic behavior of each mRNA species within dendrites, we employed a semiautomated tracking approach. Using a custom-written analysis pipeline (*Materials and Methods*) we quantified the beacon mRNA dynamics (Fig. 2 *A–C*), cumulative distance traveled (Fig. 2*D*), and transport velocity (Fig. 2*E*) for all three mRNA targets. To assess mRNA dynamics, we measured the percentage of time (during the entire imaging epoch) a detected granule spent actively moving within the dendrite (either anterogradely: away from the cell body; or retrogradely: toward the cell body) or exhibited a confined behavior. For all experiments we acquired images at one frame per second for up to 20 min (*Materials and Methods*). "Confined" behavior was assigned to periods of time when an mRNA granule exhibited restricted (<0.5 μm) movement within the dendrite (*Materials and Methods*).

Similar to previous reports (22, 32), we found that all three mRNAs spent most of their time in a confined state (fraction population; *Camk2a*: 0.59 ± 0.10; *β-actin*: 0.56 ± 0.11; *Psd95*: 0.50 ± 0.14; mean fraction of time ± SEM). For active movement all three mRNAs displayed a slight bias for anterograde transport (fraction population, anterograde vs. retrograde: *Camk2a*: 0.23 ± 0.06 vs. 0.18 ± 0.07; *β-actin*: 0.23 ± 0.09 vs. 0.22 ± 0.06; *Psd95*: 0.31 ± 0.11 vs. 0.20 ± 0.09) (Fig. 2*A*), explaining how mRNAs can eventually populate more distal regions of the dendrite. Interestingly, *Psd95* granules exhibited enhanced motility (less in the confined state) (Fig. 2*C*) compared with *β-actin* and *Camk2α*. All three mRNAs traveled similar distances (~20 μm on average) over the imaging epoch and exhibited similar velocities (~1 μm/s) for both anterograde and retrograde transport, consistent with the mixed polarity of microtubules within the dendrite (34). We noted that while the majority of mRNA molecules we measured (orange and magenta highlighted puncta in Fig. 2 *A* and *B*) alternated between periods of confined vs. active transport, a small fraction of particles (green in Fig. 2 *A* and *B*) showed little to no active transport during the entire imaging session. We therefore further distinguished "confined" vs. truly "stationary" events (*Materials and Methods* and *SI Appendix*, Fig. S2*A*) and found ~6% of the confined population were better characterized as stationary events. In all subsequent analyses, we removed these stationary events from the analysis.

Translational Inhibition Alters mRNA Dynamics within the Dendrite. With the above measurements of basal mRNAs dynamics, we next assessed if we could alter their dynamic properties. We first assessed if perturbing the translational status of an mRNA could affect its motility. To alter the translation status of an mRNA, we used two mechanistically distinct translational elongation inhibitors (Fig. 3*A*): puromycin, which causes release of the nascent peptide chain and ribosomal dissociation from the mRNA (35), and anisomycin, which freezes elongating ribosomes on mRNAs

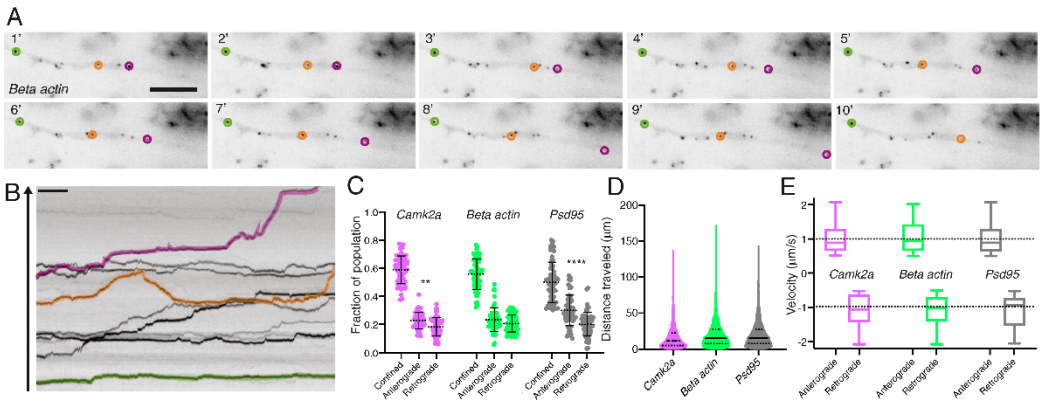

Fig. 2. Tracking and classifying mRNA dynamics along dendrites in live neurons. (*A*) Still images from a *β-actin* Atto647N-labeled dendrite (Movie S6), shown are single frames every minute for 10 min (of 20 total). Individual mRNA puncta are highlighted to illustrate distinct dynamic profiles, mainly stationary (green) or confined with periods of motility (orange and magenta). (Scale bar, 5 μm.) (*B*) Kymograph from the first 10 min of (Movie S6). Arrow denotes the anterograde direction along the dendrite. (Scale bar, 1 min.) (*C*) Quantification of mRNA dynamic state: confined, anterograde vs. retrograde for Atto565 *Camk2a*, Atto565 *β-actin*, and Atto565 *Psd95*. $n = 59$ cells. $^{**}P < 0.01$, $^{****}P < 0.0001$ Holm–Sidak's multiple comparison test. (*D*) Quantification of cumulative distance traveled for Atto565 *Camk2a*, Atto565 *β-actin*, and Atto565 *Psd95*. $n = 59$ cells. (*E*) Quantification of mRNA velocity for anterograde and retrograde for Atto565 *Camk2a* (1.013 ± 0.450; −1.083 ± 0.480), Atto565 *β-actin* (1.054 ± 0.493; −1.110 ± 0.452), and Atto565 *Psd95* (0.997 ± 0.426; −1.111 ± 0.479). $n = 59$ cells.

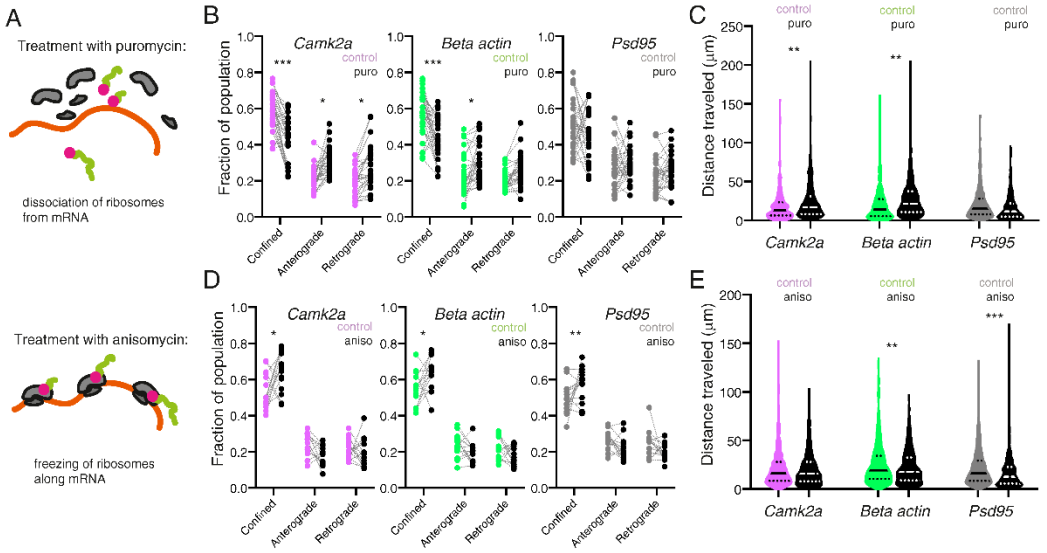

Fig. 3. Manipulating ribosome association of mRNAs results in transcript-specific alterations in mRNA dynamics. (*A*) Schematic representation of the effects of puromycin (*Upper*) or anisomycin (*Lower*) on ribosomal association with mRNA. Puromycin results in ribosomal subunit disassembly, whereas anisomycin results in stalling of elongating ribosomes. (*B*) Quantification of mRNA dynamic state: confined, anterograde vs. retrograde for Atto647N *Camk2a*, Atto647N *β-actin*, and Atto647N *Psd95* for control vs. puro treated samples. $n = 29$ cells per condition. $^{*}P < 0.05$; $^{***}P < 0.001$. Paired *t* test. (*C*) Quantification of cumulative distance traveled for Atto647N *Camk2a*, Atto647N *β-actin*, and Atto647N *Psd95* for control vs. puro-treated samples. $n = 29$ cells per condition. $^{**}P < 0.01$ Sidak's multiple comparisons test. (*D*) Quantification of mRNA dynamic state: confined, anterograde vs. retrograde for Atto647N *Camk2a*, Atto647N *β-actin*, and Atto647N *Psd95* for control vs. anisomycin-treated samples. $n = 15$ cells per condition. $^{*}P < 0.05$; $^{**}P < 0.01$ paired *t* test. (*E*) Quantification of cumulative distance traveled for Atto647N *Camk2a*, Atto647N *β-actin*, and Atto647N *Psd95* for control vs. anisomycin-treated samples. $n = 15$ cells per condition. $^{**}P < 0.01$; $^{***}P < 0.001$ Sidak's multiple comparisons test.

(36). As such, puromycin promotes the transition to a ribosome-free mRNA state, whereas anisomycin causes ribosome accumulation on mRNAs. Using our analysis pipeline, we quantified the effects of these treatments on mRNA dynamics (Fig. 3 *B*–*E*). For *Camk2α* and *β-actin*, puromycin displacement of ribosomes led to enhanced mRNA motility (reduced confinement) (fraction population confined; *Camk2a*: 0.59 ± 0.10 vs. 0.43 ± 0.13; *β-actin*: 0.56 ± 0.13 vs. 0.44 ± 0.12; mean ± SEM) (Fig. 3*B*) and cumulative distance traveled (distance in micrometers; *Camk2a*: 18.14 ± 20.26 vs. 24.48 ± 25.70; *β-actin*: 19.64 ± 20.73 vs. 27.59 ± 24.78) (Fig. 3*C*). In contrast, *Psd95* motility (fraction population confined; *Psd95*: 0.51 ± 0.14 vs. 0.45 ± 0.14) (Fig. 3*B*) and cumulative distance traveled (Fig. 3*C*) (distance in micrometers; *Psd95*: 20.71 ± 19.21 vs. 17.44 ± 20.41) was not significantly changed by puromycin treatment. This difference may reflect a higher basal translational state for *Camk2α* and *β-actin* mRNAs, consistent with *Psd95* mRNA being slightly more dynamic relative to the other two mRNAs (Fig. 2).

Since displacing ribosomes for *Camk2α* and *β-actin* enhanced mRNA motility, we predicted that freezing the ribosomes on the mRNA should lead to the opposite effect. Indeed, anisomycin treatment led to decreased mRNA motility (Fig. 3*D*) for all three mRNAs (fraction population confined; *Camk2a*: 0.54 ± 0.10 vs. 0.64 ± 0.11; *β-actin*: 0.55 ± 0.09 vs. 0.63 ± 0.09; *Psd95*: 0.49 ± 0.09 vs. 0.58 ± 0.09; mean ± SEM) and cumulative distance traveled (Fig. 3*E*) for *β-actin* and *Psd95* (distance in micrometers; *Camk2a*: 21.39 ± 19.24 vs. 20.06 ± 17.85; *β-actin*: 25.65 ± 22.24 vs. 22.32 ± 17.66; *Psd95*: 21.47 ± 17.70 vs. 16.96 ± 16.75). Interestingly, neither displacing nor freezing ribosomes had an effect on the active transport velocity of any mRNA (*SI Appendix*, Fig. S2 *B* and *C*). Furthermore, neither puromycin nor anisomycin affected the stationary population (*SI Appendix*, Fig. S2 *D* and *E*). Given that transport velocity was unaffected by either perturbation of translation (*SI Appendix*, Fig. S2 *B* and *C*), our data are consistent with the idea that mRNAs are transported in a quiescent nontranslating state (23, 37). Taken together, these data illustrate that the translational status of a given mRNA will affect its dynamics within the dendrite.

Plasticity Stalls mRNA Transport and Accumulates mRNAs near Dendritic Spines. We next assessed if we could modulate mRNA dynamics with physiologically relevant manipulations, specifically synaptic plasticity. We examined how mRNA dynamics were altered during two forms of protein synthesis-dependent plasticity, cLTP (38) and mGluR-LTD (39) (*SI Appendix*, Fig. S3 *A* and *B*). cLTP induction (*Materials and Methods*) was performed by a 5-min incubation in magnesium-free buffer supplemented with glycine and picrotoxin, whereas as mGluR-LTD was induced with 100 μM (S)-3,5-Dihydroxyphenylglycine hydrate (S-DHPG) for 5 min. Following cLTP (Fig. 4 *A* and *B* and *SI Appendix*, Fig. S3*C*) or mGluR-LTD (Fig. 4 *C* and *D* and *SI Appendix*, Fig. S3*D*) mRNA dynamics were monitored immediately after agonist washout. Induction of cLTP led to decreased mRNA motility (Fig. 3*D*) for all three mRNAs (fraction population confined; *Camk2a*: 0.54 ± 0.09 vs. 0.63 ± 0.08; *β-actin*: 0.53 ± 0.10 vs. 0.62. ± 0.06; *Psd95*: 0.47 ± 0.06 vs. 0.58 ± 0.10; mean ± SEM) and reduced cumulative distance traveled (Fig. 4*B*) (total cumulative distance traveled in microns: *Camk2a*:

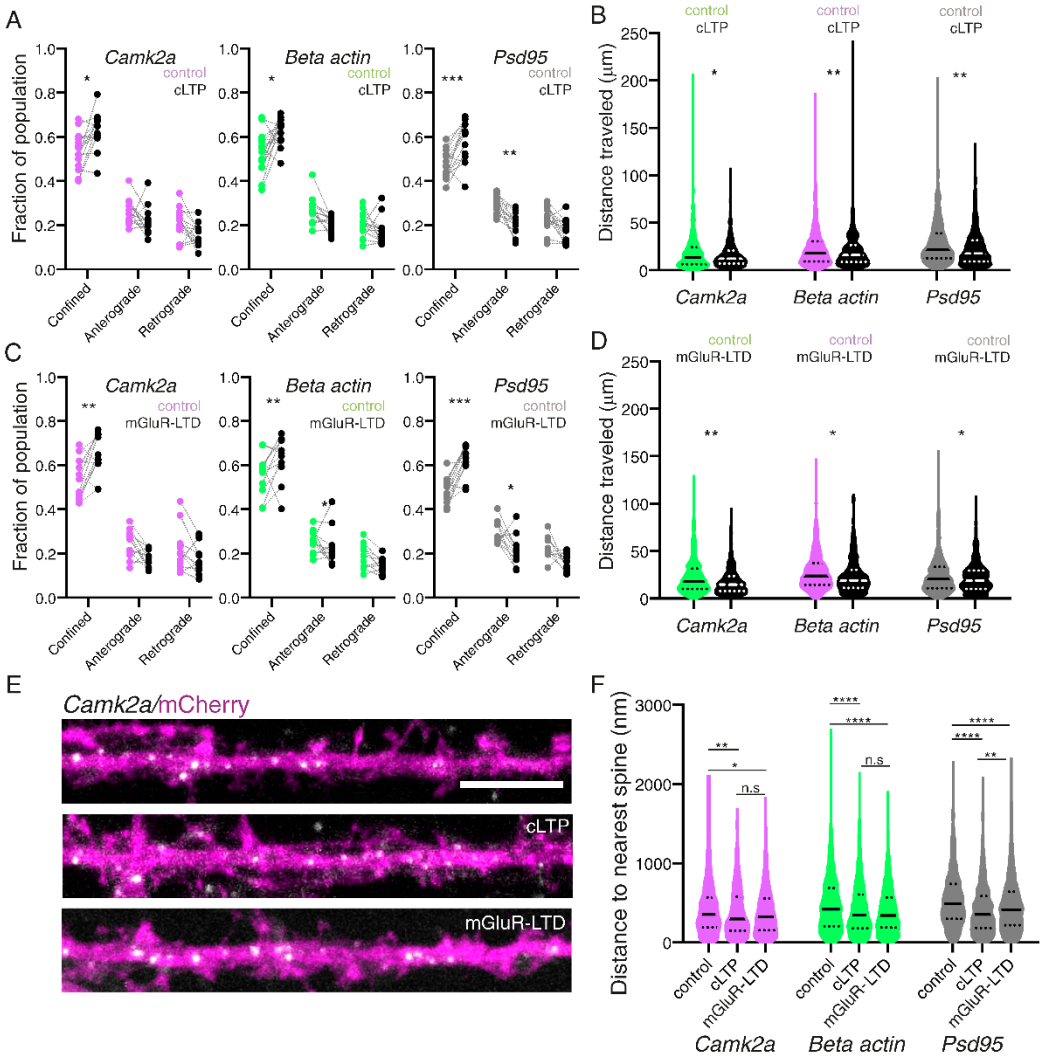

Fig. 4. Two distinct forms of synaptic plasticity attenuate mRNA dynamics near dendritic spines. (*A*) Quantification of mRNA dynamic state: confined, anterograde vs. retrograde for Atto647N *Camk2a*, Atto647N *β-actin*, and Atto647N *Psd95* for control vs. cLTP induced samples. $n = 14$ cells per condition. $^{*}P < 0.05$; $^{**}P < 0.01$; $^{***}P < 0.001$. Paired *t* test. (*B*) Quantification of cumulative distance traveled for Atto647N *Camk2a*, Atto647N *β-actin*, and Atto647N *Psd95* for control vs. cLTP induced samples. $n = 14$ cells per condition. $^{*}P < 0.05$; $^{**}P < 0.01$. Sidak's multiple comparisons test. (*C*) Quantification of mRNA dynamic state: confined, anterograde vs. retrograde for Atto647N *Camk2a*, Atto647N *β-actin*, and Atto647N *Psd95* for control vs. mGluR-LTD induced samples. $n = 14$ cells per condition. $^{*}P < 0.05$; $^{**}P < 0.01$; $^{***}P < 0.001$. Paired *t* test. (*D*) Quantification of cumulative distance traveled for Atto647N *Camk2a*, Atto647N *β-actin*, and Atto647N *Psd95* for control vs. mGluR-LTD–induced samples. $n = 14$ cells per condition. ; $^{*}P < 0.05$; $^{**}P < 0.01$. Sidak's multiple comparisons test. (*E*) Example images of Camk2a RNA FISH signal in neurons volume filled with mCherry under control, +cLTP and +mGluR-LTD conditions. (Scale bar, 2.5 μm.) (*F*) Quantification of mRNA distance to the nearest spine reveals a slight decrease in the distance for all three mRNAs during plasticity. Control, cLTP, mGluR-LTD ± SD: *Camk2a* (411.6 ± 300.7; 376.8 ± 292.5; 375.0 ± 275.4), *β-actin* (474.3 ± 327.1; 413.8 ± 312.3; 391.0 ± 275.8), and *Psd95* (537.2 ± 334.3; 403.3 ± 283.7; 454.6 ± 304.7) $^{*}P < 0.05$; $^{**}P < 0.01$; $^{****}P < 0.0001$; n.s., not significant. Dunn's multiple comparisons test. $n = 15$ cells per condition.

23.36 ± 19.86 vs. 20.54 ± 18.97; *β-actin*: 18.95 ± 19.75 vs. 16.25 ± 14.52; *Psd95*: 28.95 ± 23.29 vs. 22.87 ± 18.91). Induction of mGluR-LTD led to decreased mRNA motility (Fig. 4*C*) for all three mRNAs (fraction population confined; *Camk2a*: 0.54 ± 0.09 vs. 0.64 ± 0.09; *β-actin*: 0.56 ± 0.10 vs. 0.63 ± 0.10; *Psd95*: 0.48 ± 0.06 vs. 0.62 ± 0.07; mean ± SEM) and reduced cumulative distance traveled (Fig. 4*D*) (total cumulative distance traveled in microns: *Camk2a*: 28.81 ± 20.55 vs. 23.66 ± 18.48;

β-actin: 23.37 ± 19.34 vs. 17.97 ± 14.00; *Psd95*: 25.54 ± 20.68 vs. 21.84 ± 16.05). To summarize, we observed a significant decrease in the time all three mRNAs spent moving and a reduced cumulative distance traveled within the dendrite following induction of both forms of plasticity.

To assess more precisely the location of mRNA deposition during these enhanced periods of mRNA confinement, we performed high-resolution smFISH in dendrites immediately after induction of cLTP or mGluR-LTD (*Materials and Methods* and Fig. 4 *E* and *F*). We measured the mean distance of an mRNA granule to its nearest dendritic spine and found that this distance decreased significantly with both cLTP and mGluR-LTD induction for all three mRNAs (Fig. 4*F*). Taken together with the altered dynamics observed with the molecular beacons (Fig. 4 *A* and *C*), our data suggest increased spine association of these mRNAs during plasticity. This enhanced association may fuel local translation of these mRNAs to induce and maintain both forms of structural plasticity.

Exploring the Dynamics of Protein Synthesis in Real Time. To assess directly whether translation of these three mRNAs was altered during cLTP or mGluR-LTD, we used translational reporters (18) (Fig. 5) comprising a codon optimized superfolder GFP (40) (sfGFP) (*Materials and Methods*) flanked by the corresponding dendritically-enriched 3′UTR (41) of *Cam2a*, *β-actin*, or *Psd-95*. Each 3′UTR was included to confer both transcript-specific localization and translational regulation to the translational reporter (41). We used cell-wide fluorescence recovery after photobleaching (FRAP) to visualize newly synthesized proteins. Following whole-cell photobleaching, we measured the emergence and time course of the protein synthesis-dependent fluorescence signal to assess the kinetics and extent of the translational responses for each mRNA. We found that all three transcript-specific reporters showed protein synthesis-dependence in their recovery compared with the no UTR control (Fig. 5*D* and *SI Appendix*, Fig. S4, black vs. gray curves), indicating that these reporters are effective readouts for active translation. The induction of either cLTP or mGluR-LTD resulted in an enhancement of the mobile fraction (Fig. 5*D*) and total fluorescence recovery (*SI Appendix*, Fig. S4) for both the CAMK2α and β-ACTIN reporter, indicating enhanced protein synthesis. Conversely, PSD-95 showed enhanced translation following cLTP induction (Fig. 5*D* and *SI Appendix*, Fig. S4), but no change following mGluR-LTD. Interestingly, we noticed a strong bias for the emergence of fluorescence in spines during cLTP and mGluR-LTD (Fig. 5*C*). To assess if this represented a bias for spine accumulation of newly synthesized protein, we assessed the ratio of fluorescence recovery for the spine over the shaft (Fig. 5*E*). Plasticity induction indeed resulted in a higher rate of spine recovery, except for PSD-95 during mGluR-LTD, suggesting that protein production near spines could drive the emergence of new fluorescence in the spines. Taken together, these data indicate that there can be a functional disconnect between transcript-specific changes in mRNA dynamics seen during plasticity (Fig. 3) and the downstream translational state of that mRNA species.

To assess if the same pattern of translation following plasticity was also observed with the endogenous transcripts, we used CRISPR/Cas9 gene editing in neurons (42) to tag endogenous CAMK2α or β-ACTIN (N terminal) or PSD-95 (C terminal) protein with the fast-folding Venus fluorescent protein (43) (Fig. 6*A* and *SI Appendix*, Fig. S4). The fast-folding nature of Venus ($t_{1/2\ \mathrm{maturation}} = 2$ to 5 min) allowed us to rapidly assess the translational regulation of these three proteins. All three proteins were successfully tagged and exhibited their characteristic localization patterns (*SI Appendix*, Fig. S5). Venus-tagged CAMK2α and β-ACTIN were enriched in axons and dendrites, and most strongly enriched in dendritic spines and axonal boutons, while PSD-95–tagged Venus was exclusively enriched within postsynaptic compartments. As before, we performed cell-wide FRAP (*Materials and Methods*, Fig. 6 *B–E*, and *SI Appendix*, Fig. S6 and Table S2). We tracked the emergence and time course of the protein synthesis-dependent fluorescence signal to assess the kinetics and the extent of the translational responses for each mRNA (*SI Appendix*, Fig. S6 *B–D*). For all proteins, treatment with the protein synthesis inhibitor anisomycin significantly reduced the emergence of new fluorescent signal (*SI Appendix*, Fig. S6*B*) and attenuated the mobile population during recovery (Fig. 6*C*) (fraction mobile population; CAMK2α: 0.21 ± 0.01 vs. 0.13 ± 0.06; β-ACTIN: 0.21 ± 0.01 vs. 0.11 ± 0.007; PSD-95: 0.35 ± 0.03 vs. 0.21 ± 0.02; mean ± SEM), confirming our ability to visualize new protein synthesis in real-time for endogenous proteins.

In line with our reporter observations, we found that cLTP induction significantly enhanced the emergence of fluorescence for all three proteins (*SI Appendix*, Fig. S6*C*) and enhanced the mobile population (Fig. 6*D*) (fraction mobile population; CAMK2α: 0.23 ± 0.02 vs. 0.3 ± 0.01; β-ACTIN: 0.21 ± 0.01 vs. 0.30 ± 0.02; PSD-95: 0.35 ± 0.03 vs. 0.45 ± 0.02; mean ± SEM), indicating enhanced protein synthesis. Induction of mGluR-LTD, however, elicited a transcript-specific enhancement of protein synthesis for CAMK2α and β-ACTIN but not PSD-95 (fraction mobile population; CAMK2α: 0.20 ± 0.02 vs. 0.29 ± 0.02; β-ACTIN: 0.23 ± 0.02 vs. 0.32 ± 0.02; PSD-95: 0.33 ± 0.03 vs. 0.37 ± 0.02; mean ± SEM), (Fig. 6*E* and *SI Appendix*, Fig. S6*D*). In the above experiments, a brief (5 min) application of DHPG did not enhance the synthesis of PSD-95. Prior studies (16, 17, 44) have shown that a sustained application of the DHPG can stimulate PSD-95 translation. To assess the effect of a longer period of mGluR activation, we treated neurons for with DHPG throughout the FRAP experiment (~60 min) (*SI Appendix*, Fig. S7 *A* and *B* and Table S3). We found that the mobile fraction of PSD-95 Venus was enhanced by the long duration DHPG application (*SI Appendix*, Fig. S7*B*), and this effect was blocked by pretreatment with anisomycin. We found no change in the CAMK2a or β-ACTIN (*SI Appendix*, Fig. S7*C*) mobile fraction. These data are consistent with PSD-95 translation regulation by long-term but not brief (mGluR-LTD) mGluR activation.

To obtain better temporal and spatial resolution on the translational responses to plasticity induction, we validated the above findings with a method that couples general metabolic labeling of nascent proteins (puromycin) with a specific label for a protein-of-interest using the proximity ligation assay (Puro-PLA) (45) (*Materials and Methods* and *SI Appendix*, Fig. S8*A*). We examined changes in dendritic protein synthesis during plasticity (Fig. 6 *F* and *G* and *SI Appendix*, Fig. S8 *B* and *C*). Consistent with previous observations (45), we observed that there was a protein synthesis dependence to the Puro-PLA signal for all three proteins (black vs. gray bars in Fig. 6*G*) (normalized PLA density; CAMK2α: 0.26 ± 0.13; β-ACTIN: 0.26 ± 0.14; PSD-95: 0.32 ± 0.17; mean ± SEM). Furthermore, cLTP induction enhanced the dendritic synthesis of all three mRNAs (normalized PLA density; CAMK2α: 1.50 ± 0.58; β-ACTIN: 1.38 ± 0.57; PSD-95: 1.43 ± 0.58; mean ± SEM), while induction of mGluR-LTD only enhanced the synthesis of CAMK2α and β-ACTIN (normalized PLA density; CAMK2α: 1.47 ± 0.55; β-ACTIN: 1.26 ± 0.52; PSD-95: 1.02 ± 0.61; mean ± SEM). These data not only validate and support our real-time translational response observations, but also support that this translation can occur locally within the dendrite where we detect changes in mRNA dynamics. Taken together, these data indicate that alterations in mRNA dynamics and protein synthesis underlie the manifestation of specific forms of synaptic plasticity.

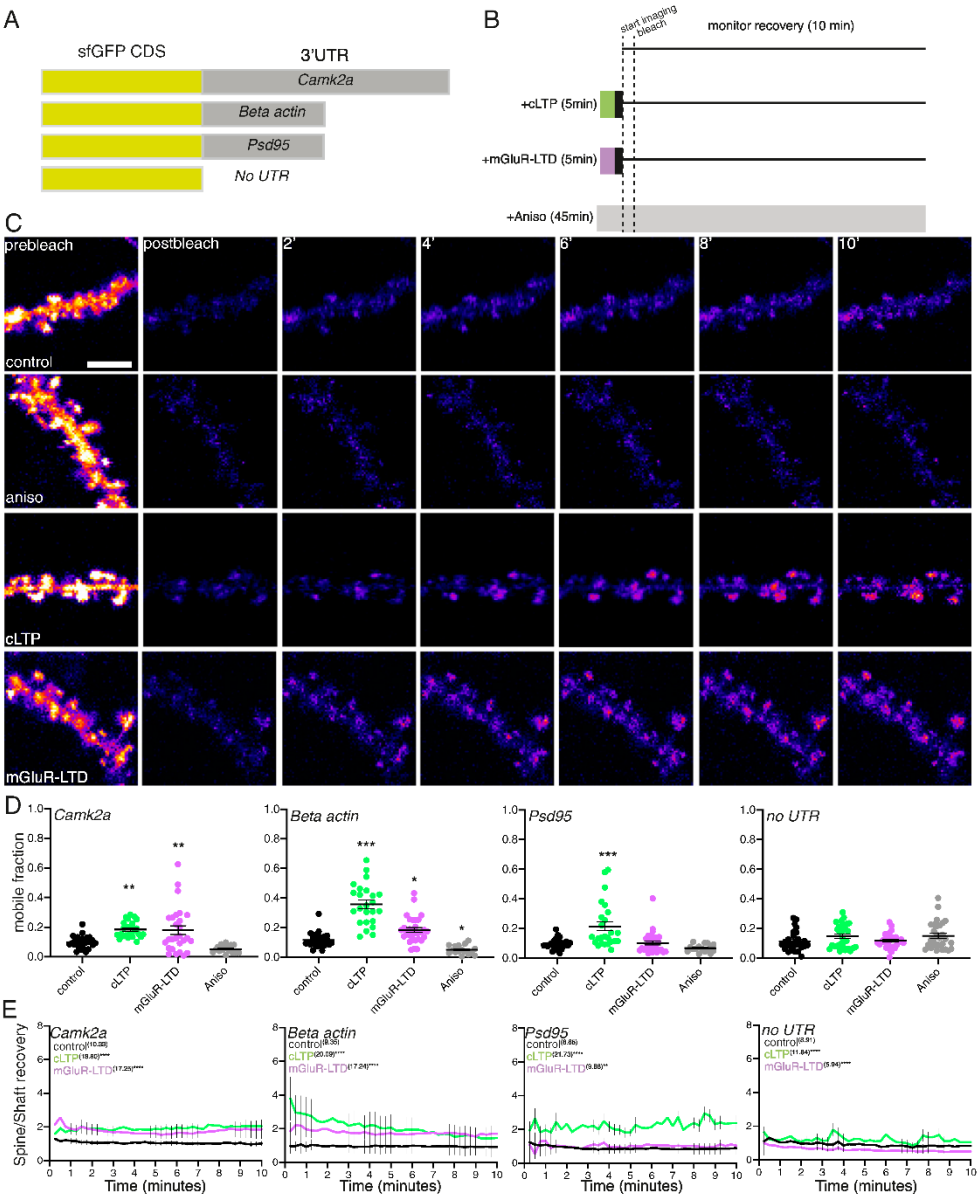

Fig. 5. Real-time visualization of 3′UTR regulated translation during synaptic potentiation and depression. (*A*) Scheme for the reporters used to assess real-time 3′UTR regulated translational dynamics in live neurons. (*B*) Scheme of workflow for the treatment and visualization of plasticity regulated protein synthesis. Following induction of cLTP or mGluR-LTD, the indicated pharmacological treatment was washed out (black box) and the samples were then imaged for 2 min every 15 s to acquire a baseline measurement. The cells were then bleached and the fluorescence recovery was monitored every 15 s for 10 min. For controls, either no treatment or treatment with the translational inhibitor anisomycin was used for comparison. (*C*) Example image of a Camk2a sfGFP reporter under control (top row) +anisomycin (second row), +cLTP (third row), or +mGluR-LTD conditions before bleaching and during the phase of fluorescence recovery. (Scale bar, 5 μm.) (*D*) Mobile fractions calculated for the translational reporters during control, plasticity induction and anisomycin treatment. $*P < 0.05$; $**P < 0.01$; $***P < 0.001$. Dunnett's multiple comparisons test for treated vs. control condition for each construct; $n = >14$ cells per condition. (*E*) Recovery rate of fluorescence of dendritic spines to shafts demonstrates a bias for spine fluorescence recovery during plasticity. Kruskal-Wallis test. $**P < 0.01$; $****P < 0.0001$. $n = >14$ cells per condition.

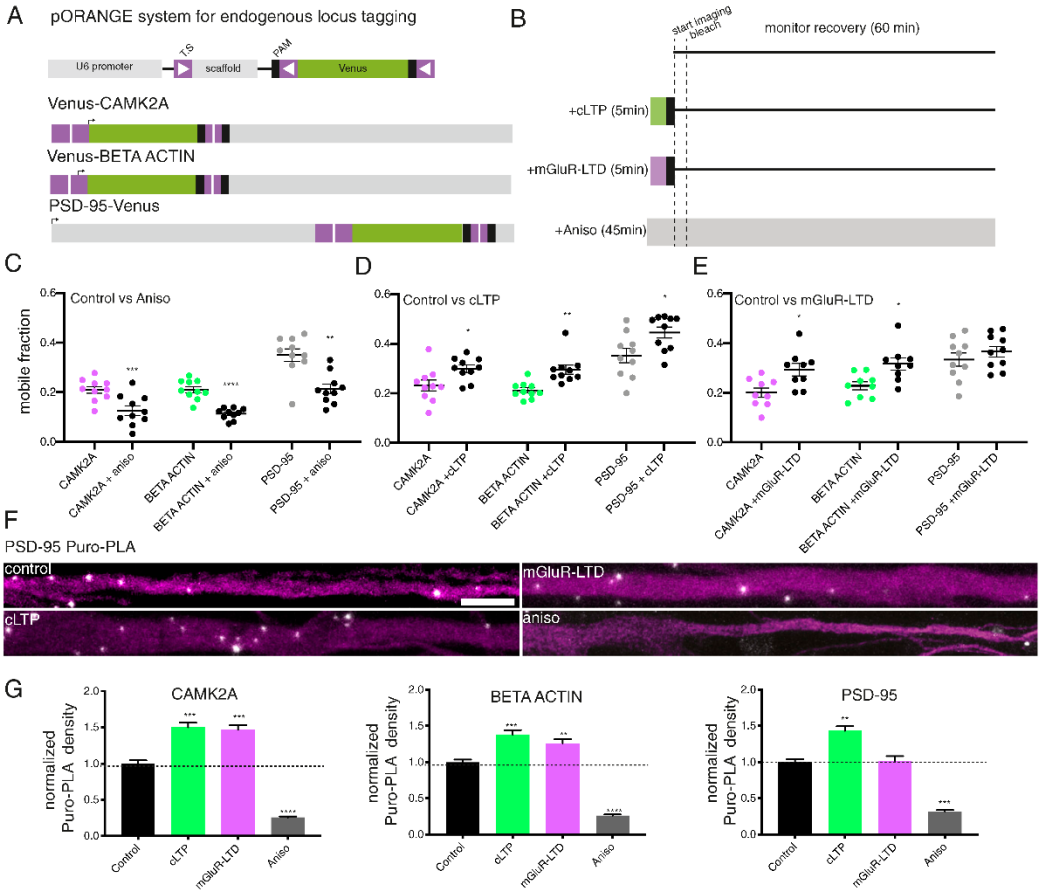

Fig. 6. Visualizing endogenous protein translation in real-time during synaptic potentiation and depression. (*A*) Scheme for the modification of endogenous gene tagging of *Camk2a*/*β-actin*/*Psd95* with Venus fluorescent protein. T.S.; targeting sequence; arrow indicates start codon. (*B*) Scheme of workflow for the treatment and visualization of plasticity regulated protein synthesis. Following induction of cLTP or mGluR-LTD, the pharmacological treatment was washed out (black box) and the samples were then imaged for 2 min every 15 s to acquire a baseline measurement. The cells were then bleached and the fluorescence recovery was then monitored every 15 s for 60 min. For controls, either no treatment or treatment with the protein synthesis inhibitor anisomycin was used for comparison. (*C*) Mobile population during the FRAP recovery for Venus-CAMK2a, Venus–β-ACTIN, and PSD-95–Venus during control and anisomycin treatment. $n = 10$ cells per condition. Two-tailed paired t test. $^{**}P < 0.01$; $^{***}P < 0.001$; $^{****}P < 0.0001$. (*D*) Mobile population during the FRAP recovery for Venus-CAMK2a, Venus–β-ACTIN, and PSD-95–Venus during control and cLTP. $n = 10$ cells per condition. Two-tailed paired t test. $^{*}P < 0.05$; $^{**}P < 0.01$. (*E*) Mobile population during the FRAP recovery for Venus-CAMK2a, Venus–β-ACTIN, and PSD-95-Venus during control and mGluR-LTD. $n = 9$ to 10 cells per condition. Two-tailed paired t test. $^{*}P < 0.05$. (*F*) Example images dendritically localized (MAP2, magenta) Puro-PLA signal for PSD-95 (white) under control and stimulated conditions. (Scale bar, 10 μm.) (*G*) Puro-PLA quantification reveals local protein synthesis underlies the translational responses of CAMK2a, β-ACTIN, and PSD-95 during cLTP and mGluR-LTD. $n = 85$ cells per condition. Dunnett's multiple comparisons test. $^{**}P < 0.01$; $^{***}P < 0.001$; $^{****}P < 0.0001$.

Discussion

Here we investigated the interplay between mRNA dynamics and translation within neuronal dendrites during two different forms of synaptic plasticity. We characterized the dynamics and translation of three individual endogenous mRNAs: *Camk2a*, *β-actin*, and *Psd95*, during basal neuronal activity and plasticity. In live hippocampal neurons we provide evidence that mRNAs exist in heterogenous copy number organizational states (Fig. 1). The preference for single mRNA copy vs. higher-order state may be a transcript-specific feature, as *Camk2a* and *Psd95* exhibit an enhanced preference for higher-order multimeric states compared with the previously described single mRNA state of *β-actin* (29). We found that, on average, different mRNA transcripts displayed remarkably similar dynamic properties (velocity, time spent motile, distance traveled) within the dendrite. Only subtle differences were seen, with *Psd95* showing a higher fraction of time spent motile than *β-actin* or *Camk2a*. The factors influencing *Psd95*'s higher motility remain to be elucidated, but may reflect a difference in its translational efficiency (46) as an FMRP-regulated transcript (17, 30). We found that ribosome

association directly influences mRNA dynamics, suggesting that mRNA translation is likely restricted to nontransporting mRNAs exclusively within the dendrite. Consistent with our data, previous work in fibroblasts (47) and axons (32) has shown that diffusion of *β-actin* increases when ribosomes are displaced. These data fit with recent proteomic analysis on isolated mRNA transport granules (48), which detected only a subset of ribosomal proteins associated with granules.

In our experiments, mRNAs were sequestered, exhibiting reduced mobility following plasticity. The mechanisms underlying the initial capture and enduring sequestration of mRNAs are not well understood. Recent work with *Rgs4* indicated that neuronal activity is essential for the capture of mRNAs at dendritic spines; inhibition of neuronal activity with TTX suppressed mRNA-spine association (24). An activity dependence for spine capture has also been reported with *β-actin* during glutamate uncaging (22). This was proposed to be dependent on underlying actin remodeling from the structural plasticity induced by the glutamate uncaging. Indeed, the structural spine plasticity characteristic of both cLTP and mGluR-LTD involves modulation of the actin cytoskeleton (49). Whether actin remodeling broadly promotes mRNA sequestration at or near dendritic spines remains to be assessed. The translation of all three mRNAs was enhanced by cLTP, but mGluR-LTD only enhanced the translation of *Camk2a* and *β-actin* indicating mRNA sequesteration alone does not lead to translation. Taken together, our data dissociate the accumulation and association of mRNAs near synapses from their translational status.

Psd95 mRNA has previously been characterized as an mGluR-regulated transcript (16, 30, 44); however, following washout of the mGluR agonist (similar to the conditions used here), PSD-95 protein is rapidly degraded (50). This functional switch from promoting PSD-95 mRNA translation to degrading PSD-95 protein might be an essential step for the manifestation of spine shrinkage in mGluR-LTD. Activation of mGluR signaling has previously been linked to phosphorylation of eIF2a, promoting the translation of transcripts with 5′UTR containing upstream open reading frames (uORFs) (51). During the long-term DHPG treatment, we observed an enhancement of PSD-95 protein synthesis (*SI Appendix*, Fig. S7*B*); this may be similarly dependent on eIF2a phosphorylation. After the DHPG is washed out, and presumably eIF2a returns to a non-phosphorylated state, then PSD-95 translation may return to baseline levels. A similar functional switch in translational output of *Psd95* mRNA has been previously described for FMRP-regulated translation in mGluR signaling (17, 30). We note that currently available methods for the induction of mGluR-dependent mGluR-LTD are limited to bath application of mGluR-agonists; the development of a caged mGluR agonists would enable the analysis of single spines.

How mRNAs associated with activated synapses become translational competent likely depends on signaling cascades underlying various forms of synaptic plasticity. Given that specific signaling cascades are turned on by distinct forms of plasticity (2), these cascades likely influence changes in posttranslational modifications of RBPs on particular transcripts, regulating their "translatability." Consistent with this, activation of PKA signaling alone is sufficient to enhance dendritic protein synthesis (11). cLTP, known classically for its dependence on CamkII signaling (52), also triggers a number of other classic signaling cascades, including PKA (53), PKC (54, 55), MAPK/ERK (56), PI3K (57), mTOR (58), and Src (59). mGluR-LTD on the other hand, is less clear in its signaling requirements; it involves activation of PKC (60) and PI3K/AKT/mTOR (61). However, the role of CamkII (62, 63) is debated. Once sequestered by an active synapse, mRNAs could be "synaptically decoded" by the activation of these signaling pathways to determine whether and when a given mRNA species will be translated or not.

Materials and Methods

Molecular Beacon Structure and Design.

Solid-phase synthesis. Milli-Q water was treated with DEPC (0.1%) overnight and autoclaved.

The following oligonucleotides were synthesized on an ABI392 instrument:

PSD95_1: 5′- M CACGACCAUCCCUCCCCUUUUCCCAAAAAAAUAUCGUG Q_1 -3′

PSD95_2: 5′- M CACGAAUAAAAUCCCAGAAAAAAAAAAAAGCCUCGUG Q_2 S -3′;

CAMK2_1: 5′- M CACGAGGUAAAAACUUCCCCUCACUCCUCUUCCUCGUG Q_1 -3′;

CAMK2_2: 5′- M CACGAUUUUUCUUCUUUUUUGUUUUGCUCUUCGUG Q_2 S -3′;

β-Actin_1: 5′- M CACGACAAAACAAAACAAAAAAACUUAAAAAAAAUCG UG Q_1 -3′;

β-Actin_2: 5′- M CACGAUUCACCGUUCCAGUU UUUAAAUCCUGUCGUG Q_2 S -3′;

GFP_1: 5′- M CACGAACUUCUUCAAGUGUGCGAUGCCAGAAGGGUCGUG Q_1 -3′;

M = Fmoc-Amino-DMT C-3 CED phosphoramidite (ChemGenes);

Q_1 = 3′-BHQ-2 CPG 1000 (LinkTech);

Q_2 = BBQ-650-(DMT)-CE-Phosphoramidite (LinkTech);

S = 3′-Spacer C3 SynBase CPG 1000/110 (LinkTech);

A = 2′-OMe-Pac-A-CE Phosphoramidite (LinkTech);

C = 2′-OMe-Ac-C-CE Phosphoramidite (Linktech);

G = 2′-OMe-*i*Pr-Pac-G-CE Phosphoramidite (LinkTech);

U = 2′-OMe-U-CE Phosphoramidite (LinkTech).

For all synthesized oligonucleotides, Pac_2O was used as capping reagent. 0.3 M BTT (emp Biotech) was used as activator. Coupling time for A, C, G, U, and M was 6 min, Q_2 for 15 min. Synthesis was performed in DMTr-On mode. The cyanoethyl groups were removed by flushing the columns with 20% diethylamine (emp Biotech) for 10 min, followed by washing with MeCN, Argon, and drying in vacuum. Cleavage from the solid-phase was performed with aqueous ammonia (32%) (Merck) for 4 h at room temperature. After spin filtration, the solvent was removed at 4 °C using a vacuum concentrator (SpeedVac, Thermo Fischer).

Purification. The DMTr-On oligonucleotides were purified by RP-HPLC on an Agilent 1200 equipped with a Waters XBridge BEH C18 OBD column (300 Å, 5 μm, 19 × 250 mm, 4 mL/min, 60 °C). As solvents 400 mM hexafluoroisopropanol (Fluorochem), 16.3 mM Et_3N (Merck), pH 8.3, and MeOH (Fluka) were used with a gradient from 5 to 100% MeOH in 30 min. After separation, the solvent was evaporated in a vacuum concentrator at 4 °C. The DMTr group was removed by incubation of the oligonucleotides in 400 μL 80% aqueous AcOH (Merck) at room temperature for 20 min, followed by evaporating the solvent in a vacuum concentrator at 4 °C. The RNAs were again purified by RP-HPLC under the same conditions as above.

Fluorophore labeling. For fluorophone labeling, 10 nmol of each RNA were dissolved in 150 μL borate-buffer (0.1 M sodium tetraborate (Merck), pH 8.4). GFP_1, PSD95_1, CAMK2_1 and β-actin_1 were incubated with 200 nmol ATTO565 NHS (ATTO-TEC), dissolved in 50 μL DMF (Lumiprobe, labeling grade), for 4 h at 37 °C. PSD95_2, CAMK2_2 and Beta Actin_2 were incubated with 200 nmol ATTO647N NHS (ATTO-TEC), dissolved in 50 μL DMF, for 4 h at 37 °C. Buffer and the excess of fluorophore were removed by size-exclusion chromatography (NAP 25, GE Healthcare). The solvent was evaporated at 4 °C using a vacuum concentrator. The residue was purified by RP-HPLC on an Agilent 1200 equipped with an Xbridge BEH C18 OBD (300 Å, 3.5 μm, 4.6 × 250 mm, 1 mL/min, 60 °C). As solvents 400 mM hexafluoroisopropanol, 16.3 mM Et_3N, pH 8.3 and MeOH were used with a gradient from 5% MeOH to 100% MeOH in 50 min.

Sample preparation for in vivo use. For use in living cells, the remaining HPLC buffer ions had to be removed. Therefore, the oligonucleotides were dissolved in 0.3 M NaOAc (Merck) (10 μL per 1 nmol RNA). EtOH (Fluka,

prechilled to −20 °C, 40 μL per 1 nmol RNA) was added. The mixture was cooled to −20 °C for at least 6 h. The precipitant was pelletized by centrifugation at 4 °C, 20,000 × *g* for 20 min. The residue was redissolved in 0.3 M NaOAc and the precipitation steps were repeated three times. To remove sodium ions, the oligonucleotides were desalted using a 1-k cutoff membrane filter (Microsep Advance Centrifugal Devices with Omega Membrane 1K, PALL). Before adding the oligonucleotides, each filter was washed five times with DEPC water at 15,000 × *g*, 15 °C for 20 min. The desalting step was repeated three times.

Characterization. Analytical RP-HPLC was performed on an Agilent 1200 equipped with a BEH C18 OBD (300 Å, 3.5 μm, 4.6 × 250 mm, 1 mL/min, 60 °C). As solvents 400 mM hexafluoroisopropanol (Fluorochem), 16.3 mM Et_3N (Merck), pH 8.3 and MeOH (Fluka) were used with a gradient from 5 to 100% MeOH in 39 min. Electrospray ionization-MS spectra were recorded on a Bruker micrOTOF-Q device in negative ionization mode.

Hippocampal Neurons. Dissociated rat hippocampal neuron cultures were prepared and maintained as described previously (18). Cells were plated at a density of 30 − 40 × 10^3 cells/cm^2 on poly-D-lysine–coated glass-bottom Petri dishes (MatTek). Hippocampal neurons were maintained and matured in a humidified atmosphere at 37 °C and 5% CO_2 in growth medium (Neurobasal-A supplemented with B27 and GlutaMAX-I; Life Technologies) for 18 to 21 DIV to ensure synapse maturation. All experiments complied with national animal care guidelines and the guidelines issued by the Max Planck Society and were approved by local authorities.

Transfection of Plasmid DNA. For transfection of fluorescent proteins and reporters, DIV 17 to 19 neurons were transfected with mCherry-C1 (Clonetech), myr-sfGFP translational reporters (described below) or myr-Venus using Effectene (Qiagen), as previously described (38). pCAG:myr-Venus (64) was a gift from Anna-Katerina Hadjantonakis (Sloan-Kettering Institute, New York) (Addgene plasmid # 32602; n2t.net/addgene:32602; RRID:Addgene_32602). Transfected cells were imaged or fixed (described below) 12 to 18 h posttransfection.

Transfection of Molecular Beacons. For transfection of molecular beacons, DIV 17 to 19 neurons were transfected with Attractene (Qiagen). For each MatTek dish, 20 pmol of molecular beacon was resuspended in 75 μL of buffer EC (Qiagen) along with 2 μL of Attractene. The beacon-attractene mixture was incubated for 20 min at room temperature before being added to neurons. Samples were imaged 1 to 12 h posttransfection. We found that imaging beacons <1 or >12 h after transfection resulted in higher background noise, with short incubations resulting in stronger nuclear staining and long incubations resulting in accumulation and aggregation in vesicular structures. Prior to imaging, samples were washed in fresh media to remove nontransfected beacons.

Electroporation of Plasmid DNA. Following isolation, 1 million hippocampal neurons were spun down at 500 rpm for 5 min at 4 °C. Cells were resuspended in electroporation solution (Lonza) along with 1 μg pORANGE plasmid DNA construct. Cells were electroporated with the hippocampal/cortical high-viability protocol (Lonza) and resuspended in 2 mL cell growth media. Cells were then plated at a density of 100 × 10^3 in MatTek dishes coated with poly-D-lysine for 2 h to allow for cell attachment. Following attachment, 1.3 mL media was added, and cells were fed with 500 μL fresh neuronal growth media once a week until the time of experiments.

Cell Treatments. Drugs treatments were performed as follows: For puromycin labeling experiments (Puro-PLA), cultured neurons were treated with 10 μM puromycin for 5 to 10 min. For Puro inhibition experiments, cultured neurons were treated with 100 μM puromycin for 5 min. Anisomycin treatment (40 μM) was performed 20 to 45 min prior to puromycin labeling, FRAP or molecular beacon experiments, and was kept in the media through the duration of experiment. mGluR-LTD was induced using DHPG (100 μM) for 5 min and then washed out or in long-term treatments 50 μM for the duration of imaging. cLTP was induced as previously described (38) in E4 buffer supplemented with B27, Glutamax, and MEM amino acids (Thermofisher). The day before the experiment, 50 μM APV (Tocris) was added to neuronal cultures. The day of induction, neurons were incubated in Mg_2^+-free E4 media supplemented with 200 μM glycine (Sigma) and 100 μM picrotoxin (Tocris) for 5 min. Following induction, cells were washed and returned to normal media or E4 with calcium and magnesium.

Imaging of Molecular Beacons. Investigation of the mRNA dynamics was carried out using a Leica DMi8 total internal reflection fluorescence (TIRF) microscope. Differential interference contrast (DIC) microscopy was used to identify neurons with well-isolated dendrites. mRNA dynamics were recorded for 20 min at a rate of 1 Hz in epi-fluorescence mode. ATTO565 fluorophores were excited using a 561-nm diode laser which provided 1.8 kW/cm^2 of intensity at the sample plane. ATTO647n was imaged with a 638-nm laser, which produced 2.0 kW/cm^2 at the sample plane. The fluorescence was recorded with a scientific-CMOS camera (Leica-DFC9000GT). The exposure time was fixed to 200 ms and 2 × 2 camera binning and set the digitalization to 12 bit (low noise) was used to limit the data volume. A 100× oil objective (HC PL APO 100×/1.47 OIL) was used to record a field-of-view of 133 μm × 133 μm. With these settings our pixel size was 130 nm, matching the Nyquist sampling frequency. Neurons were left in their glia-conditioned neurobasal, B27, and Glutamax media because of a Pecon TempController 2000-1 and a Pecon CO_2-Controller 2000, which kept the samples at 37 °C in a 5% CO_2 atmosphere.

Quantification of Beacon Number per Puncta. To quantify the copy numbers of mRNAs within individual mRNA granules, a commercially synthesized standard containing a single ATTO647N fluorophore anchored on a glass slide (GATTA-Brightness R1 in 0.5 TBE and 11 mM Mg on glass slide; GattaQuant) was used as a normalization standard. This sample was imaged using the same settings for the molecular beacons at different laser powers, ranging from 90 μW (1%) to 6.85 mW (50%), at which point we could observe saturation of the fluorescence. To benchmark the mean counts recorded from a single ATTO647N fluorophore, the maximum intensity around the detected puncta was measured and subtracted the neighboring background. This benchmark intensity was then set to the value $n = 1$ fluorophore and used to normalize the background-subtracted intensity recorded from hippocampal neurons.

Quantifying mRNA Dynamics. To extract information on the mRNA dynamics, a custom MATLAB script was used. For each neuron a single dendrite was segmented by manually drawing its profile. The script was divided into filtering the images and rendering the puncta, tracking the mRNAs and extracting information regarding their dynamics. To render the puncta, the background was subtracted by applying a mean filter. The pixel that represents the local maximum around a region of ∼400 nm × 400 nm was then identified and selected. Puncta were rendered in a binary array. This pipeline was repeated each frame of the time series and exported as a movie. mRNA tracking was performed using the Motion-Based Multiple Object Tracking function of MATLAB taking the first 100 frames as training for the model. Any particle that did not appear in consecutive frames was discarded. After tracking was complete, puncta that appear for longer than 20 frames (20 s) were retained and information—such as the puncta coordinates, their distance traveled, their velocities, and directionalities—was extracted. Puncta that moved less than 500 nm throughout the imaging session were classified as fully stationary and were not included in directionality calculations. From the velocity datasets per puncta, the percent of time spent in the confined state was calculated by assessing the total number of frames in which a puncta was detected and how many frames this puncta exhibited a velocity from −500 nm/s to 500 nm/s. Similarly, the percent time spent anterograde or retrograde was calculated by the fraction of time >500 nm/s or <−500 nm/s over the total number of frames detected. For all events detected in the cell, the average time spent in confined, anterograde or retrograde was calculated.

Translational Inhibitors and mRNA Dynamics Experiments. Beacons were transfected and imaged as described above, and puromycin and anisomycin were used at the concentrations indicated above. For assessing translational inhibitor effect on mRNA dynamics, two similarly looking neurons (containing a similar number of beacons and a similar morphology) were selected per MatTek dish. The first neuron was imaged as a control reference cell. Following the 20-min imaging window for the control neuron, puromycin was added for 5 min or anisomycin was added for 20 min, prior to the start of imaging for the second, treated, cell. Pairwise assessment (Fig. 3 *B* and *D*) between the control and treated cell per dish was used to assess the effect of the drugs on mRNA dynamic properties.

Spine Size Experiments. Neurons DIV 17+ were transfected with myrVenus 12 h prior to imaging and then imaged using a Leica DMi8 TIRF microscope. A 100× oil objective (HC PL APO 100×/1.47 OIL) was used to record a field-of-view of 133 μm × 133 μm using a 488-nm laser line. Samples were imaged for 10 min at baseline one frame every minute. Mock treatment,

mGluR-LTD, or cLTP was induced for 5 min, and samples were imaged one frame per minute during the induction phase. Following washout of drugs, neurons were imaged for 90 min postinduction. For anisomycin treatments, anisomycin was added 20 min prior to the start of the experiment and kept in the media continuously throughout the experiment. Drift was corrected using the built-in correct three-dimensional drift plugin in ImageJ/FIJI. An area of 5 to 10 spines per dendrite were then quantified over the imaging window, using the mean size of the first 10 baseline frames for normalization.

Plasticity and mRNA Dynamics Experiments. Beacons were transfected and imaged and plasticity was induced as described above. For assessing the effect of plasticity on mRNA dynamics, two similar neurons (beacon number and morphology) were selected per MatTek dish. The first neuron was imaged as a control reference neuron. Following the 20-min imaging window for the control neuron, plasticity was induced and the stimulation washed out, prior to commencing imaging of the second, treated, cell. Pairwise assessment (Fig. 4 *A* and *C*) between the control and treated cell per dish was used to assess the effect of plasticity on mRNA dynamic properties.

FISH. Hippocampal neurons (DIV 18+) expressing mCherry were fixed in 4% paraformaldehyde lysine phosphate buffer pH 7.4 supplemented with 2.5% sucrose for 15 to 20 min. Cells were permeabilized for 10 min in PBS containing 0.5% Triton-X 100 (Sigma). Target specific in situ hybridization was performed using StellarisTM probes (LGC Bioresearch) as previously described (10). Following fixation, cells were washed in PBS + 5 mM $MgCl_2$, followed by dehydration in 80% ethanol overnight at −20 °C. Following rehydration samples were washed 2× in 1× sodium citrate (SSC) buffer, followed by a 5-min wash in 2× SSC + 30% formamide for 5 min at 37 °C. Biotin-labeled probes for *Camk2a*, *β-actin*, and *Psd95* (Stellaris, Biosearch Technology) were diluted into 100 μL hybridization buffer and incubated with cells for 4 h at 37 °C. Following probe hybridization, samples were washed twice in 2× SSC + 30% formamide for 30 min each, followed by five 1× SSC washes. After completion of in situ hybridization, samples were washed with phosphate buffered saline (PBS) and subsequently processed for immunofluorescence. Immunofluorescence was performed on fixed and permeabilized samples with or without in situ hybridization using the following protocol: samples were incubated in biotin-free blocking buffer (4% biotin free BSA in PBS) for 30 min and then incubated for 1.5 h at room temperature or overnight at 4 °C with primary antibodies in blocking buffer. After three washes in PBS for 5 min each, samples were incubated in blocking buffer (4% goat serum in PBS) for 1 to 2 h with secondary antibodies. The following antibodies were used: rabbit anti-biotin (Cell Signaling; 1:1,000), rat anti-mCherry (Abcam; 1:1,000), goat anti-rabbit Alexa 488, and goat anti-rat Alexa 568. Samples were imaged using Zeiss LSM780/880 confocal microscopes and a 63× oil objective. Images spanning the entire volume of a neuron were obtained and analyzed using ImageJ. The distance to the nearest spine was measured by performing line-scan analysis through a punctum of interest to the base of nearby spines. From the value of peak intensity of the mRNA puncta (the centroid) we assessed the recorded the shortest distance as the RNA to spine distance.

For FISH experiments in 1D&E, a similar procedure was performed using Quasar 570 labeled smFISH probes (Stellaris). Forty-four probes per transcript were used. Following wash steps samples were imaged with a scientific-CMOS camera (Leica-DFC9000GT). The exposure time was fixed to 700 ms. A 100× oil objective (HC PL APO 100×/1.47 OIL) was used to record a field-of-view of 133 μm × 133 μm. On dendritic segments, particles were automatically detected based on size (Fiji) and the integrated density of the particles were recorded from 50 mRNA puncta per dendritic segment.

FRAP Translational Reporters. A codon-optimized superfolder GFP was custom synthesized (Eurofins) and cloned into a plasmid backbone driven by a CMV promoter. The 3′UTRs corresponding to the most highly dendritically localized isoforms (41) for *Camk2a*, *β-actin*, and *Psd95* were cloned upstream of a SV40 polyadenylation sequence. sfGFP reporters were transfected into neurons 12 h prior to imaging. Cells were imaged at 63× on a LSM780 (NA 1.4, PSF: 0.240/0.258/0.729), with a temperature-regulated environmental chamber. Cells were maintained in E4 buffer (38) supplemented with B27, Glutamax, and 1× MEM amino acids (Thermofisher). Whole-cell photobleaching was accomplished using a 488-nm argon laser (1.49 mW) with an intensity of 2,900 kW/cm^2 for 40 to 50 s. Cells were imaged at 0.067 Hz for 2 min prior to and 10 min following the bleaching step. Fluorescence intensity was measured in a 50-μm dendritic segment from the raw image. FRAP was calculated from background-corrected fluorescence intensity by normalizing the change in fluorescence ($F–F_0$) to prephotobleaching fluorescence (F_i). Mobile fraction and $t_{1/2}$ values were extracted from data fitted to a one-phase exponential association.

Endogenous FRAP. Venus tagging pORANGE CRISPR/Cas9 constructs (42) were generated from previously described GFP tagging plasmids (Addgene plasmids #131477, #131479, #131484; gifts from Harold MacGillavry, Universiteit Utrecht, Utrecht, Netherlands). Neurons were electroporated (see above) at the day of plating and maintained until DIV 17 to 21 for FRAP experiments. FRAP and imaging was carried out using a Leica DMi8 TIRF microscope. FRAP was performed using a 488-nm laser, providing 7.78-mW/cm^2 intensity. Cells were imaged for 2 min at baseline with a 488-nm LED every 15 s prior to bleaching for a baseline measurement. Whole-cell bleaching was performed with 20 to 30 s of bleaching (PSD-95) or 50 to 70 s of bleaching (CAMK2a and β-ACTIN). Cells were the imaged in epi-fluorescence mode with the LED every 15 s for 60 min. Fluorescence intensity was measured in a 50-μm dendritic segment from the raw image. FRAP was calculated from background-corrected fluorescence intensity by normalizing the change in fluorescence ($F–F_0$) to prephotobleaching fluorescence (F_i). Mobile fraction and $t_{1/2}$ values were extracted from data fitted to a one phase exponential association.

Puro-PLA. Detection of newly synthesized proteins by PLA was performed as previously described (5, 10, 45). Immunostaining using mouse antipuromycin (Kerafast; 1:500) antibody in combination with rabbit anti–β-actin (Abcam; 1:1,000), rabbit anti–PSD-95 (cell signaling technologies; 1:1,000), or rabbit anti-Camk2a (Thermo; 1:1,000) was performed overnight at 4 °C. Following 5× PBS washes, PLA was performed (Sigma). Rabbit PLA^{plus} and mouse PLA^{minus} probes were used. PLA was performed according to the manufacture's guidelines. Following PLA, anti-Map2 immunostaining (guinea pig anti-Map2, Cell Signaling; 1:5,000) was performed to label dendrites. Samples were imaged using a 40× oil objective on a LSM780 or LSM880. *Z*-stacks (0.43 μm) spanned the entire volume of imaged neurons. Images were analyzed using ImageJ. A 100-μm segment of the dendrite was assessed for the number of Puro-PLA puncta and the density of signal was calculated.

Statistics. Statistical significance, the tests performed, and the number of cells/replicates are indicated in the figure legends. Statistical analysis was performed using GraphPad Prism.

Data Availability. Analysis scripts are deposited on GitHub (https://gitlab.mpcdf.mpg.de/mpibrcpo/beacon-tracker). Plasmids will be made available through Addgene. All other data, including sequences used for the molecular beacons, are available in the article and *SI Appendix*.

ACKNOWLEDGMENTS. We thank I. Bartnik, N. Fuerst, A. Staab, D. Vogel, and C. Thum for the preparation of cultured neurons. P.G.D.-A. is supported by the Peter and Traudl Engelhard Stiftung and the Alexander von Humboldt Foundation (USA-1198990-HFST-P). E.M.S. is funded by the Max Planck Society, an Advanced Investigator award from the European Research Council, Deutsche Forschungsgemeinschaft (DFG) CRC 1080: Molecular and Cellular Mechanisms of Neural Homeostasis and DFG CRC 902: Molecular Principles of RNA-based Regulation. This project has received funding from the European Research Council under the European Union's Horizon 2020 research and innovation program (Grant agreement 743216). A.H. is funded by DFG CRC 902: Molecular Principles of RNA-based Regulation.

1. D. C. Dieterich, M. R. Kreutz, Proteomics of the synapse—A quantitative approach to neuronal plasticity. *Mol. Cell. Proteomics* **15**, 368–381 (2016).
2. R. C. Malenka, M. F. Bear, LTP and LTD: An embarrassment of riches. *Neuron* **44**, 5–21 (2004).
3. C. M. Alberini, Transcription factors in long-term memory and synaptic plasticity. *Physiol. Rev.* **89**, 121–145 (2009).
4. S. A. Buffington, W. Huang, M. Costa-Mattioli, Translational control in synaptic plasticity and cognitive dysfunction. *Annu. Rev. Neurosci.* **37**, 17–38 (2014).
5. A. Biever *et al.*, Monosomes actively translate synaptic mRNAs in neuronal processes. *Science* **367**, eaay4991 (2020).
6. H. Kang, E. M. Schuman, A requirement for local protein synthesis in neurotrophin-induced hippocampal synaptic plasticity. *Science* **273**, 1402–1406 (1996).
7. K. M. Huber, M. S. Kayser, M. F. Bear, Role for rapid dendritic protein synthesis in hippocampal mGluR-dependent long-term depression. *Science* **288**, 1254–1257 (2000).
8. J. N. Gelinas, P. V. Nguyen, β-adrenergic receptor activation facilitates induction of a protein synthesis-dependent late phase of long-term potentiation. *J. Neurosci.* **25**, 3294–3303 (2005).
9. K. D. Bradshaw, N. J. Emptage, T. V. P. Bliss, A role for dendritic protein synthesis in hippocampal late LTP. *Eur. J. Neurosci.* **18**, 3150–3152 (2003).

10. A.-S. S. Hafner, P. G. Donlin-Asp, B. Leitch, E. Herzog, E. M. Schuman, Local protein synthesis is a ubiquitous feature of neuronal pre- and postsynaptic compartments. *Science* **364**, eaau3644 (2019).
11. W. B. Smith, S. R. Starck, R. W. Roberts, E. M. Schuman, Dopaminergic stimulation of local protein synthesis enhances surface expression of GluR1 and synaptic transmission in hippocampal neurons. *Neuron* **45**, 765–779 (2005).
12. D. C. Dieterich *et al*., In situ visualization and dynamics of newly synthesized proteins in rat hippocampal neurons. *Nat. Neurosci.* **13**, 897–905 (2010).
13. S. Park *et al*., Elongation factor 2 and fragile X mental retardation protein control the dynamic translation of Arc/Arg3.1 essential for mGluR-LTD. *Neuron* **59**, 70–83 (2008).
14. W. Link *et al*., Somatodendritic expression of an immediate early gene is regulated by synaptic activity. *Proc. Natl. Acad. Sci. U.S.A.* **92**, 5734–5738 (1995).
15. G. L. Lyford *et al*., Arc, a growth factor and activity-regulated gene, encodes a novel cytoskeleton-associated protein that is enriched in neuronal dendrites. *Neuron* **14**, 433–445 (1995).
16. P. K. Todd, K. J. Mack, J. S. Malter, The fragile X mental retardation protein is required for type-I metabotropic glutamate receptor-dependent translation of PSD-95. *Proc. Natl. Acad. Sci. U.S.A.* **100**, 14374–14378 (2003).
17. R. S. Muddashetty, S. Kelić, C. Gross, M. Xu, G. J. Bassell, Dysregulated metabotropic glutamate receptor-dependent translation of AMPA receptor and postsynaptic density-95 mRNAs at synapses in a mouse model of fragile X syndrome. *J. Neurosci.* **27**, 5338–5348 (2007).
18. G. Aakalu, W. B. Smith, N. Nguyen, C. Jiang, E. M. Schuman, Dynamic visualization of local protein synthesis in hippocampal neurons. *Neuron* **30**, 489–502 (2001).
19. S. Das, R. H. Singer, Y. J. Yoon, The travels of mRNAs in neurons: Do they know where they are going? *Curr. Opin. Neurobiol.* **57**, 110–116 (2019).
20. S. Baumann *et al*., A reconstituted mammalian APC-kinesin complex selectively transports defined packages of axonal mRNAs. *Sci. Adv.* **6**, eaaz1588 (2020).
21. J. W. B. Hershey, N. Sonenberg, M. B. Mathews, Principles of translational control: An overview. *Cold Spring Harb. Perspect. Biol.* **4**, a011528 (2012).
22. Y. J. Yoon *et al*., Glutamate-induced RNA localization and translation in neurons. *Proc. Natl. Acad. Sci. U.S.A.* **113**, E6877–E6886 (2016).
23. M. Doyle, M. A. Kiebler, Mechanisms of dendritic mRNA transport and its role in synaptic tagging. *EMBO J.* **30**, 3540–3552 (2011).
24. K. E. Bauer *et al*., Live cell imaging reveals 3′-UTR dependent mRNA sorting to synapses. *Nat. Commun.* **10**, 3178 (2019).
25. H. Y. Park *et al*., Visualization of dynamics of single endogenous mRNA labeled in live mouse. *Science* **343**, 422–424 (2014).
26. M. S. Rook, M. Lu, K. S. Kosik, CaMKIIalpha 3′ untranslated region-directed mRNA translocation in living neurons: Visualization by GFP linkage. *J. Neurosci.* **20**, 6385–6393 (2000).
27. S. Das, H. C. Moon, R. H. Singer, H. Y. Park, A transgenic mouse for imaging activity-dependent dynamics of endogenous Arc mRNA in live neurons. *Sci. Adv.* **4**, eaar3448 (2018).
28. I. J. Cajigas *et al*., The local transcriptome in the synaptic neuropil revealed by deep sequencing and high-resolution imaging. *Neuron* **74**, 453–466 (2012).
29. A. R. Buxbaum, B. Wu, R. H. Singer, Single β-actin mRNA detection in neurons reveals a mechanism for regulating its translatability. *Science* **343**, 419–422 (2014).
30. R. S. Muddashetty *et al*., Reversible inhibition of PSD-95 mRNA translation by miR-125a, FMRP phosphorylation, and mGluR signaling. *Mol. Cell* **42**, 673–688 (2011).
31. J. S. Rinne, T. P. Kaminski, U. Kubitscheck, A. Heckel, Light-inducible molecular beacons for spatio-temporally highly defined activation. *Chem. Commun. (Camb.)* **49**, 5375–5377 (2013).
32. B. Turner-Bridger *et al*., Single-molecule analysis of endogenous β-actin mRNA trafficking reveals a mechanism for compartmentalized mRNA localization in axons. *Proc. Natl. Acad. Sci. U.S.A.* **115**, E9697–E9706 (2018).
33. K. S. Kosik, Life at low copy number: How dendrites manage with so few mRNAs. *Neuron* **92**, 1168–1180 (2016).
34. K. W. Yau *et al*., Dendrites in vitro and in vivo contain microtubules of opposite polarity and axon formation correlates with uniform plus-end-out microtubule orientation. *J. Neurosci.* **36**, 1071–1085 (2016).
35. M. E. Azzam, I. D. Algranati, Mechanism of puromycin action: Fate of ribosomes after release of nascent protein chains from polysomes. *Proc. Natl. Acad. Sci. U.S.A.* **70**, 3866–3869 (1973).
36. A. P. Grollman, Inhibitors of protein biosynthesis. II. Mode of action of anisomycin. *J. Biol. Chem.* **242**, 3226–3233 (1967).
37. T. E. Graber *et al*., Reactivation of stalled polyribosomes in synaptic plasticity. *Proc. Natl. Acad. Sci. U.S.A.* **110**, 16205–16210 (2013).
38. A.-S. Hafner *et al*., Lengthening of the Stargazin cytoplasmic tail increases synaptic transmission by promoting interaction to deeper domains of PSD-95. *Neuron* **86**, 475–489 (2015).
39. Y. Ramiro-Cortés, I. Israely, Long lasting protein synthesis- and activity-dependent spine shrinkage and elimination after synaptic depression. *PLoS One* **8**, e71155 (2013).
40. J. D. Pédelacq, S. Cabantous, T. Tran, T. C. Terwilliger, G. S. Waldo, Engineering and characterization of a superfolder green fluorescent protein. *Nat. Biotechnol.* **24**, 79–88 (2006).
41. G. Tushev *et al*., Alternative 3′ UTRs modify the localization, regulatory potential, stability, and plasticity of mRNAs in neuronal compartments. *Neuron* **98**, 495–511.e6 (2018).
42. J. Willems *et al*., ORANGE: A CRISPR/Cas9-based genome editing toolbox for epitope tagging of endogenous proteins in neurons. *PLoS Biol.* **18**, e3000665 (2020).
43. T. Nagai *et al*., A variant of yellow fluorescent protein with fast and efficient maturation for cell-biological applications. *Nat. Biotechnol.* **20**, 87–90 (2002).
44. M. F. Ifrim, K. R. Williams, G. J. Bassell, Single-molecule imaging of PSD-95 mRNA translation in dendrites and its dysregulation in a mouse model of fragile X syndrome. *J. Neurosci.* **35**, 7116–7130 (2015).
45. S. tom Dieck *et al*., Direct visualization of newly synthesized target proteins in situ. *Nat. Methods* **12**, 411–414 (2015).
46. A. Biever, P. G. Donlin-Asp, E. M. Schuman, Local translation in neuronal processes. *Curr. Opin. Neurobiol.* **57**, 141–148 (2019).
47. Z. B. Katz *et al*., Mapping translation 'hot-spots' in live cells by tracking single molecules of mRNA and ribosomes. *eLife* **5**, e10415 (2016).
48. R. Fritzsche *et al*., Interactome of two diverse RNA granules links mRNA localization to translational repression in neurons. *Cell Rep.* **5**, 1749–1762 (2013).
49. E. F. Spence, S. H. Soderling, Actin out: Regulation of the synaptic cytoskeleton. *J. Biol. Chem.* **290**, 28613–28622 (2015).
50. M. E. Klein, P. E. Castillo, B. A. Jordan, Coordination between translation and degradation regulates inducibility of mGluR-LTD. *Cell Rep.* **10**, 1459–1466 (2015).
51. G. V. Di Prisco *et al*., Translational control of mGluR-dependent long-term depression and object-place learning by eIF2α. *Nat. Neurosci.* **17**, 1073–1082 (2014).
52. J. Lisman, H. Schulman, H. Cline, The molecular basis of CaMKII function in synaptic and behavioural memory. *Nat. Rev. Neurosci.* **3**, 175–190 (2002).
53. H. Yasuda, A. L. Barth, D. Stellwagen, R. C. Malenka, A developmental switch in the signaling cascades for LTP induction. *Nat. Neurosci.* **6**, 15–16 (2003).
54. D. J. Linden, A. Routtenberg, The role of protein kinase C in long-term potentiation: A testable model. *Brain Res. Brain Res. Rev.* **14**, 279–296 (1989).
55. G. Y. Hu *et al*., Protein kinase C injection into hippocampal pyramidal cells elicits features of long term potentiation. *Nature* **328**, 426–429 (1987).
56. G. M. Thomas, R. L. Huganir, MAPK cascade signalling and synaptic plasticity. *Nat. Rev. Neurosci.* **5**, 173–183 (2004).
57. H. Y. Man *et al*., Activation of PI3-kinase is required for AMPA receptor insertion during LTP of mEPSCs in cultured hippocampal neurons. *Neuron* **38**, 611–624 (2003).
58. C. A. Hoeffer, E. Klann, mTOR signaling: At the crossroads of plasticity, memory and disease. *Trends Neurosci.* **33**, 67–75 (2010).
59. M. W. Salter, L. V. Kalia, Src kinases: A hub for NMDA receptor regulation. *Nat. Rev. Neurosci.* **5**, 317–328 (2004).
60. S. Nakanishi, Metabotropic glutamate receptors: Synaptic transmission, modulation, and plasticity. *Neuron* **13**, 1031–1037 (1994).
61. C. Lüscher, K. M. Huber, Group 1 mGluR-dependent synaptic long-term depression: Mechanisms and implications for circuitry and disease. *Neuron* **65**, 445–459 (2010).
62. B. G. Mockett *et al*., Calcium/calmodulin-dependent protein kinase II mediates group I metabotropic glutamate receptor-dependent protein synthesis and long-term depression in rat hippocampus. *J. Neurosci.* **31**, 7380–7391 (2011).
63. R. Schnabel, I. C. Kilpatrick, G. L. Collingridge, An investigation into signal transduction mechanisms involved in DHPG-induced LTD in the CA1 region of the hippocampus. *Neuropharmacology* **38**, 1585–1596 (1999).
64. J. M. Rhee *et al*., In vivo imaging and differential localization of lipid-modified GFP-variant fusions in embryonic stem cells and mice. *Genesis* **44**, 202–218 (2006).

Reference [II]: „Visible light-activatable Q-dye molecular beacons for long-term mRNA monitoring in neurons”

Klimek, R.; Donlin-Asp, P. G.; Polisseni, C.; Hanff, V.; Schuman, E. M.; Heckel, A., Chem. Commun. **2021**, *57*, 12683-12686.

Author contributions:

Robin Klimek:

- chemical synthesis of visible-light activatable phosphoramidites
- design and synthesis of light-activatable molecular beacons
- preparation of molecular beacons for live-cell use
- fluorescence measurements *in vitro*
- photolysis experiments *in vitro*
- wrote and edited the manuscript

Paul G. Donlin-Asp:

- transfected light-activatable molecular beacons in neurons
- imaged mRNA-MB hybrids
- analyzed puncta for mRNA monitoring
- wrote and edited the manuscript

Claudio Polisseni:

- developed analysis tool pipeline
- designed cell experiments
- edited the manuscript

Vanessa Hanff:

- chemical synthesis of light-activatable molecular beacons
- fluorescence measurements *in vitro*
- edited the manuscript

Erin M. Schuman:

- supervised project and experiments
- edited the manuscript

Alexander Heckel:

- supervised project and experiments
- edited the manuscript

ChemComm

COMMUNICATION

View Article Online
View Journal | View Issue

Cite this: *Chem. Commun.*, 2021, 57, 12683

Received 12th October 2021,
Accepted 4th November 2021

DOI: 10.1039/d1cc05664f

rsc.li/chemcomm

Visible light-activatable Q-dye molecular beacons for long-term mRNA monitoring in neurons†

Robin Klimek,[a] Paul G. Donlin-Asp,[b] Claudio Polisseni,[b] Vanessa Hanff,[a] Erin M. Schuman*[b] and Alexander Heckel *[a]

Herein, we present a new class of Q-dye molecular beacons (MBs) that can be locally activated with visible light in hippocampal neurons. Our novel architecture increases the available monitoring time for neuronal mRNA from several minutes to 14 hours, since a lower light-sampling rate is required for tracking.

Intracellular RNA transport and regulation has received a lot of attention in recent years.[1–3] Today, a variety of tools are available to visualize or chemically label different RNA species.[4,5] Most of them can be categorized into (i) fluorescent proteins, (ii) fluorophore-aptamer pairs, (iii) dye and quencher pairs, and (iv) hybridization-based oligonucleotides – as recently reviewed.[6] However, many techniques are only suitable for labelling and visualizing non-endogenous RNA. The most prominent visualization tool for endogenous RNA is molecular beacons (MBs).[7] MBs consist of a stem-loop structure that is equipped with a fluorophore and a quencher at the opposite ends. So far, MBs have been used for monitoring miRNA,[8] mRNA,[9,10] rRNA[11,12] and many other RNA species. While molecular beacons are a very useful tool for monitoring bulk RNA, much more sophisticated applications are possible as well. We have shown that single molecule feed-back tracking allows to study mobility state transitions in RNA trajectories.[13] Furthermore, we used molecular beacons to show differential regulation of local mRNA dynamics following long-term potentiation and depression in neurons.[9]

Analyses using MBs can be taken to an even more advanced level: the application of MBs that can be activated with light allowing the user to precisely control the location and starting time of the monitoring. This technique has the potential to greatly improve the quality of the analysis by strongly reducing background fluorescence outside the activation area. In general, the regulation of biomolecules with light has attracted much attention in recent years.[14–19] So far, several attempts have been made to make MBs light-activatable.[20–24] For monitoring mRNA dynamics, light-activatable Q-dye beacons[25] are particularly suitable (Fig. 1). The fluorophore of a Q-dye beacon is covalently linked to a second quencher *via* a photolabile protecting group. This quencher can be cleaved from the MB with light, independent of the hybridization state. The first advantage is a very low background fluorescence in the non-activated state. Second, they can bind to the target RNA even before activation and thus do not have a kinetic hybridization barrier. Third, Q-dye beacons can be prepared quickly and efficiently *via* solid-phase synthesis. Only when the beacon

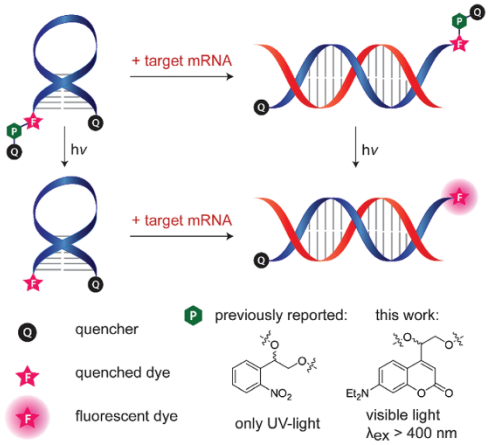

Fig. 1 General functionality of Q-dye molecular beacons (MBs). The fluorophore is covalently linked to a second quencher *via* a photolabile protecting group (PPG). Only when the beacon has hybridized with the RNA as well as been activated with light does it emit a fluorescent signal.

[a] *Institute of Organic Chemistry and Chemical Biology, Goethe-University Frankfurt, Max-von-Laue-Straße 9, Frankfurt am Main 60438, Germany. E-mail: heckel@uni-frankfurt.de*
[b] *Max Planck Institute for Brain Research, Max-von-Laue Str. 4, Frankfurt am Main 60438, Germany. E-mail: erin.schuman@brain.mpg.de*

† Electronic supplementary information (ESI) available. See DOI: 10.1039/d1cc05664f

has hybridized with the RNA and been activated with light it shows a fluorescent signal. Despite all the positive properties mentioned, a clear disadvantage of the Q-dye MBs used so far is the activation wavelength, which was only in the UV (ultraviolet) range. Longer irradiation times of UV light can cause damage in organisms ranging from microorganisms to humans.[26–28] Due to the potential cell damage, the Q-dye beacons described so far can only be used in biological applications to a limited extent, *i.e.* using only short observation times after the irradiation.

In this work, we show how the limitation caused by the high-energy wavelength can be circumvented. By using a different photocage, we shifted the wavelength needed for activation from the UV to the visible spectrum. In direct comparison with Q-dye beacons known from literature,[25] we demonstrate that cell damage can be significantly reduced by light activation with lower energy light. We adapt the concept to an application in neurons and show its advantages in the tracking of mRNAs. Spatially resolved activation of RNA subpopulations allowed us, for the first time, to drastically reduce the light sampling rate needed for RNA monitoring. Using this technique, we were able to increase the observation time of neuronal RNA from about 12–30 minutes (conventional MBs from literature)[9,10] to 840 minutes (Q-dye beacons in this work). It is important to note that with such long experiment times UV light must be avoided, since phototoxic effects would otherwise dominate the cellular behaviour.

To prepare Q-dye MBs that can be activated with light of more than 405 nm, it was necessary to synthesize a suitable photolabile linker. Here, it is important that the photolabile linker can be activated with lower energy light, but at the same time the absorption spectrum does not overlap with that of the fluorophore and quencher used. For this reason, we chose a 7-diethylaminocoumarin (DEACM) derivative (**1**) (see Fig. 2), which can induce a strand break by absorbing light at 405 nm.[29] At the same time, most far-red fluorophores used in biological systems show negligible extinction at this wavelength. This is important in order to avoid unintended, premature activation of the MB due to probing of the fluorophore.

The linker synthesis starting from commercially available materials is shown in Fig. 2 (detailed information see ESI†). 7-Diethylaminocoumarin (**2**) reacts with DMF–DMA to enamine (**3**). Oxidative cleavage of the exocyclic double bond with $NaIO_4$ results in aldehyde (**4**) which can be reduced to alcohol (**5**) using $NaBH_4$. The following reaction with 4-methylsulfonic acid chloride leads to chloride (**6**). Subsequent Wittig reaction of (**6**) with triphenylphosphine and formaldehyde led to alkene (**7**), which was oxidized to diol (**8**) in an Upjohn dihydroxylation using OsO_4 and *N*-methylmorpholine-*N*-oxide. To use the coumarin in RNA solid phase synthesis, the primary hydroxy group of (**8**) was selectively tritylated with DMTr-Cl. The resulting compound (**9**) was reacted with 2-cyanoethoxy-*N*,*N*-diisopropyl-aminochlorophosphine yielding in phosphoramidite (**1**).

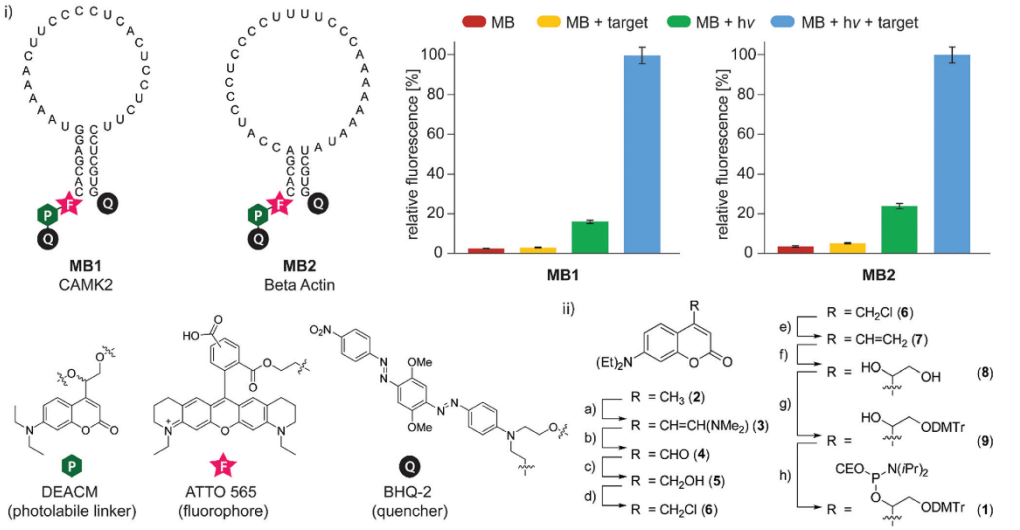

Fig. 2 (i) Structures, chemical modifications and target mRNAs of **MB1** and **MB2** (top). Fluorescence measurements of **MB1** and **MB2** (100 pmol, 100 µL, 1 µM) in buffer (135 mM NaCl, 5.4 mM KCl, 1 mM $MgCl_2$, 5 mM HEPES, pH 7.4). Irradiation was performed with a 405 nm LED until the maximum fluorescence did not increase upon further light exposure (15–25 min). (ii) Synthesis of phosphoramidite (**1**). (a) *N*,*N*-Dimethylformamide-dimethylacetal, DMF, 94%. (b) $NaIO_4$, THF/H_2O, 97%. (c) $NaBH_4$, EtOH, 64%. (d) 4-Toluenesulfonyl chloride, DIPEA, DCM, 81%. (e) **1**. Triphenylphosphine, MeCN. 2. Formaldehyde, H_2O, 65%. (f) OsO_4, NMO, acetone, 59%. (g) 4,4′-Dimethoxytrityl chloride, DIPEA, THF, 72%. (h) 2-Cyanoethoxy-*N*,*N*-diisopropylaminochlorophosphine, DIPEA, DCM, 95%.

For solid-phase RNA synthesis, chemically modified 2′-*O*-methyl RNA (2′-OMe) building blocks were used to effectively protect the MBs against endonuclease activity. We designed MBs with loop lenghts of 25 and 28 nucleotides and stems of five and seven base pairs. To only emit a fluorescent signal when they are bound to their target, it is important to carefully select the fluorophore/quencher pair. Therefore, it is necessary to select fluorophores with a high photostability, to ensure long tracking times in the cells. The beacons used here are equipped with ATTO565 as fluorophore and BHQ2 as quencher. We focused on CamKII and Beta actin mRNA as target sequences. These are particularly suitable for investigation because their dynamics in cultured hippocampal neurons have already been examined.[9] Details of solid-phase synthesis are described in the ESI.†

After successful preparation of molecular beacons **MB1** (target: CAMK2) and **MB2** (target: Beta actin), their fluorescence properties were evaluated *in vitro* (Fig. 2). As expected, the MBs did not show significant background fluorescence. The background intensity was 2.5% and 3.6%, respectively, compared to the maximum fluorescence after uncaging and addition of the target. When target RNA was added, the fluorescence slightly increased to 3.0% and 5.2%. This was the first evidence of the quenching efficiency of the covalently attached quencher. Even when both ends of the stem were separated, the fluorophore emission remained quenched. This result further demonstrates that **MB1** and **MB2** are already bound before light activation. Consequently, kinetic binding delays are avoided, and it allows for the fast visualization of the bound mRNA in real-time experiments. The second indication of the additional quencher benefit was the fluorescence intensity after excitation with 405 nm light. It was expected that background fluorescence would increase when the second quencher was cleaved. And indeed, after photolysis of the covalently linked BHQ-2 the background fluorescence increased to about 17% and 24% of the maximum intensity before mRNA addition. These values are in a range typical for conventional MBs. Finally, when both conditions, light activation and addition of target, were met, there was a very significant increase in fluorescence (40-fold for **MB1** and 28-fold for **MB2**). It is clear that the quencher linked *via* coumarin **1** has a higher efficiency than the quencher at the opposite end of the strand. This is due to the close proximity of the two chromophores and the resulting possibility of contact quenching. It clearly indicates hybridization with the complementary RNA strand, which was ultimately visualized by a light pulse.

However, more important than the fluorescence performance *in vitro* are the characteristics of the light-activatable MBs in living cells (Fig. 3). Therefore, we transfected **MB1** and **MB2** into cultured hippocampal neurons (Fig. 3i and ii). As expected, little background fluorescence was detected in the neuronal cell body before light-activation (ESI† Videos S1 and S2). On the one hand, this shows effective quenching by the second, photolabile-linked quencher. It also indicates that no MB was degraded by nucleases between transfection and monitoring.

Light activation was performed within the cell body. The 405 nm laser pulse allowed for the visualization of subpopulations of MBs hybridized with the target mRNA. Successful light-activation allowed tracking of the now visible mRNAs by

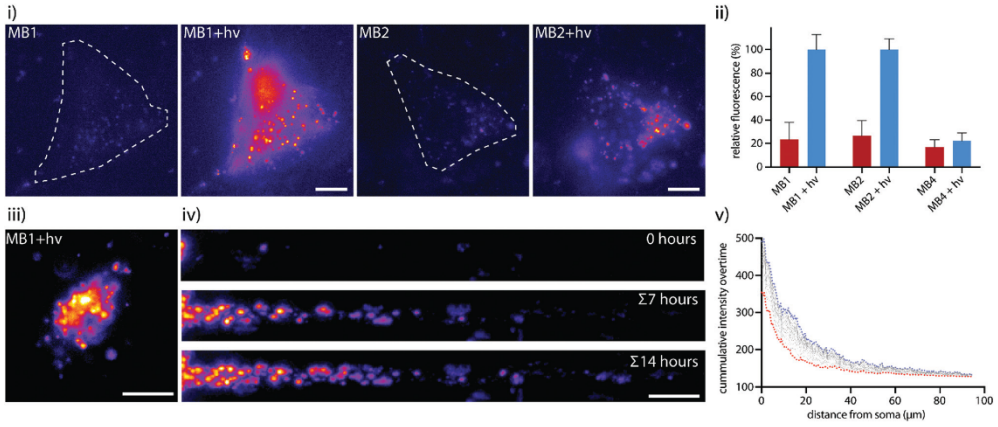

Fig. 3 (i) Hippocampal neuronal somas transfected with **MB1** (left, ESI† Video S1) and **MB2** (right, ESI† Video S2) before and after irradiation with 405 nm illumination. Scale bar = 5 µm. (ii) Quantification of soma fluorescence intensity of **MB1**, **MB2** and **MB4** before and after 405 nm illumination. Intensity of **MB4** is scaled relative to intensity of **MB1**. n = 50 cells per condition. (iii) A neuronal soma transfected with **MB1** (ESI† Video S3) post illumination which was imaged every ten minutes for 14 hours (ESI† Videos S4 and S5). Scale bar = 10 µm. (iv) Visualization of mRNA populating a dendrite from the neuron shown in (iii), the signal in the dendrite right after 405 illumination (0 hours); the sum of the signal for the first 7 hours (Σ7 hours) and the sum of the signal for the entire 14 hours (Σ14 hours). Scale bar = 5 µm. (v) Quantification of (iv), red line = 0 hours, blue line = Σ14 hours, grey lines = Σ1–13 hours. n = 13 cells.

repeated excitation of the fluorophore. In previous studies, individual MBs were only monitored over periods of minutes.[9,10] This was the result of a high light sampling rate of $\geq 1\ s^{-1}$ necessary to precisely track single molecules. Frequent excitation resulted in rapid bleaching of the attached chromophores. Here, by visualizing only a local subpopulation of RNAs from a defined spatial origin due to the localized uncaging laser irradiation, the light sampling rate could be reduced to $1.7 \times 10^{-3}\ s^{-1}$ (every 10 min). The reduced excitation frequency allowed us to monitor the locally activated mRNAs for 14 hours and more (Fig. 3iii–v and ESI† Videos S3–S5). In previous studies, RNA monitoring was only possible for a few minutes.[9,10] During the whole observation period, we did not observe any significant photobleaching.

Maximum intensity projections over time are shown (Fig. 3iii, $\sum$7 hours & $\sum$14 hours) to illustrate how these beacons can be used to monitor mRNA dynamics over hours. We used these 14+ hours of data on mRNA dynamics to assess how long it takes to populate an individual dendrite with Beta actin mRNA. Plotting the intensity of the dendrite overtime (Fig. 3v), we calculated the $t_{1/2}$ to populate the dendrite was around 3 hours, which is in agreement with the reported half-life of Beta actin mRNA in neurons of around 4 hours.[30] These data strongly emphasize the biological applicability of our novel Q-dye beacons in studying the dynamics of subcellularly localized mRNAs overtime.

To highlight the high benefit of the new coumarin protecting group, which can be activated with visible light, a reference beacon to **MB2** was synthesized. **MB3** (see ESI†) has the same sequence and structure as **MB2**, but carries a nitrobenzyl-based protecting group instead of coumarin. Light activation in the cell body was also possible for **MB3**. However, it can be clearly seen that the high light intensities required for this cause severe cell damage in the case of **MB3**. The light-activated RNA hybrids showed little movement in the cell (ESI† Videos S6–S8). Furthermore, the cell died after a short time (ESI† Videos S7 and S8). This observation underscores the high benefit of the coumarin protecting group in **MB1** and **MB2** that can be activated with visible light. In both cases, the neuron remained alive for the complete observation period of more than 14 hours. Last, we synthesized and transfected a Q-dye beacon **MB4** (see SI) against GFP mRNA as a negative control. As expected, no significant fluorescence increase was observed upon light-activation in cells (Fig. 3ii and ESI† Video S9). This verifies target specificity of our new Q-dye beacons.

In summary, we have shown that the newly designed Q-dye MBs in this work are excellent candidates for mRNA monitoring. In contrast to all light-activatable MBs known from literature,[20,22,25] they can be uncaged not only with UV but also with visible light $\geq$ 405 nm. This greatly improves the viability of photo-exposed cells compared to conventional Q-dye beacons. Furthermore, we demonstrated the clear benefit of the fluorescent probes presented here for tracking neuronal mRNA over periods of more than 14 hours without significant photobleaching. We anticipate that the MBs shown here will find broad applications in chemical biology, biochemistry, and neuroscience.

The manuscript was written through contributions of all authors. All authors have given approval to the final version of the manuscript.

Open Access funding provided by the Max Planck Society.

Conflicts of interest

There are no conflicts of interest to declare.

Notes and references

1 A. R. Buxbaum, G. Haimovich and R. H. Singer, *Nat. Rev. Mol. Cell Biol.*, 2015, **16**, 95–109.
2 S. Das, M. Vera, V. Gandin, R. H. Singer and E. Tutucci, *Nat. Rev. Mol. Cell Biol.*, 2021, 1–22.
3 S. H. Kim, M. Vieira, J. Y. Shim, H. Choi and H. Y. Park, *RNA Biol.*, 2019, **16**, 1108–1118.
4 K. Rau and A. Rentmeister, *ACS Cent. Sci.*, 2017, **3**, 701–707.
5 H. Depmeier, E. Hoffmann, L. Bornewasser and S. Kath-Schorr, *ChemBioChem*, 2021, **22**, 1–23.
6 E. Braselmann, C. Rathbun, E. M. Richards and A. E. Palmer, *Cell Chem. Biol.*, 2020, **27**, 891–903.
7 S. Tyagi and F. R. Kramer, *Nat. Biotechnol.*, 1996, **14**, 303–308.
8 N. Bidar, F. Oroojalian, B. Baradaran, S. Eyvazi, M. Amini, A. Jebelli, S. S. Hosseini, P. Pashazadeh-Panahi, A. Mokhtarzadeh and M. de la Guardia, *TrAC, Trends Anal. Chem.*, 2020, **131**, 116021.
9 P. G. Donlin-Asp, C. Polisseni, R. Klimek, A. Heckel and E. M. Schuman, *Proc. Natl. Acad. Sci. U. S. A.*, 2021, **118**, 2017578118.
10 B. Turner-Bridger, M. Jakobs, L. Muresan, H. H. W. Wong, K. Franze, W. A. Harris and C. E. Holt, *Proc. Natl. Acad. Sci. U. S. A.*, 2018, **115**, E9697–E9706.
11 C. Xi, M. Balberg, S. A. Boppart and L. Raskin, *Appl. Environ. Microbiol.*, 2003, **69**, 5673–5678.
12 Y. V. Gerasimova and D. M. Kolpashchikov, *Biosens. Bioelectron.*, 2013, **41**, 386–390.
13 J.-H. Spille, T. P. Kaminski, K. Scherer, J. S. Rinne, A. Heckel and U. Kubitscheck, *Nucleic Acids Res.*, 2015, **43**, e14.
14 J. Thevarpadam, I. Bessi, O. Binas, D. P. N. Gonçalves, C. Slavov, H. R. A. Jonker, C. Richter, J. Wachtveitl, H. Schwalbe and A. Heckel, *Angew. Chem., Int. Ed.*, 2016, **55**, 2738–2742.
15 F. Schäfer, J. Wagner, A. Knau, S. Dimmeler and A. Heckel, *Angew. Chem., Int. Ed.*, 2013, **52**, 13558–13561.
16 C. Brieke, F. Rohrbach, A. Gottschalk, G. Mayer and A. Heckel, *Angew. Chem., Int. Ed.*, 2012, **51**, 8446–8476.
17 N. Ankenbruck, T. Courtney, Y. Naro and A. Deiters, *Angew. Chem., Int. Ed.*, 2018, **57**, 2768–2798.
18 R. Weinstain, T. Slanina, D. Kand and P. Klán, *Chem. Rev.*, 2020, **120**, 13135–13272.
19 A. Chakrapani, V. V. Hausnerová, O. Ruiz-Larrabeiti, R. Pohl, L. Krásný and M. Hocek, *Org. Lett.*, 2020, **22**, 9081–9085.
20 Z. Zou, Z. Luo, X. Xu, S. Yang, Z. Qing, J. Liu and R. Yang, *TrAC, Trends Anal. Chem.*, 2020, **125**, 115811.
21 R. Klimek, M. Wang, V. R. McKenney, E. M. Schuman and A. Heckel, *Chem. Commun.*, 2021, **57**, 615–618.
22 L. Yang and I. J. Dmochowski, *Molecules*, 2021, **26**, 1481.
23 K. Ballabh Joshi, A. Vlachos, V. Mikat, T. Deller and A. Heckel, *Chem. Commun.*, 2012, **48**, 2746–2748.
24 C. Wang, Z. Zhu, Y. Song, H. Lin, C. J. Yang and W. Tan, *Chem. Commun.*, 2011, **47**, 5708–5710.
25 J. S. Rinne, T. P. Kaminski, U. Kubitscheck and A. Heckel, *Chem. Commun.*, 2013, **49**, 5375–5377.
26 H. Farrell, J. Hayes, J. Laffey and N. Rowan, *J. Microbiol. Methods*, 2011, **84**, 317–326.
27 S. Nakajima, L. Lan, S. Kanno, M. Takao, K. Yamamoto, A. P. M. Eker and A. Yasui, *J. Biol. Chem.*, 2004, **279**, 46674–46677.
28 R. P. Sinha and D.-P. Häder, *Photochem. Photobiol. Sci.*, 2002, **1**, 225–236.
29 X. M. M. Weyel, M. A. H. Fichte and A. Heckel, *ACS Chem. Biol.*, 2017, **12**, 2183–2190.
30 G. Tushev, C. Glock, M. Heumüller, A. Biever, M. Jovanovic and E. M. Schuman, *Neuron*, 2018, **98**(49–511), e6.

Reference [III]: „ Photo-tethered molecular beacons for superior light induction”

Klimek, R.; Wang, M.; McKenney, V. R.; Schuman, E. M.; Heckel, A., Chem. Commun. **2021**, *57* (5), 615–618.

Author contributions:

Robin Klimek:

- chemical synthesis of photocleavable phosphoramidites
- design and synthesis of non-light-activatable and light-activatable molecular beacons
- analytical HPLC and mass-spectrometry experiments of synthesized oligonucleotides
- preparation of molecular beacons for live-cell use
- fluorescence measurements *in vitro*
- photolysis experiments *in vitro*
- wrote and edited the manuscript

Mantian Wang:

- designed molecular beacons
- transfected light-activatable molecular beacons in neurons
- imaged miRNA-MB hybrids
- performed uncaging experiments in neurons
- wrote and edited the manuscript

Vivien R. McKenney:

- solid-phase synthesis of oligonucleotides
- preparation of molecular beacons for live-cell use
- fluorescence experiments *in vitro*
- edited the manuscript

Erin M. Schuman:

- supervised project and experiments
- edited the manuscript

Alexander Heckel:

- supervised project and experiments
- edited the manuscript

ChemComm

COMMUNICATION

View Article Online
View Journal | View Issue

Cite this: *Chem. Commun.*, 2021, **57**, 615

Received 7th October 2020,
Accepted 1st December 2020

DOI: 10.1039/d0cc06704k

rsc.li/chemcomm

Photo-tethered molecular beacons for superior light-induction†

Robin Klimek,‡[a] Mantian Wang,‡[b] Vivien R. McKenney,[a] Erin M. Schuman*[b] and Alexander Heckel *[a]

We developed a superior class of light-activatable molecular beacons with photo-tethered loop regions. Two simple modifications and probe cyclisation prevent the molecular beacon from hybridising with the target RNA before light-activation. Full activity of the molecular beacon is elicited upon illumination with 365 nm light.

Many biochemical processes, such as DNA transcription, RNA processing or protein expression require precise spatial and temporal regulation. The study of such biological processes is enabled and enhanced by biochemical tools that can be locally activated. Hence, photocaging strategies have become powerful methods in chemical biology.[1–5] Using light as an external trigger, caged biomolecules can be activated with high spatiotemporal resolution and have provided insights into many biochemical processes such as protein dimerisation,[6] DNA recombination,[7] DNA transcription[8] or transmembrane porin activity.[9]

One spatially and temporally regulated biological process is the subcellular localisation of RNA molecules.[10,11] To investigate RNA dynamics in living cells, fluorescent probes have been developed for RNA visualisation.[12–14] A widely used class of probes are the molecular beacons (MBs).[15] MBs consist of an oligonucleotide strand that is complementary to the target RNA sequence (loop region). Two short nucleotide sequences at the 3′ and 5′ end of the MB prevent the binding of the MB to the target RNA by forming a stem. Furthermore, the MB is equipped with a fluorescent reporter and a quencher at either end, which enable the visualisation of successful target RNA binding. Tyagi and Kramer[16] showed that MBs only emit a hybridisation-sensing fluorophore signal when they are bound to the target DNA or RNA. However, MBs fluoresce immediately once they find their target after transfection. To control the activity of MBs with spatial and temporal resolution, three types of light-activatable MBs have been developed in the past: The Tan group introduced a photolabile linker between hybridisation-sensing fluorophore and quencher to prevent the binding of the MB to the target sequence.[17] In this design, however, the loop region of the MB remained partially accessible for the target DNA sequence, hence a notable fluorescence increase was observed before light-activation. This MB design was adopted in a related study by Dmochowski *et al.*, that improved synthesis of cyclised MBs.[18] Our group also synthesised probes with caged nucleobases in the loop-region.[19] The caged oligonucleotides were prevented from forming Watson–Crick base pairs until the photolabile protecting groups were removed with light. This approach resulted in less background signal before activation when compared to the Tan study. However, the disadvantage of this method was the high number of photocages required to effectively prevent the binding of the target RNA before light-activation (seven cages for a 19 nt loop). With this design, the incomplete removal of all photocages can lead to the formation of partially activated MB intermediates. Moreover, the high light intensities required for light-activation of several photocages can lead to photodamage of biological systems.[20] In an effort to increase the signal-to-noise ratio of the hybridisation-sensing fluorophore, our group inserted a photolabile linker between the fluorophore and a second quencher.[21] However, this caging strategy did not prevent the MB from hybridising to the target sequence before photo-activation, but rather allowed the experimenter to control the visualisation of labelled RNA with high spatiotemporal resolution.

In this work, we developed photo-tethered molecular beacons (ptMBs) that circumvent the limitations of the above described approaches (Fig. 1). ptMBs feature a photolabile, intramolecular circularisation. Two phosphoramidites with an alkyne-modified photolabile protecting group[22] are installed in the loop-region *via* solid-phase synthesis. Circularisation (photo-tethering) is achieved by copper-catalysed cycloaddition with a bisazide.[23]

[a] *Goethe University Frankfurt, Institute for Organic Chemistry and Chemical Biology, Max-von-Laue Str. 9, 60438 Frankfurt a.M, Germany. E-mail: heckel@uni-frankfurt.de*
[b] *Max Planck Institute for Brain Research, Max-von-Laue-Str. 4, 60438 Frankfurt a.M, Germany*

† Electronic supplementary information (ESI) available. See DOI: 10.1039/d0cc06704k

‡ Authors contributed equally to this work.

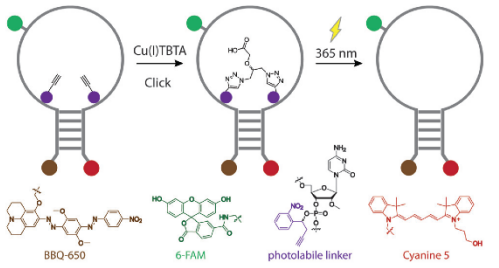

Fig. 1 Functionality of photo-tethered molecular beacons (ptMBs). Fluorophore (red) and quencher (brown) are attached at opposite ends of the stem. A second fluorescent reporter (green) is installed in the loop-region. Two alkyne-modified photolabile nitrobenzyl protecting groups (purple) are circularised *via* Cu(I)-catalysed cycloaddition. The resulting ptMB is not able to form a duplex with target RNA. After illumination with 365 nm light, the photo-tether is cleaved and full functionality of the MB is restored.

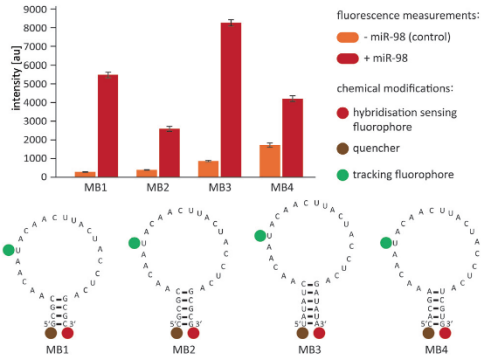

Fig. 2 Fluorescence measurements and predicted secondary structures of **MB1–MB4** in absence and presence of target miR-98 in brain buffer at 37 °C (50 pmol, 100 µL, 500 nM, experiment repeated 5×).

The tethered MB is unable to bind the target RNA sequence, due to the high persistence length of a duplex compared to a single strand. Upon UV-light exposure, the photo-tether is cleaved off and the MB hybridises to its target sequence. The addition of a second fluorophore enables the live-tracking of the MB. Moreover, the co-localisation of the tracking and hybridisation signal can be used to distinguish true hybridisation events from false positive signals (induced, for example, by nuclease degradation).[24] A full 2′OMe-RNA backbone is employed to increase the MBs' nuclease stability and affinity towards target RNA for *in vivo* use. For hybridisation-sensing, cyanine-5 and BBQ-650 are used. 6-FAM is installed in the loop-region for tracking. We tested the efficiency of the ptMBs by targeting miR-98 in primary cultured hippocampal neurons.

To determine an optimal MB-stem length and composition, we synthesised four different anti-miR-98 MBs without photocleavable element. We quantified the intensity of hybridisation-sensing fluorophore signal before and after miR-98 addition. The results of *in vitro* fluorescence studies with **MB1–MB4** are summarised in Fig. 2. After miR-98 addition, a 20- or 10-fold increase in hybridisation signal (on/off ratio) was observed with **MB1** and **MB3**, respectively. The hybridisation fluorescence increase of **MB2** was modest after addition of miR-98 and **MB4** showed a considerably higher background signal than other MB variants before target RNA addition. Therefore, circularisation and further fluorescence studies were performed with **MB1**- and **MB3**-analogues (see Fig. 4 and Fig. S2, ESI†). Furthermore, we tested whether the interaction between the MBs and miR-98 is specific. To examine specificity we conducted fluorescence measurements with **MB1–MB4** and miR-181a as a negative control. This miRNA is also highly abundant in hippocampal neurons.[25] The results are summarised in Fig. S3 (ESI,† Section 7). As expected, **MB1–MB4** did not show an increase in hybridisation signal when miR-181a was added.

To generate light-activatable MBs, we first synthesised the photolabile protected 2′OMe-phosphoramidite **4** (Fig. 3). Therefore, benzaldehyde **1** was converted into alcohol **2** in a Barbier-reaction. Compound **3** was obtained in a nucleophilic substitution of **2** with bis(diisopropylamino)–chlorophosphine. To isolate the final cytidine-phosphoramidite **4**, compound **3** was reacted with the respective DMTr-protected 2′OMe-C^{Ac} nucleoside.

The resulting compound **4** was installed at two positions in the loop-region close to the stem of previously characterised **MB3** *via* solid-phase synthesis. The postsynthetic circularisation was carried out with 2-((1,3-diazidopropan-2-yl)oxy)acetic acid as bifunctional linker under Cu(I)–TBTA catalysis. A ratio of 1 : 1 MB/linker was used to avoid a double addition. Owing to the proximity of the alkyne-modified photolabile protecting groups, the circularisation worked fast and resulted in acceptable yields of the tethered product **ptMB3**. It was expected that the hydrophilic carboxylic acid group of the coupled bifunctional linker would cause a shift to lower retention times on RP-HPLC, which would allow for easy purification. Despite the hydrophilic character, circularised MBs did not show a lower, but rather a higher retention time on RP-HPLC.

In the next step, we evaluated the fluorescence properties of **ptMB3** compared to unmodified **MB3** (Fig. 4). The background fluorescence of **ptMB3** before light-activation (3% of the signal obtained with **MB3** and target) was notably lower than the

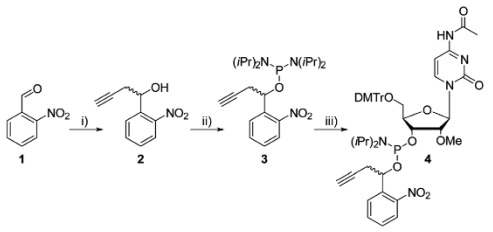

Fig. 3 Synthesis of phosphoramidite **4**. (i) Propargylbromide, Zn*, DMF, 99%. (ii) P[N(iPr)$_2$]$_2$Cl, DIPEA, MeCN, 64%. (iii) *N*-Acetyl-5′-*O*-[bis(4-methoxyphenyl)-phenylmethyl]-2′-*O*-methyl-cytidine, 5-benzylthio-1-*H*-tetrazole, MeCN, 73%.

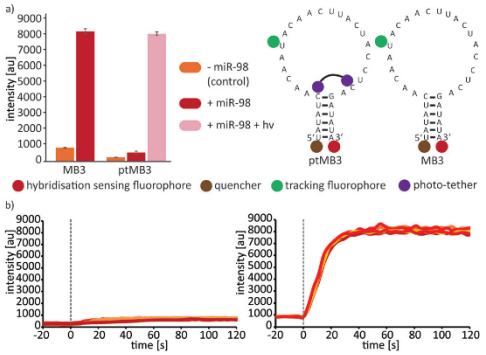

Fig. 4 (a) Fluorescence measurements of **ptMB3** and reference **MB3** with and without miR-98 in brain buffer at 37 °C (50 pmol, 100 µL, 500 nM). Irradiation was performed with a 365 nm LED for 8 minutes (350 mA). Sequence and molecular constitution of **ptMB3** and its expected photo-product **MB3**. (b) Hybridisation kinetics of **ptMB3** (left) and **MB3** (right) in brain buffer at 37 °C (50 pmol, 100 µL, 500 nM, experiment repeated 3–5×). Time zero (dashed line) indicates addition of target miR-98. The individual lines represent individual experiments.

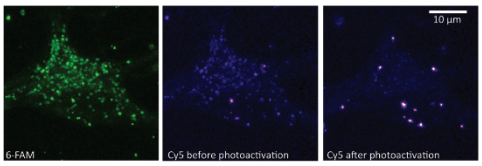

Fig. 5 Images of **ptMB3** transfected into a cultured hippocampal neuron. 6-FAM tracking fluorophore shows punctate structured distribution of **ptMB3** four hours after transfection (left). Before photo-activation with a 355 nm laser (50 mW), no significant Cy5 hybridisation signal is present (middle). Ten minutes after photo-activation a clear increase in hybridisation signal is observed (right). This indicates a light-triggered hybridisation with miR-98 in live-cells.

background fluorescence of **MB3** alone (10%). This reduction was most likely a result of restricted flexibility of 3′- and 5′-end due to photo-tethering. The covalent bond close to the stem stabilises the stem-loop structure. When miR-98 was added to **ptMB3**, a negligible fluorescence was observed (7%). This indicates that miR-98 is not able to efficiently form a double helix with **ptMB3** in the photo-tethered conformation. Upon light-activation and in the presence of miR-98, **ptMB3** showed a strong increase in hybridisation signal, which reached 98% of the maximum hybridisation fluorescence intensity that was observed with **MB3**. This observation indicates that irradiation fully restored the functionality of the photo-tethered MB. To verify that the hybridisation of **ptMB3** and miR-98 is permanently disabled and not kinetically decelerated, we performed fluorescence kinetics measurements (Fig. 4b). **MB3** was used as reference for the maximum fluorescence increase that was observed within 40 seconds with 50 pmol of **MB3** after the addition of miR-98. In comparison, **ptMB3** displayed a marginal signal increase within 40 seconds, which remained constant over the duration of 120 s.

Importantly, this ptMB combines all the positive aspects of photo-activatable MBs of previous studies without their respective drawbacks. First, the hybridisation signal before light-activation is much lower than with cyclised MBs generated by Tan *et al.*[17] Furthermore, we achieved a significant shift from a binding-incompetent ptMB to a binding-competent MB after light-induction without the use of seven photolabile groups.[19] Lastly, the emergence of the hybridisation fluorescent signal is the result of the binding of the ptMB to its target RNA sequence.[21]

Beyond fluorescence studies of **ptMB3** shown in Fig. 4, we investigated whether one can inhibit target hybridisation by using other photo-tether positions. Additionally, we tested if adding a second quencher to the stem would reduce the background fluorescence.[26] We found that these changes did not improve the ptMB's performance in terms of signal to noise or light-induction. For detailed information, see ESI,† Section 7.

To further test whether photo-tethered molecular beacons could be used *in vivo*, we transfected **ptMB3** into cultured hippocampal neurons. Two to four hours after transfection, live-cell imaging was performed. The tracking fluorophore 6-FAM was used to identify transfected neurons and **ptMB3** showed a punctate distribution over the entire soma (Fig. 5). Before photo-activation, no significant Cy5 hybridisation signal was observed. This observation is in agreement with our *in vitro* studies and indicates that hybridisation between **ptMB3** and miR-98 is inhibited in the tethered state of **ptMB3**. After photo-activation of the soma with a 355 nm laser, a clear increase in hybridisation fluorescence was detected in several spots that co-localised with tracking signal. This result indicates that ptMBs can be used for a spatio-temporally controlled hybridisation to miR-98 in living cells.

We conclude that ptMBs are a novel, superior class of light-activatable molecular beacons that display significant advantages to previously described approaches. ptMBs require just two (rather than seven[19]) photolabile protecting groups to successfully prevent the hybridisation to target miR-98. Before light-activation ptMBs exhibited a minimal background fluorescence in presence of miR-98; the signal increases 32-fold (for **ptMB3**) upon light-activation. The full activity of ptMBs was restored by the cleavage of a single photolabile protecting group, hence partially activated intermediates[19] do not exist. In contrast to the previously described caged Q-dye beacons,[21] ptMBs cannot bind their target sequence before light-activation, which is essential for time-resolved regulation. Furthermore, the synthesis of the photolabile-protected phosphoramidite is straightforward and consists of only three synthesis steps. The addition of a second fluorophore in the loop-region enables the tracking of transfected cells. Moreover, detection precision can be improved by the co-localisation of both tracking and hybridisation fluorophores.[24] Lastly, we demonstrated the successful application of ptMBs in cultured hippocampal neurons.

This work was supported by the Deutsche Forschungsgesellschaft through SFB902 (Molecular Principles of RNA-based Regulation). We thank Franziska Bachmeier and Prof. Alexander Vogel for HRMS measurements.

Open Access funding provided by the Max Planck Society.

Conflicts of interest

The authors declare no conflict of interest.

Notes and references

1 N. Ankenbruck, T. Courtney, Y. Naro and A. Deiters, *Angew. Chem., Int. Ed.*, 2018, **57**, 2768–2798.
2 C. Brieke, F. Rohrbach, A. Gottschalk, G. Mayer and A. Heckel, *Angew. Chem., Int. Ed.*, 2012, **51**, 8446–8476.
3 M. M. Lerch, W. Szymański and B. L. Feringa, *Chem. Soc. Rev.*, 2018, **47**, 1910–1937.
4 P. Klán, T. Šolomek, C. G. Bochet, A. Blanc, R. Givens, M. Rubina, V. Popik, A. Kostikov and J. Wirz, *Chem. Rev.*, 2013, **113**, 119–191.
5 B. K. Ruble, S. B. Yeldell and I. J. Dmochowski, *J. Inorg. Biochem.*, 2015, **150**, 182–188.
6 K. A. Brown, Y. Zou, D. Shirvanyants, J. Zhang, S. Samanta, P. K. Mantravadi, N. V. Dokholyan and A. Deiters, *Chem. Commun.*, 2015, **51**, 5702–5705.
7 J. Luo, E. Arbely, J. Zhang, C. Chou, R. Uprety, J. W. Chin and A. Deiters, *Chem. Commun.*, 2016, **52**, 8529–8532.
8 Z. Vaníková, M. Janoušková, M. Kamboová, L. Krásný and M. Hocek, *Chem. Sci.*, 2019, **10**, 3937–3942.
9 J. Kahlstatt, P. Reiß, T. Halbritter, L. O. Essen, U. Koert and A. Heckel, *Chem. Commun.*, 2018, **54**, 9623–9626.
10 A. R. Buxbaum, G. Haimovich and R. H. Singer, *Nat. Rev. Mol. Cell Biol.*, 2015, **16**, 95–109.
11 C. Glock, M. Heumüller and E. M. Schuman, *Curr. Opin. Neurobiol.*, 2017, **45**, 169–177.
12 K. Rau and A. Rentmeister, *ACS Cent. Sci.*, 2017, **3**, 701–707.
13 K. J. Westerich, K. S. Chandrasekaran, T. Gross-Thebing, N. Kueck, E. Raz and A. Rentmeister, *Chem. Sci.*, 2020, **11**, 3089–3095.
14 E. Braselmann, C. Rathbun, E. M. Richards and A. E. Palmer, *Cell Chem. Biol.*, 2020, **27**, 891–903.
15 J. Zheng, R. Yang, M. Shi, C. Wu, X. Fang, Y. Li, J. Li and W. Tan, *Chem. Soc. Rev.*, 2015, **44**, 3036–3055.
16 S. Tyagi and F. R. Kramer, *Nat. Biotechnol.*, 1996, **14**, 303–308.
17 C. Wang, Z. Zhu, Y. Song, H. Lin, C. J. Yang and W. Tan, *Chem. Commun.*, 2011, **47**, 5708–5710.
18 L. Yang, H. B. Kim, J.-Y. Sul, S. B. Yeldell, J. H. Eberwine and I. J. Dmochowski, *ChemBioChem*, 2018, **19**, 1250–1254.
19 K. Ballabh Joshi, A. Vlachos, V. Mikat, T. Deller and A. Heckel, *Chem. Commun.*, 2012, **48**, 2746–2748.
20 V. Magidson and A. Khodjakov, *Methods in Cell Biology*, Academic Press Inc., 2013, vol. 114, pp. 545–560.
21 J. S. Rinne, T. P. Kaminski, U. Kubitscheck and A. Heckel, *Chem. Commun.*, 2013, **49**, 5375–5377.
22 P. Müller, P. Seyfried, A. Frühauf and A. Heckel, *Methods in Enzymology*, Academic Press Inc., 2019, vol. 624, pp. 89–111.
23 P. Seyfried, L. Eiden, N. Grebenovsky, G. Mayer and A. Heckel, *Angew. Chem., Int. Ed.*, 2017, **56**, 359–363.
24 X. Feng, W. Kang, X. Wu, S. Wang and F. Liu, *ACS Appl. Mater. Interfaces*, 2019, **11**, 28752–28761.
25 S. Sambandan, G. Akbalik, L. Kochen, J. Rinne, J. Kahlstatt, C. Glock, G. Tushev, B. Alvarez-Castelao, A. Heckel and E. M. Schuman, *Science*, 2017, **355**, 634–637.
26 C. J. Yang, H. Lin and W. Tan, *J. Am. Chem. Soc.*, 2005, **127**, 12772–12773.

Reference [IV]: „Inactivation of Competitive Decay Channels Leads to Enhanced Coumarin Photochemistry”

Klimek, R.; Asido, M.; Hermanns, V.; Junek, S.; Wachtveitl, J.; Heckel, A., Chem. - Eur. J., **2022**, e202200647.

Author contributions:

Robin Klimek:

- design and synthesis of photolabile protecting groups
- steady-state absorption and fluorescence measurements
- photolysis experiments
- wrote and edited the manuscript

Marvin Asido:

- steady-state absorption und fluorescence measurements
- ultrafast transient absorption spectroscopy
- time-correlated single photon counting experiments
- wrote and edited the manuscript

Volker Hermanns:

- steady-state absorption und fluorescence measurements
- photolysis experiments
- edited the manuscript

Stephan Junek:

- designed fluorescence experiments
- edited the manuscript

Josef Wachtveitl:

- supervised project and experiments
- edited the manuscript

Alexander Heckel:

- supervised project and experiments
- edited the manuscript

Chemistry–A European Journal | Research Article
doi.org/10.1002/chem.202200647
Chemistry Europe
European Chemical Societies Publishing
www.chemeurj.org

Inactivation of Competitive Decay Channels Leads to Enhanced Coumarin Photochemistry

Special Collection

Robin Klimek[+],[a] Marvin Asido[+],[b] Volker Hermanns,[a] Stephan Junek,[c] Josef Wachtveitl,*[b] and Alexander Heckel*[a]

Abstract: In the development of photolabile protecting groups, it is of high interest to selectively modify photochemical properties with structural changes as simple as possible. In this work, knowledge of fluorophore optimization was adopted and used to design new coumarin- based photocages. Photolysis efficiency was selectively modulated by inactivating competitive decay channels, such as twisted intramolecular charge transfer (TICT) or hydrogen-bonding, and the photolytic release of the neurotransmitter serotonin was demonstrated. Structural modifications inspired by the fluorophore ATTO 390 led to a significant increase in the uncaging cross section that can be further improved by the simple addition of a double bond. Ultrafast transient absorption spectroscopy gave insights into the underlying solvent-dependent photophysical dynamics. The chromophores presented here are excellently suited as new photocages in the visible wavelength range due to their simple synthesis and their superior photochemical properties.

Introduction

In recent years, the use of light has gained enormous interest in the life sciences. An increasing number of research groups focusses on the use of photolabile protective groups (so-called "photocages") to regulate biological processes.[1–5] Aside from the application, however, also the development of new photocages is of high interest.[6,7] In order to be able to use light for targeted regulation, the photo-physical and -chemical properties of protecting groups have to match the requirements of the biological context. Here, especially two parameters are of crucial importance. The first is the excitation wavelength, preferably in the red range of the visible light spectrum and the second is the uncaging efficiency of the respective photocage. Regarding the first parameter, many studies have been published that focused on shifting the extinction maximum to longer wavelengths.[8,9]

Taking the coumarin photocage as an example, popular methods were the extension of the π-system, or the addition of donor and acceptor substituents (see Figure 1a).[10–13] Also with other photolabile protecting groups, for example BODIPY,[14,15] fluorenol,[16,17] or nitrobenzyl[18,19] a considerable red-shift was achieved with similar approaches. Nevertheless, the improvement of the second parameter, the uncaging efficiency, has not

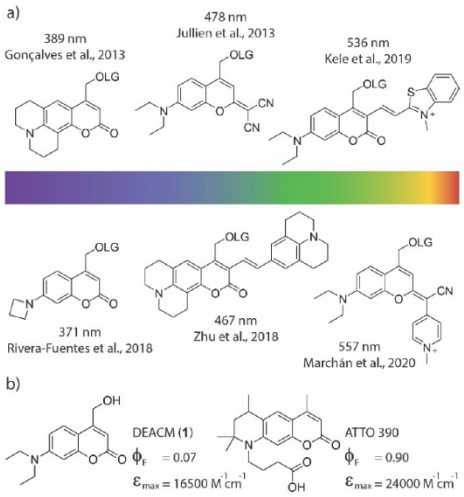

Figure 1. a) Selection of prominent coumarin based photocages in recent years and their reported absorption maxima. LG = leaving group. b) Structures and photophysical properties of DEACM 1 and ATTO 390.[20]

[a] R. Klimek,[+] V. Hermanns, Prof. Dr. A. Heckel
Institute for Organic Chemistry and Chemical Biology
Goethe University Frankfurt
Max-von-Laue Str. 9, 60438 Frankfurt (Germany)
E-mail: heckel@uni-frankfurt.de
[b] M. Asido,[+] Prof. Dr. J. Wachtveitl
Institute of Physical and Theoretical Chemistry
Goethe University Frankfurt
Max-von-Laue Str. 9, 60438 Frankfurt (Germany)
E-mail: wveitl@theochem.uni-frankfurt.de
[c] Dr. S. Junek
Max Planck Institute for Brain Research
Max-von-Laue Str. 4, 60438 Frankfurt (Germany)
[ ] These authors contributed equally to this work.
Supporting information for this article is available on the WWW under https://doi.org/10.1002/chem.202200647
Special Collection This manuscript is part of an Indo-German special collection.

been studied as systematically in the recent literature. Still, this is highly important, because if the applied light can be used more efficiently, side effects such as cell damage can be reduced.

Efficient photolysis means that the chromophore must have both a high extinction coefficient (ε) and a good uncaging quantum yield (ϕ_u). To increase the uncaging efficiency of a photocage, it is important to understand what other processes compete with the photolytic cleavage of a leaving group. A molecule in the excited state can release its energy through a variety of pathways (see Jablonski diagram, Figure 2a). In the fast range, there are rotations, vibrations, and isomerization around single atoms or bonds. Also, internal conversion (heat loss to the solvent)[20] or hydrogen-bonding[21] can lead to relaxation to the ground state.[22] If the excited state lives long enough (e.g. nanoseconds) and does not decay in any of the faster channels, the molecule can also release the energy via luminescence,[23] or a directed bond cleavage.

To date, there is only little information on how to rationally optimize the uncaging quantum yield of photocages. However, there are many advanced studies that have successfully optimized the performance of fluorophores.[24–26] Extinction coefficients and absorbance maxima have been modified. Unwanted photoreactions (e.g. photobleaching) and the amount of deactivation processes that happen earlier than fluorescence have been reduced. In many cases also the water solubility has been improved. Therefore, a possible strategy to develop new photocages with improved photolysis can be to use an optimized fluorophore with one major decay channel as a guide – an analogy that has recently also been followed by *Rivera-Fuentes* et al.[27] – and divert the excited state population into an uncaging reaction pathway.

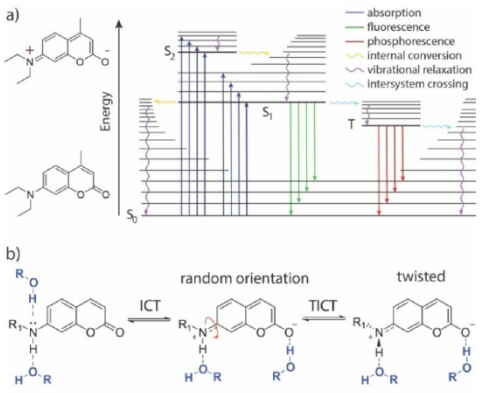

Figure 2. a) Jablonski diagram showing relevant transitions of coumarin chromophores when excited with light. S_0: ground state, S_1: first electronically excited singlet state, S_2: second electronically excited singlet state, T: triplet state. b) General model for twisted intramolecular charge transfer (TICT) in coumarin dyes. In addition, possible hydrogen-bonding sites are shown, that can affect non-radiative decay.

In this study, we explored this idea using ATTO 390[28,29] as an example, which has a fluorescence quantum yield of more than 90% in aqueous solution. Here, we show how to improve the uncaging cross section ($\varepsilon\phi_u$) of new ATTO 390-based photocages by up to one order of magnitude compared to literature known DEACM (**1**) (Figure 1b), applying principles from fluorophore optimization. Using ultrafast transient absorption spectroscopy, we gain insight into the fundamental photophysical processes that are critical both for fluorescence as well as for photolytic cleavage of a leaving group. Overall, we demonstrate that understanding excited state decay channels in fluorophores can be helpful for developing new photocages.

Results and Discussion

In coumarin fluorophores substituted like the one shown in Figure 2b, it is known that the molecule can adopt an intramolecular charge transfer (ICT) state.[30–32] After excitation, a rotation around the C–N bond at the donor moiety can occur. Thereby, repulsive interactions are minimized and charge separation is stabilized. The resulting twisted intramolecular charge transfer (TICT) state can release its energy to the medium non-radiatively.[33,34] In addition, as indicated in Figure 2b, it is possible that coumarins release their energy to the environment via hydrogen bonding.[21,35–37] However, a restricted rotation around the C–N bond is known to supress the TICT and therefore increase fluorescence.[38] This can be observed, for example, with ATTO 390, in which the exocyclic nitrogen atom is fixed by a six-membered ring. Therefore, ATTO 390 shows a high fluorescence quantum yield in comparison to freely rotating coumarins like DEACM (**1**).

Guided by this principle, we synthesized four new coumarin photocages **7a–d** (see Figure 3) which have a structure similar to ATTO 390. In all four compounds, the rotation around the C–N bond is restricted by a six-membered ring. Compounds **7a** and **7b** were additionally equipped with a double bond at the 6-position, which should make the framework even more rigid and the rotation more confined (see Figure 3b). By using this double bond, we hoped to limit non-radiative energy release on short time scales. The coumarin photocage should be even less capable of forming a TICT. However, derivatives **7b** and **7d** also featured an additional ethyl group on the nitrogen atom at the 7-position. This exhibits an electron donating character compared to the proton in **7a** and **7c** and should thus enhance the charge transfer character formation originating from the nitrogen that is necessary for uncaging. The absence of a hydrogen-atom can also prevent possible non-radiative decay upon hydrogen-bonding with protic solvents[34–37,39] and eliminates a potentially photoacidic site.[40,41]

The synthesis of compounds **7a–d** started from commercially available *m*-aminophenol **2** (see Figure 3a). In the first step, the hydroxy group of **2** was protected with *tert*-butyldimethylsilyl (TBDMS) in a quantitative yield. The resulting compound **3** was reacted with acetone under Yb^{3+} catalysis to quinoline **4a** in a Doebner-Miller type reaction.[42] Starting from **4a**, compound **4b** was obtained via alkylation with iodoethane

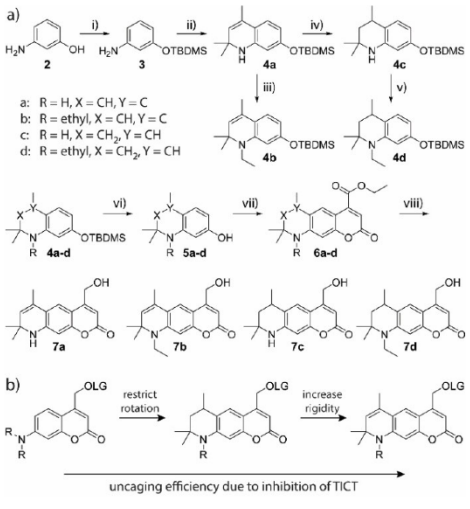

Figure 3. a) Synthesis of compounds **7a–d**. i) TBDMS–Cl, imidazole, DCM, quant. ii) $Yb(OTf)_3$, acetone, 77%. iii) iodoethane, Cs_2CO_3, MeCN, 78%. iv) Pd/C, H_2, MeOH, 98%. v) iodoethane, Cs_2CO_3, MeCN, 83%. vi) TBAF, AcOH, THF, 89–94%. vii) sodium diethyl oxalacetate, EtOH, 31–47%,. viii) $NaBH_4$, MeOH, 37–62%. TBDMS = tert-butyldimethylsilyl. b) Evolution of new coumarin-photocages with improved uncaging efficiency due to inhibition if intramolecular twisting. LG: leaving group, R: H/ethyl, TICT: twisted intramolecular charge transfer.

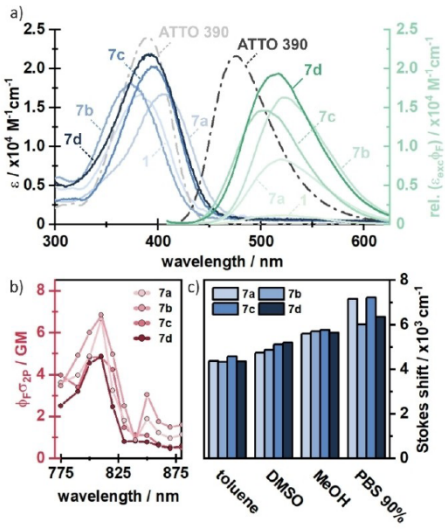

Figure 4. a) Steady-state absorption and fluorescence spectra of compounds **7a–d** in PBS. Spectra of ATTO 390 (taken from ATTO-tec)[29] and compound **1** are added for comparison. b) Two-photon absorption spectra of compounds **7a–d**. c) Stokes shifts in different solvents with different polarity.

Table 1. Photophysical properties of compounds **1**, ATTO 390[29] and **7a–d**.

	ε_{max} (PBS) [$M^{-1}cm^{-1}$]	λ_{abs} (PBS) [nm]	λ_{em} (PBS) [nm]	ϕ_F (PBS)	ϕ_F (DMSO)
1	16500	385	520	0.07	0.74
ATTO 390	24000	390	476	0.90	–
7a	16700	383	528	0.50	0.51
7b	18100	405	536	0.90	0.51
7c	20300	373	511	0.72	0.89
7d	21500	394	526	0.95	0.92

and Cs_2CO_3 under microwave irradiation and **4c** was isolated after selective hydration with H_2, Pd/C under atmospheric pressure in excellent yields. Hydration needed to be performed before the silyl protecting group was removed. Otherwise, we observed cleavage of the C–N bond at 7-position with H_2, Pd even at very short reaction times. The reduced compound **4c** was also alkylated with iodoeth ane to get **4d**. The TBDMS-groups of **4a–d** were removed with tetrabutylammonium fluoride (TBAF) and glacial acetic acid in 89–94% yields to give alcohols **5a–d**. Pechmann-condensation based on a procedure of Begoyan et al.[43] resulted in coumarin esters **6a–d**. During the reaction, several side products occurred that were hard to separate from the main product by column chromatography. Recrystallization further removed impurities but also resulted in poorer yields. Therefore, we decided to use compounds **6a–d** for further reactions after single column chromatography with minor impurities. After the reduction of the respective esters with $NaBH_4$, the alcohols **7a–d** were isolated in good yields and purities.

To evaluate the photophysical properties of compounds **7a–d**, one-photon (1P) absorption and fluorescence spectra were recorded in different solvents (see Figure 4 and Table 1). We compared the data to the most commonly used coumarin photocage DEACM (**1**) and ATTO 390 as reference compounds. In PBS (phosphate-buffered saline), compounds **7a–d** showed higher extinction coefficients in their absorption maxima (ε_{max}) than DEACM (**1**). Compared to ATTO 390 the ε_{max} of **7a–d** were slightly smaller. Compound **7d**, which has the most similar structure to ATTO 390 has also the lowest difference in the extinction coefficient. In general, an increased extinction coefficient compared to DEACM (**1**) is already a promising start towards the desired increase of the uncaging cross section $\varepsilon\phi_u$. The absorption maxima themselves (λ_{max}) were located between 373 nm and 405 nm. Thus, they were in the same range as the absorption maxima of DEACM and ATTO 390. The strongest shift was observed for compound **7b**, which had a 20 nm bathochromic wavelength shift relative to DEACM. Nevertheless, a minimal blue shift of 13 nm could also be observed for compound **7c**. In comparison, the data indicated that the compounds with the additional ethyl group showed a more red-shifted absorption spectrum. Compound **7d** (λ_{max} = 394 nm) absorbs most similarly to ATTO 390 (λ_{max} = 390 nm), what again can be rationalized with their very similar structure. The additional double bond in compound **7b** (λ_{max} = 405 nm) further increases the absorption wavelength. This red-shifting

effect of the double bond can also be observed when comparing compounds **7c** (λ_{max} = 373 nm) and **7a** (λ_{max} = 383 nm).

To evaluate whether our new coumarin compounds can also be excited with NIR light, we measured two photon absorption spectra of compounds **7a–d**. Here, we observe a two-photon absorption of 5–7 GM at 800–810 nm for all measured compounds (Figure 4b), which is in the same range as ATTO 390 (13 GM).[44] This 2P-transition is energetically equivalent to the main absorption maxima found at around 380–410 nm (Figure 4a), indicating that the proposed compounds can be one- or two-photon activated. This measurement shows that excitation is also possible in the so-called phototherapeutic window (650–950 nm), in which light has a particularly high penetration depth into biological tissue.[45]

To get a first impression of how the newly synthesized chromophores release their excitation energy, we measured fluorescence quantum yields (see Table 1). Since fluorescence and uncaging occur on approximately the same time scale, this parameter may provide a first indication of successful inactivation of faster decay channels. Additionally, comparing polar solvents (such as PBS) to less polar ones (such as DMSO) may indicate whether TICT is involved. For medium polar solvents like DMSO, it is known that coumarin charge separation is only stabilized to a limited extent, resulting in a high ϕ_F, independent of their flexibility.[46] It is also possible that rotation around the C–N bond is hindered in solvents with relatively high viscosity, such as DMSO.[47]

In aqueous solution, however, the amine substituent can rotate freely if it is not fixed by a six-membered ring, since water is less viscous. This is in agreement with the measured high ϕ_F for compounds **7a–d** and DEACM (**1**) in DMSO, ranging between 51% and 95%. When DMSO was replaced by PBS, the ϕ_F of DEACM (**1**) was reduced from 74% to 7% whereas fluorescence of **7a–d** remained on a high level. This reduction in fluorescence suggests that rotation around the C–N bond in DEACM is possible in less viscous PBS, but it is inhibited in all newly synthesized derivatives **7a–d**. In turn, this points towards a TICT state in DEACM, which is hindered in compounds **7a–d**. The fluorescence quantum yields further show that the two compounds with the ethyl group **7b** and **7d** emit best in PBS. This can be explained by the fact that the ethyl group can stabilize the charge separation more effectively over a longer period of time. A similar quantum yield in PBS (90%) is shown by ATTO 390 itself, which also carries an alkyl group at the nitrogen atom.

To investigate the effect of stabilization of charge separation in more detail, we also studied the Stokes shifts in different polar solvents (see Figure 4c). Again, the polarity of the solvent is expected to have a strong influence on the emission wavelength. We observed that all compounds **7a–d** showed already large Stokes shifts in unpolar solvents (4334–4583 cm^{-1} in toluene). When the polarity of the solvent was increased, an overall rise in the Stokes shifts was observed. The largest Stokes shifts were measured in PBS buffer (6035–7240 cm^{-1}), supporting that there is charge transfer in all molecules which is stabilized by the solvent to different degrees.

To gain an even deeper insight into the photophysical dynamics of the newly synthesized compounds, we employed ultrafast UV/vis transient absorption spectroscopy in different solvents. Here, the general spectral features of these compounds shall be explained exemplarily in the case of compound **7a** in MeOH (see Figure 5a). The photoexcitation from the ground state leads to a broad excited state absorption (ESA_S) signature, which spans from 620 nm up to more than 730 nm. Simultaneously, the stimulated emission (SE_1) from S_1 to S_0 can be found in the range of 430–550 nm, which is consistent with the steady state fluorescence spectra. After about 300–500 fs, an additional absorption signal (ESA_{ICT}) appears at approximately 400 nm and 430 nm. The amplitude of the 430 nm component rises further on the 1–50 ps timescale, which is accompanied by a decrease of the ESA_S band and a strong red-shift of the stimulated emission by 40 nm forming SE_2 (Figure 5a and 5c). The latter effect is related to the excited state intramolecular charge transfer (ICT) from the nitrogen of the amine group to the oxygen of the carbonyl group, which is further stabilised by the solvent response on the ps timescale.

In contrast to compound **7a**, it can be observed that in compound **7b** (Figure S1b, Supporting Information) the blue component of the ESA_{ICT} feature at around 400 nm is mainly populated, which means that the excited state is more stabilized in **7b** relative to **7a**. The less pronounced stabilization of the excited state in **7a** most likely results from a hydrogen

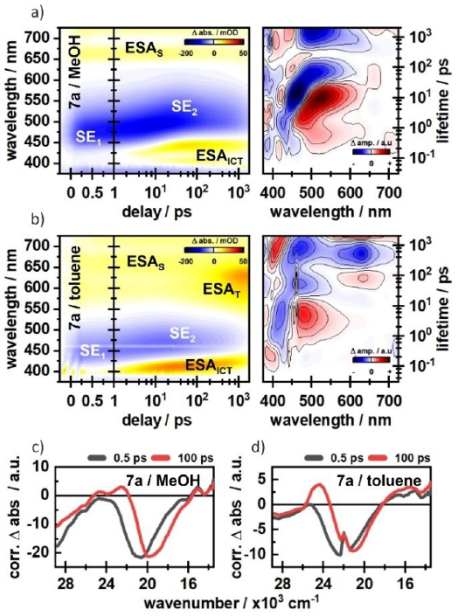

Figure 5. Transient absorption spectra of compound **7a** in MeOH (a) and toluene (b). Time slices at 0.5 ps and 100 ps underline the dynamic stokes shifts in c) MeOH and d) toluene.

bond at the nitrogen, which is formed in addition to the stabilizing hydrogen bond at the carbonyl group.[27] In toluene, compound **7a** shows a miniscule dynamic Stokes-shift of the SE band (Figure 5b and 5d). However, the ESA_{ICT} is still formed, indicating a population of an ICT state, which is less stabilised by the surrounding solvent. Instead, an additional absorption (ESA_T) around 600 nm is formed on the 100 ps timescale, which we tentatively assign to triplet formation. A similar ESA_T signature is found for **7a** in DMSO (Figure S1c, Supporting Information), which is also aprotic but significantly more polar. Therefore, the excited state dynamics are not just strongly influenced by the solvent polarity, but also by the solvent proticity and the general accessibility of hydrogen bonding interactions. Besides the obvious stabilization of the excited state in polar solvents, the effect of solvent proticity is more complicated, since there are different sites for hydrogen bonding. Whereas hydrogen bonds with the carbonyl oxygen or the nitrogen-bound proton are reported to have a stabilising effect on the excited state, a hydrogen bond with the lone-pair of nitrogen has the opposite effect.[35–37] The reduction of energy in the ICT state due to these effects leads to a favourable ICT-population. In contrast, the population of the triplet state is seemingly facilitated in the case of missing hydrogen bonding.[48–50] Further details on the solvent effects as well as cross-comparisons between the compounds are given in the Supporting Information of this article. The transient absorption measurements demonstrated that all four new compounds form an ICT state. The ethyl group in compound **7b** seems to further stabilize the charge separation in comparison to compound **7a** as can be seen in the significantly increased ESA_{ICT} amplitudes (Figure S1, Supporting Information). However, this effect is not seen in the direct comparison of compounds **7d** and **7c** (see Figure S2, Supporting Information), which lack the additional double bond.

But even more interesting to us was, whether the added rigidity of the new compounds would also lead to improved photolysis. Therefore, we attached serotonin as a biologically active leaving group (see Figure 6). Serotonin is an important

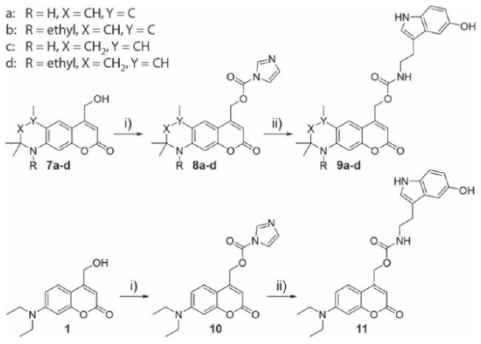

Figure 6. Synthesis of compounds **9a–d** and **11**. i) CDI, DCM, 79–89 %. ii) 5-Hydroxytryptamine hydrochloride, Et_3N, DMF, 56–77 %.

neurotransmitter that plays a crucial role in signal transduction in the central nervous system.[51] The synthesis started by reacting compounds **7a–d** with carbonyldiimidazole (CDI) under microwave irradiation resulting in **8a–d**. To generate the final photolabile protected serotonin-derivatives **9a–d**, compounds **8a–d** were reacted with 5-hydroxytryptamine hydrochloride. The same procedure was used to synthesize DEACM-protected serotonin **11**, starting from DEACM (1) as a reference.

After preparation we performed first photolysis tests in PBS/DMSO (9:1). We added this small amount of DMSO because the photocages were only moderately soluble in pure PBS. To make the photolysis results comparable, the quantum yields for compounds **9a–d** and **11** were determined at 405 nm using a fulgide derivative as actinometer.[52] The decrease of starting materials was monitored by HPLC with the addition of an internal standard. After the experiments, we were surprised that the uncaging quantum yields for compounds **9a–d** and **11** differed only minimally from each other. This contradicted all assumptions from previous literature and the earlier determined fluorescence behaviour of the compounds. The fluorescence experiments indicated that competitive relaxation pathways in compounds **7a–d** were blocked which in turn leads to an increased fluorescence quantum yield compared to DEACM. Since fluorescence and uncaging occur on the same time scale, the uncaging quantum yield of compounds **9a–d** should also be enhanced in direct comparison to reference compound **11**.

To investigate this unexpected outcome in more detail, we performed ultrafast transient absorption spectroscopy in PBS/DMSO (9:1). Interestingly, in this solvent, the amplitudes of the difference signals are significantly reduced (Figure S1b and f, S2b and f). This becomes most obvious in the ESA_{ICT} band, which is the dominant feature in all measurements. In contrast to the other tested solvents, the ESA_{ICT} does not show a major rise in amplitude on the 10–100 ps timescale in PBS/DMSO (Figure S3), implying a less pronounced population of the CT state. However, it was shown in recent work[53] that the charge separation is crucial in order to facilitate elongation of the C–C bond, which is cleaved in the subsequent uncaging process. Additionally, the solvent response due to the ultrafast change in dipole moment is somewhat more complicated in PBS/DMSO mixtures. It is reported that DMSO and H_2O form strong hydrogen bond clusters even at small amounts of DMSO.[54,55] For simple coumarin-based compounds this means that the solvent reorganization in the excited state is mostly driven by DMSO, which "drags" H_2O along through their H-bond network.[56] It is therefore possible that DMSO at the photochemically relevant site suppresses photocleavage in a PBS/DMSO mixture due to the less pronounced CT character and a possible shielding from H_2O. The latter aspect is especially relevant since water molecules (or other nucleophiles) are needed to capture the carbo-cation which is formed during uncaging.[57]

Therefore, we substituted PBS/DMSO with PBS/MeOH (1:1) in further experiments, because MeOH and H_2O do not interact as strongly, and MeOH itself can serve as a nucleophile to trap the exocyclic carbocation in the coumarin scaffold formed

during uncaging. After changing the solvent, we were now able to see clear differences in uncaging quantum yield between the newly synthesized compounds **9a–d** and the reference DEACM derivative **11**. The photolysis results are shown in Table 2. An exemplary photolysis curve of compound **9b** is shown in Figure 7, the remaining curves are shown in Figures S6–S10. Our experiments show, that the uncaging quantum yield (ϕ_u) was already significantly increased by the ring closure in **9c** and **9d**. While **11** releases serotonin with a ϕ_u of 0.56%, it is increased by a factor of 2–3 in compounds **9c** (0.96%) and **9d** (1.63%). This already shows the positive effect of the restricted rotation. If an additional double bond is now introduced, a further increase in the uncaging quantum yield can be observed. Compound **9a** releases serotonin with a quantum yield of 2.56% and **9b** even with 2.97%. As expected, this increase in quantum yield clearly indicates that the additional restricted rotation suppresses competitive decay channels. Therefore, a more than fivefold increase in uncaging quantum yield was observed for **9b** compared to **11**. The improvement of the photochemical properties becomes even more obvious if the extinction coefficient ε at the excitation wavelength is included in order to study the uncaging cross section ($\phi_u\varepsilon$). It can be seen in Table 2, that solely adding a six-membered ring leads to an increase by a factor of 3–4 compared to DEACM. When the double bond is additionally introduced, the uncaging cross section at 405 nm raises by one order of magnitude. While **11** photolyzes with 50 $L\,mol^{-1}\,cm^{-1}$ at 405 nm, the best compound **9b** shows 617 $L\,mol^{-1}\,cm^{-1}$. Compound **9d**, on the other hand, which has a similar structure as **9b** only without a double bond, has a cross section of 184 $L\,mol^{-1}\,cm^{-1}$. At this point, it is clear that the simple introduction of a double bond can lead to a more than threefold increase in photolysis efficiency.

In the last step, we wanted to investigate whether uncaging as an additional excitation pathway can also be observed using ultrafast UV/vis pump-probe transient absorption spectroscopy. For this purpose, we sought to compare the derivatives with leaving group (**9a–d**) with those previously measured without leaving group (**7a–d**, see Figure 5). The measurements of **9a–d** revealed very similar photophysical signatures compared to **7a–d**. All compounds show the characteristic solvent- and time-dependent ESA and Stokes shifts on the picosecond timescale. More interestingly, we observed that the excited state (ES) decay of **9a–d** is shifted towards earlier times compared to **7a–d**, which can be seen in the lifetime density distribution of the respective measurements (Figures 8a and 8b, and Figure S5). To validate this temporal shift we performed time correlated single photon counting (TCSPC) measurements in PBS/MeOH (1:1) (Figure 8c). These experiments showed a very clear difference in the fluorescence lifetimes of **7a–d** and **9a–d**. While the fluorescence lifetimes of **7a–d** are found to be between 4.6 and 5.4 ns, the fluorescent states of **9a–d** are depopulated between 2 and 2.6 ns (Table S1), being consistent with the lifetimes found in the TA-experiments (Figure S5). This more than 2-fold reduction of radiative decay lifetimes is most likely due to added possibility to undergo photocleavage, which is competing with fluorescence. An overview of the proposed energy pathways is given in Figure 8d.

Table 2. Photophysical and photochemical properties of compounds **9a–d** and reference DEACM **11** at 405 nm used for uncaging experiments in PBS/MeOH (1:1).

	ϕ_u (405 nm) (PBS/MeOH)	ε (405 nm) (PBS/MeOH) [$M^{-1}\,cm^{-1}$]	$\phi_u\varepsilon$ (405 nm) (PBS/MeOH) [$M^{-1}\,cm^{-1}$]
11	0.0056	9097	50
9a	0.0256	19666	504
9b	0.0297	20788	617
9c	0.0163	10606	173
9d	0.0096	19268	184

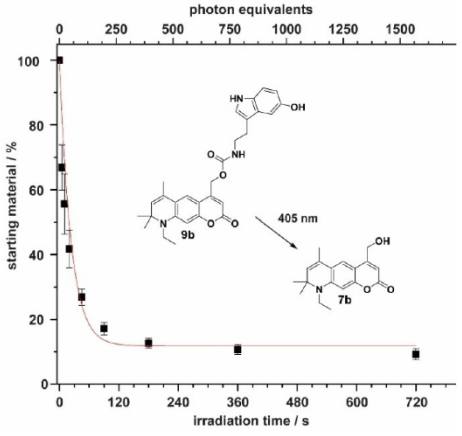

Figure 7. Exemplary photolysis curve of compound **9b** in PBS/MeOH (1:1). Photolysis product **7b** was identified via mass spectrometry.

Conclusion

In this work, we show a systematic investigation of uncaging efficiency of coumarin photolabile protecting groups. Guided by the principles of fluorophore optimization, we wanted to reduce competitive decay channels on new ATTO 390-based photocages. To improve the photolysis, in a first step, the rotation around the electron donor on the coumarin scaffold was prevented using a simple six-membered ring (compounds **7c** and **7d**). This already increased the uncaging efficiency by a factor of 3–4 compared to DEACM (**1**). However, the simple introduction of an additional double bond on that six-membered ring had an even stronger effect. Again, the efficiency of light-induced release of serotonin was increased by a factor of 2–3 (compounds **6a** and **6b**). This is the first time that such a minimal change to the coumarin backbone has resulted in a significant improvement in photolysis efficiency. We used ultrafast transient absorption spectroscopy to investigate the underlying photophysical dynamics. The newly synthesized photocages showed strong solvent dependencies

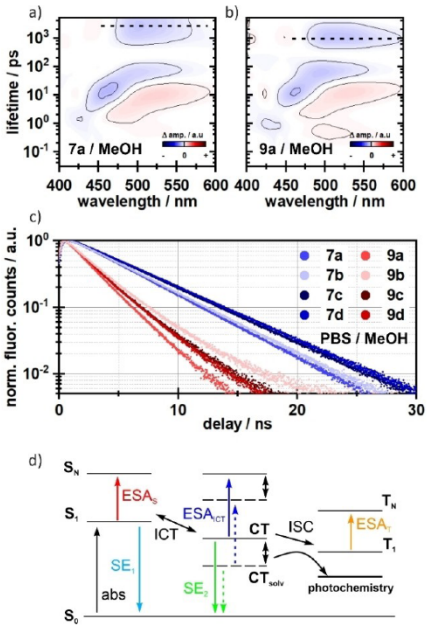

Figure 8. Lifetime density analysis of **7a** (a) and **9a** (b) measured in MeOH. The ES decay is faster in compound **9a** (indicated as dashed lines), whereas the dynamics on the fs- to ps-timescale do not differ. A similar pattern is seen in the TCSPC measurements (c). The fluorescence lifetimes of compounds **9a–d** are roughly 2-fold faster. The corresponding lifetime components are given in the Supporting Information. d) Schematic representation of possible energy pathways. After excitation, an equilibrium between the locally excited state S_1 and the CT state is formed. The CT state is further stabilized by the solvent (indicated by double-sided arrows), which increases the population of the CT state. Without this stabilization an additional channel for triplet formation becomes relevant, which then competes with the actual photochemistry.

in their fluorescence and uncaging properties. It became clear that the charge-transfer state in coumarin chromophores is not just well stabilized by polar solvents, but also essential for photolysis. The new photocages described here are easy to synthesize and, due to their photophysical properties, can be used for both one-photon applications using blue light and in the phototherapeutic window (700–900 nm) using two-photon excitation. In summary, we think that the development of photolabile protecting groups can indeed very well profit from what has already been learned in the optimization of fluorophores. This can be a good guiding principle for future development.

Experimental Section

Chemical synthesis: All reactions were performed under an argon atmosphere unless otherwise specified. Solvents and reagents were purchased from commercial sources. DEACM **1** was synthesized according to literature.[58] Synthetic procedures of new compounds and their characterization are provided in the Supporting Information. Microwave reactions were performed in a *Biotage Initiator* system. NMR spectra of new compounds were recorded on (250 MHz, 300 MHz, 400 MHz, 500 MHz and 600 MHz) *Bruker* instruments. MALDI HRMS spectra were recorded on a *ThermoScientific MALDI LTQ Orbitrap XL* instrument.

Ultrafast TA-spectroscopy: The time-resolved transient absorption measurements were performed using a home-built pump-probe setup. A Ti:Sa chirped pulse regenerative amplifier (MXR-CPA-iSeries, Clark-MXR Inc., USA) with a central output wavelength of 775 nm, a 1 kHz repetition rate, and a pulse width of 150 fs was used as the fs-laser source. The fundamental was split for pump and probe pulse generation. Pump pulses at a central wavelength of 388 nm were generated in a second harmonic generation (SHG). The temporal FWHM of the final pump pulses was determined to be ~120–130 fs. The excitation energy was set to 90 nJ/pulse at the sample position. The supercontinuum for the probe pulses was generated by focusing the fundamental in a constantly moving CaF_2 window of 5 mm thickness, leading to stable white light in the range of 375–740 nm. The white light was then split and guided through the sample and the reference arm of the detection setup. Each arm makes use of a spectrograph (Multimode, AMKO, Germany), which is equipped with two gratings (300 nm/500 nm blaze, 600/1200 grooves per mm), a photodiode array (S8865-64, Hamamatsu Photonics, Japan) and a corresponding driver circuit (C9118, Hamamatsu Photonics, Japan). The signals were digitized by a 16 bits data acquisition card (NI-PCI-6110, National Instruments, USA). The pump and probe pulses were set to the magic angle configuration at 54.7° to account for anisotropic effects. The sample-compartment was constantly moved to minimize sample degradation.

Fluorescence lifetimes: The fluorescence decays of the compounds **7a–d** and **9a–d** were determined by the time-correlated single photon counting (TCSPC) technique. Our home-built TCSPC setup is composed of a single-photon detection photomultiplier tube (PMA-C 182 M, PicoQuant, Germany) and a PCIe card (TimeHarp 260 PICO Single, PicoQuant) for sub-ns data processing. Pulsed orthogonal excitation of the samples was achieved by a pulsed LED (PLS360, PicoQuant) with a peak wavelength of 360 nm and a FWHM <800 ps. Deconvolution with the IRF and multi-exponential fitting of the temporal traces was performed with FluoFit Pro 4.6 (PicoQuant) based on the following equation[59]

$$I(t) = \int_{\infty}^{t} IRF(t') \sum_{i=1}^{n} A_i e^{-\frac{t-t_i}{\tau_i}} dt'$$

The samples were measured in 4×10 mm quartz glass cuvettes with an OD of ~0.1 on 10 mm optical pathlength.

Determination of quantum yields: Three stock solutions of each compound **9a–d** and **11** were prepared by diluting approx. 1.0 mg in MeOH/PBS (1:1). For photolysis 50 µL were taken and irradiated at nine different irradiation times (t = 0 s, 5 s, 10 s, 20 s, 45 s, 90 s, 180 s, 360 s, 720 s) with a 405 nm LED (*Thorlabs*), resulting in 27 differently irradiated solutions for each compound. The photon flux for the setup was determined with a fulgide-derivative – as described in literature.[52] The photolysis was analyzed via RP-HPLC (*Agilent 1200*) as the ratio of the peak areas of starting material and uridine as internal standard – as described in literature.[16]

Acknowledgements

We gratefully acknowledge funding of the Deutsche Forschungsgemeinschaft (DFG) through the research training group "CLiC" (GRK 1986, Complex Light-Control) and the CRC902 "Molecular principles of RNA-based regulation". Open Access funding enabled and organized by Projekt DEAL.

Conflict of Interest

The authors declare no conflict of interest.

Data Availability Statement

The data that support the findings of this study are available in the supplementary material of this article.

Keywords: ATTO 390 · coumarin · fluorophore · photocage · TICT

[1] N. Ankenbruck, T. Courtney, Y. Naro, A. Deiters, *Angew. Chem. Int. Ed.* **2018**, *57*, 2768–2798; *Angew. Chem.* **2018**, *130*, 2816–2848.
[2] G. Bort, T. Gallavardin, D. Ogden, P. I. Dalko, *Angew. Chem. Int. Ed.* **2013**, *52*, 4526–4537; *Angew. Chem.* **2013**, *125*, 4622–4634.
[3] W. Szymański, J. M. Beierle, H. A. V. Kistemaker, W. A. Velema, B. L. Feringa, *Chem. Rev.* **2013**, *113*, 6114–6178.
[4] V. M. Lechner, M. Nappi, P. J. Deneny, S. Folliet, J. C. K. Chu, M. J. Gaunt, *Chem. Rev.* **2022**, *122*, 1752–1829.
[5] C. Brieke, F. Rohrbach, A. Gottschalk, G. Mayer, A. Heckel, *Angew. Chem. Int. Ed.* **2012**, *51*, 8446–8476; *Angew. Chem.* **2012**, *124*, 8572–8604.
[6] P. Klán, T. Šolomek, C. G. Bochet, A. Blanc, R. Givens, M. Rubina, V. Popik, A. Kostikov, J. Wirz, *Chem. Rev.* **2013**, *113*, 119–191.
[7] R. Weinstain, T. Slanina, D. Kand, P. Klán, *Chem. Rev.* **2020**, *120*, 13135–13272.
[8] L. Josa-Culleré, A. Llebaria, *ChemPhotoChem* **2021**, *5*, 298–316.
[9] P. Štacko, T. Šolomek, *Chimia* **2021**, *75*, 873–881.
[10] L. Fournier, I. Aujard, T. Le Saux, S. Maurin, S. Beaupierre, J. B. Baudin, L. Jullien, *Chem. Eur. J.* **2013**, *19*, 17494–17507.
[11] Q. Lin, L. Yang, Z. Wang, Y. Hua, D. Zhang, B. Bao, C. Bao, X. Gong, L. Zhu, *Angew. Chem. Int. Ed.* **2018**, *57*, 3722–3726; *Angew. Chem.* **2018**, *130*, 3784–3788.
[12] M. Bojtár, A. Kormos, K. Kis-Petik, M. Kellermayer, P. Kele, *Org. Lett.* **2019**, *21*, 9410–9414.
[13] M. López-Corrales, A. Rovira, A. Gandioso, M. Bosch, S. Nonell, V. Marchán, *Chem. Eur. J.* **2020**, *26*, 16222–16227.
[14] P. Shrestha, K. C. Dissanayake, E. J. Gehrmann, C. S. Wijesooriya, A. Mukhopadhyay, E. A. Smith, A. H. Winter, *J. Am. Chem. Soc.* **2020**, *142*, 15505–15512.
[15] T. Slanina, P. Shrestha, E. Palao, D. Kand, J. A. Peterson, A. S. Dutton, N. Rubinstein, R. Weinstain, A. H. Winter, P. Klán, *J. Am. Chem. Soc.* **2017**, *139*, 15168–15175.
[16] M. Reinfelds, J. von Cosel, K. Falahati, C. Hamerla, T. Slanina, I. Burghardt, A. Heckel, *Chem. Eur. J.* **2018**, *24*, 13026–13035.
[17] V. Hermanns, M. Scheurer, N. F. Kersten, C. Abdellaoui, J. Wachtveitl, A. Dreuw, A. Heckel, *Chem. Eur. J.* **2021**, *27*, 14121–14127.
[18] Y. Becker, E. Unger, M. A. H. Fichte, D. A. Gacek, A. Dreuw, J. Wachtveitl, P. J. Walla, A. Heckel, *Chem. Sci.* **2018**, *9*, 2797–2802.
[19] Y. Becker, S. Roth, M. Scheurer, A. Jakob, D. A. Gacek, P. J. Walla, A. Dreuw, J. Wachtveitl, A. Heckel, *Chem. Eur. J.* **2021**, *27*, 2212–2218.
[20] C. Reichardt, *Chem. Rev.* **1994**, *94*, 2319–2358.
[21] G. J. Zhao, K. L. Han, *Acc. Chem. Res.* **2012**, *45*, 404–413.
[22] C. A. Hoelzel, H. Hu, C. H. Wolstenholme, B. A. Karim, K. T. Munson, K. H. Jung, H. Zhang, Y. Liu, H. P. Yennawar, J. B. Asbury, X. Li, X. Zhang, *Angew. Chem. Int. Ed.* **2020**, *132*, 4815–4822.
[23] L. B. McGown, K. Nithipahkom, *Appl. Spectrosc. Rev.* **2000**, *35*, 353–393.
[24] J. B. Grimm, A. K. Muthusamy, Y. Liang, T. A. Brown, W. C. Lemon, R. Patel, R. Lu, J. J. Macklin, P. J. Keller, N. Ji, L. D. Lavis, *Nat. Methods* **2017**, *14*, 987–994.
[25] J. B. Grimm, L. D. Lavis, *Nat. Methods* **2022**, *19*, 149–158.
[26] M. V. Sednev, V. N. Belov, S. W. Hell, *Methods Appl. Fluoresc.* **2015**, *3*, 042004.
[27] G. Bassolino, C. Nançoz, Z. Thiel, E. Bois, E. Vauthey, P. Rivera-Fuentes, *Chem. Sci.* **2018**, *9*, 387–391.
[28] D. Luo, C. Kuang, X. Liu, G. Wang, *Opt. Laser Technol.* **2013**, *45*, 723–725.
[29] "ATTO-TEC GmbH – ATTO 390," can be found under https://www.atto-tec.com/product_info.php?info=p1_atto-390.html.
[30] T. Debnath, H. N. Ghosh, *ChemistrySelect* **2020**, *5*, 9461–9476.
[31] D. Cao, Z. Liu, P. Verwilst, S. Koo, P. Jangjili, J. S. Kim, W. Lin, *Chem. Rev.* **2019**, *119*, 10403–10519.
[32] J. V. Jun, D. M. Chenoweth, E. J. Petersson, *Org. Biomol. Chem.* **2020**, *18*, 5747–5763.
[33] A. Barik, M. Kumbhakar, S. Nath, H. Pal, *Chem. Phys.* **2005**, *315*, 277–285.
[34] G. Jones, W. R. Jackson, C. Y. Choi, W. R. Bergmark, *J. Phys. Chem.* **1985**, *89*, 294–300.
[35] Y. Liu, J. Ding, R. Liu, D. Shi, J. Sun, *J. Photochem. Photobiol. A* **2009**, *201*, 203–207.
[36] N. P. Wells, M. J. McGrath, J. I. Siepmann, D. F. Underwood, D. A. Blank, *J. Phys. Chem. A* **2008**, *112*, 2511–2514.
[37] P. Zhou, P. Song, J. Liu, K. Han, G. He, *Phys. Chem. Chem. Phys.* **2009**, *11*, 9440–9449.
[38] C. Wang, W. Chi, Q. Qiao, D. Tan, Z. Xu, X. Liu, *Chem. Soc. Rev.* **2021**, *50*, 12656–12678.
[39] T. López Arbeloa, F. López Arbeloa, M. J. Tapia Estévez, I. López Arbeloa, *J. Lumin.* **1994**, *59*, 369–375.
[40] T. Halbritter, C. Kaiser, J. Wachtveitl, A. Heckel, *J. Org. Chem.* **2017**, *82*, 8040–8047.
[41] C. Kaiser, T. Halbritter, A. Heckel, J. Wachtveitl, *Chem. Eur. J.* **2021**, *27*, 9160–9173.
[42] S. A. Yamashkin, E. A. Oreshkina, *Chem. Heterocycl. Compd.* **2006**, *42*, 701–718.
[43] V. V. Begoyan, L. J. Weseliński, S. Xia, J. Fedie, S. Kannan, A. Ferrier, S. Rao, M. Tanasova, *Chem. Commun.* **2018**, *54*, 3855–3858.
[44] C. A. Hammer, K. Falahati, A. Jakob, R. Klimek, I. Burghardt, A. Heckel, J. Wachtveitl, *J. Phys. Chem. Lett.* **2018**, *9*, 1448–1453.
[45] A. M. Smith, M. C. Mancini, S. Nie, *Nat. Nanotechnol.* **2009**, *4*, 710–711.
[46] R. Misra, S. P. Bhattacharyya, in *Intramol. Charg. Transf.*, Wiley-VCH Verlag GmbH & Co. KGaA, Weinheim, Germany, **2018**, pp. 115–148.
[47] D. Liese, G. Haberhauer, *Isr. J. Chem.* **2018**, *58*, 813–826.
[48] G. J. Zhao, K. L. Han, *J. Phys. Chem. A* **2007**, *111*, 9218–9223.
[49] G. J. Zhao, K. L. Han, *J. Phys. Chem. A* **2009**, *113*, 14329–14335.
[50] L. Biczók, T. Bérces, T. Yatsuhashi, H. Tachibana, H. Inoue, *Phys. Chem. Chem. Phys.* **2001**, *3*, 980–985.
[51] R. L. Carhart-Harris, D. J. Nutt, *J. Psychopharmacol.* **2017**, *31*, 1091–1120.
[52] M. Reinfelds, V. Hermanns, T. Halbritter, J. Wachtveitl, M. Braun, T. Slanina, A. Heckel, *ChemPhotoChem* **2019**, *3*, 441–449.
[53] C. Hamerla, C. Neumann, K. Falahati, J. Von Cosel, L. J. G. W. Van Wilderen, M. S. Niraghatam, D. Kern-Michler, N. Mielke, M. Reinfelds, A. Rodrigues-Correia, A. Heckel, J. Bredenbeck, I. Burghardt, *Phys. Chem. Chem. Phys.* **2020**, *22*, 13418–13430.
[54] A. K. Soper, A. Luzar, *J. Phys. Chem.* **1996**, *100*, 1357–1367.
[55] I. I. Vaisman, M. L. Berkowitz, *J. Am. Chem. Soc.* **1992**, *114*, 7889–7896.
[56] L. R. Martins, A. Tamashiro, D. Laria, M. S. Skaf, *J. Chem. Phys.* **2003**, *118*, 5955–5963.
[57] T. Eckardt, V. Hagen, B. Schade, R. Schmidt, C. Schweitzer, J. Bendig, *J. Org. Chem.* **2002**, *67*, 703–710.
[58] T. Weinrich, M. Gränz, C. Grünewald, T. F. Prisner, M. W. Göbel, *Eur. J. Org. Chem.* **2017**, *2017*, 491–496.
[59] J. Enderlein, R. Erdmann, *Opt. Commun.* **1997**, *134*, 371–378.

Manuscript received: February 28, 2022
Accepted manuscript online: April 14, 2022
Version of record online: May 12, 2022